University of Alberta

Characterization and Evaluation of Aged 20Cr32Ni1Nb Stainless Steels

by

Matthew Dewar

A thesis submitted to the Faculty of Graduate Studies and Research in partial fulfillment of the requirements for the degree of

Master of Science

in

Materials Engineering

Department of Chemical and Materials Engineering

Spring 2013

Edmonton, Alberta

I would like to dedicate this thesis to my loving parents, who were gracious enough to let me live in their home for the duration of my studies. Without you I would have had to face the harsh, cruel realities of the actual world.

Abstract

20Cr-32Ni-1Nb stainless steel alloys are commonly used in hydrogen reformer manifolds for transporting hot hydrogen by-products at 750-950°C. After long periods of exposure, embrittling secondary carbides and intermetallic phases can precipitate at the grain boundaries which can drastically reduce the ductility, and the repair weldability of the alloy. The intermetallic silicide, G-phase, is commonly observed in 20Cr-32Ni-1Nb stainless steels, and is prone to liquation cracking during welding operations. G-phase is deleterious to the material, where a high degree of G-phase coarsening will render the material unweldable.

The present work will investigate various methods in mitigating G-phase precipitation. Variations in casting methods, wall thickness, homogenization treatments, and alloy chemistry will be examined by evaluating their microstructure after periodically aging the samples. Thermodynamic equilibrium modeling using computational thermodynamic tools will be used to optimize the 20Cr-32Ni-1Nb chemistry following ASTM specifications.

Acknowledgements

I would like to first and foremost thank my supervisor Dr. Adrian Gerlich for his patience and support. I would also like to thank Hugh Roth for providing me with the opportunity to work on this project. I hope the results of this thesis are useful to you and your colleagues at Syncrude. I would like to thank Dr. Patricio Mendez, and colleagues of the CCWJ for keeping my head afloat in times of trouble. Lastly, I would like to acknowledge Sergei Matveev, Shihong Xu, and De-Ann Rollings for teaching, and assisting me with the electron microscopy work.

Contents

List of Tables

List of Figures

Glossary

constituent Element, or species, that occupies a specific sublattice of a specific phase. A phase can also be considered as a constituent of the total system.. 28, 39, 168

end-member The final chemical formula of a stable or metastable phase whose sublattice(s) are occupied by single constituents. For example $M_{23}C_6$ is an end member of $(Cr, Ni, Fe, Nb)_{23}C_6$.. 31

factor The independent variable of a factorial design. 41

main effect How much the change in an individual factor effects the change in the response variable of a factorial design.. 41

replicate Independent repetition of a treatment in a factorial experiment. 43

response variable The dependent variable of a factorial experiment, or a regression model.. 41

ThermoCalc A computational thermodynamics program that can calculate equilibrium phase diagrams for multicomponent systems, as well as Scheil simulations, and various thermodynamic properties (C_p, ΔH_m, ΔG_m etc...). 25

treatment A specific level of a factor in a factorial design.. 42, 49

Acronyms

AES Auger Electron Microscope. 47, 50, 56, 57, 72, 77–80, 87, 89, 95, 97
ANOVA Analysis of variance. 41, 42

BSE Backscattered Electron. 54

CEF Compound-energy formalism. 31–33

EDS Energy Dispersive X-ray Spectroscopy. 47, 52, 54–58, 64, 70, 72, 75, 77, 79, 87, 89, 91, 95
EPMA Electron Probe Microanalysis. 47, 50, 57, 58, 64, 65, 70, 72, 77, 78, 80, 85, 90, 95, 97, 185, 190

HAZ Heat Affected Zone. 18, 19

ICP Inductively coupled plasma. 47

LRO Long Range Ordering. 31

SE Secondary Electron. 54, 57
SEM Scanning Electron Microscope. 47, 50, 53, 56, 57, 64, 70, 72, 77–79, 87, 95, 97

TEM Transmission Electron Microscopy. 16

WDS Wavelength Dispersive Spectroscopy. 47, 56–58, 64, 70, 72, 77–79

XRD X-ray Diffraction. 50, 57, 58, 95, 97

Nomenclature

β_j	the effect of the ith level of factor ‘B’
ϵ_{ijk}	random error component
$\forall$	for all instances of ...
$\in$	in a set ...
μ	Overall mean effect
μ_i	Chemical potential of component or end-member i
ψ_k	the effect of the ith level of factor ‘C’
τ_i	the effect of the ith level of factor ‘A’
G	total Gibbs energy; $G = \sum_\alpha m^\alpha \cdot G_m^\alpha$
G_i^α	partial Gibbs energy of component i in phase α; $G_i^\alpha = \left(\frac{\partial G^\alpha}{\partial N_i}\right)_{T,P,N_j}$
G_m^α	integral molar Gibbs energy of a phase
I_i	constituent array of order i
L_I	interaction parameter of compound I
m^α	fraction of a phase
N_i	moles of component i
R	gas constant, $8.314 Jmol^{-1}K^{-1}$
R^2	coefficient of multiple determination
S_m^α	molar entropy of a phase
T	Temperature (K)
x_i	total mol fraction of component i; $x_i = \sum_\alpha m^\alpha \cdot x_i^\alpha$
x_i^α	mole fraction of component i in phase α

Chapter 1

Introduction

High temperature stainless steels have been used for the last 60 years in reformer furnaces as furnace tubes, outlet pigtails, and manifold components. The operating temperatures of these furnace components range from 750-950°C where these steels contain large concentrations of chromium (18-25 wt%), and nickel (20-38 wt%), and low concentrations of carbon (0.1 wt%) to provide resistance to oxidation, carburization, and corrosion effects [1]. Due to the low carbon concentrations, poor creep properties and service lives resulted in the manifold [5]. To improve the strength, and creep rupture properties of the alloy, carbon concentrations were increased to 0.4-0.5wt%, which promoted precipitation strengthening through the formation of $M_{23}C_6$ and M_7C_3 carbides. In an attempt to further increase the strength and creep life of the alloy, $\sim$ 1wt% niobium and other microalloy elements, such as titanium, tungsten, and zirconium were introduced, to stabilize the microstructure against formation of $M_{23}C_6$ with the precipitation of primary MC carbides. The increase in carbon content, while increasing the properties of the steel, also embrittles the steel due to the coarsening of secondary chrome carbide precipitates, reducing the steels ductility, and serviceability. Failure in these alloys has occurred due to ductility dip in the heat affected zone (HAZ) during repair welding [4].

The 20Cr32Ni1Nb (2032Nb) alloy was developed to decrease embrittlement, and $M_{23}C_6$ fraction in the reformer furnace components by reducing the carbon content to $\sim$ 0.1wt%. The 2032Nb alloy was also considered as a cost effective alternative offering comparable corrosion and creep resistance to its predecessor. As a result of reducing carbon, an intermetallic silicide called G-phase consumes the primary MC carbides after long periods at elevated temperatures. A recent failure of the 2032Nb alloy at a hydrogen reforming plant determined that G-phase was responsible for the failure causing ductility dip, and liquation cracking in the interdendritic regions of the casting [2]. While G-phase does not embrittle the material to the extent of $M_{23}C_6$, G-phase is unable to be repair welded due to its low melting point causing liquation cracking in the HAZ.

Currently after long periods in service, the ductility of the 2032Nb component is recovered by solution annealing at 1150-1230°C for 1-3 hours. During this treatment all of the G-phase, and $M_{23}C_6$ are dissolved. Secondary precipitate recovery is not permanent through solution annealing, and costs a large amount of energy and resources to perform. Modifications to the 2032Nb chemistry have been proposed to increase creep rupture strength, and ductility of the steel [18], as well as minimize G-phase stability [11]. The modified 2032Nb is currently being promoted for use in reformer furnaces, however up until this point a detailed thermodynamic study has not been done to fully optimize the chemistry of these alloys. Additions of other alloying elements such as nitrogen, and titanium have also been neglected. Furthermore, the precipitation, and coarsening rates of the 2032Nb microstructure, and how they differ with various casting methods (static cast vs centrifugal cast), homogenization treatments, and casting wall thicknesses has not yet been analyzed.

1.1 Hydrogen reforming process & mechanical design

The purpose of a catalytic reformer is to upgrade the quality of petroleum byproducts by converting natural gas, or hydrocarbons into hydrogen which then can be used to synthesize useful products such as ammonia (NH_3), hydrogen (H_2), or methanol (CH_3OH) [1]. Equation 1.1 shows that this is a endothermic reaction requiring energy which can be obtained from burning natural gas or naphtha [19]. The by-products of the catalytic reaction are now at a high temperature between 750-950°C causing axial stresses of 1-4 MPa on the pipes collecting and transporting the gas. Figure 1.1 shows the operating temperature and pressure ranges for the three types of products [1]. These temperatures and pressures cause axial and hoop stresses on the pipe, leading to longitudinal and circumferential creep, which reduces the operational life expectancy of the part [19]. These conditions require the pipe and manifold components to be cast from alloys that displays resistance to oxidation, and corrosion at high temperatures, as well as have a high creep resistance.

$$\mathrm{CH_4} + \mathrm{H_2O} \xrightarrow{755-1089\ \mathrm{K}} 3\mathrm{H_2} + \mathrm{CO} \tag{1.1}$$

An illustration of a typical steam reformer furnace is shown in Fig. 1.2. The catalyst tubes is where Eq. 1.1 occurs from the gas burners, which is then transported to the subheader via pigtails. The gas is collected in the subheader and pumped into a transfer line which will transport it for storage. During operation the outlet manifold system, including the subheader, and subcollector, will be at 800-850 °C. A survey from 24 refining companies reported operating upsets for the reformer manifolds ranged from 0.2 to 6 per year, with an average of 2 upsets per year [1].

Most outlet manifold systems today are made out of cast 2032Nb, however a few reformers are still reported to have manifold systems with the old non-niobium stabilized wrought 800HT alloy [1]. Outlet pigtails with wrought 800HT are still commonly used in operation. Any damage detected in the pigtails will not cause an emergency shutdown of the reformer, as the pigtails can be 'nipped' and 'binded' where they will then be replaced with the next scheduled shutdown. Damage, or cracking in the outlet manifold is more concerning, and can cause catastrophic damage if any cracks in the material are not

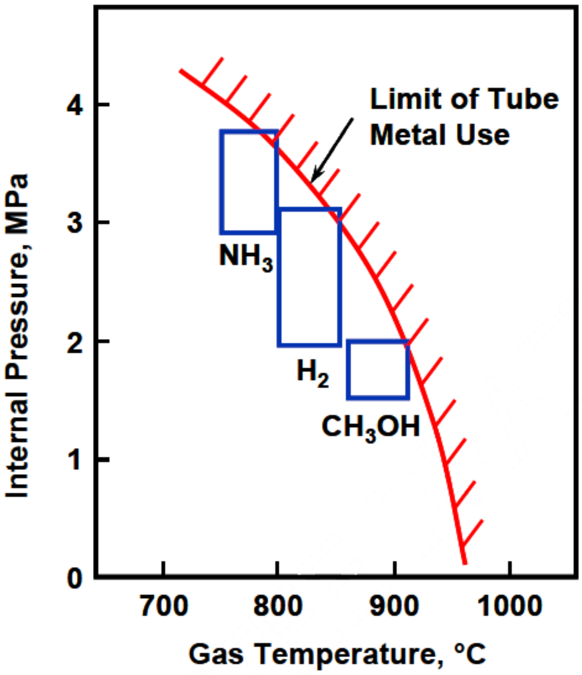

Figure 1.1: Temperature and pressure ranges for ammonia, hydrogen, and methanol reforming processes [1]

tended to. Unless the component can be effectively repair welded without any complications from severe embrittlement of the part, or liquation cracking from G-phase, the reformer must be shutdown to either replace, or heat treat the damaged component. A photograph of the major outlet manifold components is shown in Fig. 1.3, consisting of a reducer cone which ranges in thickness from 1-3 inches, connected to a bull tee, which has a constant thickness of one inch. The reducer cone must be centrifugally cast due to changes in thickness, in order to minimize macro- and micro-segregational effects that will vary the properties of the component from top to bottom.

1.2 History of stainless steels used for the outlet manifold

Figure 1.4 illustrates the history of austenitic stainless steels used for the hydrogen reformer outlet manifolds. Alloy 800, 800H, and 800HT variants were first used in production after 1965. Each variant of alloy 800 contains progressively less carbon, and high concentrations of aluminum and titanium. The microstructure of these variants consists of mostly $M_{23}C_6$, and Ti(C,N), where the creep strength is fairly poor due to the low carbon concentration where a larger wall thickness will be needed to compensate for higher loads. All of the 800 variants have similar corrosion resistance, and the 800H variant has a low tendency towards embrittlement. The HU40, and HK40 variants contain a higher carbon concentration around 0.4%, improving the creep strength of the alloy by precipitating higher concentrations of $M_{23}C_6$

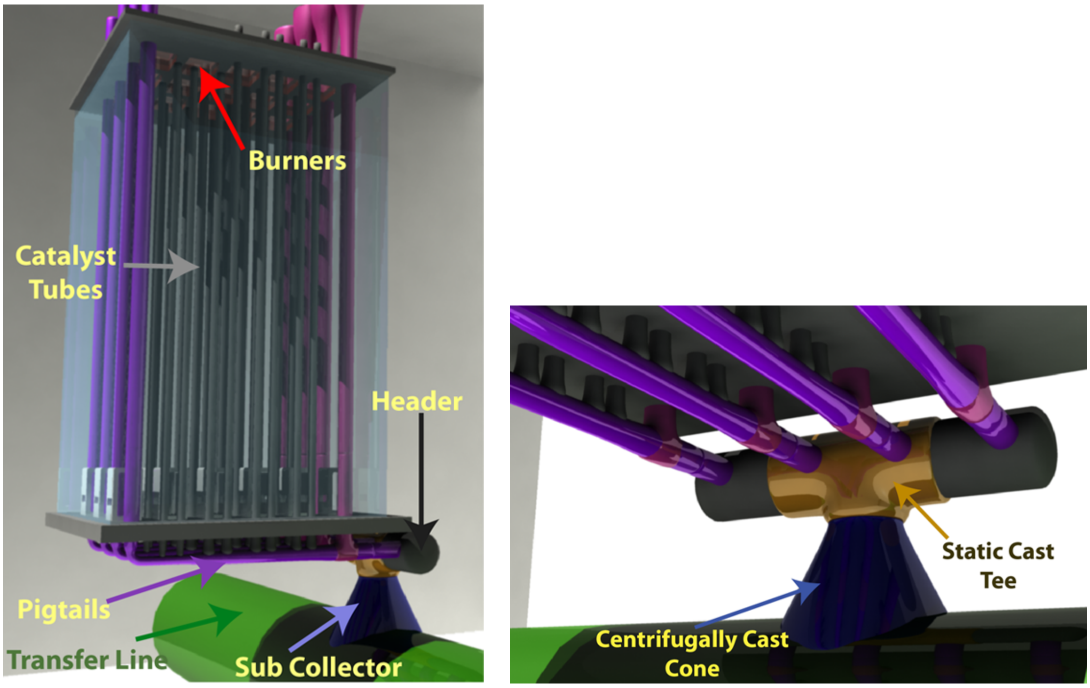

Figure 1.2: 3D illustration of hydrogen reformer furnace with a hot oulet manifold system. The manifold system is cast as two seperate parts with different casting methods. The reducer cone of the manifold is centrifugally cast and then welded to the statically cast tee component.

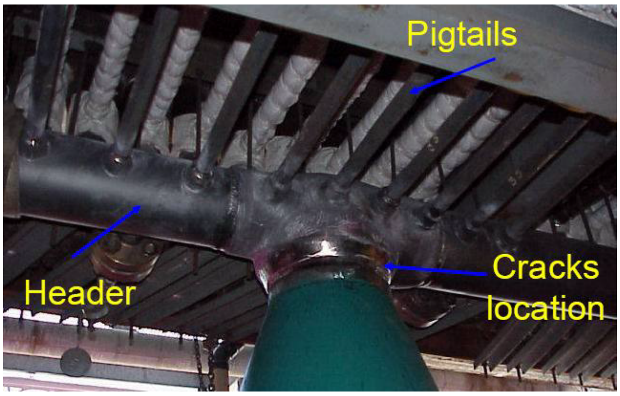

Figure 1.3: Photograph of a hydrogen reformer manifold, where a new reducer cone was welded to an existing tee [4].

and M_7C_3. Due to the higher strengths in the HU40 and HK40 steels, the wall thickness of these alloys can be reduced. Creep damage was found in both the HU40 and HK40 manifolds due to embrittlement caused by the precipitation of the secondary carbides [7]. Approximately 1wt% niobium was added to create the HPNb variant in order to stabilize the microstructure producing a lower secondary carbide fraction, and precipitating fine NbC carbides. MC carbides greatly improve creep strength, but also reduce the ductility of the alloy. After long periods of aging, these MC carbides transform into M_6C, also known at η-phase, leading to further ductility loss in the dendrite cell boundaries. Microalloy additions of titanium, zirconium, tungsten, and tantalum were introduced to the HPNb alloy in order to increase its creep life in excess of 100,000 hours [5]. Carbon content in the 2032Nb alloy was reduced to < 0.1wt%, showing creep strength levels comparable to the HK40 alloy. The 2032Nb variant is seen as a cost effective alternative to the HK40, and HPMA variants. The lower carbon levels permit the transformation of NbC into the brittle silicide G-phase after long periods in-service. G-phase and $M_{23}C_6$ produces coarse, agglomerated, continuous precipitates in the 2032Nb alloy, which increases the possibility of fracture due to liquation cracking susceptibility of G-phase. The recent development of Super 2032Nb alloy has been optimized to minimize G-phase fraction, and G-phase coarsening, limiting the propagation of liquation cracks produced during repair welding.

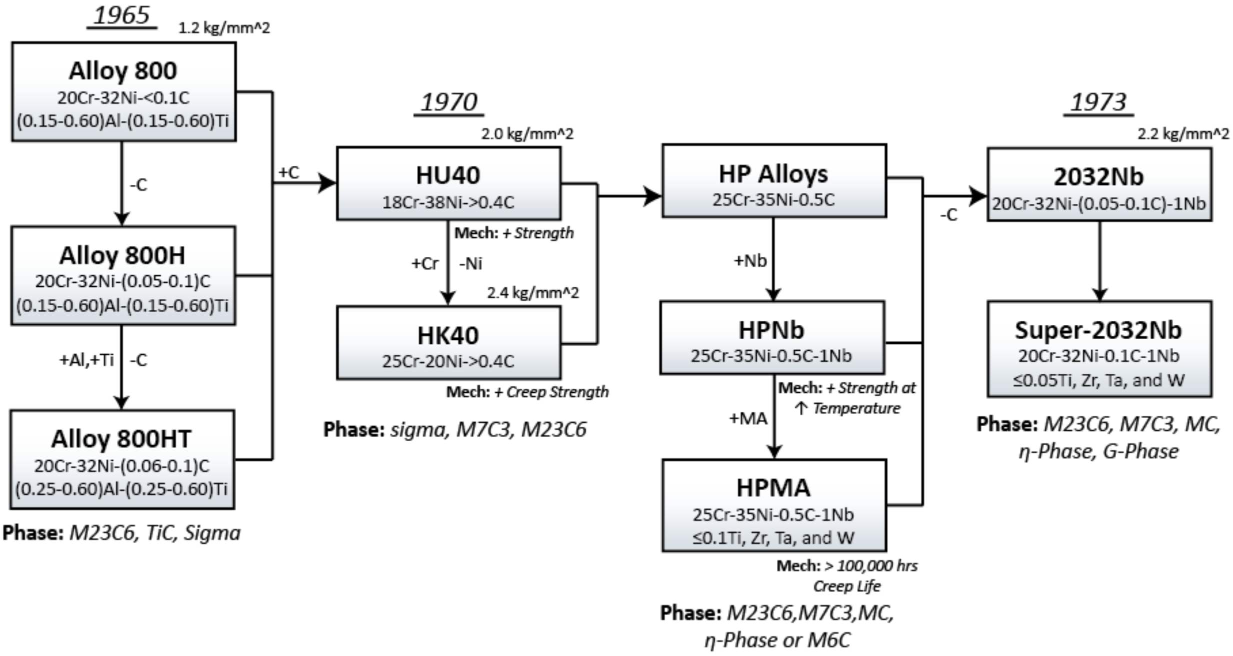

Figure 1.4: Alloy history and development of austenitic stainless steels for use in hydrogen reformer furnaces [5, 6, 7]. The number at the top right of the alloy represents the creep rupture strength in 100,00 hrs at 850°C[7].

1.3 Objectives

The purpose of this work is to optimize the serviceability of the 2032Nb manifold components in terms of its chemistry, and casting parameters. No direct mechanical tests evaluating the parts serviceability are performed; however, the microstructural evolution of the alloy can be related to its serviceability based on prior knowledge and research of embrittling, and liquating precipitates. Primarily G-phase stability will need to be minimized, as eliminating G-phase, or minimizing the size and fraction of G-phase precipitates will avoid liquation cracking in the part. If liquation cracking is eliminated the components will be able to be repair welded in-service, reducing plant shutdown times. Furthermore, any interdendritic carbides, or interdendritic intermetallic phases will need to be moderated in order to limit the amount of embrittlement the component experiences during long periods in service.

Initial characterization of the microstructure of an ex-service 2032Nb hydrogen manifold will be performed with Scanning Electron Microscope (SEM), Energy Dispersive X-ray Spectroscopy (EDS), Auger Electron Microscope (AES), Electron Probe Microanalysis (EPMA), Wavelength Dispersive Spectroscopy (WDS), and X-ray Diffraction (XRD). Quantitative measurements of grain size, dendrite size, phase chemistry, phase fraction, and precipitate size will be compiled. The ex-service components will then be aged up to one year from both a solution annealed, and button melted state.

Several 2032Nb casting will be experimentally aged up to one year from an as-cast state, varying the wall thickness (1 inch vs. 3 inch), casting methods (static vs. centrifugal cast), chemistry (commercial vs. modified), and post-casting homogenization treatment. The microstructural evolution of each casting will be analyzed, and the best parameters for optimizing serviceability will be discussed.

The chemistry of the 2032Nb alloy will be optimized looking at equilibrium microstructures computed from the thermodynamics software package ThermoCalc. Nitrogen and titanium additions will be analyzed to see if they can improve the microstructure, and the serviceability of the alloy. Lastly regression functions from the ThermoCalc output will be calculated, and a linear programming model will be derived to find an optimal solution.

1.4 Outline

In Chapter 2, the microstructure and mechanical properties previously analyzed in 2032Nb alloy, and similar variants such as the 20Cr25Ni1Nb variant will be reviewed, providing a detailed description of how precipitates and solute elements contribute to the mechanical properties of the alloy. Embrittlement in 2032Nb stainless steel will be discussed, as well as current repair welding techniques, and the possibility of liquation cracking caused by coarse, agglomerated G-phase. Chemistry optimization techniques will also be discussed, pertaining to the current Super 2032Nb alloy currently in the market.

Chapter 3 will present the proposed Gibbs free energy models for the 2032Nb system, as well as outline some of the techniques, and algorithms used by the thermodynamics software package ThermoCalc, used to compute the equilibrium. Chemistry optimization techniques with the use of ThermoCalc will be presented drawing from statistical factorial design modeling, and regression.

Chapter 4 includes the characterization techniques used to analyze two ex-service components, one static cast, and the other centrifugally cast. These manifold components have been in-service for 16 years, and will be aged from both the cast state and a solution annealed state to compare and contrast their microstructural evolution. A second experiment is described to study optimized 2032Nb chemistries, and how varying casting parameters such as the wall thickness, and post heat treatments effect the microstructural evolution. Metallography procedures for the samples will be described, as well as microscopy and microstructural quantification techniques including optical, SEM/EDS, AES, EPMA/WDS, and XRD. Casting variation between the ex-service components, and image analysis techniques used to calculate phase fractions will be explained.

In Chapter 5, the results from the ex-service component characterization will be presented. Microstructural differences through the thickness of both the static cast, and centrifugally cast components will be discussed. The phase fraction, and precipitate size evolution of the microstructure during aging up to one year will be presented. A discussion on the positive, and negative effects from adding nitrogen to the 2032Nb component will be proposed.

Chapter 6 will present the characterization, and microstructural evolution results of the optimized chemistries, and their various castings. Samples with two different chemistries, cast with a 1" and 3" wall thickness, and samples left in the as-cast state, and samples homogenized after casting will all be examined and compared. Aging was conducted up until two months where precipitate size, and phase fractions are presented.

Lastly, Chapter 7 will outline and discuss the ThermoCalc optimization experiments looking primarily at the introduction of nitrogen and titanium into the 2032Nb system. The results from these studies will be compared to the current chemistries, and optimization techniques current used. Regression models for each of the factorial experiments are presented, as well as some specific optimized chemistries.

Chapter 2

Hydrogen reforming process, austenitic stainless steels, and the 2032Nb variant

2.1 Composition of Austenitic Stainless Steels

Austenitic stainless steels are primarily used for high temperature applications, and consist of varying fraction of > 50wt% iron, > 12wt% chromium, and > 8wt% nickel. The austenitic structure provides sufficient mechanical strength, and creep resistance at high temperatures [4]. Figure 2.1a shows a isothermal ternary diagram of Fe-Cr-Ni at 800°C calculated from ThermoCalc, where the 2032Nb alloy, and the similar 2025Nb alloy are both entirely in the austenitic region. The high chromium concentration is known to prevent oxidation and corrosion of the material at elevated temperatures. To retain an austenitic structure a significant amount of nickel must also be added to stabilize this structure at all temperatures [20]. Alloying elements such as carbon, nitrogen, and manganese can be added to compensate the nickel concentration in stabilizing the austenite. To a similar extent alloy additions of silicon, molybdenum, niobium, titanium, and tungsten can be used to compensate for chromium, contributing to the corrosion, and sensitization resistance, as well as the overall strength of the alloy.

The addition of 1wt% niobium is used to lower the solubility of carbon and nitrogen in austenite forming stable Nb(C,N) precipitates [21], which contributes to precipitation strengthening, and the creep strength of the alloy. Niobium is also stable in a number of intermetallic compounds predicted to form at equilibrium, many of them can lead to embrittlement of the microstructure [13]. In higher carbon stainless steels ($\sim 0.5 wt\% C$), M_6C or η-phase with a stoichiometry of Cr_3Ni_2SiC will eventually transform from existing primary MC precipitates, or form from excess niobium. For lower carbon austenitic stainless steels ($< 0.1 wt\% C$), the deleterious G-phase, with a formulation $Ni_{16}Nb_6Si_7$, will form instead of η-phase.

Both these phases have a solubility for silicon; however, in order for the stainless steel to be formable during casting, approximately 0.5-1.5 wt% of silicon needs to be added to the composition. Figure 2.1b shows the ternary phase diagram of Ni-Nb-Si where G-phase is seen to precipitate in the middle of the diagram.

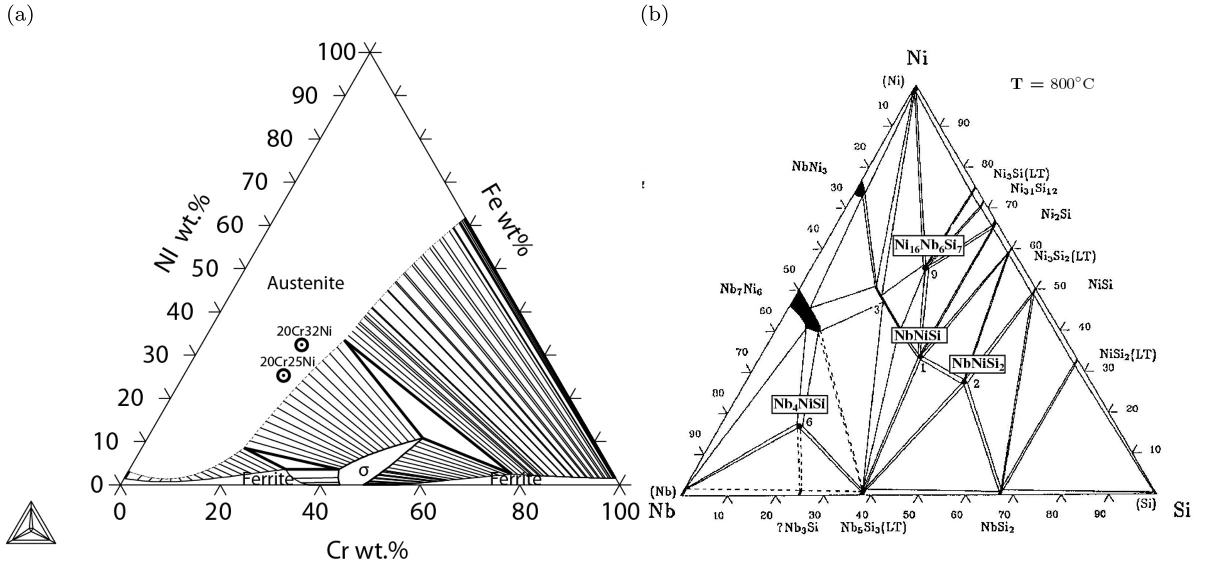

Figure 2.1: Isothermal section of the a) Fe-Cr-Ni system, and b) Ni-Nb-Si system at 800°C. a) was calculated using the TCFE6 database, and b) was taken from the *ASM Handbook* [8]

2.2 Influence of alloying elements & precipitates

2.2.1 Effects from alloying elements

Alloying elements can have different effects on how they interact with the resulting microstructure of the component. Shingledecker *et al.* defines these alloying rules as: reactant effects, catalytic effects, inhibitor effects, and interference effects [22]. Reactant effects are from elements that directly form a phase, such as niobium and carbon/nitrogen precipitating out as Nb(C,N). Catalytic effects occur from other elements that are not constituents of a phase, but participate in promoting the precipitation rate of a phase. For example, molybdenum will increase the precipitation rate of $M_{23}C_6$ [23]. Inhibitor effects are the opposite of catalytic effects where the element impedes the kinetics of a phase. For example, manganese decreases the activity of carbon in solution which in turn decreases the formation of $M_{23}C_6$. Interference effects relate to how elements compete in different phases, and alloy systems. For example both carbon and nitrogen are soluble in Nb(C,N), however nitrogen displays a higher affinity for niobium than carbon, where the Nb(C,N) can replace carbon with nitrogen to achieve a lower energy state [24].

The following will outline how the major components of 2032Nb affect the microstructure, and properties of this alloy.

2.2.1.1 Chromium

Chromium is mainly added to steel to provide corrosion, oxidation, and carburization resistance, by forming an oxide film on the surface [4]. Chromium is a ferrite stabilizer and will segregate to grain and dendrite boundaries which can lead to the formation of coarse embrittling phases such as sigma phase, and $M_{23}C_6$. Sensitization of the steel, which relates to the breakdown in corrosion resistance, can occur if abundant precipitation and coarsening of $M_{23}C_6$ and M_7C_3 develops along the grain boundaries [25]. Chromium will be depleted in these intergranular zones, where they will be susceptible to corrosion attack. Sensitization can be avoided by adding an excess of chromium into the alloy, or by sequestering the carbon into more stable phases, such as NbC or TiC.

2.2.1.2 Nickel

As discussed above, nickel is required to stabilize the austenitic phase, where an increase in chromium concentration must be compensated by an increase in nickel concentration. Increasing the nickel concentration decreases the solubility of carbon while increasing its diffusivity. This effect becomes increasingly evident in alloys with >20wt% Ni [23]. On the other hand nickel is also known to decrease the diffusivity of chromium. Nickel also has an accelerating effect on precipitating the Z-Phase nitride.

2.2.1.3 Niobium, Titanium, and Vanadium

Niobium is the important addition to high temperature stainless steels, stabilizing the microstructure by precipitating NbC carbides during solidification. Titanium, and vanadium can also form primary carbides, however they are typically only added as microalloy additions to help increase the strength of the alloy. Niobium is much more soluble in austenite than either titanium, or vanadium which is why it is primarily added to these stainless steels. Niobium, titanium, and vanadium all reduce the solubility of carbon in austenite, promoting the precipitation of primary carbides, and $M_{23}C_6$ which increases the creep strength of the material. On the other hand ductility is also lost from the precipitation of MC carbides.

2.2.1.4 Carbon and Nitrogen

Carbon and nitrogen exist as interstitial elements providing solid-solution strengthening to the alloy unless niobium, titanium, or vanadium are present, where they will instead precipitate out as primary carbides. MC particles will act to retard dislocation motion during creep [13]. While increasing the carbon concentration up to 0.5wt% increases the creep rupture strength of the part, it also facilitates a large amount of precipitation and coarsening of secondary brittle phases after long periods of aging at elevated temperatures. Most secondary precipitates embrittle the material causing ductility, and toughness loss which can eventually lead to ductility dip cracking issues. If the carbon content is not high enough the material could experience increased grain growth, and a decrease in strength from an absence of pinning particles while in service [13]. The highest creep resistance is usually achieved when steels have a large amount of carbon and nitrogen in solution as interstitial solid solution strengtheners.

Sensitization resistance can be increased by introducing nitrogen into solid solution up to 0.16wt%, as nitrogen decreases the diffusivity of chromium and carbon, retarding the precipitation and coarsening of $M_{23}C_6$ [23]. In 20Cr25Ni1Nb steels when the nitrogen concentration is higher than 0.16 wt%, M_2N is formed instead of $M_{23}C_6$ [23]. The high affinity that niobium has for nitrogen promotes the formation of NbN, increasing the creep strength of the material. If nitrogen content in the steel increases due to nitrogen uptake from the surrounding atmosphere, some Nb(C,N) precipitates could exchange carbon for nitrogen [24]. Carbon can then supersaturate the local austenite, and can precipitate out as $M_{23}C_6$. Even if no nitrogen was intentionally added to the alloy, nitrogen uptake can occur from the environment during casting, or during its service life. Nitrogen uptake has even been observed to be able to promote the formation of nitriding phases such as Z-phase, or Cr_2N after an extended period of aging [24].

2.2.1.5 Molybdenum

Molybdenum typically exists in solid solution, however can replace niobium in some intermetallic phases, such as M_6C, and G-phase [13]. Molybdenum contributes solid solution strengthening effects to the alloy improving creep properties, but also promoting the formation of σ-phase and Laves phase [20]. Increasing molybdenum concentration reduces the solubility of carbon in austenite promoting the formation of $M_{23}C_6$ and intergranular corrosion[23]. Increasing molybdenum content increases the sensitivity of alloy when silicon is added.

2.2.1.6 Manganese

Manganese decreases carbon activity and increases its solubility, slowing down precipitation of $M_{23}C_6$ carbides, reducing intergranular corrosion [23]. Manganese in amounts (up to 2wt%) increases the solubility of N. Some high strength austenitic steels contain up to 0.5 wt%N if manganese concentrations are increased to as much as 15wt%. Combinations of up to 10wt% manganese with up to 0.25wt% nitrogen can be used to replace as much as 4-7wt% of nickel, which provides cost saving benefits [13]. Manganese also increases the solubility of nitrogen in austenite, and decreases the diffusivity of niobium, reducing the driving force for Nb(C,N) precipitation [26]. Manganese combined with nitrogen displays synergistic effects in producing fine, high number density Nb(C,N) [27]. Manganese also contributes significantly to the ductility of the steel, and increases its fluidity during casting [22]. In solid solution, manganese is known to increase the strain-hardening rate of the alloy [22].

2.2.1.7 Silicon

Silicon increases the likelihood of intergranular corrosion since silicon is a ferrite stabilizer and segregates to the grain boundaries [23]. Silicon is also a solid solution strengthener. Supersaturation of silicon in austenite causes a significant increase in the activities of carbon and nitrogen both in solid solution, and in neighboring phases [28]. Silicon increases fluidity to the molten metal, and inhibits carburization attacks by forming a protective surface layer [29]. It is believed that silicon can destabilize primary carbides by supersaturating its boundaries, where it will be energetically favorable for the carbon and nitrogen to form as intermetallic phases such as η-phase, G-phase, Z-phase, and π-Phase [11, 23, 30].

2.2.2 Effects from precipitates

2.2.2.1 Nb(C,N)

Niobium carbonitrides are typically formed during solidification, and coarsen during the initial stages of aging. Nb(C,N) act to divert carbon from forming secondary chrome carbide precipitates, thus preventing intergranular corrosion. Nb(C,N) are usually fine, and spherical in morphology, existing in high number fractions, usually at grain, and dendrite boundaries, as niobium is a ferrite stabilizer. The size and distribution of these carbides allow them to pin dislocations effectively, providing recovery resistance, and increasing the creep resistance of the alloy. Nb(C,N) precipitation occurs primarily on dislocation sites due to a large misfit in lattice parameters with austenite [13]. Between Nb(C,N) and austenite the crystallographic orientation relationship is:
$\left\langle \begin{matrix} 0 & 0 & 1 \end{matrix} \right\rangle_{\mathrm{Nb(C,N)}} // \left\langle \begin{matrix} 0 & 0 & 1 \end{matrix} \right\rangle_{\gamma}$, and $\left\langle \begin{matrix} 1 & 1 & 2 \end{matrix} \right\rangle_{\mathrm{Nb(C,N)}} // \left\langle \begin{matrix} 1 & 1 & 2 \end{matrix} \right\rangle_{\gamma}$ [24]

Cold working after solution annealing treatments has been found to accelerate MC precipitation in stainless steels. Increasing the dislocation density, as well as homogenizing the distribution of niobium in the microstructure encourages the precipitation of intradendritic MC carbides. These intradendritic carbides are seen have an increased stability within the alloy, and a decreased susceptibility to coarsening. Homogeneous distributions of primary carbides also result in a reduction in secondary creep rate [11]. A shortage of dislocation sites, or a strong segregation of niobium is found to cause high precipitate clustering levels, producing weaker creep properties.

If nitrogen is present in solution, NbC and Nb(C,N) will exist concurrently within the microstructure, where the carbides will prefer to exist as NbN which are more stable than NbC. The two solubility relationships used for NbC, and Nb(C,N) precipitates in 20Cr25Ni steels are

$$\log[\mathrm{Nb}][\mathrm{C}] = 4.07 - \frac{8358}{T(K)} \tag{2.1}$$

$$\log[\mathrm{Nb}][\mathrm{C}+6/7\mathrm{N}] = 3.21 - \frac{6750}{T(K)} \tag{2.2}$$

From these solubility relationships it is observed that the introduction of nitrogen into NbC will increase its solubility which will decrease the volume fraction of primary carbides [13]. Although nitrogen increases the solubility of niobium, recrystallization in the alloy becomes more difficult. The increased Nb(C,N) stability has also been observed to decrease the rate of Nb(C,N) transformation into brittle intermetallic phases such as M_6C, and Z-phase [21]. Niobium is soluble in a variety of intermetallic phases common in high temperature stainless steels. Interdendritic NbC precipitates are more susceptible to destabilization where these intermetallic phases can then form, due to a supersaturation of ferrite stabilizers (i.e. silicon, chromium, and molybdenum) at the dendrite boundaries upon aging.

Maximixing Nb(C,N) precipitation is typically done by providing a stoichiometric ratio of niobium, carbon and nitrogen to the alloy. Eq. 2.3 is referred to as the stabilization ratio, and is critical for the optimization of creep resistant stainless steels.

$$\frac{Nb}{C + 6/7N} = 7.7 \tag{2.3}$$

2.2.2.2 Ti(C,N)

Microalloy additions of titanium are added to niobium stabilized stainless steels to further increase the creep strength of the alloy. If the concentration of titanium is great enough TiC, or TiN carbides can precipitate. Sourmail and Bhadeshia discovered coarse, cubodial, TiN precipitates in the primary stages of aging a NF709 steel, which is a 20Cr25Ni variant with a significant fraction of nitrogen ($\sim 0.15 - 0.2wt\%$) [31]. These TiN precipitates were up to 5μm in size from an alloy that contained only 0.05wt% titanium. The solubility for titanium carbides is much smaller than for niobium carbides, precipitating out of solution below 1000°C[32]. Piekarski discovered aggregated, cubodial TiC carbides embedded within larger globular G-phase precipitates in 18Cr30Ni stainless steels aged at 900°C for 300 hours [9]. The titanium carbides were irregularly distributed, and multiphased, showing a region between the G-phase and TiC that contained a significant site fraction of niobium. Figure 2.2 shows the morphology of the aggregated TiC carbides with the quantitative results from EDS displayed to the right. It was shown in the as-cast microstructure that the G-phase regions in the aged microstructure where once NbC, and the embedded TiC was less aggregated, showing only a thin (Ti,Nb)C region. Eq. 2.4 is the solubility equation for TiC derived by *Kikuchi et al.* for a 20/25 steel [20]. Its solubility is seen to be lower than that for NbC or Nb(C,N). The stoichiometric ratio of titanium to carbon is Ti/C = 3.99.

$$\log[\mathrm{Ti}][\mathrm{C}] = 3.42 - \frac{10475}{\mathrm{T(K)}} \tag{2.4}$$

2.2.2.3 M23C6

$M_{23}C_6$ is an FCC carbide where the M represents notation for substitutional elements such as chromium, nickel, iron, and molybdenum. In stainless steel the M constituent is primarily chromium. During the initial stages of aging the composition of $M_{23}C_6$ fluctuates drastically containing as much as 40 wt%

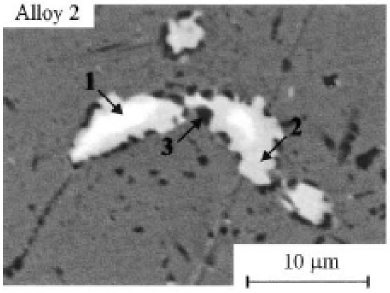

	Si	Fe	Cr	Ni	Nb
1	0.45	1.1	1.6	2.15	94.7
2	8.0	6.3	2.6	35.9	47.2
3	0.36	15.0	76.5	6.44	1.7
matrix	2.10	47.9	19.2	30.8	—

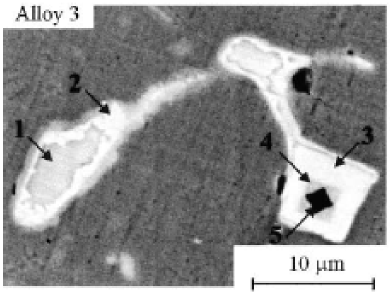

	Si	Fe	Cr	Ni	Nb	Ti
1	—	0.6	0.7	0.7	71.7	26.3
2	7.3	4.2	1.1	33.3	40.0	14.1
3	—	0.7	0.4	0.3	74.5	24.1
4	—	0.6	0.5	0.4	68.8	29.7
5	—	0.6	0.5	0.4	33.6	64.9
matrix	1.6	48.3	20.0	29.6	—	0.5

Figure 2.2: 18Cr-30Ni cast steel alloys containing 0.05-0.83 wt.% titanium [9]. Multiphase aggregated carbides of TiC and NbC are seen in the alloy with 0.83 wt.% titanium.

ifron in some instances [20]. Although, nitrogen has been observed to be soluble in the second sublattice of $M_{23}C_6$ [33], it is rarely reported in literature and is actually believed to destabilize these carbides [34]. $M_{23}C_6$ has a cube-to-cube orientation relationship with austenite, and a lattice parameter three times that of the matrix. $M_{23}C_6$ primarily nucleates at the grain boundaries, but can also nucleate on incoherent, and coherent twin boundaries, and intragranular dislocation sites [20]. The stability range of $M_{23}C_6$ in 2032Nb steels is between 550-1075°C[35].

Without the formation of primary precipitates there is no restrictions on the precipitation of $M_{23}C_6$ in stainless steels other than the amount of carbon added to solution. Solid solution elements like nitrogen, and molybdenum can assist or impede the precipitation rate, and driving force of $M_{23}C_6$ but these effects are minimal. During the destabilization of NbC, and its transformation into an intermetallic phase, the carbon rejected back into solution will be freed up to precipitate out as $M_{23}C_6$. $M_{23}C_6$ also coarsens more rapidly than either NbC or Z-Phase [21] if enough carbon is in solution. Centrifugally casting, and homogenization procedures can favor the formation or intradendritic $M_{23}C_6$ which is unobserved in traditionally static cast niobium stabilized stainless steels [17]. Intradendritic $M_{23}C_6$ close to the grain boundaries have a tendency to dissolve, and be absorbed by the coarser interdendritic $M_{23}C_6$. Interdendritic $M_{23}C_6$ can take only a matter of hours to precipitate at temperatures between 650 to 850°C [4].

2.2.2.4 G-Phase

Intermetallic G-phase is composed of nickel, silicon, and niobium with a stoichiometry of $Ni_{16}Nb_6Si_7$. G-phase is describes as a silicide with an FCC structure, which is fairly brittle, and has a low melting point relative to the austenite matrix. G-phase precipitates due to a decomposition of primary NbC occurring from a supersaturation of silicon in the surrounding austenite. Ecob *et al.* proposes that the co-segregation of oxygen and silicon towards the grain boundaries leads to the instability of NbC, favoring the formation of G-phase [30]. The dissolution of NbC precipitates causes the precipitation of $M_{23}C_6$. Soares *et al.* developed a TTP curve of the Ni-Nb silicide for HP-Nb alloys, where the curves nose was discovered at 950 $°C$ in a temperature range between 700-1000$°C$ [36]. G-phase is normally distinguished by a drop in the ductility of the material after prolonged periods of aging. A study at 650°C was done aging 20/25 alloy for 10,000 hours were no loss in ductility was observed, where microstructurally only NbC coarsening was observed [11]. The primary nucleation sites for G-phase are on residual NbC boundaries, and bordering $M_{23}C_6$ interfaces. While initially the morphology of G-phase is mainly plate like at high temperatures it can become more of a large, and blocky type of morphology as the phase coarsens. G-phase can become very coarse during aging, in which multiple G-phase precipitates can agglomerate together. Intragranular G-phase which forms from intragranular NbC is much finer being between $\sim 1 - 2\mu$m in size. Precipitation rates for intradendritic G-phase are much slower than for interdendritic G-phase due to the diffusion of nickel, and silicon to the dendrite boundaries. In earlier reports G-phase was commonly mistaken for M_6C, or η (eta) phase, which has a similar lattice parameter, and a similar space group, where G-phase has a space group of $Fm3m$, and M_6C has a space group of $Fd3m$ [31]. G-phase can be differentiated from M_6C by the differences in composition where in niobium stabilized stainless steels M_6C has a stoichiometry of Cr_3Ni_2SiC. In nitrogen bearing steels M_6C, or η-phase is predominant, replacing G-phase as the primary intermetallic precipitate [31]. The high concentration of silicon in G-phase causes these precipitates to liquate during repair welding. Liquation occurs in G-phase due to its low melting point, where G-phase can actually melt and produce a liquid film from the rapid thermal cycles that occur in the heat affected zone. Contraction of the weld on cooling will lead to a tensile force being exerted on this liquid film, and propagate a crack in the heat affected zone. If the G-phase precipitates are small enough, and have not agglomerated together, any cracks that occur from liquation may be too small to propagate.

2.2.2.5 Z-Phase

Z-phase is a tetragonal phase with a stoichiometry of $Cr_2Nb_2N_2$ that forms similar to M_6C, and G-phase through a transformation process with NbC in nitrogen bearing stainless steels [10]. Extensive work from Danielsen, and Hald on nitrogen bearing 9-12wt% chromium martensitic steel has been done to characterize Z-phase [10, 37]. Z-phase is a lot like M_6C where it negatively affects the creep strength due to its consumption of MX precipitates during nucleation and growth. Long term aging of nitrogen bearing steels was conducted in NF709, and HP50 variants, where precipitation of Z-phase was seen to embrittle the alloy if allowed coarsen [6, 31]. Works from Hughes [38], and Knowles and Andren [39] on 19Cr13Ni and 20Cr25Ni stainless steels respectively, both show that very small additions of nitrogen (0.061, and 0.028 wt% nitrogen respectively) can have adverse effects on precipitating a significant amount of Z-phase out of solution. The orientation relationship between Z-phase and austenite is described as: [24] $\begin{bmatrix} 0 & 1 & 0 \end{bmatrix}_Z // \begin{bmatrix} 1 & 1 & 0 \end{bmatrix}_\gamma$, $\begin{bmatrix} 1 & 1 & 0 \end{bmatrix}_Z // \begin{bmatrix} 1 & 0 & 0 \end{bmatrix}_\gamma$, and $\begin{bmatrix} 0 & 0 & 1 \end{bmatrix}_Z // \begin{bmatrix} 0 & 0 & 1 \end{bmatrix}_\gamma$

Sourmail and Bhadeshia observed the Z-phase precipitates in NF709 steel to be very fine, only around 50-100 nm in diameter [31]. If Z-phase is allowed to coarsen severely they do not contribute to the creep strength, and will begin to embrittle the material. Golpayegani *et al.* discovered Z-phase in 9-12% chromium steel, where after 40,000 hours at 650°C the Z-phase precipitates had coarsened to 600-700nm, and were found to decrease the creep resistance of the alloy [40]. After long testing times both large (>500nm) and small (<50nm) precipitates have been found, indicating nucleation occurs continuously during creep life. The breakdown in creep strength was found in part to be due to the transformation of NbC to Z-phase [41]. The nucleation sequence proposed by Danielsen and Hald is illustrated in Fig. 2.3. Z-phase precipitates due to the diffusion and supersaturation of chromium and nitrogen towards the NbC precipitate, destabilizing NbC to form Z-phase. The diffusion of chromium into NbC was discovered to control the driving force for Z-phase formation. NbC particles are preferred nucleation sites because of their semi-coherent interface with Z-phase. Z-phase will grow by consuming MX particles. Larger chromium concentrations increase the precipitation rate of Z-phase, where 9% Cr Steels took 100,000 hours to precipitate Z-phase, while 11-12% Cr may develop Z-phase after a few thousand hours.

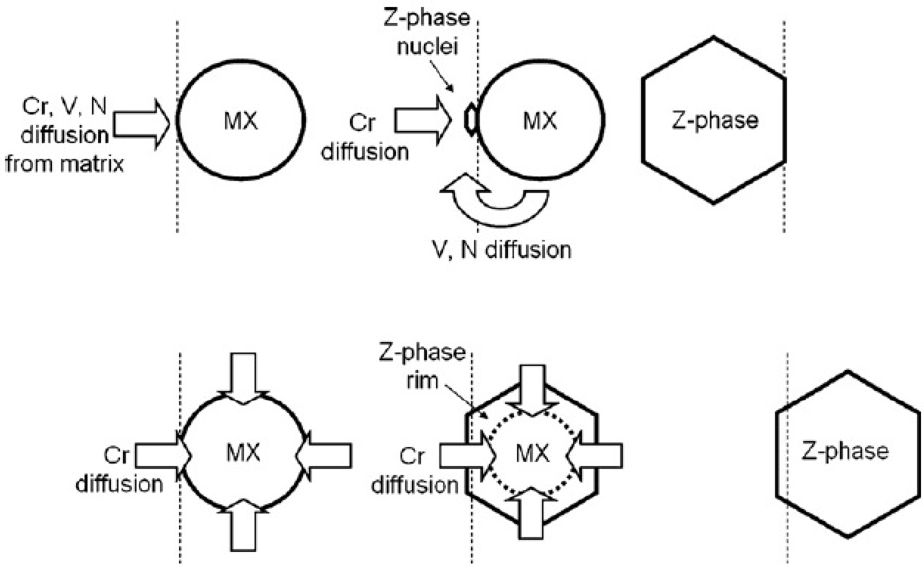

Figure 2.3: Z-phase nucleation on top, and transformation of MX to Z-phase on bottom [10]

2.2.2.6 Pi-Phase

In nitrogen bearing steels a brittle intermetallic phase called π-Phase ($M_{11}(CN)_2$ where M is chromium, silicon, iron, and nickel) is proposed to precipitate with increasing silicon content [23]. π-Phase is stable above 600°C, where increased precipitation decreases the precipitation rate of $M_{23}C_6$.

2.3 20Cr25Ni1Nb Precipitation Sequence

The literature review thus far has not included any detailed studies on the precipitation sequence for 2032Nb alloys, however a study on the microstructural evolution of 2025Nb by Powell *et al.* was conducted [11]. The steel was aged at various temperatures between 500-850°C for up to 2 years. The samples were solution annealed at 1050°C for 1 hr followed by 30% cold work, and further subjected to a second anneal at 930°C for one hour, and a 3% strain at room temperature. After this thermo-mechanical treatment the microstructure was analyzed to contain fine Nb(CN) precipitates, where the intradendritic Nb(CN) were measured to be between 0.1-0.5 μm, and the interdendritic Nb(CN) were measured at 1.5-4.0 μm. After two days of aging at 650°C fine G-phase precipitates, and larger $M_{23}C_6$ precipitates were observed by Transmission Electron Microscopy (TEM). After three months G-phase had enveloped the entire grain boundaries, while very little change in $M_{23}C_6$ was observed. Residual NbC carbides persisted in the microstructure up until 1.5 months, where it was then completely consumed by G-phase. Sigma phase was also identified after one week of aging along with G-phase.

TTP curves were generated from the microstructural analysis at the various aging temperatures in Fig. 2.4. The nose for G-phase precipitation is seen between 750-800°C, precipitating only after a few hours of aging. Sigma phase stability was observed to be between 575-700°C. Intragranular Nb(CN) stability was seen to be limited below 800°C, precipitating after one week at the nose of the curve at 675°C. The transformation to intradendritic G-phase was severely retarded, only occurring after one year of aging.

A comparison of the microstructural evolution of the thermo-mechanically treated material to the fully recrystallized material is shown in Fig. 2.5. A delay in G-phase, $M_{23}C_6$, and sigma phase precipitation was seen in recrystallized material.

2.4 Grain & Dendrite Size

Large grain sizes produced from thick castings, or high solution annealing temperatures, can reduce creep strain from increased elemental diffusion, and segregation distances [21]. Increased diffusional distances also decrease precipitation rates of secondary phases. However, they also reduce grain boundary area, and produce coarser intergranular precipitates increasing embrittlement, decreasing rupture ductility, and toughness.

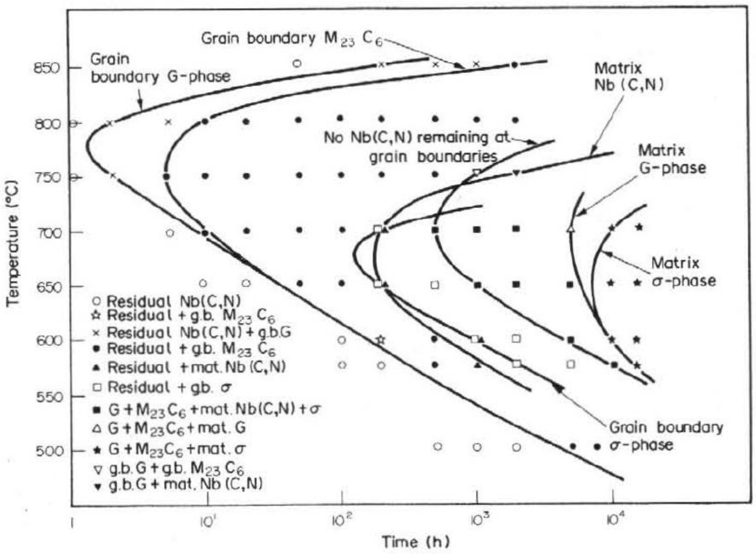

Figure 2.4: Time-Temperature-precipitation curves for 20Cr25Ni1Nb Stabilized stainless steel [11]

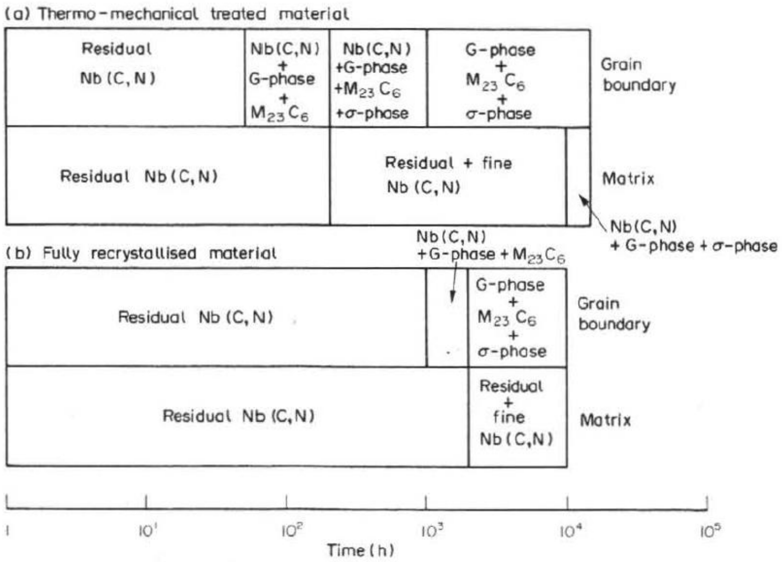

Figure 2.5: Precipitation sequence for 20/25/Nb Stabilized stainless steel [11]

2.5 Embrittlement and Liquation Cracking

During the long-term aging of niobium stabilized stainless steels, a significant drop in rupture ductility is experienced due to the precipitation, and coarsening of embrittling intergranular secondary carbides and intermetallic phases. The embrittlement of the intergranular region can lead to ductility dip cracking during repair welding processes depending on the extent of coarsening of the precipitates. HK-40 steels experience less embrittlement than their niobium stabilized HPNb counterparts, however are less commonly used due to their lower creep properties [17].

While all niobium stabilized stainless steels experience some degree of embrittlement, the 2032Nb alloy is exceptional as it has also been reported to experience liquation cracking issues caused by the formation of G-phase [42]. Liquation cracking can occur at the fusion boundary, and more commonly in the Heat Affected Zone (HAZ) during repair welding. In the HAZ the material experiences rapid thermal cycles, and can exceed the melting temperature of the low melting point G-phase near the fusion zone. With a sufficient heat rate, there will not be enough time for the the dissolution of larger G-phase precipitates with the passing of the welding arc, melting the precipitates, producing a liquid film. Once this liquid film starts to resolidify, tensile forces are exerted around this film, propagating a crack. Although, it may not be possible to completely avoid G-phase precipitation through compositional variations, liquation cracking only occurs when a sufficient volume of liquid fully wets the grain boundaries. Fine G-phase precipitates, or intragranular G-phase precipitates are not expected to cause liquation cracking. In the 2032Nb alloy liquation cracking was much more severe in the static cast tee than the centrifugally cast cone [29]. The cause of increased liquation cracking was reasoned to be because of the higher fraction, and coarser secondary precipitates in the aged tee.

In HK40 and HPNb steels G-phase is partially, or completely substituted by η-phase, which has a lower tendency to promote liquation cracking. The higher carbon content also promotes the decomposition of G-phase at lower temperatures on heating, and precipitates $M_{23}C_6$ at higher temperatures on cooling [42]. As a result, increasing carbon content helps to retain the ductility, and fracture stress of the manifold. Constitutional liquation is also important to consider when replacing G-phase with other intermetallic phases, as a diffusional reaction zone around the austenite, G-phase, and other intermetallic phase could significantly suppress the melting temperature, causing melting.

2.6 Solution Annealing

Solution annealing or heat treating the component is typically done in order to restore the ductility of the part, before repair welding procedures can be performed. The precipitation and coarsening of secondary precipitates occurs in the castings during long periods of being in-service at elevated temperatures. Especially in higher carbon, low manganese alloys, interdendritic secondary carbides can drastically embrittle the material, where cracking would result in the HAZ during welding. Solution annealing redissolves any secondary precipitates that would have formed within the microstructure during aging. There is no set time and temperature for solution annealing 2032Nb alloys, reported anywhere between 1100-1200°C for 1-3 hours [2, 43, 44]. Knowles *et al.*[43], and Hoffman [29] solution annealed at 1100°C for 3 hrs, while Colwell *et al.* solution annealed at 1177°C for 4.5 hrs [44], and Powell *et al.* annealed 20Cr25Ni samples for 1 hour at 1050°C followed by 30% cold work [11].

Some solution annealing treatments use high temperatures to dissolve deleterious phases, however this can lead to secondary recrystallisation and coarse grain sizes [21]. Thermo-mechanical treatments commonly used in series 347 stainless steels involving high solution annealing, cold working, and a regular solution annealing can control the amount of recrystallization, and the final grain size of the component [21].

2.7 Repair Welding

The wrought 800H variant stainless steel are generally shown to have better repair weldability than the the cast HPNb variants due to their higher alloying fractions [4]. Alloy embrittlement causes major challenges when trying to repair weld these components. Certain recommendations have been made when trying to weld embrittled stainless steels including minimizing base metal temperature (narrow bead, high travel speed, and limiting interpass time), avoiding welding on previous HAZ regions, and shot peening the weld beads directly after deposition [4]. Sometimes ductility dip cracking cannot be avoided during repair welding, and the component must be solution annealed beforehand.

2.7.1 Choice of Weld Metal In 2032Nb Manifolds

The choice of weld metal for joining the pigtail and manifold components together is critical for maximizing the creep rupture strength of the system. Jaske [12] tested five types of weldments (Inconel 182, Inconel 112, IncoWeld A, Inconel 82, and Inconel 617) against Alloy 800, 800H, 800HT, and 2032Nb base metals. The creep rupture strengths for the filler metals, and the weld metals were tested at various temperatures. Figure 2.6 shows the creep rupture strength tests at 816°C. Inconel 617 filler metal showed comparible, if not higher creep rupture strength than the 2032Nb base metal, where all other weldments had creep strengths below the 2032Nb base material. Inconel 112 was found to have the next highest creep strength of all the weldments which has a lower nickel and cobalt content, and a higher chromium content than the other metals. Table 2.1 shows the chemical compositions for the various weldments. Kobrin [1] achieved exceptional results from using Inconel 82, and a Alloy 625 filler metal, and Inconel 112 welding 2023Nb metals.

Table 2.1: Specifications and compositions of welding consumables for 800H, and 2032Nb alloys used in hydrogen reformer manifolds and pigtails [1]

	Composition (wt.pct)											
Common Name	Ni	C	Mn	Fe	Si	Cu	Cr	Ti	Al	Nb + Ta	Mo	Application Temperature
Welding Electrodes												
Inco-Weld A	bal	0.1	1.0-3.5	12.0	0.75	0.50	13.0-17.0	–	–	0.5-3.0	0.5-2.5	< 760°C
Inconel 182	bal	0.1	5.0-9.5	10.0	1.0	0.50	13.0-17.0	1.0	–	1.0-2.5	–	–
Inconel 112	bal	0.1	1.0	7.0	0.75	0.50	20.0-23.0	–	–	3.15-4.15	8.0-10.0	> 760°C
Inconel 117	bal	0.05-0.15	0.30-2.5	5.0	0.75	0.50	21.0-26.0	–	–	1.0	8.0-10.0	> 760°C
Filler Metals												
Inconel 82	bal	0.1	2.5-3.5	3.0	0.50	0.50	18.0-22.0	0.75	–	2.0-3.0	–	< 760°C
Alloy 625	bal	0.1	0.5	5.0	0.5	–	20-23	0.4	0.4	3.15-4.15	8.0-10.0	> 760°C
Alloy 617	bal	0.05-0.15	1.0	3.0	1	0.5	20.0-24.0	0.2-0.5	0.8-1.5	–	8.0-10.0	> 760°C

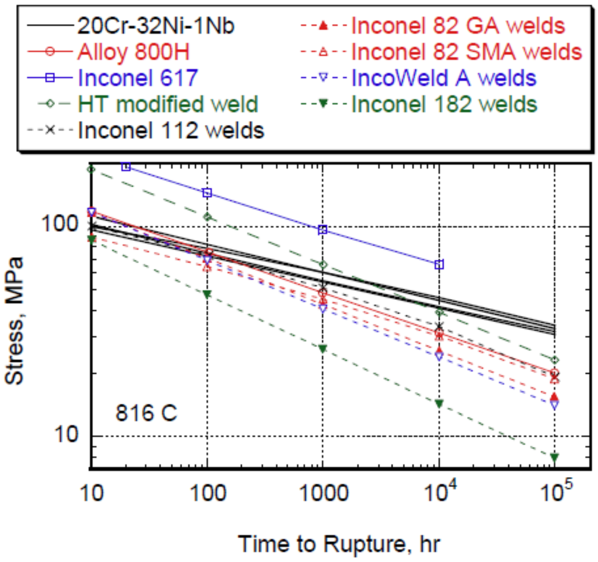

Figure 2.6: Creep ruture strength of filler metals at 816°C [12].

2.7.2 Repair Welding Cracking Susceptibility

Nishimoto *et al.* [45] investigated numerous cracking mechanisms seen in a range of HP-modified stainless steels used in the petrochemical industry. Two HP variants, the HP35 (35 wt%Ni 25 wt%Cr), and HP43 (43 wt%Ni, 31 wt%Cr) were used in this study, varying in niobium and microalloy elements (Mo, W, Ti, Zr). Hot-cracking susceptibility was simulated with the miniature spot-varestraint test between as-cast, aged, and service exposed components, where aging was done at 1100°C for 10,000 hours. Pronounced ductility-dip cracking was found in the HP-modified steels, with only few instances of liquation cracking. Ducility-dip cracking was observed to occur 1-8 mm from the fusion boundary with a crack length of 0.2-0.3mm, whereas liquation cracking only appeared near the fusion boundary with a crack length between 0.1-0.2mm. Long term aging drastically increased the ductility-dip cracking susceptibility of the alloy mostly due to carbide precipitation and coarsening in the interdendritic regions. Niobium content was found to have little effect on the total crack length.

Microstructural characterization of the HP variants was performed at several aging times from the as-cast state to 10,000 hours. The resulting microstructure was categorized between the niobium containing alloys and the niobium free alloys. In the as-cast state, the niobium containing alloys were observed to have NbC, and M_7C_3 precipitates, while the niobium free alloys contained either $M_{23}C_6$, or M_7C_3 precipitates. After the complete aging cycle, alloys contained coarse, globular, interdendritic $M_{23}C_6$ precipitates, and silicon containing intermetallic precipitates characterized as η-phase in the niobium bearing alloys, and G-phase in the niobium free alloys [46]. The substitution of niobium for chromium in G-phase has not been reported in many characterization studies of HP stainless steels, where the silicide phase is typically just referred to as η phase, or M_6C.

Geeble tests were then carried out to test the hot ductility of the HP heat-resisting alloys during aging, where Nishimoto *et al.* proved that ductility-dip cracking susceptibility was proportional to the hot ductility of an alloy [47]. The effects of aging on the hot ductility of the niobium containing, and niobium free HP alloys are shown in Fig. 2.7. Formation and coarsening of secondary $M_{23}C_6$ at the dendritic boundary was seen to decrease the hot ductility of the alloys, whereas precipitation and growth of fine intradendritic carbides slightly recovered some of the alloys hot ductility. After the onset of η-phase or G-phase precipitation, hot ductility falls drastically, and the interdendritic $M_{23}C_6$, and silicide phases continue to coarsen forming massive and globularised microconstituents which essentially concentrate stress, leading to ductility-dip cracking. Zirconium was found to improve hot cracking susceptibility by enhancing microconstituent dispersion.

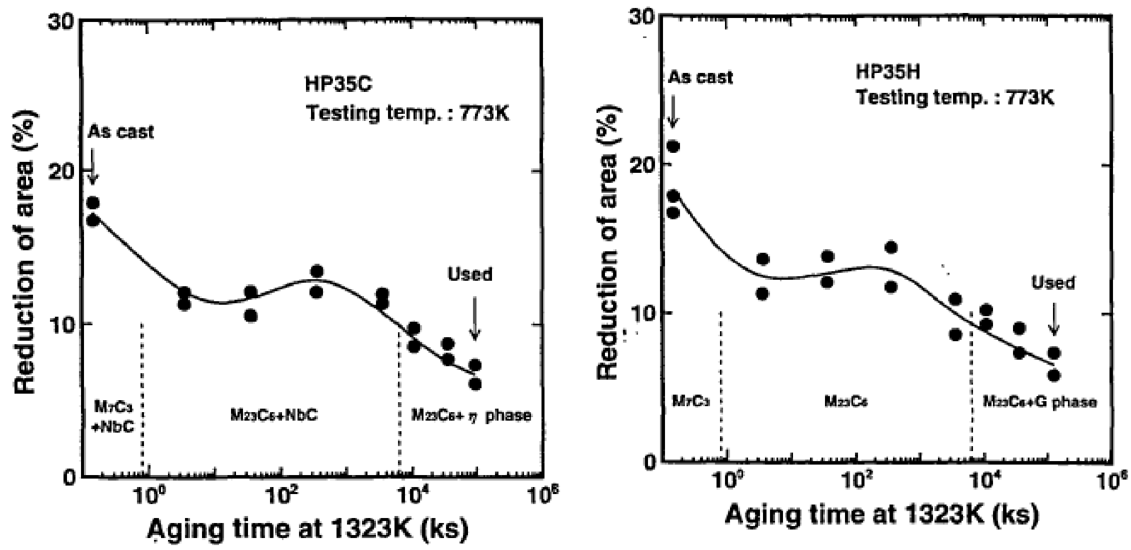
(a) Niobium containing

(b) Niobium free

Figure 2.7: Effects of aging on the hot ductility of a a) niobium containing HP35C alloy, and a b) niobium free HP35H alloy.

2.8 Chemistry Optimization Techniques

2.8.1 Nb/(C+N) Ratio

Niobium containing stainless steels typically show maximum mechanical properties, and creep strength when the ratio of Nb/(C+N) is stoichiometrically equivalent [44], or the stabilization ratio is at least Nb(wt.pct)/(C(wt.pct) + 6/7N(wt.pct)) $\geq$ 7.7 [11]. A stabilization ratio $\geq$ 7.7 ensures that the majority of carbon is sequestered as Nb(C,N) particles. If this ratio falls below 7.7 then the carbon and nitrogen will be in excess, and available to promote the precipitation of other carbide and nitride phases. However, if greater than 7.7, excess niobium will exist in solution and will be able to precipitate out as intermetallics such as G-phase or η-phase. Keown and Pickering [13] showed that deviation from stabilization ratio will produce a decrease in NbC phase fraction shown in Fig. 2.8.

Sourmail and Bhadeshia [48] trained a neural network model with various austenitic stainless steel alloys to optimize the against creep rupture strength data. For short term aging a stoichiometric Nb/C ratio was found to produce the best creep properties. However, for long term aging understabilizing the alloy (Nb/C$<$ 7.7) was reported provide the better properties, as more carbon is kept in solution.

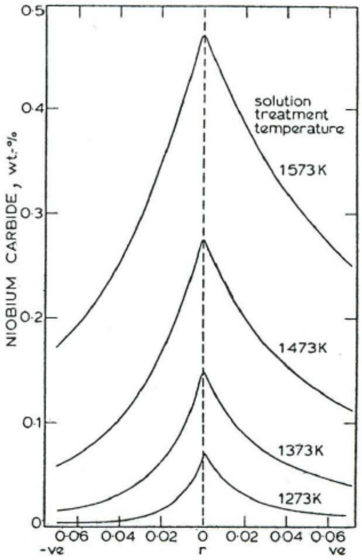

Figure 2.8: NbC available for precipitation as a function of deviation from stoichiometry [13]. Where $r = pB_T - qA_T$, p and q are the mass fractions of A and B in the compound AB_n, and A_T, and B_T are the mass fractions of these elements in the alloy.

2.8.2 P-Factor

Shibaski *et al.*[18] developed an empirical equation to maximize creep properties for high temperature stainless steels by relating chemical composition to ductility. Also known as the P-factor equation, it is defined as:

$$\begin{aligned} \mathrm{P} &= 7 \times \mathrm{C} + 5 \times \mathrm{Si} - 3 \times \mathrm{Mn} + 8 \times \mathrm{Nb} \qquad (2.5) \\ &: \mathrm{C, Si, Mn, Nb (wt.pct)} \end{aligned}$$

The P-factor equation was determined from tensile ductility data at room temperature, where a value of P above 9 (corresponding to a elongation of 5 percent) was considered unacceptable.

2.9 20Cr32Ni1Nb Microstructure and Mechanical Properties

Magnan, and Hoffman tested two statically cast 2032Nb alloys, one with a standard chemistry and the other with a modified chemistry [2]. The average compositions of the heats is listed in Table 2.2. The standard chemistries had a P-Factor > 9 and a Nb/C ratio > 7.7; characterizing the alloy as having an unacceptable ductility for creep aging, and an excess amount of niobium. The modified alloy had a P-Factors between 4.5-6, and an Nb/C ratio between 4.6-6. The ultimate tensile strength, yield strength, and ductility of the standard alloy was seen to rapidly deteriorate after 100 hrs of aging at 800°C. Solution annealing at 1150°C after 10000 hrs of aging was seen to recover most of the strength, and ductility of the alloy. The modified alloy was able to retain most of its strength and ductility with aging, however its properties were still weaker than the standard alloy after solution annealing. Yield strength of the alloys was seen to increase up to 100 hours which was attributed initially to precipitation strengthening from NbC during deformation, and to the precipitation of secondary carbides. After 100 hours, coarsening of the secondary carbides deteriorated the alloys strength. Creep rupture tests were performed at 870°C and 55.2 MPa for the two alloys. The modified chemistry was observed to have a considerably greater creep rupture life after 5000 hours.

Table 2.2: Compositions for standard, and modified 2032Nb alloys studied by *Magnan, and Hoffman* [2]

	Composition (wt%)							
Alloy	C	Mn	Si	Cr	Ni	Nb	P factor	Nb/C
Standard 2032Nb	0.13	1.25	0.50	19.60	34.01	0.71	5.37	5.28
Modified 2032Nb	0.13	1.24	0.50	19.69	33.99	0.72	5.46	5.47

Chen *et al.* examined as-cast 2032Nb alloys, and 2023Nb that had been in service for four years at 760°C, preforming SEM, and TEM to characterize the microstructure [3]. The chemistries of the as-cast and ex-service alloys are provided in Table 2.3. Large eutectic MC precipitates were found in the as-cast microstructure under SEM, while small $M_{23}C_6$ precipitates were discovered with TEM. In the ex-service alloy aged, large, continuous precipitates were found at the grain boundary. These precipitates were characterized as G-phase, and $M_{23}C_6$ under TEM. A high density of fine intradendritic G-phase was also found in the ex-service samples. An intradendritic precipitate free zone was observed around the dendrite boundaries in Fig. 2.9, due to the coarsening of the bulky interdendritic G-phase. The residual NbC that survived the four year aging period were observed to be surrounded by G-phase.

Table 2.3: Alloy Comp for 20Cr32Ni1Nb wt% [3]

	Ni	Cr	Nb	Si	Mn	C
As-Cast	31.59	20.75	1.47	1.31	0.92	0.10
Ex-Service	31.73	21.65	1.43	1.12	0.90	0.11

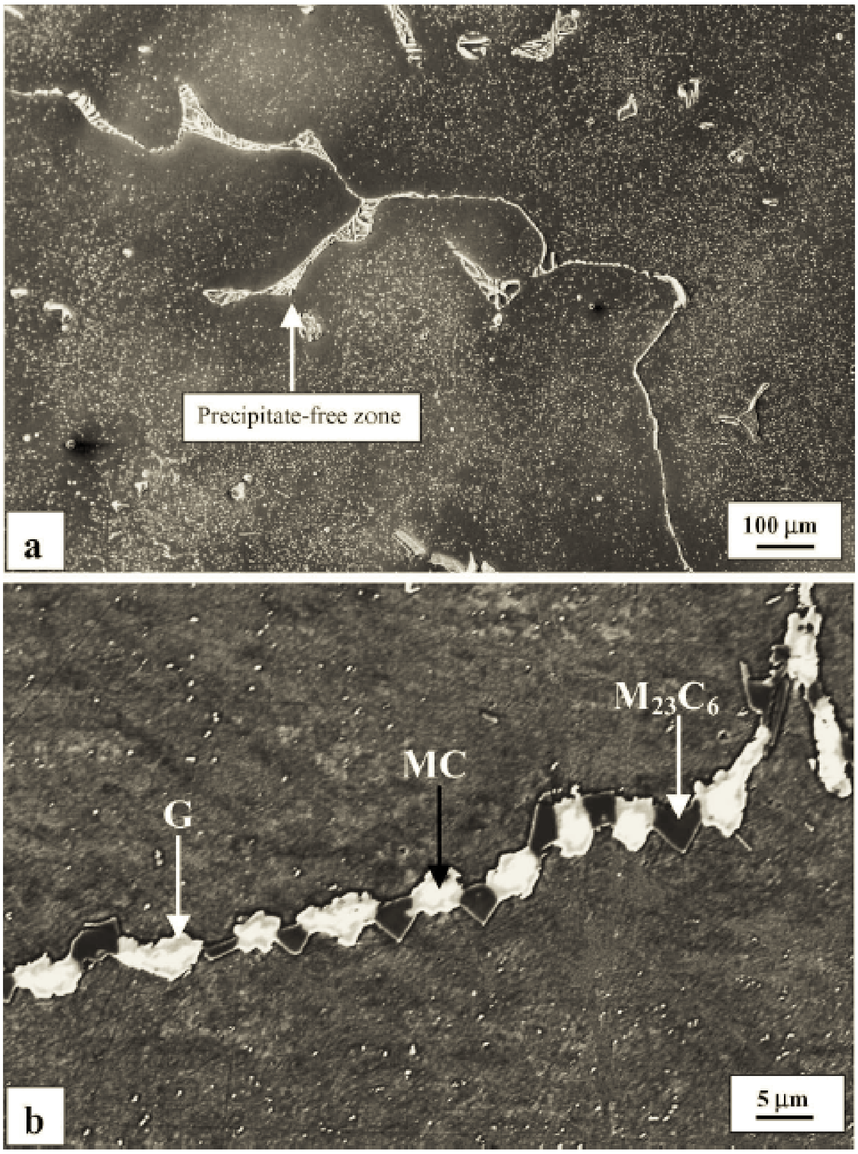

Figure 2.9: Microstructure of In-service 2032Nb alloy. (a) shows fine precipitates within the intradendritic region of alloy, and continuous precipitates along the grain boundary. A precipitate free zone lies adjacent the grain boundaries. (b) At the grain boundaries a cored structure of MC precipitates are surrounded by G-phase, inter-dispersed between $M_{23}C_6$ in a lamellar type fashion, after [3].

Chapter 3

Introduction to ThermoCalc: Theory for Multicomponent Systems & Chemistry Optimization Techniques

3.1 ThermoCalc Introduction

Potential and molar phase diagrams are the centerpiece of materials science, and are used as a visual representation of a materials system, providing critical information on how the system reacts to changes in composition, temperature, pressure, or volume. Phase diagrams also give insight into the stability of a phase, and transformation reactions that occur from crossing monovariant, or invariant phase boundaries. Although phase diagrams are a useful tool for visualizing binary, or ternary systems, there is no real method of visualization of a multicomponent system other than to reduce the dimensionality of the system to a pseudo-binary, or isoplethal diagram. While isopleths are a useful representation of multicomponent system, unless the specific alloy composition has previously been calculated, the researcher will have to do the thermodynamic calculations on their own. For large systems this can become very tedious trying to provide interaction parameters for each constituent interaction in each sublattice of each phase of the system. Thankfully a lot of work in the past two decades has gone into building large databases to compile such data. CALPHAD and ThermoCalc are the forerunners in compiling thermodynamic data, and providing computational tools to simply, and efficiently be able to analyze predicted equilibria for specific material systems.

ThermoCalc is a tremendously powerful tool for metallurgists, and materials scientists, as its simplicity does not require the user to have much understanding of material thermodynamics, but can provide a vast amount of information, and insight into the alloy the user is dealing with. Whether there is sparse literature on the alloy, or the user is looking to tweak certain variables to modify the microstructure, ThermoCalc can vastly reduce the time and money needed for experimentation, and may altogether eliminate the trail by error approach utilized in the past.

In the present work, ThermoCalc was used to analyze how additions of both nitrogen, and titanium can affect the equilibrium microstructure of a 2032Nb alloy, and which chemistry provides the most optimal microstructure. With isoplethal sectioning only one component can be an independent variable while the others remain constant. In a proper design matrix all possible permutations and combinations must be encompassed. In a system with seven elements (chromium, nickel, niobium, silicon, carbon, manganese, and nitrogen/titanium), hundreds of phase diagrams would need to be analyzed in order to determine the effects each element, and their interactions have on phase stability, phase solubility, and the driving force of a phase. In the following sections a method for analyzing, and optimizing the composition of a multicomponent system is proposed with the use of ThermoCalc as a subroutine. The next section will discuss a proposed Gibbs energy model for calculating equilibrium for a 2032Nb alloy, and a basic outline of how to use the ThermoCalc console program will be provided. Afterwords, a proposed methodology for compiling the data output by ThermoCalc will be presented, as well as ways of representing the data, to ultimately draw conclusions on how composition of the alloy affects the systems equilibrium microstructure.

3.2 Multicomponent Modeling of the 2032Nb System

From literature it is proposed the the 2032Nb system is primarily an austenitic solid solution of iron, chromium, and nickel. (Nb,Ti)(C,N) carbides are the major precipitates during solidification, while in some cases intradendritic M_7C_3 carbides are known to precipitate at higher carbon compositions [5, 17, 46]. During long-term aging interdendritic $M_{23}C_6$ is known to precipitate, and a transformation of NbC to either M_6C or G-phase will occur depending primarily of the carbon concentration , and silicon concentrations [3, 11, 47]. Nitrogen additions are proposed to also facilitate the precipitation of another intermetallic phase, Z-Phase [10, 31, 37]. With the major components of the system being chromium, nickel, silicon, niobium, carbon an manganese, the proposed equilibrium microstructure of the system will contain an austenite solid solution, NbC, $M_{23}C_6$, M_7C_3, and G-Phase. Adding nitrogen to the system, Z-phase, and Nb(C,N) should be added to proposed microstructure. Adding titanium to the microstructure TiC and M_6C should be added to the proposed microstructure. Defining which phases comprise the system to be analyzed is important for defining Gibbs energy models, and for determining the accuracy, and validity of the ThermoCalc results.

Crystal structure information for each of these phases is critical for modeling Gibbs free energy of the system. Determining the ordering and interactions of the constituents on each sublattice of the phase contributes significantly to the entropy overall energy of a phase. Table 3.1 outlines basic crystallographic information for each of the phases in the proposed system, such as the space groups, and number of sites for each phase. In the next sections, Wyckoff positions and the variable parameters will be outlined for the appropriate phases.

Table 3.1: Phase information about the observed phases. The last reference for $M_{23}C_6$, G-phase, and Z-phase contains the crystal structure reference.

Phase	Structure	Type	Space Group	Formula	Lattice Parameter (Å)	Atoms per cell	Density g/cm^3	Ref.
γ-Fe	Simple FCC	cF4	$Fm\bar{3}m$	-	3.57	-	7.38	[3],[24]
Nb(C,N)	FCC (NaCl)	cF8	$Fm\bar{3}m$	(Nb,Ni,Fe,Cr)(C,N)	4.41	8	8.17	[3], [24], [13]
NbC	FCC (NaCl)	cF8	$Fm\bar{3}m$	(Nb,Ni,Fe,Cr)C	4.43-4.47	8	7.80	[3], [24], [13]
NbN	FCC (NaCl)	cF8	$Fm\bar{3}m$	(Nb,Ni,Fe,Cr)N	4.38	8	8.39	[3], [24], [13]
M_6C	Diamond FCC	-	$Fd\bar{3}m$	$(Cr,Fe,Nb,Ni,Si)_6C_3$	10.95-11.28	-	1.38	[20]
M_7C_3	Orthorhombic	oP40	Pnma	$(Cr,Fe,Mn)_7(C)_3$	a = 4.526 b = 7.010 c = 12.142	40	6.97	[49]
$M_{23}C_6$	Complex Cubic (D84)	cF116	$Fm\bar{3}m$	$(Cr,Ni,Fe,Nb)_{23}C_6$	10.57-10.68	116	6.91	[3], [24], [20], [50]
G-Phase	Complex Cubic (D8a)	cF116	$Fm\bar{3}m$	$(Ni,Fe)_{16}Si_7(Cr,Mn,Nb)_6$	11.2	116	8.05	[3], [11], [51]
Z-Phase	Tetragonal BCC	tP6	P4/nmm	NbCrN	a = 3.04 c = 7.39	6	7.74	[20], [24], [10]

The next section will go through how ThermoCalc calculates equilibrium, and maps phase diagrams. The subsequent sections will outline the Gibbs energy models for each of the proposed phases.

3.2.1 Global Minimization

In a binary, or ternary system, equilibrium can be easily identified graphically by drawing the common tangent between the minimized Gibbs energy curves for each phase mathematically expressed as

Eq. 3.1

$$min(G) = min\left(\sum m^{\alpha} G_m^{\alpha}(T, p, x_i^{\alpha})\right) \tag{3.1}$$

This common tangent line, or plane can be formulated as

$$\mu_i = \left(\frac{\partial G^{\alpha}}{\partial x_i}\right)_{T,P,x_k} = \left(\frac{\partial G^{\beta}}{\partial x_i}\right)_{T,P,x_k} \quad \forall\, i\, \in \{1 \ldots c\}$$

Stating that the chemical potential for each component must be equal for all phases. In general terms this can be written as

$$G_i^{\alpha}(T, p, x_i^{\alpha}) = \mu_i \,\forall\, i \in \{1 \ldots c\},\ \alpha \in \{1 \ldots p\} \tag{3.2}$$

Gibbs phase rule can be derived from Eq. 3.2 as, $F = c - 2 + p$ where F is the degrees of freedom, c is the number of components, p is the number of phases, and the +2 represents temperature, and pressure variability.

For sublattice modeling commonly used in multicomponent systems, species are typically represented as constituent fractions of constituent i in sublattice s of phase α, $y_i^{(\alpha,s)}$, instead of mole fractions, x_i, with the relationship

$$x_i = \sum_s \frac{\sum_j b_{ij} y_j^{(\alpha,s)}}{a^{(s)} \sum_k \sum_j b_{kj} y_j^{(\alpha,s)}} \tag{3.3}$$

where b_{ij} is the stoichiometric factor of component i in constituent j, j represents the summations of all components, and $a^{(s)}$ are the fraction of sites on sublattice s. The constituent fraction can also be defined as $y_i^s = N_i^s / N^s$, "where N_i^s is the number of sites occupied by constituent i on sublattice s and N^s is the total number of sites on sublattice s" [15]. With G_m^α given as a function of site fractions for multicomponent systems, a Lagrange-multiplier method consisting of a set of non-linear equations is used to calculate equilibrium instead of Eq. 3.2. The constraints are:

$$\sum_\alpha m^\alpha \sum_s a^{(s)} \sum_k b_{k,i}^{(\alpha,s)} \cdot y_k^{(\alpha,s)} - N_i = 0 \quad \forall\, i \tag{3.4}$$

$$\sum_k y_k^{(\alpha,s)} - 1 = 0 \quad \forall\, s \tag{3.5}$$

$$\sum_s a^{(s)} \sum_k \nu_k^{(\alpha,s)} \cdot y_k^{(\alpha,s)} = 0 \quad \forall\, \alpha \tag{3.6}$$

$$\frac{\partial G_m^\alpha}{\partial y_k^{(\alpha,s)}} + \sum_{i=1}^{c} \mu_i \cdot a^{(s)} \cdot b_{k,i}^{\alpha,s} + \pi^{(\alpha,s)} + \pi_e^{(\alpha)} \cdot a^{(s)} \cdot \nu_k^{\alpha,s} = 0 \quad \forall\, k \tag{3.7}$$

$$G_m^\alpha - \sum_i \mu_i \sum s a^s \sum_k b_{k,i}^{\alpha,s} \cdot y_k^{(\alpha,s)} = 0 \quad \forall\, \alpha \tag{3.8}$$

where $b_{k,i}^{(\alpha,s)}$ are the stoichiometric numbers of component i in species k on sublattice s of phase α, $\nu_k^{(\alpha,s)}$ are the charges of ionized species k on sublattice l of phase α, and μ_i, $\pi^{(\alpha,s)}$ and $\pi_e^{(\alpha)}$ are the Lagrange multipliers for Eq. 3.4, Eq. 3.5 and Eq. 3.6 respectively. Eq. 3.7, and Eq. 3.8 are derived by first multiplying the respective Lagrange multipliers to Eq. 3.4, Eq. 3.5 and Eq. 3.6, adding them to the total Gibbs energy in Eq. 3.1 and taking their derivatives with respect to $y_k^{(\alpha,s)}$, and N_i. The unknowns to this set of non-linear equations are m^α, $y_i^{(\alpha,s)}$, μ_i, $\pi^{(\alpha,s)}$ and $\pi_e^{(\alpha)}$, as well as T, p, and N_i. A solutions to this set of equations can be found by employing the Newton-Raphson method (for more information on this method read [15]).

In higher order systems the common tangent is now characterized as a hyperplane of multidimensional space, where a global minimization procedure is carried out. To ensure that this global minimization procedure chooses the correct starting value for the Newton-Raphson calculation to give the global equilibrium, and not a metastable equilibrium, the Gibbs energy curve for all phases are approximated to be equal to the solution phase at the set composition, by dividing it into a dense grid of compounds and then finding the hyperplane that best represents equilibrium. These compounds along the hyperplane are then identified with which stable phase they are from. If multiple compounds are inside the same phase designated by ThermoCalc, the program will automatically create a new composition set. For example if two compounds are inside the FCC_A1 phase they will be split into $FCC\_A1\#1$, and $FCC\_A1\#2$ and given separate constitutions. In the 2032Nb system the matrix phase is austenite and designated as $FCC\_A1\#1$, while any NbC, or TiC phase which is also of FCC structure, will be designated as $FCC\_A1\#2$.

3.2.2 Driving force, phase stability, and mapping procedures

Other useful thermodynamic properties that can give insight into how certain phases behave are the driving force of a phase, which relates to the precipitation rate and kinetics of a phase, and the phases stability range. *Hillert, 2007* [14] makes the comparison of the driving force and stability to a rotating body where each of these variables can be expressed in terms of its potential energy, where driving force $= -dE/d\theta$, and stability $= 2d^2E/d\theta^2$ for angle θ. Fig. 3.1 taken from *Hillert, 2007* [14], shows how the driving force, and stability of an ellipical mechanical analogue, and a square analogue can determine if an equilibrium is stable or unstable. For the square its stability is always negative so the equilibrium of the square is always unstable. Whereas for the ellipse the stability is positive when $\theta = 0$. When the driving force is positive and increasing, a stable, or metastable equilibrium is being reached. When the driving force becomes negative the system is moving away from equilibrium. *Hillert* further went on to derive the stability condition

$$\left(\frac{\partial \mu_c}{\partial N_c}\right)_{T,P,\mu_2,\ldots,\mu_{c-1},N_1} > 0 \tag{3.9}$$

Eq. 3.9 can be expressed as the derivative of any potential variable with respect to its conjugate variable, however relating stability to the chemical potential of a phase is the most beneficial form for determining a phases stability. ThermoCalc uses Eq. 3.9 to determine which phases are stable, and which are unstable when calculating the equilibrium of a system. The stability range of a phase can then be determined where the stability condition crosses zero, which can be useful when analyzing Gibbs energy curves.

The driving force of a metastable phase can be determined by calculating the distance between the stable tangent plane, and the tangent plane parallel to the metastable phase illustrated in Fig. 3.2. It can be seen that the *FCC* phase has a larger driving force than σ phase.

mapping searches for all equilibria that are monovariant or invariant, which show up as either lines or points on the final isoplethal phase diagram. ThermoCalc starts the *mapping* procedures with an “initial equilibrium” provided by the user at a specific T,P, and x_i. Newton-Raphson calculations are employed to solve equations Eq. 3.4- Eq. 3.8, where the stable set of phases is determined at each iteration by calculating their driving forces. ThermoCalc then *enters* stable phases, and *suspends* metastable phase based off of the stability criteria in Eq. 3.9. Equilibrium for each set of stable phases is calculated in a stepwise manner incrementing the predetermined x-axis variable until an invariant point is reached, whereby a new set of stable phases are entered into equilibrium. At invariant equilibrium,

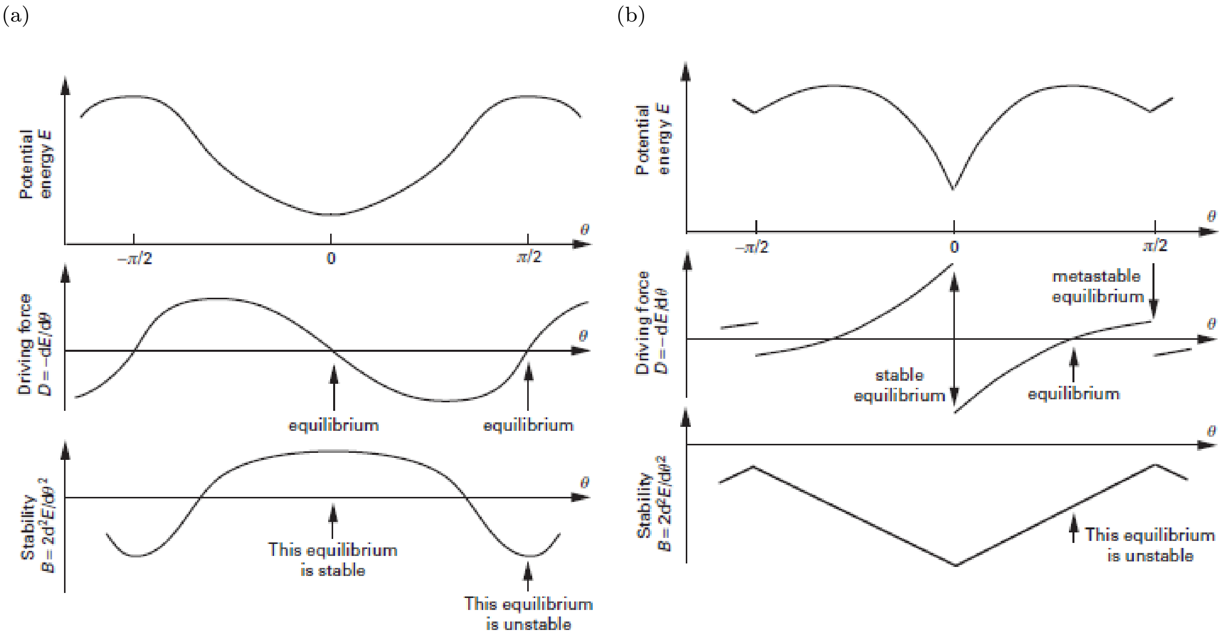

Figure 3.1: The energy, driving force, and stability of an a) elliptical analogue, and b) square analogue. This figure has been lifted from *Hillert, 2007* [14].

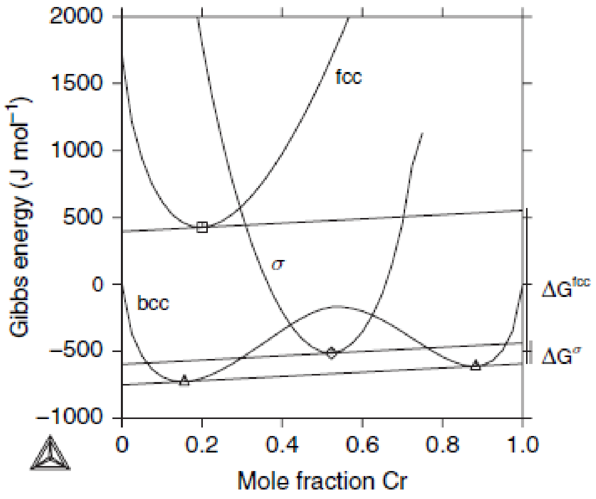

Figure 3.2: Cr-Fe phase diagram illustrating the driving force of metastable phases as the change in Gibbs energy between the stable, and metastable tangent planes. This Figure was lifted from *Lukas et.al.* [15]

$c + 1$ monovariant equilibria are known to stem from this point, where ThermoCalc chooses the next monvariant equilibria to trace, and stores the others to be traced later. This procedure of tracing is continued until the axis limits have been reached.

3.2.3 Gibbs free energy models

Modeling the appropriate Gibbs energy equation for each phase is primarily attributed to how the constituents are bonded, and their configuration in each phase. For phases where the constituents are randomly mixed, and disordered, an ideal substitutional model which is most common of ideal gas phases, and the substitutional regular solution model most common for liquid phases and solution phases should be considered. For crystalline solids with different sublattices and Long Range Ordering (LRO) effects, a more complicated model called the Compound-energy formalism (CEF) should be considered where each compounds or end-member has its own Gibbs energy of formation [15]. In general terms the total Gibbs energy of a phase is expressed as

$$G_m^\alpha =^{srf} G_m^\alpha - T \cdot^{cnf} S_m^\alpha +^E G_m^\alpha \tag{3.10}$$

where ${}^{srf}G_m^\alpha$ represents the reference state of the unreacted mixture of constituents of a phase, ${}^{cnf}S_m^\alpha$ is the configurational entropy of a phase based on the number of possible arrangements of constituents mathematically represented as $S = k \cdot ln(W)$, and ${}^{E}G_m^\alpha$ is the excess Gibbs energy term. The configurational entropy for the constituents in a phase will be assumed to undergo random mixing for each of the sublattices of a phase.

3.2.3.1 Model for liquid phase & austenite solid solution phase

The iron liquid phase can be described as a substitutional solution with Redlich-Kister excess binary contributions, where the general Gibbs energy formula is derived as

$$G_m = \sum_{i=1}^{n} x_i^o G_i + RT \sum_{i=1}^{n} x_i ln(x_i) +^E G_m \tag{3.11}$$

$${}^E G_m = \sum_i \sum_{j>1} x_i x_j L_{ij} \tag{3.12}$$

$$L_{ij} = \sum_{\nu=0}^{k} (x_i - x_j)^\nu \cdot^\nu L_{ij} \tag{3.13}$$

The binary interaction parameter term is extended to the multicomponent system with binary excess contributions from each constituent pair and calculated via Eq. 3.13. This equation is also known as the Redlich-Kister (RK) power series. ${}^\nu L_{ij}$ is an experimental parameter that is temperature dependent and can be expressed linearly by ${}^\nu L_{ij} =^\nu a_{ij} +^\nu b_{ij}T$. ν is generally ≤ 3, where a subregular solution model is where $\nu = 2$, and a subsubregular model is where $\nu = 3$. The regular-solution model describes every constituent composing the liquid to have an equal probability of occupying any site in the unit cell of the phase. Constituent interactions in this model are limited to only binary interactions, where higher-order interactions are disregarded, and assumed to be insignificant. The i, and j indices represent the components of the system (Cr,Ni,Nb,Si,C,Mn, and N/Ti).

3.2.3.2 General compound-energy formalism model

For carbide, and intermetallic phases the constituents of the phase are ordered and grouped into specific sublattices that will effect the configurational entropy, and the enthalpy of mixing of phase where the substitutional regular solutions model is no longer valid. To address the Gibbs energy of sublattice models Hillert and Staffanson (1970) derived the compound-energy formalism (CEF). The general CEF model expands Eq. 3.10 out, and defines its individual parts as

$$^{srf}G_m = \sum_{I_0} P_{I_0}(Y)^oG_{I_0} \tag{3.14}$$

$$^{cnf}S_m = -R\sum_{s=1}^{n} a_s \sum_{i=1}^{n_s} y_i^s ln(y_i^{(s)}) \tag{3.15}$$

$$^{E}G_m = \sum_{I_1} P_{I_1}(Y)L_{I_1} + \sum_{I_2} P_{I_2}(Y)L_{I_2} \tag{3.16}$$

where I_0 is the constituent array of zeroth order which specifies one constituent in each sublattice(eg. i:j:k), P_{I_0} is the product of the constituent fractions of I_0 (eg. $y_i'y_j''y_k'''$), $^oG_{I_0}$ is the Gibbs energy of formation of compound I_0, and L_{I_1} and L_{I_2} are the interaction parameters of the first order, and second order component arrays respectively. The zeroth order constituent array I_0 represents the energy contribution from each end-member compound in a phase as an individual, and unmixed species. The excess Gibbs energy term represents the energy contribution from the mixing for these end-members, where the final composition of a phase may contain multiple constituents in a phases sublattice. If only binary interactions between two constituents in a sublattice are significant, the binary excess model is suitable for describing the excess Gibbs energy term where it is formulated as

$$^{bin.E}G_m = \sum_{i=1}^{n-1}\sum_{j=i+1}^{n} y_i y_j L_{ij} \tag{3.17}$$

Where L_{ij} is calculated from the RK power series. In most cases even with more than two constituents in a sublattice a binary excess model is sufficient. Extrapolations from ternary to binary interactions can be made through models such as the Toop method, and Kohler method discussed further in *Lukas et.al.* [15]. However, if a ternary interaction parameter must be addressed the following ternary excess model can be used

$$\begin{aligned}
{}^{tern.E}G_m &= \sum_{i=1}^{n-2}\sum_{j=i+1}^{n-2}\sum_{k=j+1}^{n} y_i y_j y_k L_{ijk} \qquad (3.18)\\
L_{ijk} &= \nu^i \cdot {}^iL_{ijk} + \nu^j \cdot {}^jL_{ijk} + \nu^k \cdot {}^kL_{ijk} \qquad (3.19)\\
\nu_i &= x_i + (1 - x_i - x_j - x_k)/3\\
\nu_j &= x_j + (1 - x_i - x_j - x_k)/3\\
\nu_k &= x_k + (1 - x_i - x_j - x_k)/3
\end{aligned}$$

Where L_{ij} is calculated from the RK power series. Eq. 3.19 is a composition dependent parameter , where if the composition lies in the center of the ternary constitutional triangle the ternary term will have the largest contribution. lastly, the ν_i terms should be equally to unity.

3.2.3.3 Model for (Nb,Ti)C, and Nb(C,N)

$(Nb, Ti, Fe, Cr)_1(C, N)_1$ has an FCC crystal structure for the substitutional sublattice containing niobium, and titanium, while the carbon and nitrogen interstitial sublattice occupies octahedral sites in the unit cell which can be inferred from Fig. 3.3. In the CEF model it is proposed to add vacancy constituents to the interstitial sublattice, where the crystal structure now becomes $(Nb, Ti, Fe, Cr)_1(Va, C, N)_1$. For the vacancy constituent its chemical potential is regarded to be equal to zero. Expressing the site fraction of vacancies in the interstitial sublattice is expressed as

$$y_{Va}^{(s)} = \frac{N^{(s)} - \sum_i N_i^{(s)}}{N^{(s)}} \qquad (3.20)$$

The resulting sublattice model is $(\mathrm{Nb, Ti, Fe, Cr})_1(\mathrm{Va, C})_1$, and $(\mathrm{Nb, Fe, Cr})_1(\mathrm{Va, C, N})_1$ with the additions of titanium and nitrogen to the system respectively. The general formulation of a two sublattice CEF model for (Nb,Ti)(C,N) is

$$G_m = \sum_i\sum_j y'_i y''_j {}^{\circ}G_{i:j} + RT\left(a_1\sum_i y'_i ln(y'_i) + a_2\sum_j y''_j ln(y''_j)\right) +^E G_m \qquad (3.21)$$

where the a_i terms can be replaced with 0.5 which described the site occupancy of each of the two sublattices. Eq. 3.21 can be expanded out as

$$\begin{aligned}
G_m^{NbC} &= y'_{Nb}y''_C {}^{\circ}G_{Nb:C} + y'_{Ti}y''_C {}^{\circ}G_{Ti:C} + \ldots \qquad (3.22)\\
&+ y'_{Nb}y''_{Va} {}^{\circ}G_{Nb:Va} + y'_{Ti}y''_{Va} {}^{\circ}G_{Ti:Va} + \ldots\\
&+ 0.5RT(y'_{Nb}ln(y'_{Nb}) + y'_{Ti}ln(y'_{Ti}) + \ldots + y'_C ln(y'_C) + y'_{Va}ln(y'_{Va})) +\\
&+ {}^EG_m
\end{aligned}$$

The notation (A:B) refers to the end-member, or compound of a phase, where the colon separates different sublattices. The excess term for NbC can be defined with binary interactions, as the solubility of iron and chromium within the phase is assumed to be dilute. The expanded model extended from *Liu, 2010* [52] takes on the form

$$\begin{aligned}
{}^{E}G_m^{NbC} &= y'_{Nb}y'_{Ti}\left(y''_{C}\sum_{k=0}^{2}{}^{k}L_{Nb,Ti:C}(y'_{Nb}-y'_{Ti})^k + y''_{Va}\sum_{k=0}^{2}{}^{k}L_{Nb,Ti:Va}(y'_{Nb}-y'_{Ti})^k\right)+\dots && (3.23)\\
&+ y''_{C}y''_{Va}\left(y'_{Nb}\sum_{k=0}^{2}{}^{k}L_{Nb:C,Va}(y''_{C}-y''_{Va})^k + y'_{Ti}\sum_{k=0}^{2}{}^{k}L_{Ti:C,Va}(y'_{Nb}-y'_{Ti})^k\right)+\dots && (3.24)\\
&+ y'_{Nb}y'_{Ti}y''_{C}y''_{Va}\left({}^{0}L+{}^{1}L(y'_{Nb}-y'_{Ti})+{}^{2}L(y''_{C}-y''_{Va})\right)+ && (3.25)\\
&+ y'_{Nb}y'_{Fe}y''_{C}y''_{Va}\left({}^{0}L+{}^{1}L(y'_{Nb}-y'_{Fe})+{}^{2}L(y''_{C}-y''_{Va})\right)+\dots && (3.26)
\end{aligned}$$

A visual representation of a $(\mathrm{Nb},\mathrm{Ti})_1(\mathrm{C},\mathrm{Va})_1$ model is shown in Fig. 3.4, where the Gibbs energy of formation is calculated for each end-member, and the interaction parameters are calculated for each interaction between constituents.

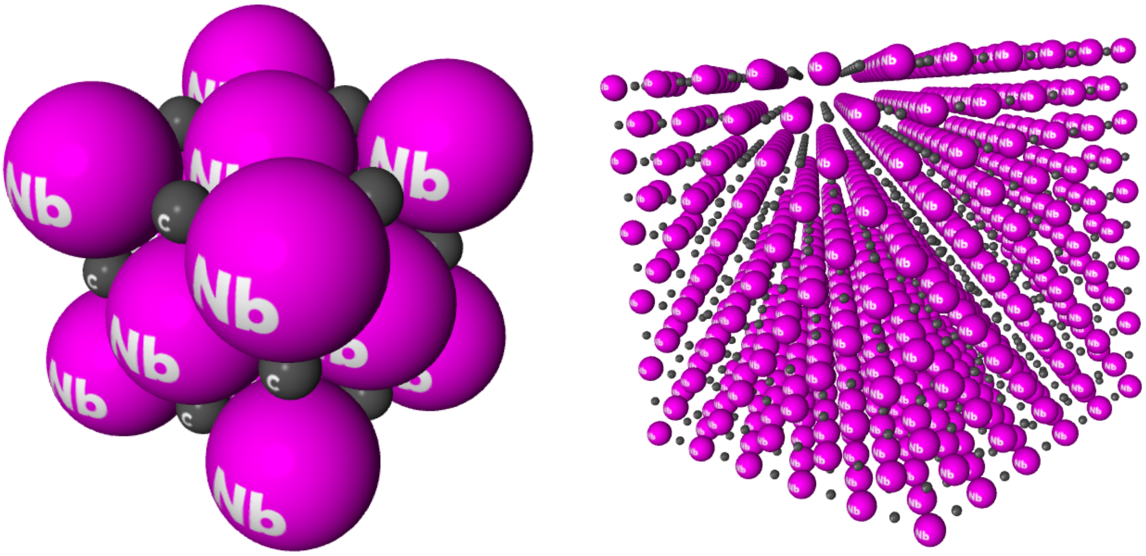

Figure 3.3: Crystal structure of NbC. 3D model can be viewed at http://tinyurl.com/9aynzy7.

3.2.3.4 Model for M23C6, and M7C3

$M_{23}C_6$ has a sublattice model of $(\mathrm{Cr},\mathrm{Fe},\mathrm{Ni})_{20}(\mathrm{Cr},\mathrm{Fe},\mathrm{Nb})_3(\mathrm{C},\mathrm{N})_6$, and M_7C_3 has a model of $(\mathrm{Cr},\mathrm{Fe},\mathrm{Mn})_7\mathrm{C}_3$. The equivalent position parameters as well as their Wyckoff positions are listed in Table 3.2. M_7C_3 will be modeled after the two-sublattice model, Eq. 3.21, similar to the Nb(C,N) model. If the the ternary excess model in Eq. 3.18 is chosen instead of the binary model the excess term for M_7C_3 will take the

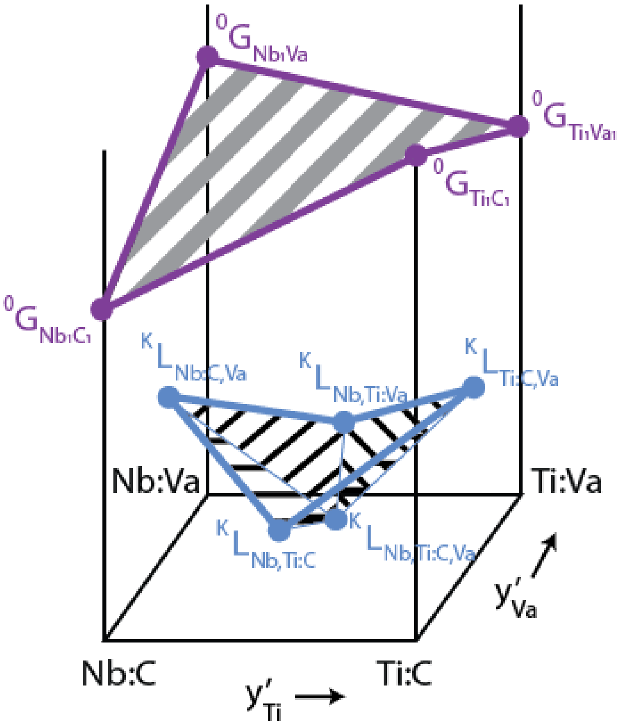

Figure 3.4: visualization of the sublattice model for $(\mathrm{Nb},\mathrm{Ti})_1(\mathrm{C},\mathrm{Va})_1$ showing the Gibbs energy of formation for each end-member, and the interaction parameters for each constituent interaction. The interaction parameter notation separates sublattices with a colon, and constituents with a comma.

form.

$$ {}^{E}G_m^{M_7C_3} = y'_{Cr}y'_{Fe}y'_{Mn}y''_{C}\left(\nu^0_{Cr}L_{Cr,Fe,Mn:C} + \nu^1_{Fe}L_{Cr,Fe,Mn:C} + \nu^1_{Mn}L_{Cr,Fe,Mn:C}\right) \tag{3.27} $$

$M_{23}C_6$ consists of three sublattices, therefore the general form for the Gibbs energy expression will be

$$ \begin{aligned} G_m = \textstyle\sum_i \sum_j \sum_k y'_i y''_j y'''_k {}^{\circ}G_{i:j:k} + RT \Big(a_1 \textstyle\sum_i y'_i ln(y'_i) + a_2 \sum_j y''_j ln(y''_j) + \ldots \\ + a_3 \textstyle\sum_j y'''_j ln(y'''_j)\Big) +^{E} G_m \end{aligned} \tag{3.28} $$

where

$$ \begin{aligned} {}^{E}G_m &= \sum_i \sum_j \sum_k \sum_{l>i} y'_i y''_j y'''_k y'_l L_{i,l:j:k} \\ &+ \sum_i \sum_j \sum_k \sum_{l>j} y'_i y''_j y'''_k y'_l L_{i:l,j:k} \\ &+ \sum_i \sum_j \sum_k \sum_{l>k} y'_i y''_j y'''_k y'_l L_{i:j:k,l} \\ &+ \sum_i \sum_j \sum_k \sum_{l>k} \sum_{m>j} y'_i y''_j y'''_k y'_l y''_m L_{i,l,m:j:k} + \ldots \end{aligned} \tag{3.29} $$

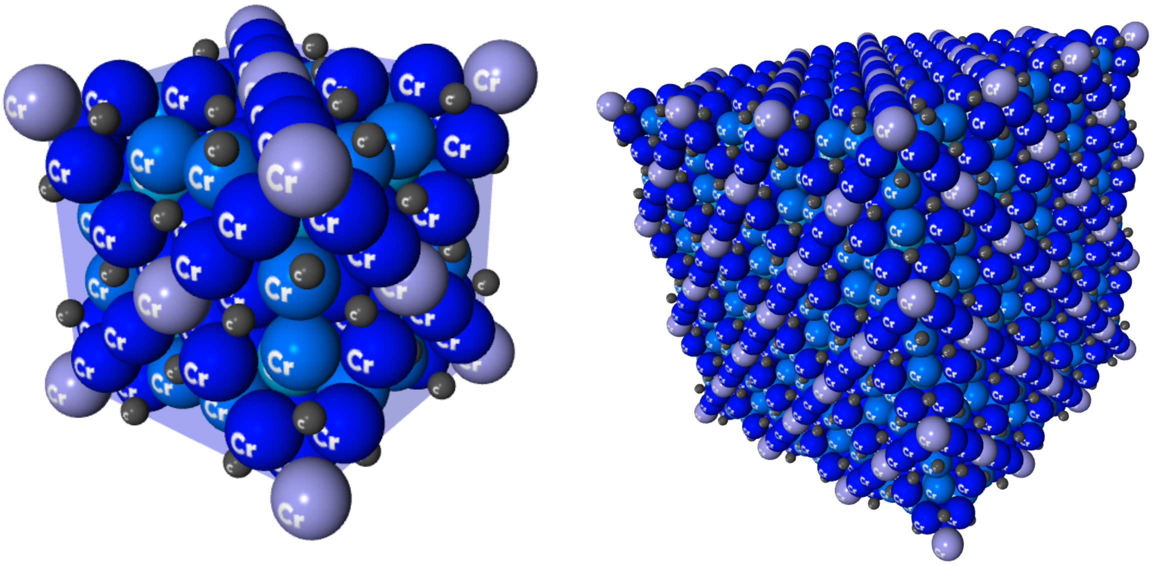

Figure 3.5: Crystal structure of $M_{23}C_6$. 3D model can be viewed at http://tinyurl.com/9km9mro.

Table 3.2: Wyckoff notation, and variable parameters (x,y,z) of atoms in M_7C_3 and $M_{23}C_6$

M7C3	ref	[49]		
atom	site	x	y	z
Cr1	8d	0.064	0.811	0.056
Cr2	4c	0.25	0.626	0.057
Cr3	4c	0.25	0.206	0.25
Cr4	4c	0.25	0.416	0.261
Cr5	8d	0.065	0.021	0.25
C1	4c	0.25	0.562	0.459
C2	8d	0.029	0.342	0.028
M23C6	ref	[53]		
atom	site	x	y	z
Cr1	4a	0	0	0
Cr2	8c	1/4	1/4	1/4
Cr3	32f	0.385	0.385	0.385
Cr4	48h	0	0.165	0.165
C	24e	0	0.1712	0.1712

3.2.3.5 Model for G-phase

G-Phase has the sublattice model $(\mathrm{Fe}, \mathrm{Ni})_{16}\mathrm{Si}_7(\mathrm{Cr}, \mathrm{Mn}, \mathrm{Nb}, \mathrm{Ti})_6$, and a crystal structure represented in Fig. 3.6 which was composed with information from *Holman et al., 2008* [51]. It should be noted that G-phase is currently not implemented in any of the iron databases of ThermoCalc, and was appended from a nickel database to be used in the study analyzed in this report. Since nickel is a constituent of the first sublattice interaction parameters, the Gibbs energy reference state may be greatly over/under-estimated. Since the stability of the other carbides and intermetallics in the system are dependent on

G-phase the relativistic effects should not change, and only the absolute equilibrium will differ from reality. Futhermore, appending G-phase from the nickel database causes the manganese constituent to occupy the majority of the sites on the third sublattice, which from the literature [2, 3, 54] niobium is suppose to be the dominant occupant. Manganese should then be suspended from the sublattice model in ThermoCalc, where the model is now $(\mathrm{Fe}, \mathrm{Ni})_{16}\mathrm{Si}_7(\mathrm{Cr}, \mathrm{Nb}, \mathrm{Ti})_6$. The model for three sublattices described in Eq. 3.28, and Eq. 3.29 will be used to formulate its Gibbs energy.

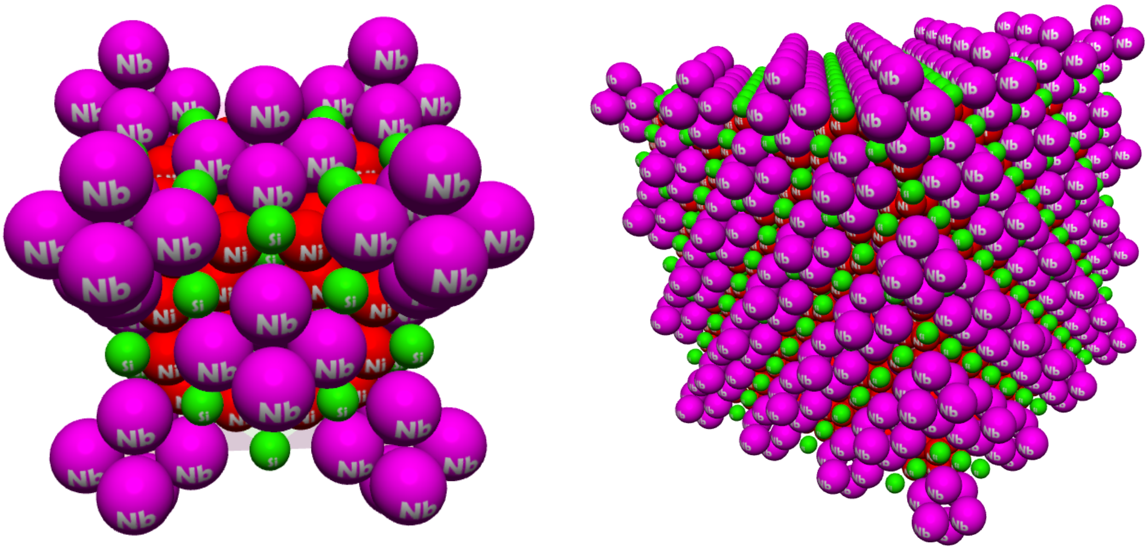

Figure 3.6: Crystal structure of G-Phase. 3D model can be viewed at http://tinyurl.com/8ftw7nj.

3.2.3.6 Model for Z-phase

Z-Phase has the sublattice model $(\mathrm{Nb})_1\mathrm{Cr}_1(\mathrm{N})_1$ and crystal structure shown in Fig. 3.7, which contains only one constituent for each of the sublattices. This simplifies the Gibbs energy expression greatly where ${}^{E}G_m = 0$ since no mixing of constituents is involved, and the surface of reference term and the configurational entropy term are described as

$$G_m^{Z-Phase} = y'_{Nb}y''_{Cr}y'''_{N}{}^{\circ}G_{Nb:Cr:N} + RT(y'_{Nb}ln(y'_{Nb}) + y''_{Cr}ln(y''_{Cr}) + y'''_{N}ln(y'''_{N})) \tag{3.30}$$

The filled thermodynamic properties for Z-phase can be obtained from *Denielsen and Hald, 2007* [41].

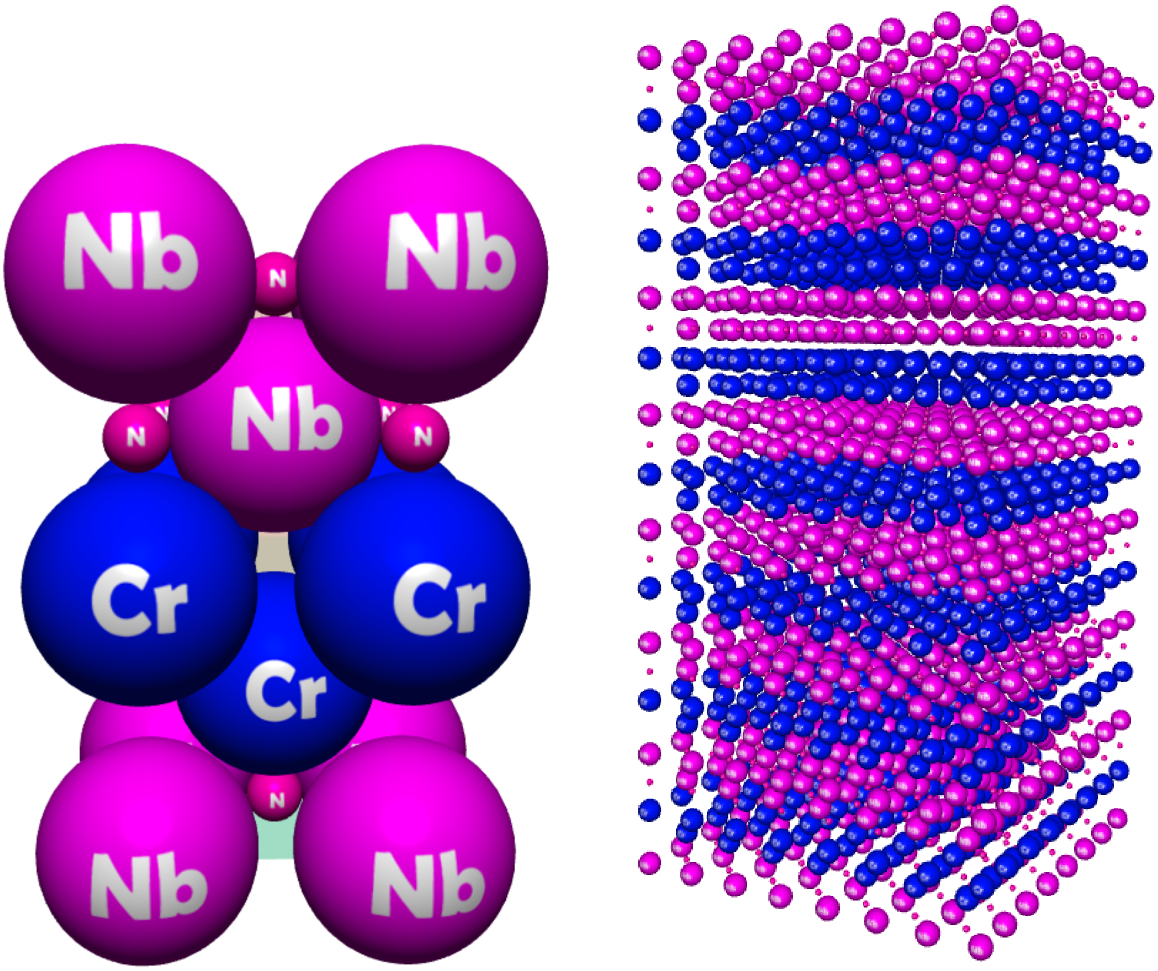

Figure 3.7: Crystal structure of Z-Phase. 3D model can be viewed at http://tinyurl.com/8o3smwg

3.3 Chemistry optimization using ThermoCalc

3.3.1 Factorial Matrix

In the present study we are interested in seeing how nitrogen, and titanium affect the resulting microstructure, as well as their interactions with the other components in a 2032Nb alloy. From the ASTM specification for 20Cr-32Ni-1Nb the compositional matrix in Table 3.3 can be used to see the ranges for each element that will be explored. In ThermoCalc the **stepping** command will be used over the temperature range $T_m - T_{rt}$ for finite compositions of the alloy. Certain levels in the compositional ranges for each element will need to be decided where then equilibrium will be calculated for all possible combinations of these finite chemistries. If a maximum, median, and minimum values are chosen for each range than ThermoCalc will need to run stepping procedures for $3^7 = 2187$ chemical compositions.

Writing these ThermoCalc files out manually would be quite time consuming, so two batch programs were written in Visual C# to automatically write and run numerous ThermoCalc log files.

Table 3.3: Range of 20-32Nb Stainless Steel compositions investigated in the ThermoCalc test matrix. Compositional ranges correspond to ASTM A351, grade CT15C.

	Ni	Cr	Nb	Si	Mn	C	N/Ti	W,Mo,Ti,Zr
Compositional Range (wt.pct)	31 - 34	19 - 21	0.5 - 1.5	0.5 - 1.5	0.15 - 1.5	0.05 - 0.15	0 - 0.3	<0.05

3.3.2 Compiling equilibrium data

The first script will be used for compiling all the relevant information about any intermetallic phases, or chrome carbides that may have precipitated during long term aging. For example, the G-phase curve in Fig. 3.8a has three definable points that can be analyzed for all the chemistries when determining the minimization of G-phase. The first definable point is the temperature at which the phase starts to precipitate, referred to as the stability temperature. The chemical formula of G-phase is $Ni_{16}Nb_6Si_7$, where niobium will be needed to facilitate the precipitation of this intermetallic. The precipitation of G-phase is known to occur through a transformation mechanism with NbC [3, 11, 17]; However, if there is excess niobium at the dendrite boundaries the G-phase will be able to precipitate without consuming NbC precipitates. Excess niobium precipitating out as G-phase is indicative of the plateau region shown in Fig. 3.8a, where NbC remains unaffected. Once a certain temperature is reached $\mathrm{M_{23}C_6}$ becomes stables, promoting the dissolution of NbC, freeing up the niobium to precipitate even more G-phase. Once all of the NbC has been dissolutioned and all the niobium has been exhausted in solution and precipitated as G-phase; the maximum, and terminal phase fraction for G-phase has been reached, denoted as point 3 on Fig. 3.8a. Point 3 must also be defined as the terminal phase fraction, meaning that for any subsequent decreases in temperature there will be only minor fluctuations in the equilibrium phase fraction. This will avoid any situations where the driving force of the examined phase would start to decrease with decreasing temperature, where it could eventually become metastable, and replaced with another phase.

The stability temperature can be defined as $m^{\alpha} > 0$, where m is the phase fraction (mol%) for phase α. Identifying the Plateau region can be achieved by finding where $\partial m^{\alpha}/\partial T \approx 0$, and $\partial^2 m^{\alpha}/\partial T^2 \approx 0$. Finding the maximum terminal phase fraction is done in the same way as the plateau region with the added conditions: $max(m^{\alpha})$, and at $max(m^{\alpha})$, $m^{\alpha}/\partial T^2 \approx 0 \ \forall \ T \in \{T_x \ldots T_{rt}\}$, where T_x is the temperature where $max(m^{\alpha})$.

The second script will be used to compile useful information on (Nb,Ti)(C,N) for each chemistry in the compositional matrix. Since (Nb,Ti)(C,N) is of a cubic NaCl structure, which is the same structure as the solution phase (austenite), ThermoCalc creates the (Nb,Ti)(C,N) phase as a new composition set of the FCC phase. Therefore, in ThermoCalc the solution phase is denoted as FCC_A1#1, and (Nb,Ti)(C,N) is denoted as FCC_A1#2. For each chemistry iteration, FCC_A1#2 contains the end members $(\mathrm{Nb,Ti})_1(\mathrm{C,N})_1$, but the site fractions, or constituents fractions are uncertain. Furthermore,

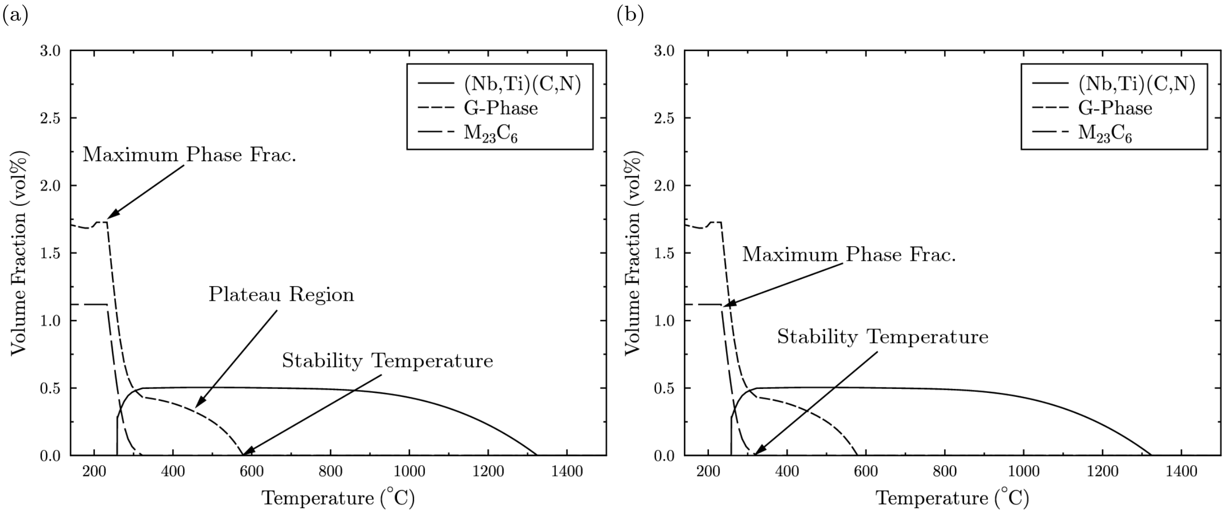

Figure 3.8: The volume fraction of each phase over a temperature range contains three notable regions; the stability temperature, the plateau region, and the maximum volume fraction. These three points are outlined for a) G-Phase, b) and $M_{23}C_6$ of an alloy with the composition Cr19-Ni31-Si0.5-Nb0.5-C0.05-Mn0.825-Ti0.05.

differentiation between NbC, and TiC is not made, and will be grouped into one phase called FCC_A1#2. This information cannot give us distinct phase fractions of NbC, and TiC, as the solubility of titanium in NbC, and niobium in TiC is unknown. For the purpose of this study it will be assumed that these two constituents (niobium, and titanium) are mutually exclusive to their respective phases, and a volume fraction of each will be presented. To determine the composition of the MC carbides, a plot consisting of the mole fraction of constituents of the FCC_A1#2 phase along the temperature range, $T_{rt} \rightarrow T_m$, must be specified. Fig. 3.9b illustrates an example of a compositional plot of FCC_A1#2, which shows that the composition of FCC_A1#2 can fluctuate based on the solubility of the elements, and the stable phases in the system. To see how the solubilities of titanium and niobium in (Nb,Ti)(C,N) change with variations in alloy composition, the element fractions in FCC_A1#2 can be extracted at specific temperatures for comparison. As illustrated in Fig. 3.9b Matlab should extract the temperatures and the constituent fraction of FCC_A1#2 at the solubility limit of titanium, the maximum phase fraction of FCC_A1#2, and the dissolution temperature of FCC_A1#2. Due to an error in ThermoCalc reporting constituent fractions of a phase, these fractions do not do not drop to zero once the phase becomes unstable as seen in Fig. 3.9b.

When analyzing Fig. 3.9 the stability, and driving force of a phase can be determined. The driving force is analogous to the change in phase fraction for a given phase. From Fig. 3.9 a phase is stable once $m^\alpha > 0$, however if $\partial m^\alpha / \partial T > 0$ the driving force of a phase is assumed to be positive. If $\partial m^\alpha / \partial T < 0$ the driving force of the phase is negative as is nearing instability.

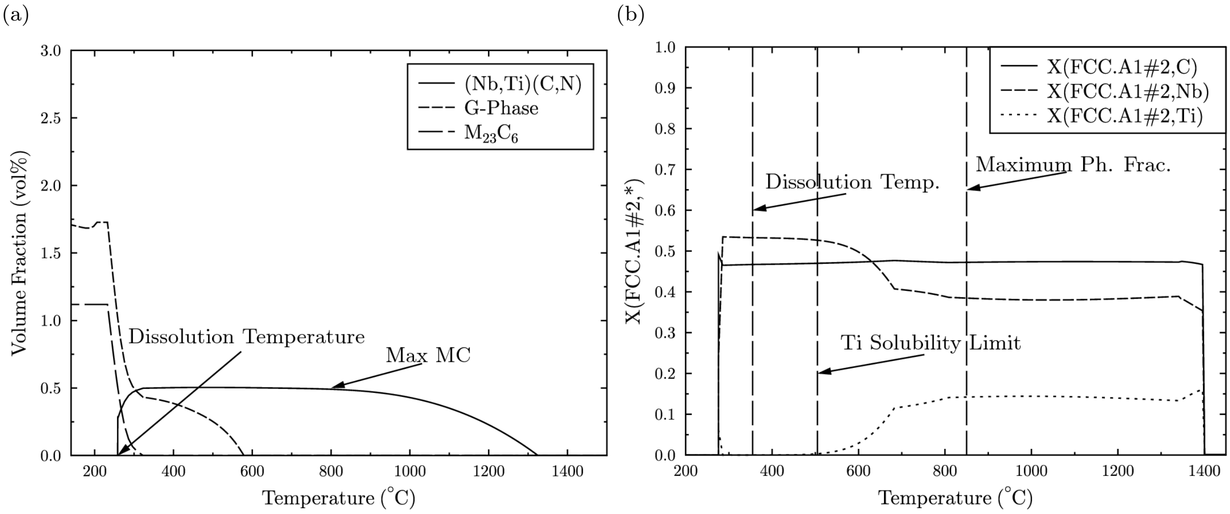

Figure 3.9: For the (Nb,Ti)(C) phase, or FCC_A1#2, a) the maximum phase fraction, and the dissolution temperature are extracted, along with b) specific composition of FCC_A1#2 at these regions, and the solubility limit of titanium.

3.3.3 Introduction to Design of Experiments

3.3.3.1 Factorial Design

In a factorial experiment the goal is to investigate all possible combinations for all of the factors, and levels of factors in the experiment. For compositional analysis of a 2032Nb alloy, seven elements, or factors need to be considered as well as their given compositional ranges listed in ASTM A351, grade CT15C, and displayed in Table 3.3. For this experiment three levels are chosen for each factor, a low, mid, and high composition. The low and high level are defined as the compositional range limits in Table 3.3, and the mid level is the median value of these ranges. To determine which individual factors are the most significant, called the main effects, and which interactions are the most significant, an Analysis of variance (ANOVA) test much be carried out on the factorial design. “Factorial experiments are the only way to discover interactions between variables” [55], which is very important for alloy composition optimization as interactions between components has been proven to be vital to the resulting microstructure (e.g. $Nb/(C + 6/7N) = 7.7$).

The most common factorial design used is the 2^k factorial design, where for each factor only two levels (low/high) are considered. However, this assumes that the response variable, or phase fraction, and the individual compositional elements have an approximately linear relationship, which cannot be assumed in the present study. To compensate for non-linearity, a third level was added at the median value for each range of factor level. 3^k experiments can be quite large, and for most instances where the data is accumulated manually this option is too cumbersome for most experiments. Several alternatives to a 3^k factorial experiment have been developed, such as adding a center point to a 2^k design, or blocking a 3^k

design. Adding a center point to a 2^k design is used to test a curvature hypothesis to see if the main factor or interaction has significant curvature. More information about this can be found in *Montgomery and Runger*,2006 [55]. Blocking is typically used to split up and group certain treatments if some of the experiments were not all performed under homogenous conditions. Blocking could also be used to reduce a 3^k experiment down to multiple 2^k experiments, were low/high, low/med, and med/high levels are run independently.

A 3^3 factorial matrix illustrated in Fig. 3.10 visually represent a 3^3 model where each treatment of the design can be calculated out from the formula:

$$\begin{aligned} Y_{ijk} &= \mu + \tau_i + \beta_j + \psi_k + \tau\beta_{ij} + \tau\psi_{ik} + \beta\psi_{jk} + \tau\beta\psi_{ijk} + \epsilon_{ijk} \\ \forall &\quad \{i \in (0,1,2), j \in (0,1,2), k \in (0,1,2)\} \end{aligned} \tag{3.31}$$

where μ is the contribution from the overall mean effect, τ, β, ψ and the effects from the three individual factors, plus their interactions, and ϵ is the random component error [55]. i, j, and k represent the various levels of each factor (high, medium, and low). In Fig. 3.10 each node of the cube lattice represents the response variable of the associated treatment. For example the node in the center of the cube ($Nb_1Si_1C_1$), represents the the response, or the phase fraction of a specific phase, when the composition of the alloy is 1wt%Nb, 1wt%Si, and 0.1wt%C. To test whether any of the single elements (main effects), or any of the interactions between the components significantly effect changes in the response variable, a set hypotheses will need to be proven by the resulting ANOVA model:

1. $H_0 : \tau_i = 0 \,\forall\, i$ (No Main effect of factor A)
   H_1 : at least one $\tau_i \neq 0$

2. $H_0 : \beta_j = 0 \,\forall\, j$ (No Main effect of factor B)
   H_1 : at least one $\beta_i \neq 0$

3. $H_0 : \psi_j = 0 \,\forall\, k$ (No Main effect of factor C)
   H_1 : at least one $\psi_i \neq 0$

4. $H_0 : \tau\beta_{ij} = 0 \,\forall\, i, j$ (No two-way interaction)
   H_1 : at least one $\tau\beta_{ij} \neq 0$
   $\vdots$

5. $H_0 : \tau\beta\psi_{ijk} = 0 \,\forall\, i, j, k$ (No three-way interaction)
   H_1 : at least one $\tau\beta\psi_{ij} \neq 0$

If any of the null hypotheses are rejected then that factor, or interaction has a significant effect on the response variable. To reject or accept a hypothesis the total sum of squares must first be decomposed, $SS_T = SS_A + SS_B + SS_C + SS_{AB} + SS_{AC} + SS_{BC} + SS_E$, where SS_E represents the error term. The

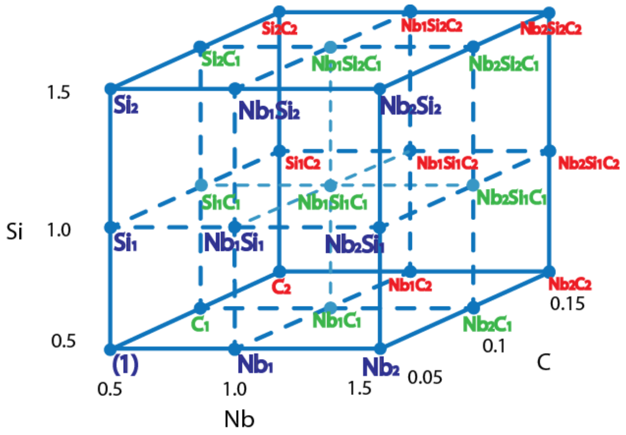

Figure 3.10: Illustration of a 3^3 factorial design matrix.

sum of squares for any effect or interaction is calculated as,

$$SS = \frac{(Contrast)^2}{n3^k} \tag{3.32}$$

where the contrast is calculated from the effect,

$$Effect = \frac{Contrast}{n3^{k-1}} \tag{3.33}$$

where n is the number of replicates, and k is the number of factors. The contrast of the $main - effects$ can be solved for by:

$$Y = \sum_i c_i (\sum_j \sum_k y_{ijk}) \tag{3.34}$$

Where Y is the effect of a single factor, c_i is the coefficient of factor y at level i (eg. $Nb_1 = 0.5$, $Nb_2 = 1.0$), and y_{ijk} is the treatment for levels $i = 0, 1, 2$, $j = 0, 1, 2$, and $k = 0, 1, 2$ (eg. phase fraction where $Nb_i Si_j C_k$, Fig. 3.10). Eq. 3.34 is visually represented in Fig. 3.11a. Fig. 3.11b, and Fig. 3.11c represent contrast of two-factor, and three-factor interactions, assuming a linear relationship between the levels and the response variable. Solving for the contrasts in a two-factor, or three-factor interaction in a 3^k design is much more complicated, and is outside of the scope of this work. However, more information on 3^k formulations can be read from Spliid, 2002 [56].

Mean squares for each main effect, and interactions, are calculated as:

$$MS_x = \frac{SS_x}{(k-1)^a} \tag{3.35}$$

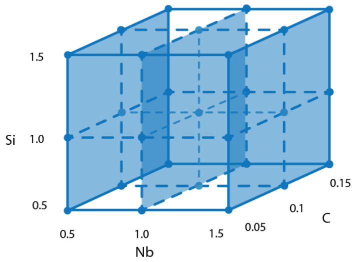

(a) Main Effects for Nb, Si, and C respectively

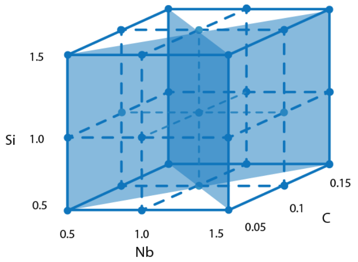

(b) Two Factor Interaction for Nb×C, Si×C, and Si×Nb respectively

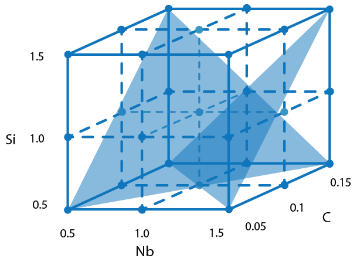

(c) Three Factor Interaction for Nb×Si×C

Figure 3.11: 3^3 factorial matrix depicting a) main effect, b) two-factor interactions c) three-factor interactions

where x is the factor or interaction, and $a = 1$ if a main effect, $a = 2$ if a two-factor interaction ,and $a = 3$ if a three-factor interaction. Where finally an F-distribution test can be conducted to reject of accept the null hypothesis, where:

$$F_0 = \frac{MS_x}{MS_E} \tag{3.36}$$

if $f_0 > f_{\alpha,\nu_1,\nu_2}$, where α is the level of significance (in this case it is 0.05, or 95%), and ν_1, and ν_2 are the degrees of freedom of x and ϵ_{ijk}, the null hypothesis is rejected and factor x is significant.

3.3.3.2 Multiple Linear Regression Modelling

After all of the significant factors, and interactions have been identified in the factorial design, the data can be fit to a regression model

$$Y = \beta_0 + \beta_1 x_1 + \beta_2 x_2 + \ldots + \beta_k x_k + \epsilon \tag{3.37}$$

Where Y is the response variable, x_k are the independent variables, or factors, β_k are the unknown parameter coefficients, and ϵ is the error term. Determining the β coefficients will allow for us to describe the relationship between independent variables, and the response variable (dependent variable) through an approximate function. Since there are multiple phases that compose the 2032Nb system, a set of regressions functions will need to be determined to appropriately describe the system. After these functions have been approximated, a model for optimizing the system can be drawn, either through statistical or linear programming methods.

Using linear regression models to fit the factorial design data, assumes that the data fits linearly with the response variable. This assumption neglects any significant interactions that were uncovered in the factorial design, as they would be regarded as polynomial terms. However, a linear model may still be used by approximating these polynomial terms as new variables. For example if the significant terms in the regression model were Si,Nb, and Si × Nb, the regression function would be $Y = \beta_0 + \beta_1 Si + \beta_2 Nb + \beta_3 NbSi + \epsilon$. If we let $x_3 = NbSi$ this modifies the equation from containing two independent variables to incorporating three independent variables, and can now be considered a linear function.

The linear coefficient can be solved for using the *Least Squares Method* described in the next section. The regression function should then be tested for significance, and how well if fits with the original data. The easiest way to compare the fit of the approximated function is to calculate the coefficient of multiple determination , or R^2 value. R^2 is calculated as

$$R^2 = 1 - \frac{SS_E}{SS_T} \tag{3.38}$$

The R^2 value will be a fraction of how much of the model accounts for the variability in the original data. For example if $R^2 = 0.95$, 95% of the variability of the response data is accounted for in the regression model. There are some short-comings of the R^2 value as it keeps improving as more terms are added to the model. This is compensated for in the adjusted R^2 value, but for the purposes of this study only the regular R^2 value will be reported.

3.3.3.3 Least Squares Method

The least squares method is an effective method in solving a system of linear equations, and is used in both regression modelling, and fitting experimental data to Gibbs energy models. If a set of linear equations are described as

$$y_i = \beta_0 + \sum_{j=1}^{k} \beta_j x_{ij} + \epsilon_i \, \forall \, i \; \in \{1, 2, \ldots, n\} \tag{3.39}$$

Where x_{ij} is the ith observation of the k total independent variables x_j, y_i is the dependent variable of observation i, β_j is the coefficient for the jth term, and ϵ is the error between the calculated $\hat{y}_i$ and the measured y_i values [55]. The best fits for the β_j coefficients are determined by the minimization of the least squares function,

$$min \, w.r.t. \, \beta_j = \sum_{i=1}^{n} \epsilon_i^2 = \sum_{i=1}^{n} \left(y_i - \beta_0 - \sum_{j=1}^{k} \beta_j x_{ij} \right)^2 \tag{3.40}$$

which can be expressed as

$$\sum_{i=1}^{n} \epsilon_i \cdot \frac{\partial \epsilon_i}{\partial \beta_j} = 0 \, \forall \, j \quad \in \{1, \ldots, k\} \tag{3.41}$$

Rearranging for y_i a set of n equations can be solved for providing the best estimates for β_j.

Chapter 4

Characterization techniques for 2032Nb stainless steel

4.1 Introduction

This chapter will outline the 203Nb alloys used in this document, including ex-service manifold material, and modified 2032Nb chemistries with various casting thickness, and homogenization treatments. Experimental conditions will also be listed. The subsequent sections will outline the metallography procedures used on the 2032Nb samples, as well as various etching methods, and the spectroscopy methods used to analyze the microstructure. Imaging techniques include optical microscopy, SEM, EPMA, AES, where EPMA was primarily used for element mapping. Single point chemical quantification was performed with EDS, WDS, and AES to gather compositional data for the precipitates in the alloy. The advantages and disadvantages of all the quantification methods are listed. An overview of casting structure is provided, along with Scheil solidification and its use in the thermodynamics software package ThermoCalc. Lastly, image analysis techniques will be discussed in order to quantify the phase fractions of the microstructure.

4.2 Alloy Information

4.2.1 In-service 2032Nb alloy from Syncrude

The material investigated in the first part of this study is a 20Cr32Ni1Nb stainless steel alloy, often designated as 20-32Nb, and was studied in the form of a centrifugally cast pipe, and statically cast tee. The composition for each of these pieces was determined by Inductively coupled plasma (ICP) mass spectrometry in Table 4.1. The material under investigation was extracted from an Ex-service hydrogen reformer manifold, provided by Syncrude Canada Ltd., where the manifold had been used in service for

16 years, at 843-871°C. It should be noted that the hydrogen reformation process is endothermic where the actual temperature experienced by the steel might be lower (800-850°C). The manifold's pipe was centrifugally cast in a cone shape with extracted samples having a variable thickness between 25mm - 52mm, and the tee was statically cast cylindrically with a constant thickness of 22mm. Three years before being removed from service the static cast tee had undergone a solution annealing treatment at 1148°C for 1.5hrs.

Some of the samples extracted from the aged components were button melted in order to return them to a cast state, and others where solution annealed to homogenize the alloy. The solution annealing treatment was performed at 1200°C for 1 hour, and then quenched in water. This annealing treatment is similar to the pre-weld annealing treatments done on the tee sections of the manifold to fully dissolve any low melting point silicon rich intermetallics that may have developed during aging [57].

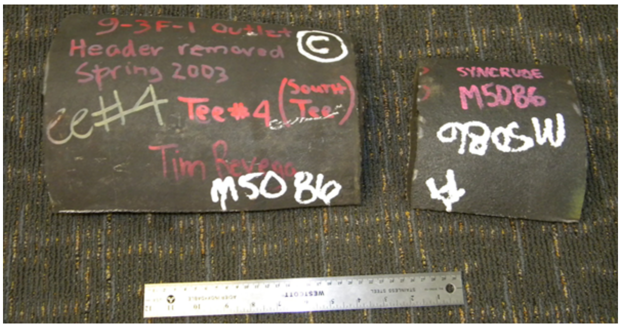

Figure 4.1: 2032Nb centrifugally cast pipe (left), and statically cast tee (slab). Both pieces were in-service for 16 years, where the static cast tee has undergone a solution annealing treatment three years prior to being removed from service.

Table 4.1: Composition of the ex-service 2032Nb stainless steel alloy for the centrifugally cast pipe, and statically cast tee. The last column provides the NbC stability ratio for each piece. The sample material was provided by Syncrude Canada.

	Composition (wt.pct)									
	Cr	Ni	Mn	Si	C	Nb	N	W,V,Mo,Ti,Ta,Zr	P,S	$\frac{Nb}{(C+6/7N)}$ Ratio
CC 2032Nb	20.5	33.6	0.96	0.99	0.087	1.17	0.051	< 0.05	< 0.015	8.95
SC 2032Nb	20.7	31.8	0.99	1.00	0.085	1.08	0.050	< 0.05	< 0.015	8.45

To recreate the as-cast microstructure a button melting apparatus was used to remelt the aged samples. The remelting was conducted in an argon atmosphere on a water-cooled copper hearth. The samples were then aged in a chamber furnace at 800°C, in an open air environment. Fluctuations in furnace temperature were monitored with a k-type thermocouple, where the actual temperature in the middle of the furnace was found to be between 802.7-806.3°C.

Samples of both the button melt group, and the solution annealed group were periodically taken out of the furnace at logarithmic time increments for metallographic analysis (ie. not aged, 1 week, 2 weeks, 1 months, 2 months, 4 months, 8 months, 1 year).

4.2.2 Commercial 2032Nb & Modified Super 2032Nb Experimental Matrix

The second part of this thesis examine eight different castings of 2032Nb steel, aged for up to 1 year, and then compared on the basis of microstructural evolution, and microstructural variations. The design of the experiment is shown in Table 4.2, where a 2^3 factorial design can be generated. The last column shows how many samples must be sectioned in order to account for the various aging time in which the samples will need to be analyzed (ie. unaged, 1 week, 2 weeks, 1 months, 2 months, 4 months, 8 months, 1 year). The eight treatments of the design are designated by varying alloy composition (Commercial 2032Nb or Super 2032Nb), the thickness of the castings (1” or 3”), and the post cast processing heat treatment (no heat treatment, or homogenization heat treatment).

Each treatment will be labeled by the factorial design constitution, which categorizes the three effects as *A*-Composition, *B*-Section thickness, and *C*-Heat Treatment. Any treatment with an *a* in its name designates that it has a Super 2032Nb composition, where if it does not have an *a* it has a Commercial 2032Nb chemistry. Similarly if the treatment has a *b* in its label it has a 3” wall thickness, where if it does not have a *b* it has a 1” wall thickness. Lastly, if the treatment has a *c* in its label that means that it has been homogenized, whereas if it does not contain a *c* it has not undergone a homogenization treatment. For example the treatment labeled (1) does not contain any letters so it has a commercial 2032Nb chemistry, a 1” wall thickness, and was not homogenized. On the other hand, the treatment *abc* contains all of the letters so it has a Super 2032Nb chemistry, a 3” wall thickness, and is homogenized.

During the heat treatment the furnace ramps up from room temperature to 1213°C in 3.5 hrs, holds at 1213°C for 4.75 hrs, and then decreases to 1121°C for one hour where the samples are then water quenched. The two compositions analyzed in this study are listed in Table 4.3. Due to the agreement with MetalTek International the exact chemistry for these alloys cannot be reported. Mechanical properties data for each of the treatments can be found in the Section A.13, where the alloys have yield strengths from 186-226 MPa, ultimate tensile strengths of 422-495 MPa, and elongations of 18.1-44.4%.

Table 4.2: Design matrix for investigating the influence of chemistry on microstructure in commercial 2032Nb or Super 2032Nb, section thickness (1” or 3”), and post cast processing heat treatment (as-cast, homogenized). The last row, and column designates how many samples will be needed for each set of treatments.

	Section thickness (B)				
Composition (A)	**1” finished wall**		**3” finished wall**		
	heat treatment (C)		**heat treatment (C)**		
	as-cast	**homogenized**	**as-cast**	**homogenized**	y_i
Comerical 2032Nb	(1)	c	b	bc	32
Modified Super 2032Nb	a	ac	ab	abc	32
y_i	16	16	16	16	64

Table 4.3: Composition ranges for commercial 2032Nb and Super 2032Nb alloys provided by MetalTek International.

	Composition (wt.pct)								
	Cr	Ni	Mn	Si	C	Nb	W,Mo,Ti,Zr	P,S	Pb
Commercial 2032Nb	19-21	31-34	0.5-1.5	0.5-1.0	0.90-1.35	1.17	0	≤ 0.05	≤ 0.01
Super 2032Nb	20	33	1.25	0.60	0.12	0.90	≤ 0.05	≤ 0.05	0

4.3 Sectioning, Mounting & Polishing Procedure

4.3.1 Sectioning

Each casting was cut into eight 0.5cm thick pieces using a Modern Tool 9” X 16” Horizontal Band Saw, and then sectioned into 1” × 1” samples using a Struers Labotom-3 Wet Saw. The samples were then placed in the Chamber Furnace at 800°C, and taken out periodically at time increments of 1 week, 2 weeks, 1 month, 2 months, 4 months, 8 months, and 1 year.

Once taken out of the furnace the surface of each sample was ground down to remove the oxide layer, and well as to confirm that the surface is flat before mounting. The samples were then precision cut with a Presi Mecatome T180 Micro-cutter to specific dimensions for each of the respective microscopy methods. For AES, and XRD each sample must be cut to a 1cm×1cm specification. For EPMA, and SEM the samples were sectioned to less than $2cm^2$ to fit in the mounts. The sides of each sample were then ground off to remove any excess material to make sure that the sample will lay perfectly flat in the hot mounting system.

4.3.2 mounting

Hot mounting of the samples was performed with a Buehler Simplimet 1000 Automatic Mounting Press, and EpoMet G molding compound. It is important the the samples lay perfectly flat in the mounting chamber to keep molding compound from getting underneath the sample, and lifting it up during the compression process. When done properly, the entire surface of the sample should be visible after mounting, making the polishing process much easier.

4.3.3 Grinding & Polishing

After the samples have been mounted they need to be polished to a mirror finish in order to inspect the microstructure. The grinding and polishing procedure listed in Table 4.4 was carried out on a Buehler AutoMet/EcoMet 300 automatic polisher. A diamond extender was also used during polishing to lubricate the polishing surface without having to use copious amounts of polishing suspension. The single force sample holder was used for the lower grit grinding steps (180, and 320 grit), while the pin force sample holder was used for all of the higher grits. Between the 600-1200 grit, and subsequent polishing steps the samples were washed with methanol, and ultrasonically cleaning for 45 seconds to remove any particle retention from the previous step. If scratches are still visible after the alumina step, go back to either 600, or 1200 grit depending on how deep the scratches are.

Table 4.4: Grinding and polishing procedure for a 2032Nb stainless steel alloy. Polishing media products were purchased from Buehler Canada, and polishing cloths were purchased from Allied High Tech Productions Inc. The direction of the base relates to which direction the sample holder is rotating. Comparative means the base and the holder are rotating the same way, while contra mean the base and the holder are rotating opposite directions.

Abrasive (Grit)	Size (um) [58]	Media	Load (Lb.)	Base speed (rpm) /Direction	Time (min)
Grinding					
8” SiC (180)	76	Water	4	240-300 Comparative	1:30
8” SiC (320)	34.3	Water	6	120-150 Comparative	3:00
8” SiC (600)	14.5	Water	6	120-150 Contra	5:00
8” SiC (1200)	6.5	Water	6	120-150 Contra	5:00
Polishing					
Allied Spec-Cloth	1	Alpha Alumina Powder + water	6	120-150 Contra	5:00
Allied Final P	1	MetaDi Supreme Suspensions	6	120-150 Contra	5:00
Allied Final P	0.05	MetaDi Supreme Suspensions	6	120-150 Contra	5:00

4.4 Microscopy

4.4.1 Etching Techniques & Optical Microscopy

High temperature stainless steels have several techniques for etching described in the literature. Shinozaki *et al.* uses two electrochemical etchants to reveal the morphologies of either carbides, intermetallic phases in the microstructure [59]. A 90% methanol, 9% acetylacetone, and 1% tetramethylammonium chloride etchant at 14V × 30s is used to view carbides such as NbC, M_7C_3, $M_{23}C_6$, while a 10% aqueous oxalic acid at 3V × 15s was used to view the intermetallic microconstituents. Murakami’s reagent consisting of 10% $K_3FE(CN)_6$, and 10% KOH in water was used for HK40, and some HP alloys. At 75°C it will darken intermetallic phases such as σ-Phase, or at room temperature to darken carbides.

In the microstructural study of HK, and HP alloys by Dechema polished samples were etched for 30 seconds at 50°C in an etchant (industry name, V2A) consisting of 100 ml H_2O, 100 ml HCl 1.19, 10 ml HNO_3 1.40, and 0.3 ml Dr. Vogel's pickle. Dr. Vogel's pickle is a mixture of 1-Methoxy- 2-propanol (40-50%), Thiourea (3-5%) and Nonylphenol-ethoxylate (5-7%) [5].

Fig. 4.2 shows how the etchants used by Shinozaki *et al.*, and Dechema react on the in-service 2032Nb alloy aged for 16 years. Fig. 4.2a was electrochemically etched with 10% aqueous oxalic acid 3V for 30 seconds, with a stainless steel cathode. The interdendritic microstructure has mostly been eroded out; however, a light phase remained unaffected from the oxalic acid. With EDS this phase was identified as being silicon rich, in which case it is most likely an intermetallic phase (G-Phase, η-Phase).

Fig. 4.2b shows the interdendritic microstructure etched with 9% acetylacetone, and 1% tetramethylammonium chloride at 14V and 30s. In the interdendritic area two phases are visible with different contrasts. Using EDS the darker phase was identified as being silicon rich, whereas the lighter phase was identified as having a high chromium concentration which is most likely a secondary chromium carbide ($M_{23}C_6$). Etched macros of both the static cast tee, and centrifugally cast pipe are presented in Fig. 4.3. The acetylacetone etchant heavily etches the austenite grains revealing a dark brown color. The different grain orientations in the static cast sample are visible due to the color etching of the austenite grains. The centrifugally cast sample has a uniform color where all of the grains are oriented in the same direction.

Fig. 4.2c is the result of etching with the V2A etchant for 30-60 seconds at 50°C. Dr.Vogel's pickle was made up from approximate concentrations of the ingredients listed above. The surfactant Nonylphenol-ethoxylate could not be acquired for this study and was omitted from the etchant. Similar to the acetylacetone etchant the interdendritic region is populated by two different phases, one of a lighter contrast, and the other of a darker contrast. From Berghof *et al.* [5] the lighter phase was identified as $M_{23}C_6$, and the darker phase categorized as either M_6C, or G-Phase. Residual NbC phases are identified as having a brownish hue, and are a slightly lighter contrast than the G-phase precipitates. NbC carbides are usually seen at the core of agglomerated G-phase particles due to the transformation process that occurs during aging with the instability of NbC, and the eventual G-phase precipitation that occurs on the NbC surface.

4.4.2 Scanning Electron Microscopy (SEM/EDS)

SEM microscopy offers higher spatial resolution over optical microscopy ($\sim 1\mu m$ spatial resolution), resolving topographical features of the sample, and providing atomic number differences over the sample. An image of the sample is produced by rastering a concentrated electron beam over the surface of the sample, where certain types of electrons will be emitted from the microstructure and collected by the appropriate detector. The accelerating potential of these emitted electrons ranges from 15-30 kV, but will generally be 20kV for the images presented in this study unless otherwise specified. Topological

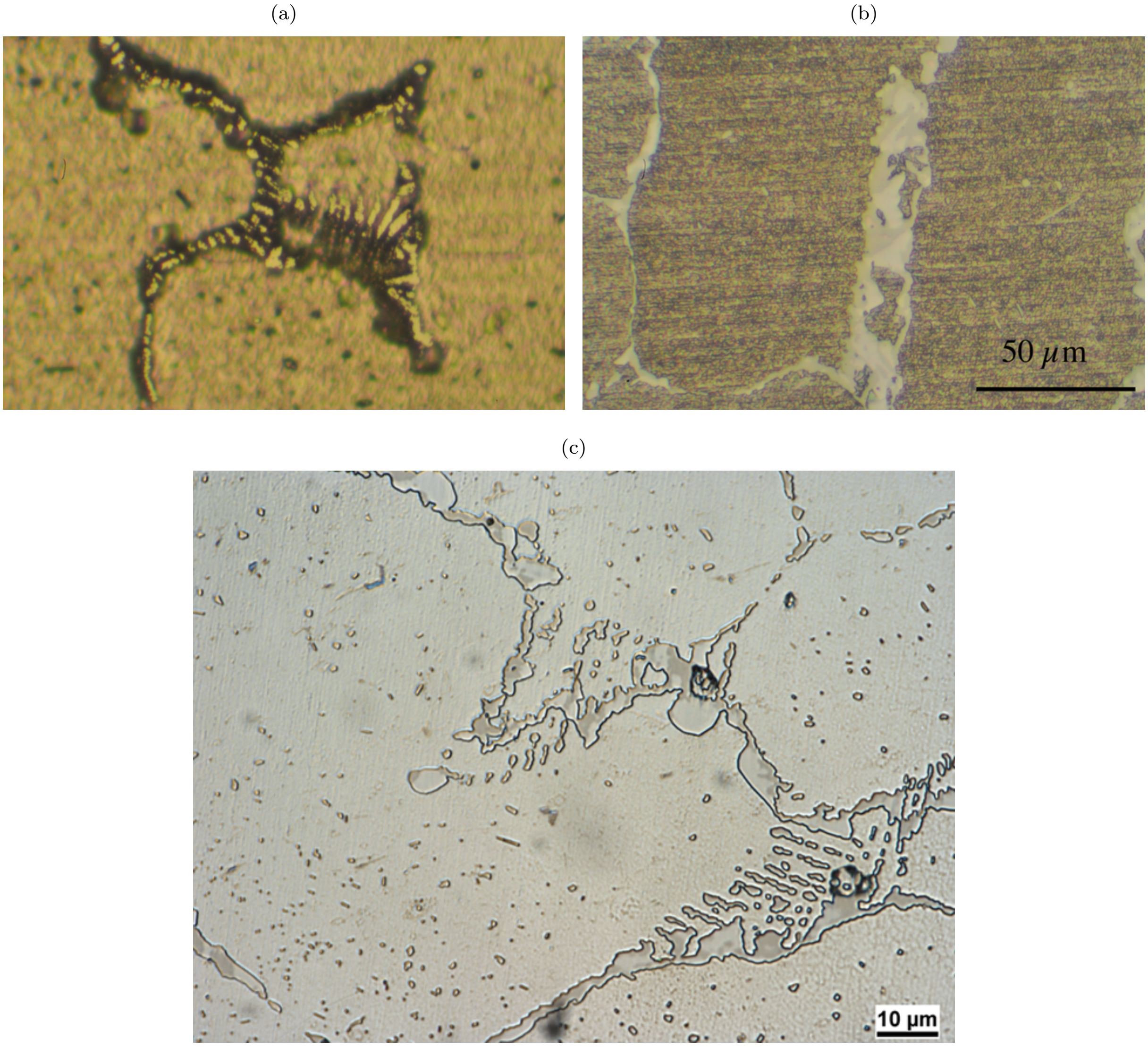

Figure 4.2: Effects of various etchants on 2032Nb aged for 16 years. a) is electrochemically etched with 10% oxalic acid, b) is electrochemically etched with 90% methanol, 9% acetylacetone, and 1% tetramethylammonium chloride, and c) is chemically etched with 100 ml H_2O, 100 ml HCl 1.19, 10 ml HNO_3 1.40, 0.3 ml Dr. Vogel's pickle. All three micrographs where captured at 100X.

features of a sample can be viewed with the photoemission mode of the SEM, where Secondary Electrons (SEs) will be emitted from inelastic collisions with electrons in the k-orbital of the specimen's atoms. Backscattered Electrons (BSEs) are elastically scattered where the scattering effect is dependent on the atomic number, Z, of the atom. The higher the atomic number the more backscattered electrons that will be elastically scattered and collected by the detector, showing a lighter contrast compared to atoms with a lower atomic number. BSE mode is useful for viewing different phases and precipitates in the

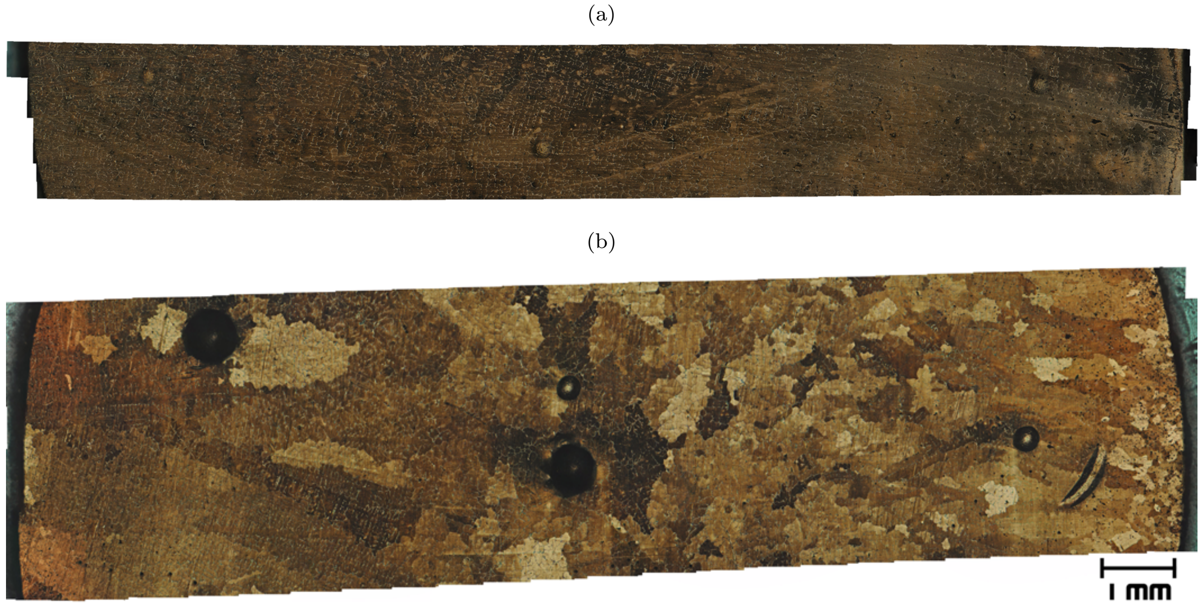

Figure 4.3: Macro panoramas of the in-service, aged a) centrifugally cast pipe, and b) the statically cast tee. Both were electrochemically etched with 90% methanol, 9% acetylacetone, and 1% tetramethylammonium chloride.

microstructure, and does not require the sample to be etched.

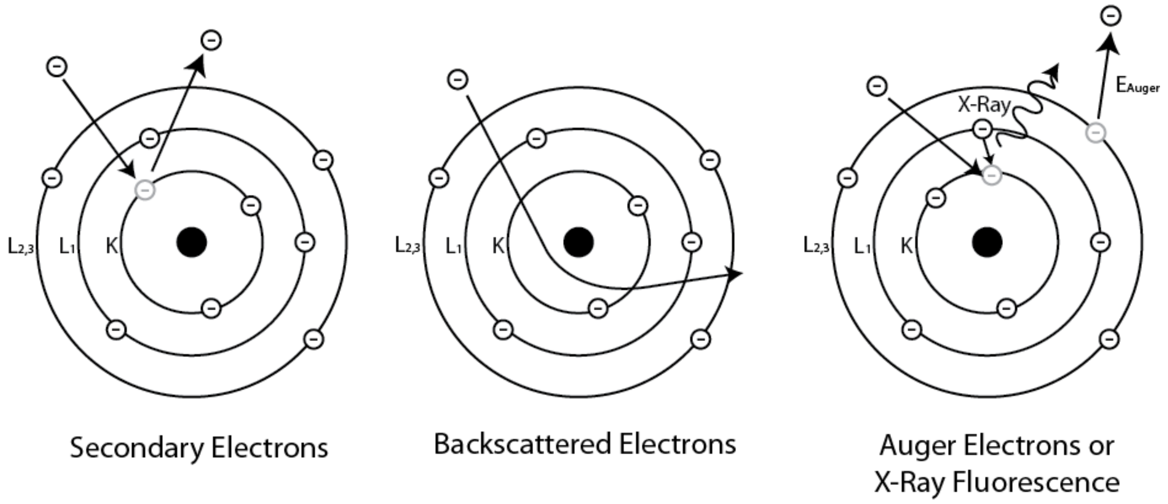

Figure 4.4: Various modes of electron emission from incident x-rays or electrons. Secondary electrons are inelastically scattered from the emission of valence electrons, backscattered electrons are elastically scattered where larger atoms deflect more electrons increasing collection rates. Auger and x-ray effects are caused by the ejection of inner shell electron compensated for by an electron in a higher orbital dropping down and filling the vacant energy level where then excess energy will either be given off in the form of a characteristic x-ray or the ejection of an outer orbital electron.

The interaction volume for the various scattering types, and imaging modes is illustrated in Fig. 4.5 where BSE electrons are seen to have a much larger interaction volume than SE electrons. The larger excitation volume results in BSE mode having a lower resolution than SE mode (BSE resolution $\sim 1\mu$m, SE resolution $\sim 10nm$).

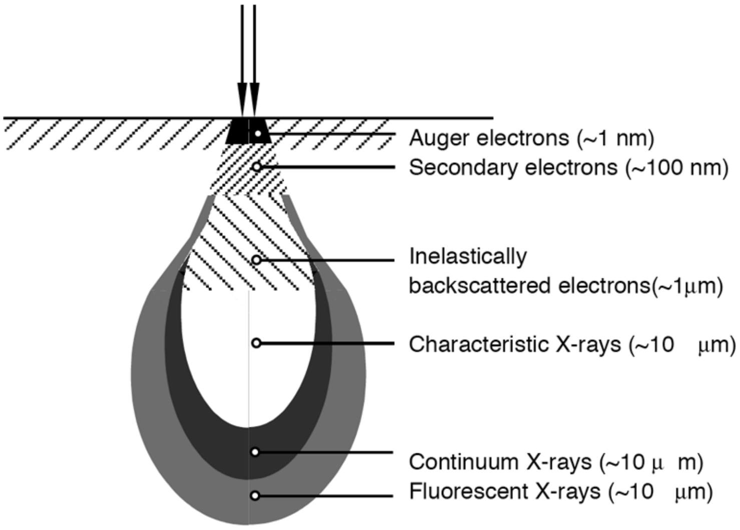

Figure 4.5: Interaction volumes is the depth range probed by the various types of scattered electrons and x-rays, where imaging resolution is dependent on the volume generated by the emission type[16].

Quantitative analysis of individual points, and constituents on the sample can be achieved with EDS, which collects characteristic x-rays emitted from excited atoms(Fig. 4.4). Each element produces an x-ray with a unique amount of energy that is collected by the EDS detector which causes a current to flow proportional to the energy of the x-ray. These current pulses are converted to voltage pulses, where once a large enough sample of x-rays are collected the intensities of voltage pulses are reported for further analysis in determining elemental concentrations at the point of interest. EDS is efficient at detecting elements with an atomic number, Z, greater than 9, however a windowless detector can detect elements greater than $Z = 5$. Due to instrument limitation for detecting carbon and nitrogen (due to the X-ray energy peak overlap, absorption, and attenuation by the detector window material), as well as surface contamination from carbon, carbon and nitrogen are generally omitted from EDS analysis. Depth resolution for EDS is 2-5μm, depending on the atomic weight of the sample and its microconstituent. Spatial resolution for EDS in SEM is $\sim 2\mu m$, where the analyzed particles should be greater than $2\mu m$ in order to obtain proper quantification without overlap from another constituent in its interaction volume.

Element maps can also be generated using EDS for SEM, where x-ray intensities are measured while the beam is rastered over a specified area of the sample. The resulting image is a brightness intensity map showing points of high concentration, and low concentration of a specific element. Element maps can be used to qualitatively determine which phases contain which elements, or quantitatively produce phase fractions if the individual phases have been properly characterized. EDS has a drastically lower collection time than WDS, but the results are less accurate and the collection efficiency of EDS is much lower.

For the in-service 2032Nb samples SEM was conducted on a Zeiss EVO MA 15 Scanning Electron Microscope (SEM) with a LaB6 crystal source. It is equipped with a Bruker Silicon Drift Detector for EDS with a peak resolution of 125 eV. SE detection has a 3nm resolution at 30kV, and BSE have a 4.5nm resolution at 30kV The samples were left uncoated, and connected to the conductive stage with copper tape. SEM for the commerical 2032Nb and Super-2032Nb samples was done with a Tescan Vega-3 Scanning Electron Microscope fitted with a Oxford Instruments Inca energy system EDXS detector. The Vega-3 is a semi-automated tabletop SEM with an accelerating voltage of 200 eV to 30 keV, capable of both BSE and SE detection. SE resolution on the Vega is 3nm at 30KV, while for BSE the resolution is 3.5nm at 30kV. Micrographs produced for this study were obtained at a 20keV operating voltage at a 11mm working distance for BSE, and 13mm working distance for EDX.

4.4.3 Auger Electron spectroscopy (AES)

AES has many advantages over SEM, and EDS as it can achieve higher depth, and spatial resolutions (< 100Å and $300nm$ respectively), where micron and sub-micron sized features can be inspected. AES is also sensitive to lighter elements than SEM, and EDS where atomic numbers of $Z < 15$ up to helium can be inspected. AES does have some disadvantages to SEM as characterization of the bulk of the sample cannot be achieved since AES is a surface sensitive technique (Fig. 4.5). Mapping procedures should typically be done with EDS or WDS for phase fraction calculations since a large enough area cannot be covered to give an accurate representation of the sample. Collection times for Auger electrons are also much longer than for EDS, where a dozen point could take over an hour to process.

The Auger effect shown in Fig. 4.4 occurs when the sample is excited with an x-ray or an electron, where the energy from the incident electron knocks out an electron from the atoms k-shell. Higher energy electrons will drop down to maintain a minimum energy level, where the excess energy is then either released as a characteristic x-ray or an outer shell electron is ejected. An Auger electron is considered to be the ejected outer shell electron, whereas the characteristic x-ray is associated with x-ray fluorescence, and is used in XRD and EDS. From Fig. 4.5 Auger electrons are only emitted from the first few nanometers of the sample making it a surface sensitive technique. Similar to EDS, AES can display the electron energy spectra for quantitative analysis. Since the interaction volume is much smaller, a more accurate composition of a specific feature can be resolved, as other phases or precipitates will not overlap within the excitation volume.

AES was performed on a JAMP-9500F Scanning Auger Microscope with 3nm SE resolution, and an 8nm probe diameter for Auger analysis. For the samples in this study the accelerating potential was set to 15keV, and the surface of the sample was ion sputtered with argon for 20 seconds to remove any surface contaminants that might have formed on the sample from the open atmosphere. However, since carbon is a significant constituent in the primary and secondary carbide phases it is necessary to calibrate its atomic sensitivity factor (ASF) to reduce the error from hydrocarbon surface contamination. The ASF for carbon was calibrated through the quantification of $M_{23}C_6$ carbides, since it has been shown that carbon is the primary element to constitute the second sublattice of $M_{23}C_6$, and any nitrogen soluble in this phase is dilute [33]. The ASF value was adjusted until the carbon concentration in the quantification of $M_{23}C_6$ was 20.7 at.pct through Eq. 4.1, where C_{carbon} is the concentration of carbon, and I_{measured} is the measured intensity of the carbon peak. The ASF value calibrated for carbon was 0.326.

$$C_{\text{carbon}} = \frac{I_{\text{measured}}}{\text{ASF}} \tag{4.1}$$

4.4.4 Electron Probe Microanalyzer (EPMA/WDS)

EPMA is a similar spectroscopy technique to SEM, however it works on the principle of WDS by using several crystal spectrometers to collect characteristic x-rays from individual elements. Various diffracting crystals with a known inter-atomic plane spacing, d, are calibrated to diffract characteristic x-rays emitted from the sample to the x-ray detectors in the spectrometers. The characteristic x-rays diffracted by the crystals are representative of predetermined elements, or components of the sample. For the 2032Nb system the EPMA instrument must be calibrated for chromium, nickel, niobium, silicon, and carbon elements. For chromium, and nickel a LLIF crystal was used, a PET crystal was used to collect characteristic niobium x-rays, a LTAP crystal for silicon x-rays, and a PC1 crystal for carbon x-rays.

WDS works on the principle of x-ray florescence where characteristic x-rays from the sample are emitted via the process shown in Fig. 4.4, and scattered in all directions. A small percentage of these characteristic x-rays reach the crystals in each of the spectrometers situated around the sample. These x-rays are incident upon the crystal, and any x-rays that obey Bragg's law will be diffracted out of the crystal towards the spectrometers detector where an argon gas will be ionized and a voltage is recorded. Bragg's law is defined as,

$$n\lambda = 2dsin\theta \tag{4.2}$$

where λ is the wavelength of the incident x-ray, θ is the angle between the x-ray and the atomic planes, and n is an integer. Due to the x-ray separation process WDS can resolve a better signal to noise ratio, and produce higher quality x-ray maps. WDS resolution is better than EDS, however collection times are longer due to lower collection efficiency. WDS can also separate x-ray peaks that are unresolved with EDS methods. WDS can detect elements as low as $Z = 5$, however precise quantitative chemical analysis is difficult for atomic numbers less than 8 (Oxygen). This implies that although WDS is more accurate than EDS for detecting carbon and nitrogen concentrations, there will still be a significant error associated with it. WDS analysis requires that the user knows which components are present in the sample, whereas EDS does not require prior knowledge of which elements are of interest.

For the purposes of this study EPMA was chosen primarily for mapping individual elements for qualitative segregation analysis, and quantitative phase fraction analysis. Mapping with WDS will give much better results than mapping with EDS due its higher peak-to-background ratio. While EPMA can map a large enough area to give an accurate representation of the samples microstructure, its spatial resolution is limited to $\sim 1\mu m$.

EPMA analysis was conducted on a CAMECA SX100 electron probe microanalyzer (EPMA) operating at 20kV. The resolution of the elemental maps was 1μm/pixel, at a dwell time of 20ms. Multiple samples were analyzed through various cross-sections for a more accurate representation of the bulk material. The area fractions were calculated from a total cross-sectional area of hundreds of mm^2 to get a number representative of the entire sample.

4.5 X-Ray Diffraction (XRD)

EDS and WDS methods are important for characterizing a material, and provide a large insight into the potential microstructural constituents (i.e. phases) of the sample. However, compositional analysis of a phase provides no insight into its crystal structure, which is necessary to define a phase with significant degree of certainty. In XRD a monochromatic beam of x-rays with a fixed wavelength are incident upon a samples surface, or powder. If Bragg's law is satisfied a certain portion of those incident x-rays will be diffracted to a detector which will record their intensities as a function of diffraction angle, 2θ. The sample is rotated 180° where a plot of intensity vs 2θ is output. The resulting I vs 2θ output is compared to a database of powder diffraction files which contain the experimentally determined relative intensity values, and diffraction angles for various phases and all of their diffracting planes. The XRD profiles for the powder diffraction files can determine the types of atoms, and the position of the atoms by the relative intensities of diffracted x-rays, and the spacing between inter-atomic diffracting planes by the diffraction angle. Unit cell spacing, and the space group for the compound can be determined from this information. If the powder diffraction file fits the XRD profile then their is a significant probability that that compound is present in the sample. The amount of each compound in the sample will be represented by the absolute intensities shown in the XRD profile. A search/match routine can be utilized in XRD data processing software (i.e. JADE), but it is useful to know the potential compounds present in the system beforehand to filter out any false positives.

Since in the 2032Nb alloy the microconstituents only consist of $\sim 5\%$ of the alloy, with some precipitates having only a $1wt\%$ concentration, the constituents will be vastly overshadowed by the matrix phase if the sample is used as polished. The interdendritic, and intradendritic precipitates will have to be extracted from the matrix by dissolving the matrix electrolytically in acid leaving behind the alloys precipitates. For a 2032Nb alloy a solution of 5% HCl, and 5×10^{-3}g/cm^3 of citric acid in methanol was used to electrolytically etch the sample at 1.5V for 12hrs, as outlined by Piekarski [9]. The cathode used for the phase extraction was a Cr-Ni wire mesh made from Chromel alloy found in K-type thermocouples. The residue left behind in the electrolyte was filtered out and dried at 70°C. Powder diffraction was then carried out with a Rigaku Geigerflex Powder Diffractometer using Co-Kα radiation.

4.6 Metallography

4.6.1 Static Cast vs Centrifugally Cast

4.6.1.1 Grain Structure

The two different casting types for both the static cast tee and the centrifugally cast pipe provide a much different microstructure in terms of grain size/morphology, and elemental segregation throughout the thickness of the sections. The static cast tee has a constant thickness of 23 mm, whereas the centrifugally cast pipe has a variable thickness between 23 mm and 50 mm. Both the pipe and tee were cast from Fahramet F20-32Nb material, it is unknown whether the material was cast in a permanent or sand mold. The static casting is poured into a stationary mold, where upon solidification the cooling rate differs through the thickness of the part producing a variable microstructure, and variable grain distribution. In a standard casting there are three definable regions, the outer wall chill zone, the inner wall columnar zone, and the central equiaxed zone, that can be identified in the static casting of the tee shown in Fig. 4.6a.

The first section of the ingot to solidify is the outer wall. Due to the large temperature differential between the molten liquid and the cold mold wall, many stable nuclei begin to form on heterogeneous nucleation sites on the mold wall. Once the mold wall starts to heat up some of these crystals will break off from turbulence in the liquid and continue to grow away from the mold wall. These crystals will grow in an equiaxed structure, and due to the high number density of stable nuclei the resulting grain structure will be very fine.

Once the mould wall has heated up and the temperature gradient has decreased the crystals from the outer wall will start to grow dendritically against the heat flow in a certain crystallographic orientation. This results in columnar grains structure between the chill zone and the center of the casting. From the inner wall the temperature gradient is not as high as it is initially at the outer wall, thus grains start to grow dendritically towards the center of the ingot. The lower undercooling at the inner wall of the casting causes fewer stable nuclei to form where a more coarse columnar structure will result. The center of the casting consists of an equiaxed zone of randomly oriented grains. A possible mechanism for the formation of these grains is detachment of secondary dendrite arms, which are then carried into the center of the melt due to convective forces in the liquid.

For the centrifugal casting the liquid is rotated around the mold using a steady electromagnetic field, producing a consistent columnar grain structure throughout. Centrifugal casting has been found to have many beneficial properties including the refinement of the grain structure and microstructure, reducing composition segregation, and enhancing the mechanical properties of the casting [60]. Even though centrifugally casting is suppose to homogenize the microstructure of the component, the pipe has a variable thickness where the microstructure and the grain structure are seen to be quite different when comparing the 23 mm sample (Fig. 4.6b) to the 50 mm sample (Fig. 4.6c). While the grain structure in Fig. 4.6b is quite consistent from the outer wall to the inner wall, Fig. 4.6c shows a decrease in

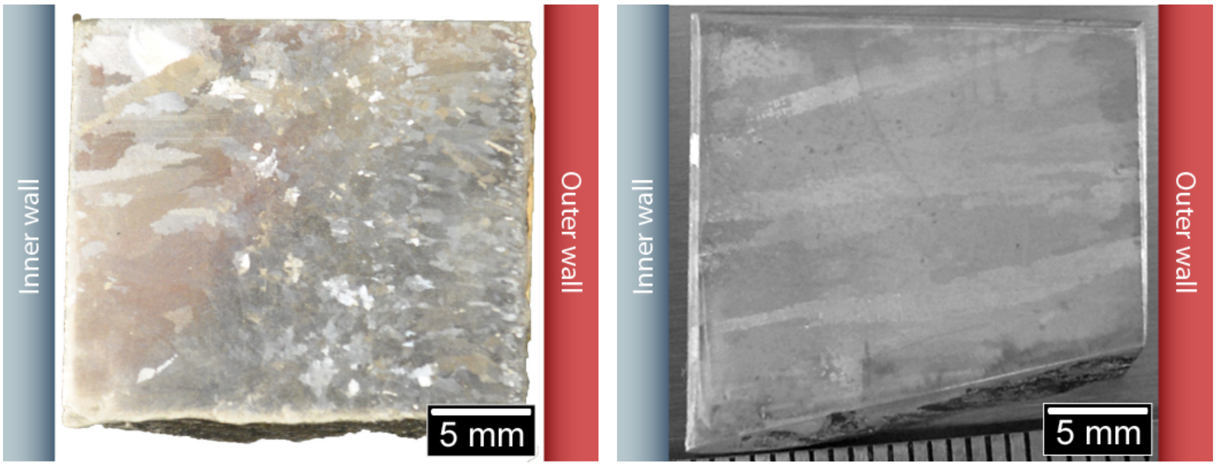
(a) Static Cast

(b) Centrifugal Cast

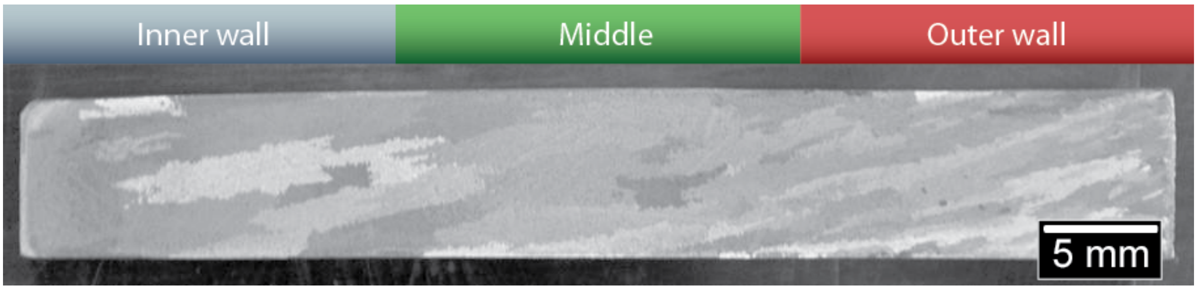
(c) Centrifugal Cast

Figure 4.6: Macrographs showing the grain structure through the thickness of a) the statically cast tee, b) the centrifugally cast pipe through the thin section, and c) the centrifugally cast pipe through the thick section.

grain size from the inner wall to the outer wall. This could be due to the centrifugal forces acting on the component where a significant force would be pushing free floating crystals in the liquid towards the outer wall. In such a thick component the heat flow may also be much larger than in the thin section, forming more stable nuclei at the outer wall than the inner wall.

4.6.2 Solidification Microstructure & Button Melting Procedure

4.6.2.1 Scheil Model

Assuming the initial molten liquid has a uniform composition of T_0, and that the liquid composition will remain homogenous throughout solidification, and that no diffusion will take place in solidified dendrites, a Scheil solidification model can be employed to define the segregation effects of the solute throughout the dendrite. The Scheil model works on the principle of conservation of solute within a volume element at the solidification interface,

$$d((1-x)C_L(x,\alpha)) + d(xC_S) = 0 \tag{4.3}$$
$$(1-x)dC_L - C_L dx = -(C_S dx + \alpha x dC_S) \tag{4.4}$$

where x is the the distance to the center of the solidified crystal, C_L and C_S is the concentration of the solute in the liquid and solid respectively, and α is a value between 0 and 1 that represents no diffusion in the solid or complete diffusion in the solid. For the Scheil model $\alpha = 0$, but for equilibrium solidification models $\alpha = 1$. the conservation of solute is illustrated in Fig. 4.7, where $1-x$ is the amount of liquid left, $C_S dx$ is the amount of solute currently solidifying, and xdC_S is the amount of solute in the solidifying layer from back-diffusion [61].

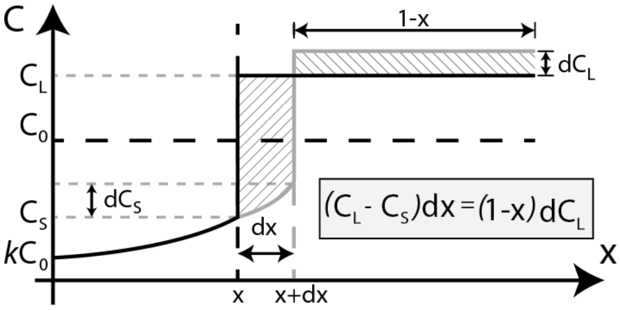

Figure 4.7: Illustration of the conservation of solute during solidification of a section of a crystal dx.

Integrating Eq. 4.4 with the condition that when $x = 0$ $C_S = kC_0$, and $C_L = C_0$ where k is the segregation coefficient of the solute, $k = C_S/C_L$ gives

$$C_L = C_0(1 + \alpha kx - x)^{(k-1)/(1-\alpha k)} \tag{4.5}$$

From Eq. 4.5 the liquid becomes progressively more concentrated during solidification, where each layer of the solidifying dendrite will fluctuate in its solutes content producing coring within the composition of the dendrite. Once the growth of the dendrite starts to impede upon each other the high concentration of solute elements in the final portion of liquid may make it energetically stable for primary carbides, or chrome carbides in 2032Nb stainless steel to precipitate at interdendritic regions.

Fig. 4.8 shows the concentration profile for chromium and silicon in a static casting. A higher concentration of chromium towards the interdendritic regions makes it more energetically favorable more chrome carbides to precipitate out of solution. The extent to which elemental segregation occurs in the dendrite will depend on the partition coefficient, k, where the element with the smaller partition coefficient will have a larger concentration gradient across the dendrite. In the case of chromium and silicon in the 2032Nb casting, $k_{Si} < k_{Cr}$. A $k = 1$ defines the solute as being a fast diffuser where it is a homogenous concentration throughout the solidified crystal. A fast diffuser is typical of small interstitial elements such as carbon and nitrogen.

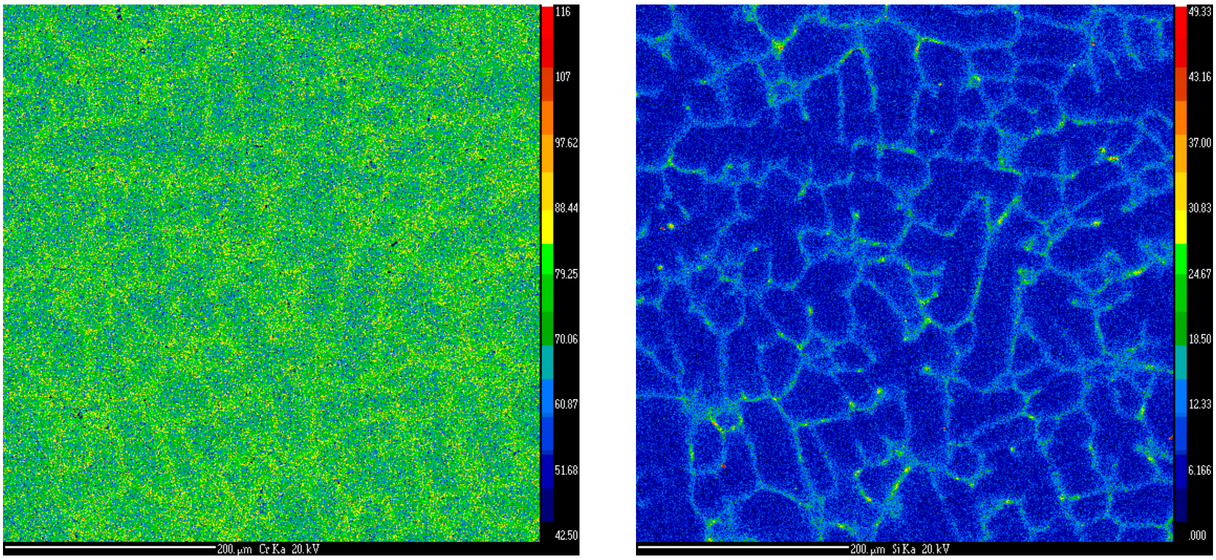
(a)

(b)

Figure 4.8: EPMA map of a) chromium segregation, and b) silicon segregation in a static cast microstructure after remelting the 2032Nb alloy with a button melter.

4.6.2.2 Scheil Simulation with ThermoCalc

ThermoCalc includes a Scheil module which calculates the equilibrium microstructure at specific temperature decrements until there is no more liquid left in the system. The Scheil module employs Eq. 4.5 to determine the composition of the solidifying element where it then calculates its equilibrium microstructure for each step along a solidification range from 0 to 1. Fig. 4.9 is an example output from the ThermoCalc Scheil module of a HP50 alloy tested by *Shi and Lippold* [17]. The dotted line represents Eq. 4.5 when $\alpha = 1$, or when there is assumed to be complete diffusion in the solid. The Scheil module also outputs the amount of each phase that precipitates during solidification, as well as the compositional changes of these phases.

4.6.2.3 Button Melting

The in-service samples provided by *Syncrude Canada Ltd.* were remelted, and solidified using a button melting apparatus. A 1” squared sample was set in a copper hearth and remelted in an argon filled gas chamber with a gas tungsten arc welding torch. The melted sample was stirred electromagnetically to homogenize the liquid, whereby it then re-solidified into a button shaped casting.

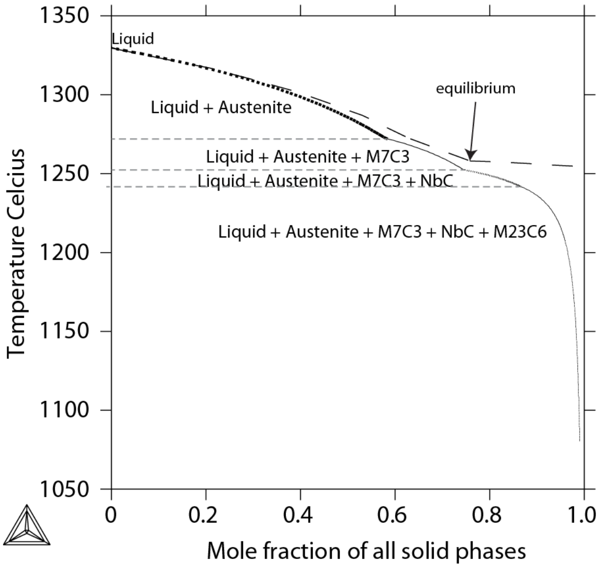

Figure 4.9: ThermoCalc Scheil output of a HP50 alloy from *Shi and Lippold* [17].

4.6.3 Grain/Dendrite Size Calculations

Grain size was calculated from samples electrochemically etched with 90% methanol, 9% acetylacetone, and 1% tetramethylammonium chloride etchant at 14V × 30s. Photoshop image processing software was used to measure a sample of grains from the macrographs taken with a standard Nikon digital SLR camera. Columnar grains were reported with a width and length measurements. Dendrite measurements were calculated by measuring the diameter between clearly defined interdendritic boundaries. Measuring the dendritic cell size instead of the secondary arm spacing was chosen as some columnar dendrites could not be clearly defined in the microstructure. Dendrite cell size can also be used to define the diffusional distances needed for elemental segregation to the interdendritic regions.

4.6.4 Hardness

Hardness measurements were carried out with a Wilson Instruments R2000 Rockwell Hardness Tester using a HRB rockwell indenter, and a 100kg load.

4.7 Image Analysis

Digital image processing has been incorperated into many scientific applications over the last decade including medical imaging, manufacturing processing with robots, and automatic vehicle driving systems. Basic concepts from image processing theory can also be applied to metallography, and assisting the user with identifying features, and quantifying the shape, size, and area fraction of these features. This is especially useful if hundreds of micrographs need to be quantified to give statistically accurate values representing the overall microstructure. In this section two methods will be proposed for assessing the area fraction of the microstructure present in 2032Nb alloys, first using elemental mapping procedures with EPMA, and WDS and then processing those maps with the *Image Analysis Toolkit* in *Matlab*, and the secondly using more complicated techniques using the *OpenCV* image processing library with *Python* to process backscattered images obtained from SEM in determining area fraction, and size of the precipitates. A few sources further describing digital image processing are the Hypermedia Image Processing Reference (HIPR2) (http://tinyurl.com/6o3n26c), the Matlab Image Processing Toolbox Documentation (http://tinyurl.com/8os5tvo), and *Digital Image Processing* by *Gonzalez and Woods* [62].

4.7.1 Thresholding

In element mapping from EPMA, x-ray intensities are collected from an array of points mapped over the sample, which are then output as false color values ranging over the visible spectrum from violet (low intensity) to red (high intensity). For the maps presented in Fig. 4.10, a 1μm/pixel resolution was used, where a $512px \times 512px$ false color image was produced. Color thresholding is then used to separate the false color pixels that are within a certain range of the color spectrum. Since certain phases are highly concentrated with specific elements, color thresholding the element maps should be able to pick out all of the precipitates in the microstructure based on their respective constituents. For example, from stoichiometry G-phase can be differentiated from NbC based off of the niobium constituent concentration where NbC consists of ∼50% niobium, whereas G-phase only consists of ∼21% niobium. This statement is under the assumption that any other constituent that is soluble in the first sublattice of NbC will be dilute, and will not offset the niobium concentration by any significant amount. This assumption should be confirmed with EDS measurements. Niobium carbides can then be separated from the niobium element map by thresholding between the first few high intensity false colors (i.e. read and orange). It should be noted that x-ray intensities from each phase are on a relative scale, and will fluctuate from session to session due to instrument calibration, and sample setup. Threshold limits for each datasets must be re-evaluated by comparing the false color maps to the backscattered images. Error associated with discrepancies between the thresheld image, and the backscattered micrograph should be incorporated into the total error.

While G-phase could also be segmented from the just the niobium map, it is more reliable to also threshold the silicon map and evaluate where areas of both high silicon, and high niobium exist. The same technique of thresholding for chromium can be done to section the chrome carbide precipitates. After thresholding, the images are converted into binary format (0 for black, 1 for other) for further analysis with *Matlab*. Thresholding procedures can either be accomplished from the *Photoshop* script (*EPMA-ColorThreshold.jsx*), or the *Matlab* script (*EPMASegmentation.m*) discussed further in Section A.5.

Fig. 4.11 shows how the silicon and niobium maps after thresholding are multiplied together to define where G-phase might exist. Since both the silicon and niobium maps after thresholding are in binary

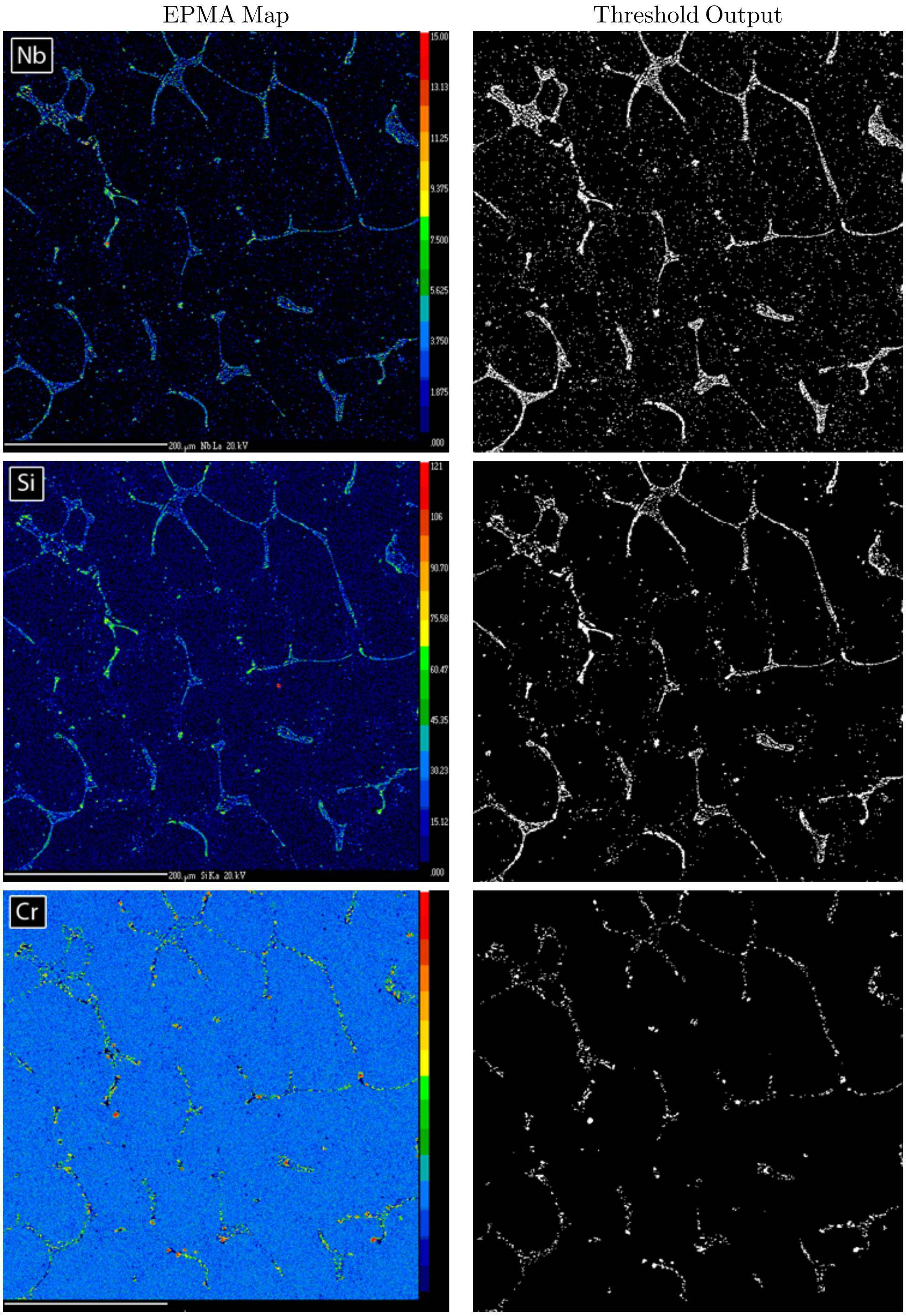

Figure 4.10: Element maps from EPMA of a static cast tee. Niobium, silicon, and chromium maps were subject to a thresholding operation to separate potential sites of precipitates.

format, only pixels for each map that are both 1's will appear when the two maps are multiplied together. The error between the multiplied map and the backscattered image are compared, and an error is added to the area fraction estimates.

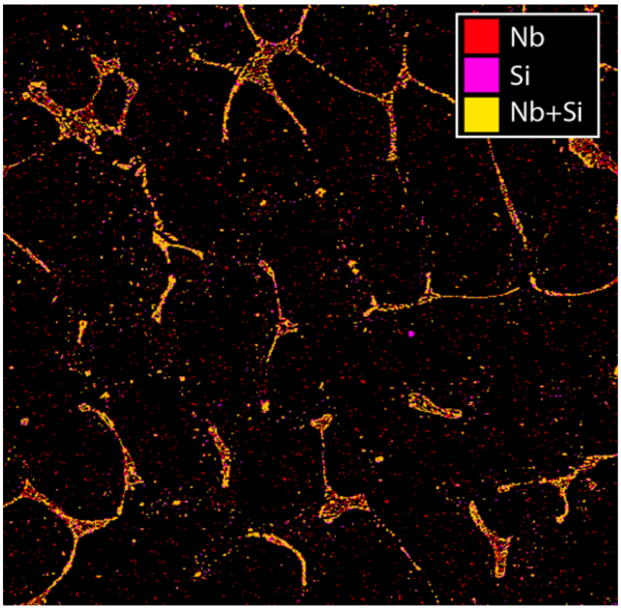

Figure 4.11: Adding the silicon and the niobium maps together after thresholding is used to define the areas where G-Phase is present represented by the yellow pixels which define where high concentrations of both silicon and niobium exist.

4.7.2 Connectivity

Converting the element maps into binary format is important for the computer to be able to distinguish between different connected components. A connected component is defined as a group of pixels that are connected either by their faces, or their edges. Fig. 4.12 illustrates the two different types of connected components as 4-connected (faces), or 8-connected (faces and edges). For area thresholding operations, and contour drawing algorithms each connected component specified by the connectivity criteria are labeled iteratively as seen in Table 4.5. Labeling the components of the image helps categorize them where they can then undergo an area, or surface area thresholding operation, or the size and area fraction data can be output. Since some of the precipitates are very fine in the microstructure ($< 1\mu m$), they cannot be fully resolved by EPMA (spatial resolution $= 1\mu m$) where two separate precipitates may be touching each other either on a pixel edge or face. A 4-connectivity is used to try and minimize any connectivity error as it is assumed that all the precipitates are elliptical or globular and would not be connected only by a single pixel edge. Improving the spatial resolution of the image will help with any connectivity issues, where features should be separated by at least a few pixels.

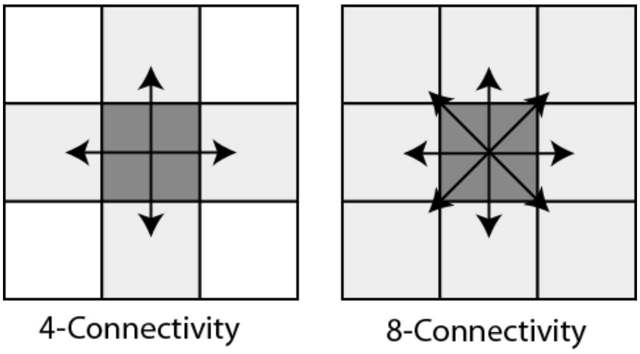

Figure 4.12: Connected components in image analysis are defined as either pixels connected by their faces (4-connectivity), or by their faces and edges (8-connectivity)

Table 4.5: Connected component labeling works by scanning the image iteratively and defining connected components based on 4-connectivity or 8-connectivity.

0	0	0	0	0	0	0	0	0	0
0	**1**	**1**	**1**	0	0	**2**	0	**2**	0
0	**1**	**1**	**1**	0	0	0	**2**	0	0
0	**1**	**1**	**1**	0	0	**2**	0	**2**	0
0	0	0	0	0	0	0	0	0	0
3	0	**5**	0	0	0	0	0	0	0
0	0	0	**5**	0	0	**6**	**6**	**6**	0
0	**4**	0	0	0	0	**6**	**6**	**6**	0
0	**4**	0	0	0	0	**6**	**6**	**6**	0
0	**4**	0	0	0	0	0	0	0	0

4.7.3 Morphological Operations

While improving the resolution of a micrograph is the best way to reduce connectivity error there are morphological operations that can be utilized to artificially reduce this error. Morphological operations deal with extracting image components that can be used to define a features shape, and its boundaries [62]. The two basic morphological operations are called **dilation**, and **erosion** which were derived using set theory. A structural element (called a kernel) which is by default a 3 × 3 pixel array is iteratively placed through a binary image where intersections with connected components cause the element to be added or subtracted from the image.

4.7.3.1 Dilation

Table 4.6 shows a dilation operation of a 2 × 2 kernel where the kernel is added to the image at any iteration where there is an intersection with a connected component. From set theory dilation is defined as,

$$A \oplus B = z|[(\hat{B})_z \cap A] \subseteq A \tag{4.6}$$

where A is the original component, B is the kernel, and z is translation of a reflected kernel $\hat{B}$ around the origin of A [62]. Eq. 4.6 defines dilation as reflected kernels that are intersecting with A which exist as a subset of A. Variability in the shape of the kernel can give rise to some interesting results, such as using a rectangular, or spherical kernel, but for this study the kernel was limited to a 3×3 square, where multiple dilation operations were performed where needed.

Table 4.6: Example of dilation with a 2 × 2 kernel

0	0	0	0	0
0	0	**1**	0	0
0	**1**	**1**	**1**	0
0	0	**1**	0	0
0	0	0	0	0

1	**1**
1	**1**

0	1	1	1	0
1	1	**1**	1	1
1	**1**	**1**	**1**	1
1	1	**1**	1	1
0	1	1	1	0

4.7.3.2 Erosion

Erosion follows the same algorithm as dilation where a kernel is iteratively moved along the boundary of a connected component, however if at least one of the pixels of the kernel is intersecting with the original component that kernel erases the intersecting pixels. Table 4.7 visually shows the erosion operation, where after the operation only one pixel remains of the original component. Erosion can be used in some cases as a basic operation for removing elements smaller than the defined kernel, or for separating objects with different morphologies, for example squares and circles of the same size. Erosion operations are less computationally intensive than size thresholding operations. The set theory definition for erosion is

$$A \ominus B = z|(B)_z \subseteq A \tag{4.7}$$

which says that translated B elements contained in A should be subtracted from A. It should be noted that any morphological operations will degrade the exact morphology of the original components by some extent no matter how small the kernal is.

Table 4.7: Example of erosion with a 2 × 2 kernel

0	0	0	0	0
0	**1**	**1**	**1**	0
0	**1**	**1**	**1**	0
0	**1**	**1**	**1**	0
0	0	0	0	0

1	**1**
1	**1**

0	0	0	0	0
0	0	0	0	0
0	0	**1**	0	0
0	0	0	0	0
0	0	0	0	0

4.7.3.3 Opening and Closing

Dilation and erosion are proved to be exact opposite operations of each other which can be easily visualized. With this in mind these two operations can be combined in different orders to obtain different effects. Opening is defined as an erosion operation followed by a dilation operation of the same structural element B. **Opening** will erode all of the elements in A, where any elements smaller than the kernel will be removed. The surviving elements will then be dilated back to their original size, and shape. Some morphology of the elements will be lost with this type of operation, but should not be drastic provided the correct kernel is chosen. On the other hand **Closing** is defined as a dilation operation followed by an erosion operation of the same kernel. The closing operation is mainly used to fill internal holes in the original element that are smaller than the kernel while still maintaining the original shape and size. Closing can also be used to join very small elements together into one component which could be useful in determining grain boundary area, or even used to get well defined grain boundaries for grain size calculations.

4.7.4 Contour Algorithm

Morphological operations are very useful for resolving resolution problems in micrographs where thresholding may cause some separate components to be joined together. However, using morphological operations will slightly degrade the morphology of the original image, and should be avoided for any size, or area fraction thresholding/analysis. Countour finding, or border following algorithms are common in many image processing libraries to compute connected components area, perimeter, and topological structure. In the border following algorithm proposed by *Suzuki and Abe* [63] border points for the outer borders of connected components are found, and then traced until it is reconnected with the original border point. Hole borders are then found inside the outer border, and traced as well. Each outer border and hole border is then labeled and categorized in a hierarchical tree. For some micrographs (especially optical), pits or holes in the microstructure can be filled by only plotting the outer borders for each component. In cases where a phase is encased by a separate phase (i.e. NbC and G-phase) holes must not be filled, or the NbC volume fraction should be subtracted from the G-phase fraction.

4.7.5 Dividing intra- and inter-dendritic species

With morphological operations interdendritic structures can be seperated from intradendritic structures. From the EPMA maps, it can be observed that the interdendritic and intradendritic G-phase exist in the fully aged microstructure. The steps of the following procedure are shown in Fig. 4.13. After thresholding the g-phase constituents described in subsection 4.7.1, the binary image (A) is dilated by a structural element B until the interdendritic regions are completely agglomerated. A closing operation is then performed to get rid of any noise in the image, followed by an area thresholding operation to subtract the intradendritic region from the image. The result can then be used as a mask on the original image to separate the interdendritic and intradendritic microstructure.

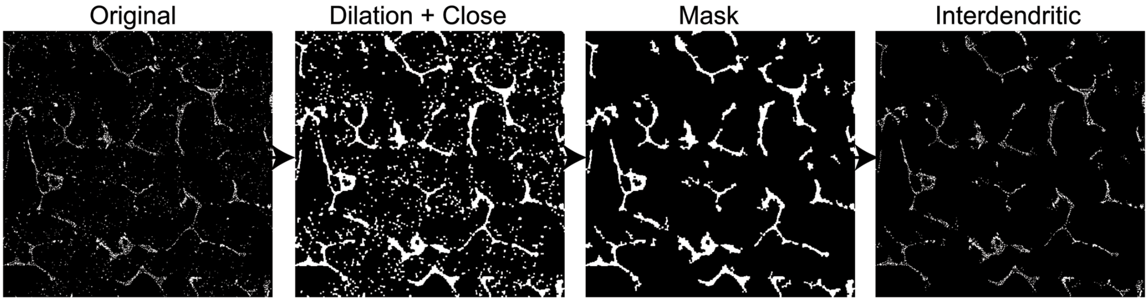

Figure 4.13: Morphological image operation to separate interdendritic and intradendritic components. A mask is produced from the morphological operations where the interdendritic structure can then be separated from the intradendritic structure.

4.7.6 Phase Fractions from Backscattered SEM

Element mapping is the major technique for evaluating phase fractions in micrographs, however using instrumentation like an EPMA can be very expensive, and time consuming. The same image analysis techniques discussed above can be applied to backscattered micrographs to determine phase fraction and the size of the precipitates in the microstructure. Producing a high resolution backscattered image in an SEM of $1000\mu m^2$ can take between 20-30 minutes to raster, whereas five element maps in EPMA of the same area can take upwards of 5-6 hours. With the current design matrix shown in Table 4.2 mapping would take over 320 hours of EPMA instrument time to process, and only 20 hours of instrument time in an SEM. Image thresholding on one greyscale backscattered image compared to five false color element maps is less reliable, and will produce much more noise and a larger error in the binary images for each phase; however morphological techniques can be utilized to minimize these factors. This requires more post processing time from the user than element mapping. This technique also assumes that proper characterization of the material has been done with EDS/WDS, and that the system is properly understood in advance. An example of the output results from the python image analysis script is shown in Fig. 4.14

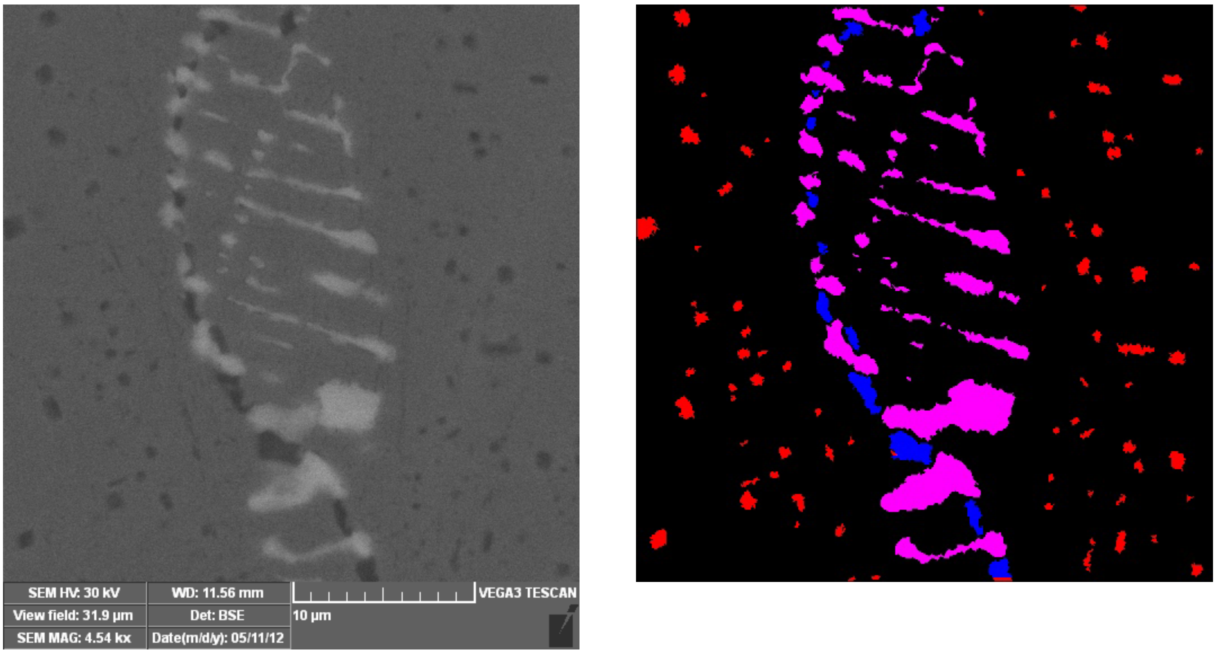
(a)

(b)

Figure 4.14: False color representation of a backscattered micrograph that has undergone image analysis. The purple color represent the niobium rich interdendritic phase, while the blue and red colors represent the interdendritic and intradendritic chromium rich phases respectively.

Chapter 5

In-service 2032Nb castings Results & Discussion

5.1 Introduction

This chapter will examine and compare the microstructure of the centrifugal cast, and static cast 2032Nb ex-service alloy in terms of grain structure, dendrite structure, microconstituents, phase fraction, and precipitate sizes. Variations in microstructure through the thickness of the components will be examined. Microstructural variations in the thickest part of the centrifugally cast component (3”) will be compared against the thinnest section of the same component (1”). Imaging techniques used to analyze the samples including SEM, EPMA, and AES will be compared, as well as EDS, WDS, and AES spectroscopy techniques used to quantify the microconstituents. The solution annealed and as-cast microstructure will be compared and contrasted, along with their elemental distributions in the austenite. Lastly, the microstructural evolution of the solution annealed centrifugal cast, solution annealed static cast, and the as-cast button melted sample will be presented, looking at their precipitation sequences, precipitation rates, and coarsening rates.

5.2 ThermoCalc Predictions

The equilibrium microstructure predicted by ThermoCalc between the static cast chemistry, and the centrifugally cast chemistry in Fig. 5.1 is observed to be nearly identical. Primary niobium carbides have a relatively constant driving force, even once Z-phase becomes stable at 820°C. However once $M_{23}C_6$ becomes stable the driving force for Nb(C,N) nucleation and growth becomes highly negative until its constituents are completely consumed by G-phase and $M_{23}C_6$. Due to the lower Nb/(C+N) ratio for the static cast chemistry less G-Phase and more $M_{23}C_6$ was found. The lower niobium concentration also depresses the stable temperature for the static cast chemistry, where an excess of niobium ($Nb/(C+N) > 7.7$) will promote the formation of G-phase before the destabilization of Nb(C,N). The discrepancies in the TTNI8 database cause the stability of $M_{23}C_6$ to be much lower than that expected for austenitic stainless steels, where $M_{23}C_6$ is expected to precipitate between 550-1075°C [35].

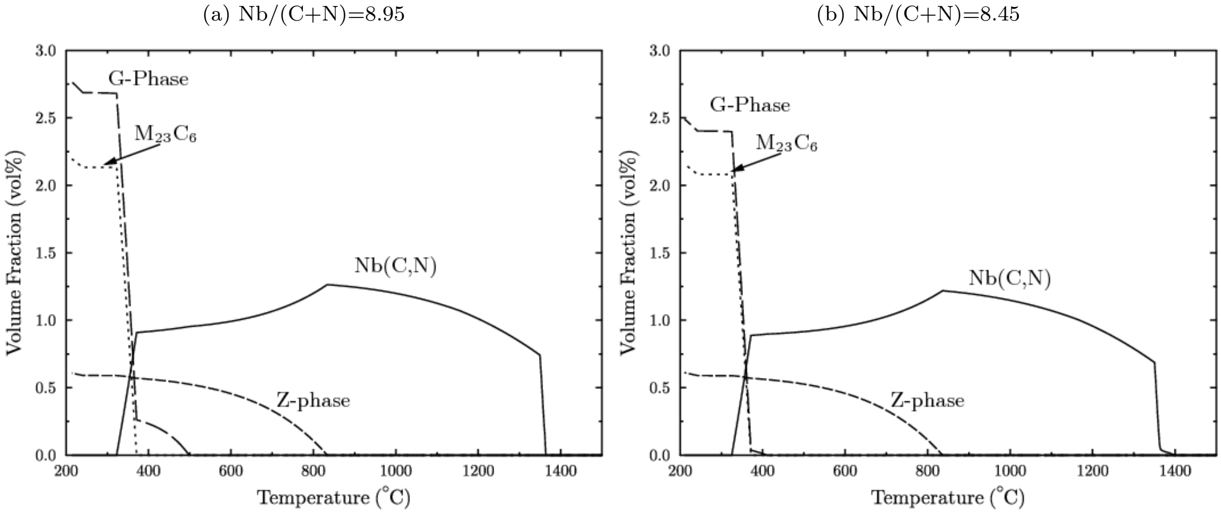
(a) Nb/(C+N)=8.95

(b) Nb/(C+N)=8.45

Figure 5.1: Equilibrium phase fraction in vol % predicted by ThermoCalc using the TTNI8 database for the a) centrifugally cast and b) statically cast in-service 2032-Nb stainless steel chemistries.

Thermodynamic modeling of scheil solidification of both in-service components is shown in Fig. 5.2 to predict the microstructure after casting. The centrifugally cast chemistry (Fig. 5.2a) is predicted to only precipitate Nb(C,N) carbides during solidification, whereas a small portion of TiN precipitates are also predicted to precipitate in the static cast chemistry. The amount of Nb(C,N) that precipitated during the Scheil solidification simulation was 0.99 vol% for the centrifugally cast chemistry, and 0.93 vol% for the static cast chemistry. The composition of Nb(C,N) precipitated during solidification predicted by ThermoCalc was $Nb(C_{.92}N_{.08})$. 0.015 vol% of TiN was calculated to be in the static cast alloy after solidification.

5.3 Characterization of the Fully Aged Manifold

5.3.1 SEM/EDS phase quantification

The microstructure of the fully aged component contains coarse, and blocky interdendritic phases as well as cubodial precipitates dispersed throughout the intradendritic regions. Fig. 5.3 shows the microstructure of an entire dendrite in the centrifugally cast pipe, where a dark blocky phase, and a light gray phase formed in a lamellar like fashion decorates the interdendritic region. The small intradendritic

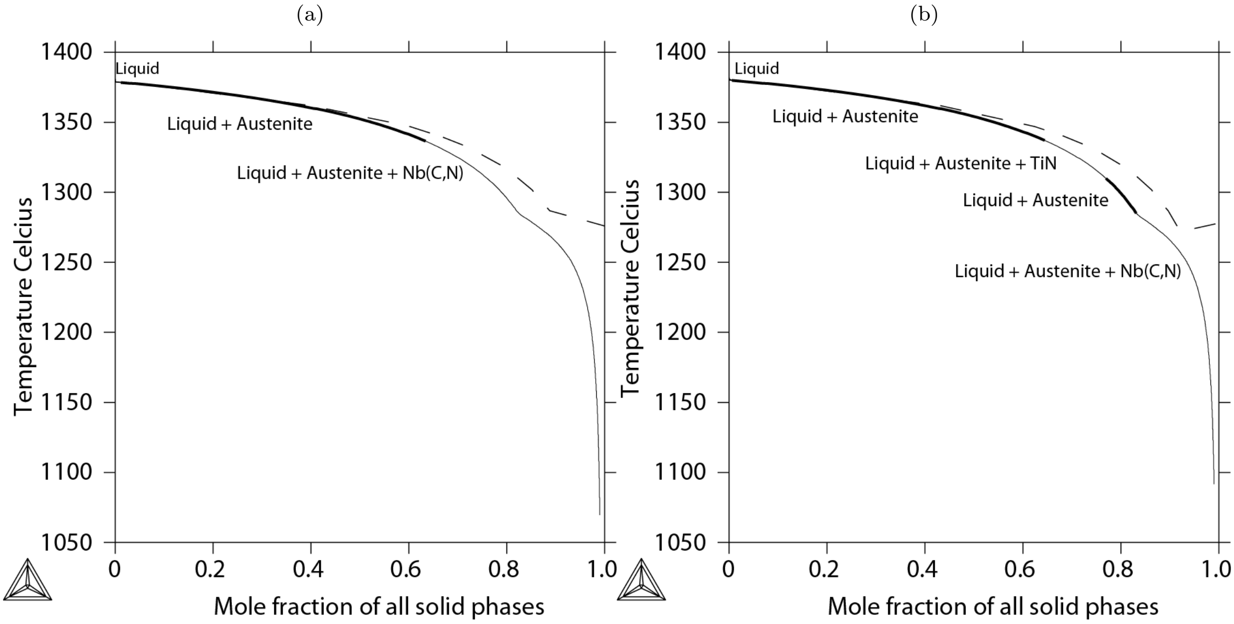

Figure 5.2: Scheil solidification predicted by ThermoCalc using the TCFE6 database for the a) centrifugally cast and b) statically cast in-service 2032-Nb stainless steel chemistries. The dotted line represents equilibrium solidification

precipitates are irregularly distributed throughout the microstructure where some dendrites contain a high number density, while others are nearly barren. Some of the coarser light gray precipitates show a white contrasted core, with a clearly defined interface separating two. This is indicative of two separate phases forming a core and rim structure, where the rim phase is likely nucleating and coarsening off of the lighter core phase.

The interdendritic microstructure of both manifold components consists of three different precipitate configurations; coarse, globular, discontinuous precipitation(Fig. 5.4a), finer continuous precipitation (Fig. 5.4b), and lamellar precipitation (Fig. 5.4c). In Fig. 5.4a very coarse, light, globular gray precipitates are found at the boundaries, with darker, blocky precipitates that are formed around it. In the center of some of the very coarse light gray phases are white contrast precipitates. Fine, micron sized precipitates similar in contrast to the light gray phase in the interdendritic region are dispersed throughout the intradendritic region. These fine precipitates are of a cubodial morphology, and are observed to have a clear orientation relationship with the austenite matrix. Most of the fine precipitates are seen to be ordered parallel or perpendicular to one another, while others are more cubic in nature and suspected to be coming out of the polishing plane.

Fig. 5.4b shows a continuous region of coarse precipitates that decorate the boundary in an intermittent fashion between the light gray intermetallic phase and the dark secondary carbide phase. In Fig. 5.4c the intermetallic light gray phase has precipitated in a lamellar fashion in the existing austenite, with

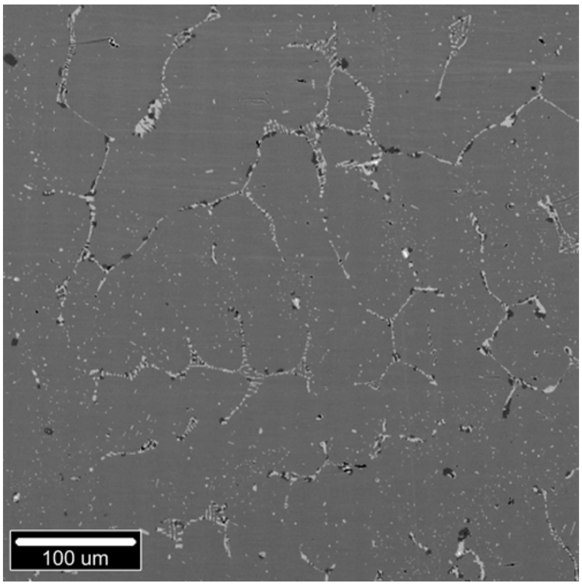

Figure 5.3: Microstructure of 2032Nb centrifugally cast component, aged for 16 years at $\sim 800°C$. The interdendritic regions are decorated primarily with $M_{23}C_6$ (dark phase), and G-phase (light grey phase). Small G-phase particles are dispersed intradendritically throughout the material.

very fine and very coarse secondary carbides precipitated beside or between them. These lamellar regions typically form at triple point regions between dendrite arms, and grain boundaries. There is a strong correlation of the orientation between the intradendritic intermetallic phase, and the lamellar interdendritic intermetallic phase. It is inferred in these regions that this intermetallic phase has a similar precipitation mechanism as the intradendritic species.

The summary of the EDS data done on both components of the ex-service manifold are shown in Table 5.1. The white contrast phase was seen to be high in niobium carbon and nitrogen which coincides with the constituents of the Nb(C,N) phase. The light gray phase was observed to be high in nickel, niobium, and silicon which are the typical constituents of either G-Phase ($Ni_{16}Nb_6Si_7$), or η-Phase ($Ni_2Nb_3(Si)C$). Due to the similarities in composition and structure of G-phase and η-Phase, information about the precipitates crystal structure must be obtained in order to conclusively decide which phase is present in the microstructure. From *Powell et al.* these two phase can be differentiated based on their lattice parameters where $a_{0,G-Phase} = 11.2\mathring{A}$, and $a_{0,\eta-Phase} = 10.9\mathring{A}$, or there space groups where G-Phase has a $Fm\overline{3}m$ space group, and η-Phase has a $Fd\overline{3}m$ space group. The dark phase in Fig. 5.4 was seen in EDS to be high in both chromium, and carbon concentrations which is representative of a chrome carbide phase, most likely $M_{23}C_6$. Secondary chromium carbides in austenitic stainless steels are normally seen to precipitate at interdendritic regions, and have been characterized is numerous other studies as $M_{23}C_6$ [3, 11, 59]. It should be noted that the carbon and nitrogen values in Table 5.1 contain a very high uncertainty due to x-ray energy peak overlap, absorption, and hydrocarbon surface contamination. While these concentrations are reported in order to compare the different spectroscopy methods used in this

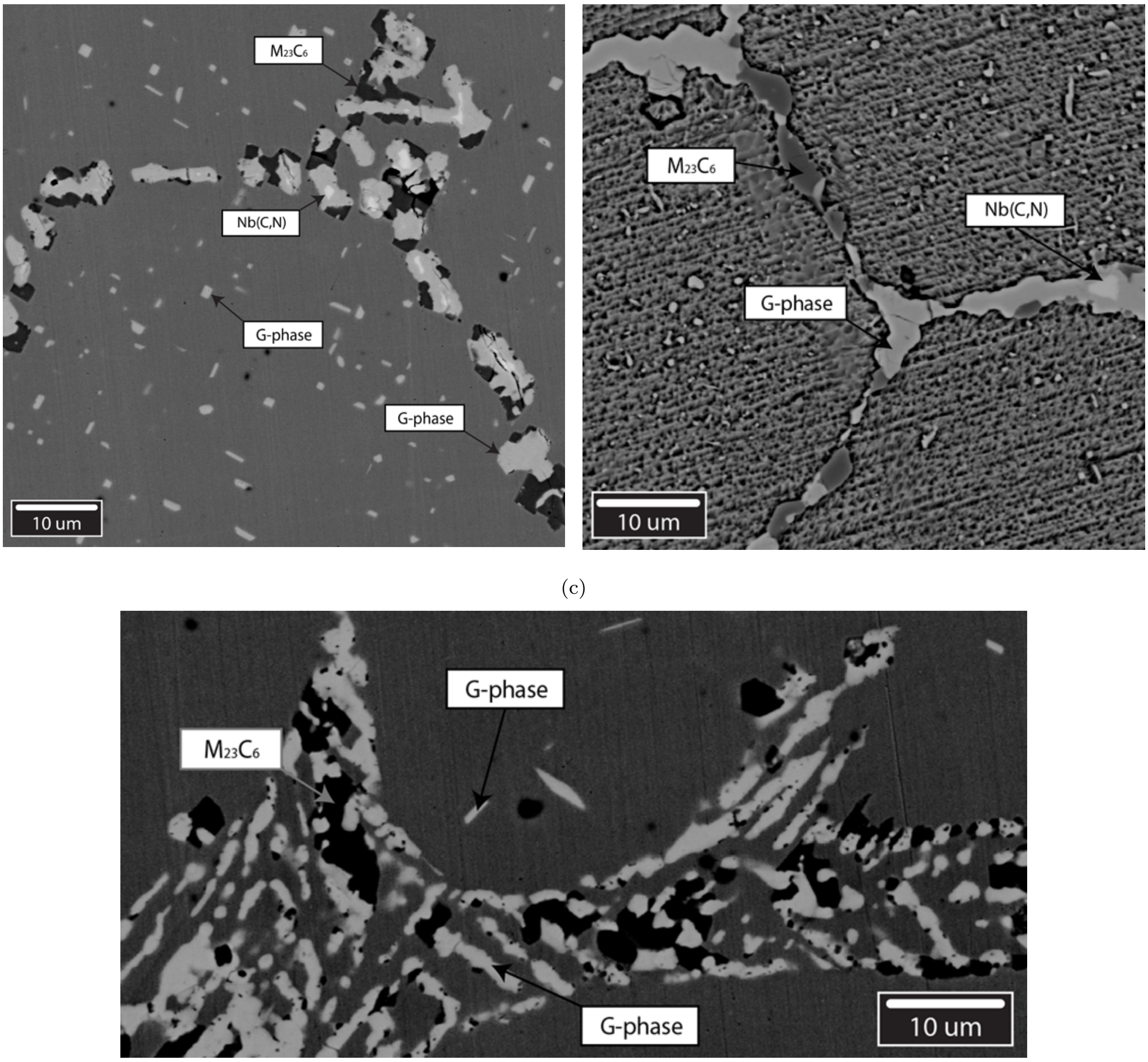
(a) (b) (c)

Figure 5.4: Backscattered (electron BSE) SEM micrographs of the interdendritic regions in both the static cast and centrifugally cast ex-service 2032Nb manifolds. a) shows coarse globular precipitation of intermetallic phases with dark secondary carbides along its interface, and NbC precipitates at its core. b) A continuous region of precipitates at the boundary interdispersed with the intermetallic phase and the secondary carbides. c) Intermetallic phase to precipitate in a lamellar like fashion with a similar orientation relationship compared to the intradendritic intermetallic precipitates.

study, they should not be used to quantitatively describe the composition of a phase.

From the compositional data of Nb(C,N) reported in Table 5.1, stoichiometrically this phase could be represented as $NbC_{0.72}N_{0.28}$ if nickel and chromium are disregarded in the first sublattice. However the ratio of nitrogen to carbon should actually be higher since the the carbon concentration is including hydrocarbon contamination of the surface of the sample, and instrument error. If the EDS data is compared to the spectroscopy data collected from AES (to be discussed later), the difference in carbon concentration for each phase characterized with each method is on average 8.8 wt%. A rough estimate for the actual stoichiometry of Nb(C,N) can then be estimated to be around $NbC_{0.67}N_{0.33}$. However it should be noted that this method is not a legitimate way of determining the actual carbon concentration from EDS data, and is only used to demonstrate what an approximate ratio of carbon to nitrogen is in the observed Nb(C,N) phase.

Table 5.1: Compositional analysis from Energy Dispersive X-ray Spectroscopy (EDS) of in-service 2032Nb microstructure that has been aged for 16 years.

EDS									
Phase	**Stage**	**Composition (wt%)**							**Number of Points**
		Fe	**Ni**	**Cr**	**Si**	**Nb**	**C**	**N**	
γ-Fe (boundary)	Fully Aged	bal	30.2 ± 0.9 (30.0 ±)	17.7 ± 0.5 (20.0 ±)	1.1 ± 0.1 (2.2 ±)	2.0 ± 0.1 (1.2 ±)	3.1 ± 0.8 (13.1 ±)	-	17
G-Phase	Fully Aged	bal	45.4 ± 9.2 (38.6 ± 7.8)	3.5 ± 3.4 (3.4 ± 3.4)	8.3 ± 1.6 (14.5 ± 3.3)	32.4 ± 8.0 (17.4 ± 4.4)	5.0 ± 1.7 (20.4 ± 6.4)	-	28
M23C6	Fully Aged	bal	5.2 ± 1.4 (4.3 ± 3.1)	77.1 ± 3.9 (61.9 ± 3.8)	0.1 ± 0.1 (0.2 ± 0.2)	0.4 ± 0.4 (0.2 ± 0.2)	7.9 ± 1.0 (26.3 ± 3.5)	-	27
Nb(C,N)	Fully Aged	bal	7.3 ± 4.6 (5.1 ± 3.0)	3.1 ± 4.0 (2.6 ± 3.5)	1.0 ± 0.4 (1.1 ± 0.3)	69.2 ± 5.8 (31.1 ± 3.4)	12.2 ± 1.7 (42.2 ± 4.0)	5.5 ± 0.7 (16.4 ± 2.0)	14
Z-Phase	Fully Aged	bal	8.3 ± 4.7 (6.2 ± 3.5)	26.3 ± 3.7 (22.1 ± 3.1)	1.1 ± 0.7 (1.7 ± 1.0)	47.3 ± 3.4 (22.3 ± 1.6)	5.9 ± 0.7 (21.5 ± 2.0)	7.5 ± 0.6 (23.4 ± 1.6)	10

A fourth phase was also discovered in the SEM, but was only visible at very high instruments contrasts. Fig. 5.5 shows a slight contrast variation in the G-phase constituents, where the darker regions were shown to have a different composition under EDS rich in chromium, niobium, and nitrogen. These constituents are typically found in the nitride phase, Z-phase, which has been characterized previously in NF709 variants [31], and 9 percent-12 percent chromium martensitic stainless steels [10]. Only very coarse Z-phase precipitates were visible with SEM under high contrast, while smaller precipitates were only visible with higher resolution microscopy methods such as AES.

5.3.2 EPMA/WDS phase quantification

EPMA micrographs in Fig. 5.6 were identical to the SEM micrographs, however no contrast experimentation was done to evaluate for Z-phase. WDS is a more accurate spectroscopy technique compared to EDS due to its higher resolution, and more precise separation of x-ray peaks. Comparing compositional data from WDS analysis in Table 5.2, to EDS analysis in Table 5.1 no drastic differences in phase composition were present, other than an increase in carbon quantification accuracy. WDS does display a higher standard deviations for quantified elements that may be due to interaction volume overlap from small precipitates, such as silicon in Nb(C,N). Both WDS and EDS quantification were collected at 20kV.

Element mapping for determining phase fractions was performed by EPMA due to increased sensitivity of

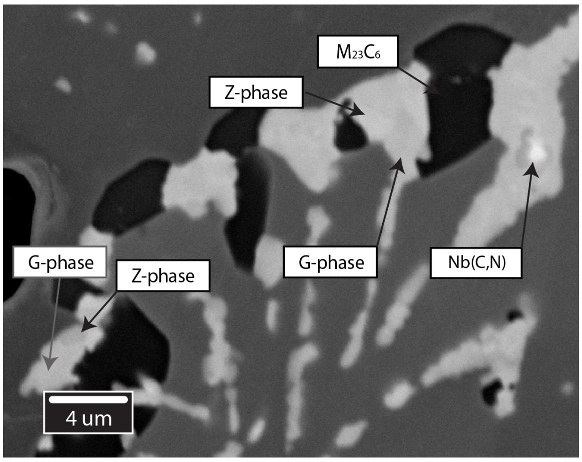

Figure 5.5: Possible Z-phase microconstituents observed by SEM, with EDS quantification showing some overlap in the interaction volume with G-phase.

the WDS detector, and the better x-ray collections compared to element mapping with SEM. An example of the element maps produced for the ex-service static cast alloy are shown in Fig. A.13 in the appendix. Poor carbon detection makes any data from the carbon spectrometer insufficient for distinguishing any features from the carbon map, and was excluded for any subsequent mapping with EPMA. As discussed in the characterization chapter the niobium map was used to find Nb(C,N), the niobium and silicon maps were used to find G-phase, and the chromium map was used to find $M_{23}C_6$. Z-phase was unable to be differentiated in the chromium map, where its phase fraction was calculated from various AES backscattered maps. Area fraction values for both components of the ex-service alloy are reported in Table 5.8, where both statistical and computational error was included by manually calculating phase fractions for a few maps.

Table 5.2: Compositional analysis from Wavelength Dispersive Spectroscopy (WDS) of in-service 2032Nb microstructure that has been aged for 16 years.

WDS									
Phase	**Stage**	**Composition (wt%)**							**Number of Points**
		Fe	**Ni**	**Cr**	**Si**	**Nb**	**C**	**N**	
γ-Fe (boundary)	Fully Aged	bal	29.1 ± 5.7 (24.9)	20.5 ± 4.9 (19.8)	1.8 ± 0.7 (3.2)	1.0 ± 0.5 (0.6)	2.7 ± 1.6 (11.4)	-	17
G-Phase	Fully Aged	bal	45.9 ± 5.6 (42.9)	5.0 ± 4.7 (5.2)	10.3 ± 1.6 (20.2)	32.3 ± 8.8 (19.0)	1.8 ± 0.8 (8.1)	-	27
M23C6	Fully Aged	bal	7.6 ± 3.7 (5.6)	82.4 ± 6.0 (68.3)	0.7 ± 0.8 (1.0)	2.4 ± 2.6 -1.1	6.6 ± 0.6 (23.4)	-	24
Nb(C,N)	Fully Aged	bal	7.5 ± 5.8 (7.5)	0.6 ± 0.3 (0.7)	1.2 ± 0.6 (2.6)	65.3 ±4.7 (41.5)	9.7 ±2.6 (47.7)	-	3

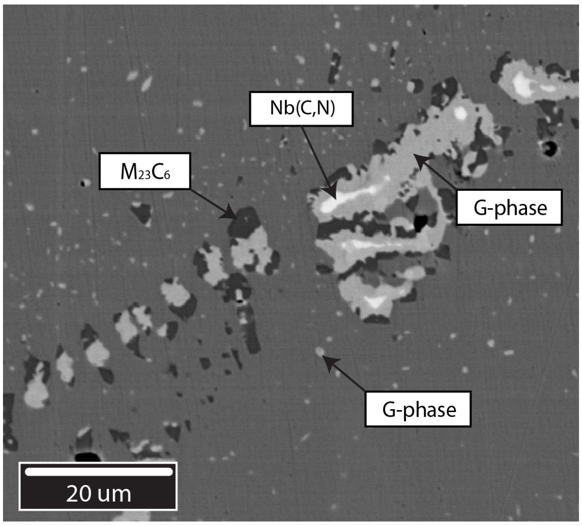

Figure 5.6: Backscattered WDS micrograph of an interdendritic region of an ex-service 2032Nb static cast tee after 3 years of aging from a solution annealed state.

5.3.3 AES phase quantification

AES imaging shown in Fig. 5.7 reveals three phases in the microstructure where the black phase was determined to be $M_{23}C_6$ from quantitative analysis, the dark gray phase was determined to be Z-phase, and the light gray phase was found to be G-phase. No Nb(C,N) phase was found with AES, where it is speculated that the interaction volume may not have penetrated deep enough to reveal all of the Nb(C,N) precipitates seen in the SEM microstructure. While there may still be some Nb(C,N) that have been sectioned through the polishing plane, which would be visible with AES, none of them were observed in the samples used to characterize the fully aged alloy, which were a few square millimeters in area.

Quantification of the observed phases is shown in Table 5.3 where the atomic sensitivity factor (ASF) of carbon was calibrated by assuming that the carbon concentration in $M_{23}C_6$ would be equal to stoichiometry, or 20.7 at.%. Calibrating the ASF factor was done in order to minimize error is carbon quantification from hydrocarbon contaminants that naturally form on the surface of the polished sample. Nitrogen has been reported to be soluble in the second sublattice of $M_{23}C_6$ in 422 stainless steel (11Cr-0.8Ni)[33]; however, the concentrations are fairly insignificant, and are assumed to be negligible. The average compositions reported from AES spectroscopy are the closest to what stoichiometry predicts when compared with results from EDS (Table 5.1), and WDS (Table 5.2). The primary constituents of G-phase predicted by AES are nickel, niobium, and silicon, where other elements that could be substituted in the lattice model such as chromium are negligible. A small amount of carbon, and nitrogen were detected in the Auger spectra, but some of the carbon could be attributed to contamination, and the standard deviation for nitrogen is almost 100% of the mean, meaning that any nitrogen found in this phase may be an artifact. Z-phase is comprised of one third chromium, niobium, and nitrogen with negligible amounts of nickel and silicon, while $M_{23}C_6$ is at nearly stoichiometric values of chromium and carbon with some solubility for nickel. The solution phase right beside the interdendritic region was found to be composed of 10 at.% carbon, and devoid of silicon, niobium, and nitrogen. The carbon concentration is most likely overestimated, and silicon, niobium, and nitrogen may still be present in the solution phase in dilute concentration, that may have been overlapped by other peaks in the spectra. AES is a surface sensitive technique and only interrogates the top 5-10nm of each precipitate in its interaction volume. This means that only a localized area of some of the larger precipitates is analyzed, and may not represent the bulk. It can be assumed that there is no compositional variation in the precipitates, or coring, however this may be a less likely assumption when looking at non-equilibrium microstructures such as the cast microstructure.

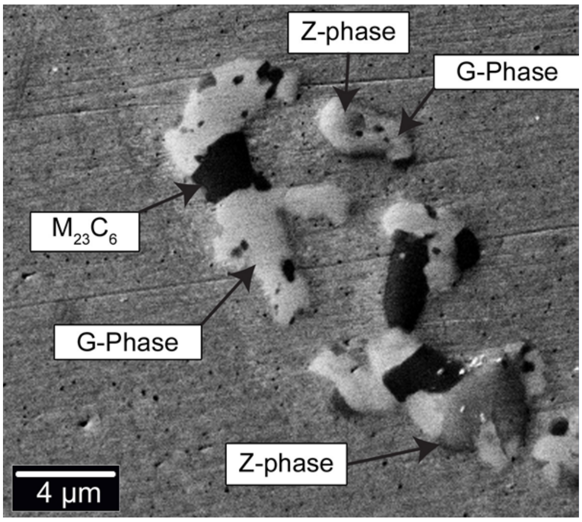

Figure 5.7: Auger Image (AES) micrograph depicting the surface microstructure of a fully aged centrifugally cast 20Cr32Ni1Nb stainless steel alloy.

The area fraction for Z-phase in the ex-service components reported in Table 5.8 were calculated using the backscattered image analysis technique explained in Chapter 3. 25 random backscattered AES micrographs were used which amounts to a total area of 0.07 cm^2. This area is smaller than that used to calculate phase fraction with the EPMA element maps, and may be less representative of the entire sample.

Element mapping using AES in Fig. 5.8 from AES, shows a clear segregation of components corresponding to different phases in the micrograph. AES mapping receives much stronger signals from low atomic number elements like carbon and nitrogen than EPMA mapping. The niobium and silicon map clearly outlines the G-phase precipitates already observed in SEM, and EDS, while regions high in nitrogen seen in the upper right hand side of the micrograph correlate to the darker gray phase in the center of multiple G-phase particles of the AES micrograph. The chromium map shows the largest degree of segregation where the dark phase characterized by EDS as $M_{23}C_6$ is clearly chromium rich, while the nitrogen bearing phase shows an intermediate detection of chromium. The Nb(C,N) particles are not readily observed in the AES backscattered image although the centers of the coarsened G-phase at the

Table 5.3: Compositional analysis from auger electron spectroscopy (AES) of in-service 2032Nb microstructure that has been aged for 16 years.

AES									
Phase	**Aging**	**Composition (wt%)**							**Number of Points**
		Fe	**Ni**	**Cr**	**Si**	**Nb**	**C**	**N**	
γ-Fe (boundary)	Fully Aged	bal	36.7 ± 1.6 (32.3 ± 2.0)	17.50 ± 3.8 (17.3 ± 3.2)	-	-	2.43 ± 1.4 (10.2 ± 5.6)	-	4
G-Phase	Fully Aged	bal	52.0 ± 3.4 (48.6 ± 2.9)	0.3 ± 0.6 (0.3 ± 0.6)	11.6 ± 1.5 (22.5 ± 2.5)	33.6 ± 4.3 (20.0 ± 3.0)	1.1 ± 0.2 (5.2 ± 0.9)	0.7 ± 0.6 (2.8 ± 2.4)	14
M23C6	Fully Aged	bal	3.3 ± 0.6 (2.5 ± 0.5)	82.7 ± 0.7 (70.9 ± 1.7)	-	-	5.3 ± 0.6 (19.6 ± 2.0)	-	12
Z-Phase	Fully Aged	bal	1.4 ± 1.6 (1.2 ± 1.4)	31.1 ± 1.2 (29.2 ± 0.7)	0.2 ± 0.6 (0.4 ± 1.0)	55.4 ± 2.0 (29.1 ± 1.7)	1.4 ± 0.3 (5.6 ± 1.0)	9.7 ± 0.8 (33.9 ± 2.0)	14

bottom left of the micrograph show a very high concentration of niobium. This high concentration could be a residual Nb(C,N) particle, or represent a dissolved Nb(C,N) precipitate. Silicon depletion, and high carbon concentration in the high niobium-rich areas also supports the notion that these regions are indeed residual Nb(C,N).

5.3.4 X-Ray Diffraction

X-ray diffraction spectra of the extracted precipitates in Fig. 5.9 indicates that the predominant peaks are two separate phases indexed on cubic cells of the $Fm\bar{3}m$ space group. These phases were identified as $Ni_{16}Nb_6Si_7$ and $M_{23}C_6$, with lattice parameters of $a = 11.24$ Å and $a = 10.65$ Å respectively. In addition to these phases, a third phase was indexed as having a tetragonal BCC cell with lattice parameters of $a = 4.28$ Å, and $c = 7.36$ Å, and identified as NbCrN, or Z-phase. The peak at 49° is characteristic of Z-phase, and provides strong evidence that Z-phase is present within the alloy even though the relative intensity of the Z-phase spectra is dwarfed by G-phase, and $M_{23}C_6$. A weak peak attributed to the residual $\mathrm{Nb(C,N)_x}$ was also observed, which has an FCC cell with a lattice parameter of $a = 4.44$ Å. Nb(C,N) constitutes a very small percentage of microconstituents where the amount of the gathered x-rays from this phase is significantly lower than G-phase, Z-phase, and $M_{23}C_6$. The low relative intensity of the Nb(C,N) characteristic peaks makes it difficult to distinguish from the background spectra, where only the first two peaks of the phase where able to be identified.

5.4 Microstructural variations between centrifugally cast and static cast

Variations in grain size and morphology shown in Fig. 4.6 between static cast and centrifugally cast components can have a large effect on the mechanical properties through the thickness of the part. In the static cast component going from the outer wall to the inner wall, the grain size and the dendrite size

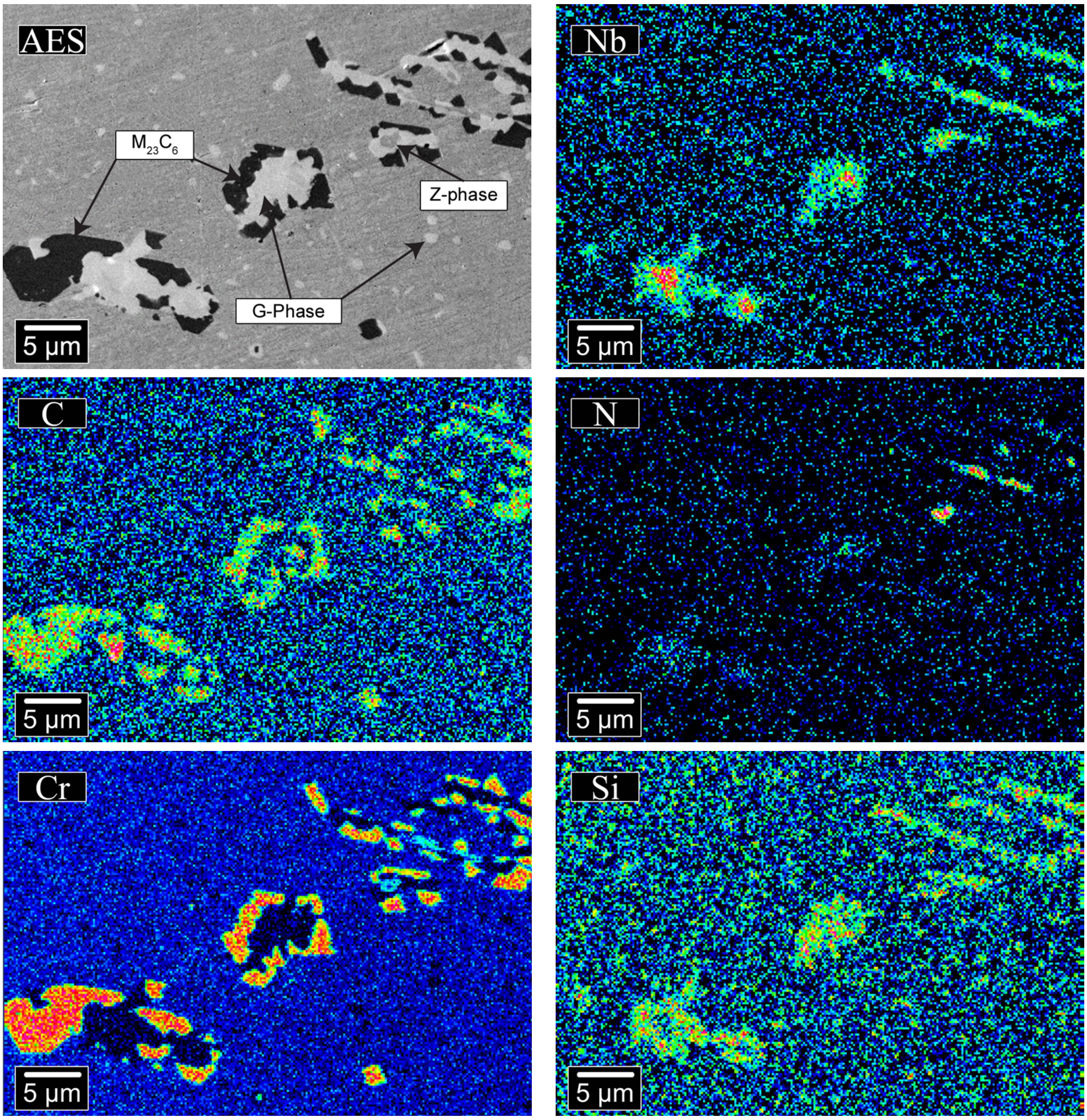

Figure 5.8: Element maps from Auger Electron Spectroscopy of an interdendritic region of a fully aged 2032Nb Stainless steel pipe.

fluctuates due to the heat flux through the melt during solidification. The outer wall chill zone, the central equiaxed zone, and the columnar inner wall zone produce varying dendrite arm spacing depending on the amount of coarsening that can occur in each grain. Fluctuating dendrite size subsequently leads to varying interdendritic regions where compounds precipitate at different distances for elements to diffuse. This will effect both the equilibrium microconstituents fractions, and the precipitation rate and coarsening rates

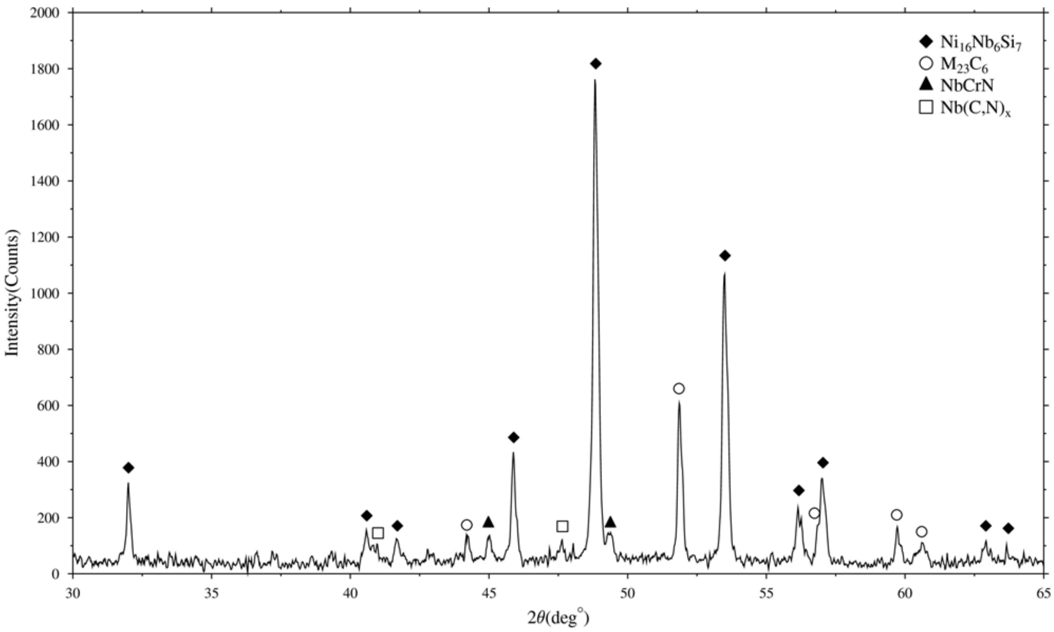

Figure 5.9: X-ray diffraction spectra of precipitates extracted from the austenite matrix of the ex-service static cast 2032Nb Stainless Steel alloy.

of the microconstituents. Along with the casting method, the finish wall thickness of the component can change the grain size, dendrite cell size, and microconstituents present, as well as their volume fractions through the thickness of the part.

Table 5.4, 5.5, and 5.6 compare the dendritic microstructure of the 1" static cast, and 1" and 3" centrifugally cast parts after they have been removed from service. The 1" centrifugally cast part shows little variability in grain size through the thickness, while the dendrite size is observed to decrease from the inner wall to the outer wall. There appear to be higher amounts of $M_{23}C_6$ carbides in the outer wall region of the 1" centrifugally cast part, etched as the light contrasted phase in the high magnification optical micrograph (Table 5.5). A more lamellar interdendritic constituent structure like that discussed in subsection 5.3.1 is seen at the inner wall region and central region, whereas a continuous interdendritic structure is seen at the outer wall region. The intradendritic G-phase fraction appears to be consistent throughout the casting. The 1" static cast part shows larger columnar dendrites growing in the inner region compared with the outer region. The middle region shows an equiaxed dendrite structure without any definable growth direction. The intradendritic regions of the static cast component are seen to be populated with a higher density of fine precipitates than the centrifugally cast component. G-phase is discovered to be coarser in some regions along the inner wall compared to the outer wall, which indicates that a higher amount of residual Nb(C,N) is retained after long term aging. The 3" centrifugally cast part shows a progressively decreasing dendrite size moving from the inner wall to the outer wall. From Fig. 4.6c the grain structure does not seem to change until approximately 15mm from the outer wall. The microconstituents at the outer wall are observed to have not coarsened as extensively as in the middle and inner areas, where the dendrites are finer and show a more uniform growth direction. The outer wall region also looks to contain more $M_{23}C_6$ carbides than the middle or inner wall regions.

Table 5.4: Optical micrographs of the microstructural differences between the inner wall, middle, and outer wall of 3” thick end of the centrifugally cast pipe

Centrifugally Cast (3” thick)		
Inner	Middle	Outer
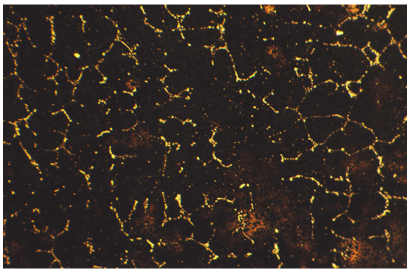	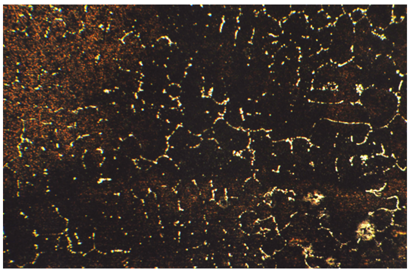	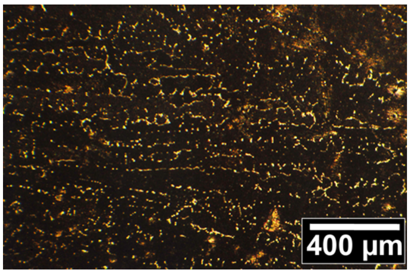
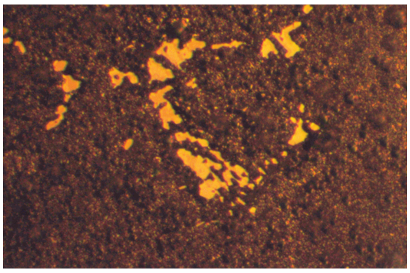	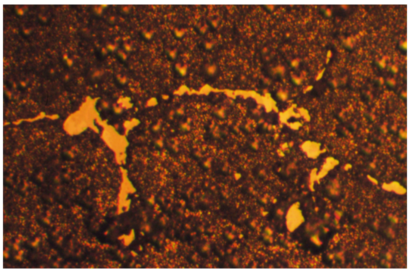	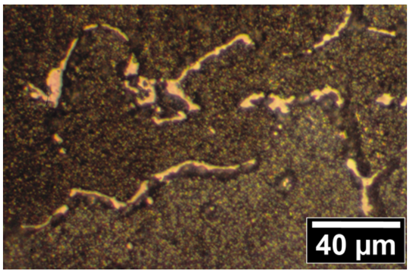

Table 5.7 displays grain size, and dendrite cell size measurements of the three casting types, and their through thickness variations. the 3” centrifugally cast section does not show any variation between the inner wall and middle regions, and a decrease in both grain size and dendrite cell size for the outer wall region. The smaller grain size at the outer wall region is attributed to centrifugal forces acting on the melt during solidification. These centrifugal forces are less apparent in the 1” centrifugally cast section that contains a fairly uniform grain size and dendrite cell size. On average both the grain size and the dendrite cell size are finer in the 3” centrifugal casting than the 1” centrifugal casting. Coarser microconstituents were observed in the inner wall region for the 3” centrifugally cast component, where Nb(C,N) precipitates were only visible at the inner wall region with the optical microscope. Dendrite cell size for the static cast component do not vary much until the outer wall region is reached, however visually in Table 5.6 the inner wall region dendrites look a lot coarser. With the large standard deviation of the inner wall and middle region measurements their is a significant variability in the dendrite cell size, and thus the diffusional distance for elements to segregate. The grain size of the static cast section is measured to be finer than the centrifugally cast section, even though the dendrite cell size is roughly the same. A larger degree of deviation is observed in the centrifugally cast part compared to the static cast, meaning that there is a larger variability in dendrite size of the static cast component.

Table 5.8 shows the results of the calculated phase fractions from element mapping with EPMA com-

Table 5.5: Optical micrographs of the microstructural differences between the inner wall, middle, and outer wall of 1” thick end of the centrifugally cast pipe

Centrifugally Cast (1” thick)		
Inner	Middle	Outer
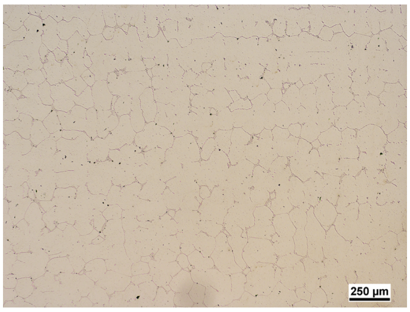	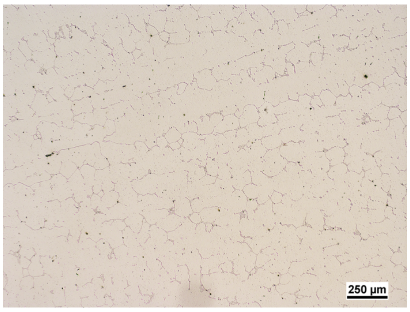	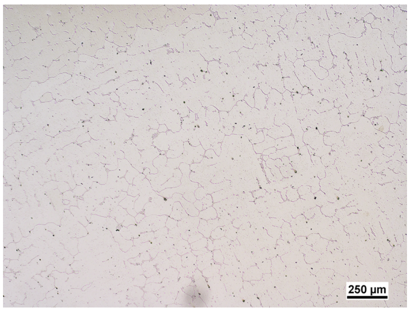
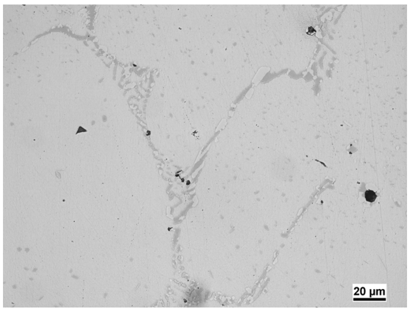	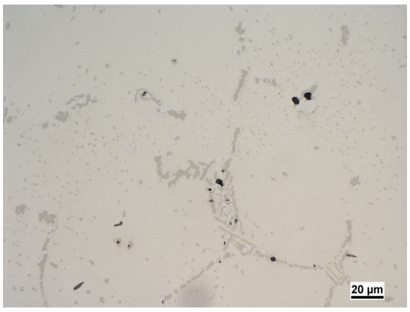	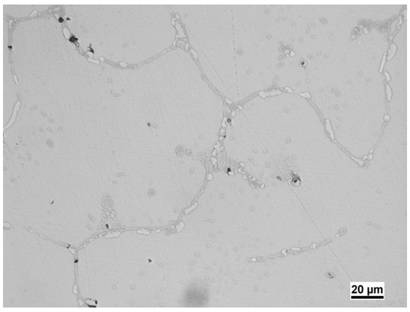

paring the 1” static cast and 1” centrifugally cast ex-service components. The total area analyzed from each component was 531 mm^2 which is assumed to be large enough to be representative of the bulk. A much larger amount of residual Nb(C,N) carbides were retained in the static cast microstructure, while nearly all the Nb(C,N) in the centrifugally cast component had been transformed into G-phase. The static cast component had undergone a solution annealing treatment and was only aged for three years until taken out of service, whereas the centrifugally cast component was aged for 16 years. The fraction of residual Nb(C,N) in the static cast component could be because the microstructure has not reached an equilibrium state, where further transformation in G-phase could still occur even after 3 years. All of the microconstituents in the static cast component make up a large fraction of the microstructure in the inner wall region than the middle or outer wall regions. Furthermore microconstituent fractions are fairly consistent between the inner wall, and middle regions of the static cast component. The lower Nb(C,N) fraction of the centrifugally cast component shows an increased fraction of G-phase and Z-phase and a lower fraction of $M_{23}C_6$ compared with the static cast component. The middle regions of the centrifugally cast component show a sizable decrease in microconstituents compared to the inner wall, and outer wall regions. A general trend when looking at the differences between the inner wall region and the outer wall region for both casting types is that the inner wall region contains less G-phase and more $M_{23}C_6$, while the outer wall region contains less G-phase and more $M_{23}C_6$. $M_{23}C_6$ fraction was found to have less variability than G-phase through the thickness of both components.

Table 5.6: Optical micrographs of the microstructural differences between the inner wall, middle, and outer wall of the static cast tee

Statically Cast (1" thick)		
Inner	Middle	Outer
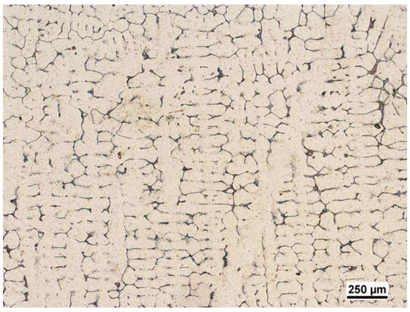	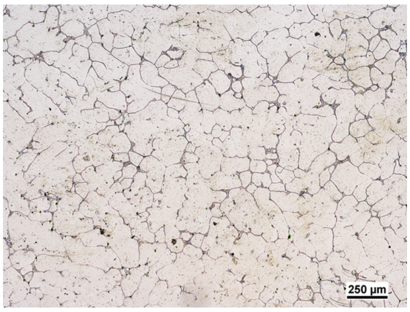	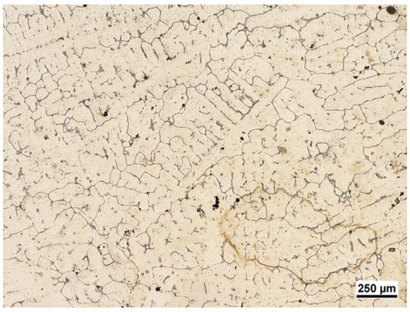
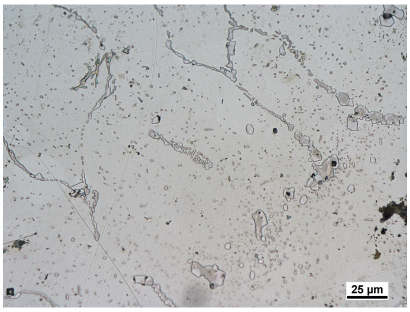	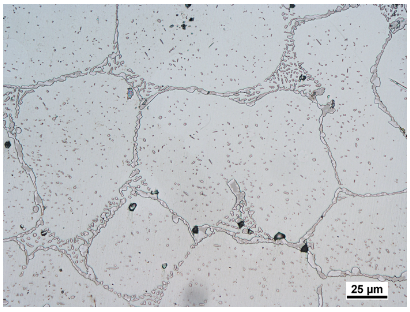	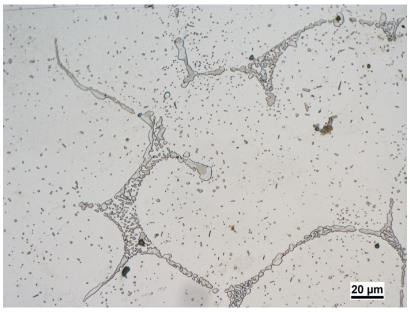

Table 5.7: Grain size, and dendrite cell size measurements of the fully aged static cast tee, and the short/long sections of the centrifugally cast cone.

Casting Type	**Region**	**Grain Size (mm)**		**Measurements**	**Dendrite Cell Size (μm)**	**Measurements**
		Width	**Length**			
Centrifugally Cast (Thick part)	Inner	1.6 ± 0.4	6.1 ± 1.9	10	112.6 ± 26.9	37
	Middle	1.4 ± 0.4	5.7 ± 2.1	10	99.8 ± 26.7	41
	Outer	0.9 ± 0.2	3.0 ± 0.9	15	70.8 ± 11.9	27
Centrifugally Cast (Thin part)	Inner				133.5 ± 28.7	39
	Middle	2.0 ± 0.8	12.9 ± 6.9	15	106.0 ± 23.3	50
	Outer				93.6 ± 28.0	70
Statically Cast (Thin part)	Inner	1.4 ± 0.4	5.9 ± 0.6	11	121.4 ± 43.8	50
	Middle	0.78 ± 0.3		36	127.8 ± 42.9	52
	Outer	0.6 ± 0.1	1.8 ± 0.5	18	100.9 ± 29.1	50

Rockwell B hardness tests show the static cast component with a higher $HRB = 69.6 \pm 2.0$ ($n = 12$) than the centrifugally cast component $HRB = 64.9 \pm 2.2$ ($n = 9$). These readings coincide with what should be expected from the phase fraction measurements in Table 5.8 where the static cast component has both a higher carbide fractions (NbC, and $M_{23}C_6$), and lower G-phase fractions. Fig. 5.10 shows the

Table 5.8: Area fractions for microconstituents or precipitates in 1” aged ex-service 2032Nb static cast, and centrifugally cast alloys at various areas through the thickness of the components

	Phase Fraction (vol%)					
	Static Cast			**Centrifugally Cast**		
Phase	**Inner**	**Middle**	**Outer**	**Inner**	**Middle**	**Outer**
NbC	0.12 ± 0.02	0.10 ± 0.03	0.08 ± 0.02	0.03 ± 0.01	0.02 ± 0. 01	0.03 ± 0.03
G-Phase (interdendritic)	2.54 ± 0.26	2.17 ± 0.56	1.51 ± 0.29	2.90 ± 0.32	1.94 ± 0.20	2.36 ± 0.57
G-Phase (intradendritic)	0.93 ± 0.17	0.78 ± 0.11	0.63 ± 0.17	1.02 ± 0.07	0.81 ± 0.08	0.90 ± 0.15
$M_{23}C_6$	1.18 ± 0.34	0.96 ± 0.35	1.03 ± 0.34	0.91 ± 0.40	0.87 ± 0.10	1.07 ± 0.31
Z-Phase		0.29 ± 0.12			0.33 ± 0.06	

Rockwell hardness profiles through the thickness of both ex-service components. The drop in hardness in the central regions is reinforced by the phase fractions of the centrifugally cast component in Table 5.8 indicating a decrease in $M_{23}C_6$ fraction. The static cast component does not show this drop in precipitate fraction at the center, having a relatively consistent $M_{23}C_6$ fraction through the thickness, and a steady decreasing G-phase fraction from the inner wall to the outer wall. Both show a decrease in hardness at the center of each component, and a low hardness at the chill zone. The outer wall and inner wall regions exhibit comparable hardness, where the outer wall region maintains a slightly higher hardness profile through a larger thickness of the component. Table 5.8 shows slightly lower $M_{23}C_6$ fractions at the outer wall compared to the inner wall, although they are both within error of each other, and G-phase fractions are both lower at the outer wall regions. Zhu *et al.* [64] speculates that the drop in secondary precipitates at the center is caused by atmospheric effects, as well as temperature differences experienced through the thickness during operation. The comparable hardness measurements of the inner and outer wall, and the consistent $M_{23}C_6$ fraction suggest that nitridation and decarburization are minimal at the inner wall. Nitridation effects could be evaluated by examining the differences in Z-phase fraction through the thickness, however this was excluded in this study due to problems resolving Z-phase with SEM or EDS.

Table 5.9 compares the precipitate sizes for all the microconstituents found in the static cast and centrifugally cast ex-service components. These measurements where calculated using the image analysis toolkit on backscattered SEM, and AES micrographs discussed in the characterization chapter. Both interdendritic and intradendritic G-phase precipitates of the centrifugally cast component are seen to be coarser than the static cast G-phase, however this could just be related to a difference in aging time. Nb(C,N) precipitates show the opposite trend of G-phase where they are coarser in the static cast component. $M_{23}C_6$ and Z-phase precipitates show less variability than G-phase where the $M_{23}C_6$ precipitates are a fairly consistent size between the two components.

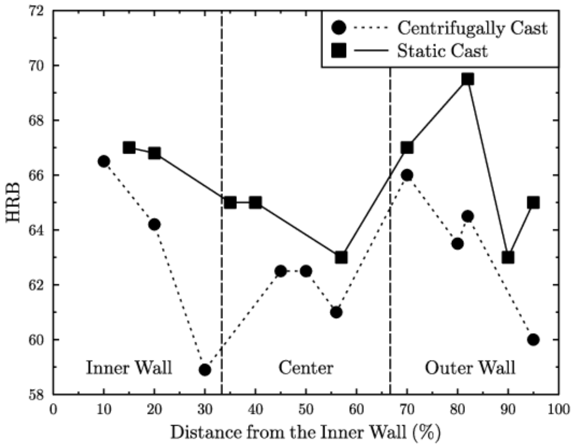

Figure 5.10: Rockwell Hardness B (HRB) profiles through the thickness of both ex-service components

Table 5.9: Precipitate sizes of the ex-service microstructure of both the static cast, and centrifugally cast components

	Particle Diameter (μm)			
Phase	**Centrifugally Cast**	**Counts**	**Static Cast**	**Counts**
Nb(C,N)	1.12 ± 0.74	10	1.73 ± 1.07	14
G-Phase (interdendritic)	4.02 ± 2.00	68	2.58 ± 1.30	122
G-Phase (intradendritic)	1.33 ± 0.30	108	1.00 ± 0.30	112
$M_{23}C_6$	2.86 ± 1.52	85	2.14 ± 1.57	106
Z-Phase	1.50 ± 0.83	49	0.99 ± 0.32	44

5.5 Characterization of Solution Annealed and Cast Microstructures

5.5.1 Solution Annealed Microstructure

G-phase, Z-phase, and the secondary $M_{23}C_6$ phases were dissolved in the static cast, and centrifugally cast components by solution annealing at 1200°C for 1 hour. Submicron Nb(C,N) particles precipitated out of solution in the regions where both interdendritic G-phase, and intradendritic G-phase once existed. Fig. 5.11 shows an interdendritic region after solution annealing, which is populated by a high number density of submicron Nb(C,N) precipitates, and a large residual Nb(C,N) precipitate that had survived the aging process prior to the heat treatment. The lamellar type structure is due to the orientation of the G-phase before solution annealing where the niobium did not have enough time to diffuse before precipitating out of solution with carbon forming Nb(C,N).

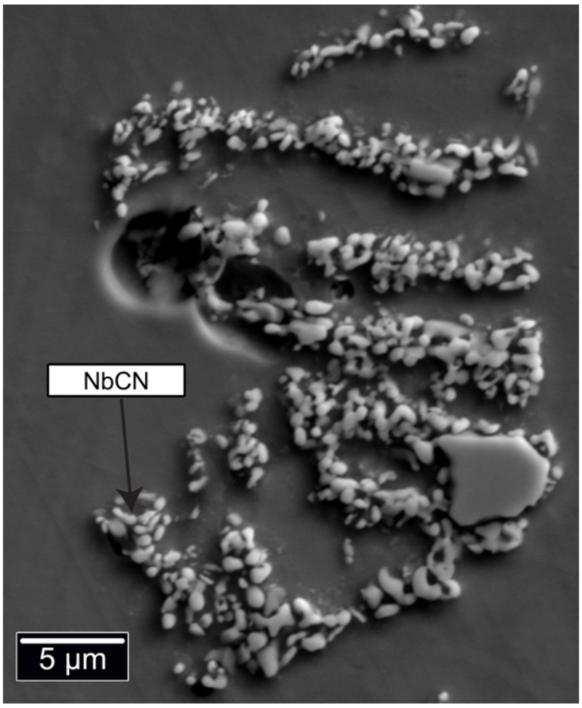

Figure 5.11: Secondary electron (SEI) SEM of solution annealed 2032Nb, at 1200°C for one hour. The small, dispersed niobium carbides are seen to precipitate in a lamellar fashion along triple point boundary.

Quantative analysis of the solution annealed microstructure using both EDS and AES spectroscopy methods is presented in Table 5.10. The solution annealed Nb(C,N) has slightly less nitrogen compared to the residual Nb(C,N) in Table 5.1, but contains roughly the same amount of carbon. Very little nitrogen uptake is seen to occur in residual Nb(C,N) carbides, and is assumed to not promote the stability of these carbides against G-phase transformation. The Nb(C,N) composition determined by AES can stiochiometrically be written as $NbC_{0.74}N_{0.26}$.

The centrifugally cast component contained on average a higher percentage of both inter- and intra-dendritic Nb(C,N) over the static cast component, where from ThermoCalc it was determined that niobium, carbon and nitrogen are less soluble in the centrifugally cast component ($k_s = 1.31 * 10^{-10}$) than the static cast component ($k_s = 1.34 * 10^{-10}$). Area fractions for the solution annealed microconstituents are found in Table 5.11, where the centrifugally cast component precipitates more Nb(C,N) during solution annealing than the static cast component. In Table 5.12, Nb(C,N) precipitates in the static cast component after heat treating appears to be slightly coarser than the centrifugally cast component. ThermoCalc calculates the Nb(C,N) phase fraction at 1200°C to be 0.85 vol%, and 0.82 vol% for the centrifugally cast, and static cast components respectively. It is assumed that a 1 hour heat treatment time may not represent the microstructure at equilibrium, which could in part explain this discrepancy. The submicron size of the precipitates may also increase the phase fraction error as the spatial resolution limit with EPMA is $1\mu m/px$, which might not be sufficient to resolve Nb(C,N) precipitates.

Table 5.10: Compositonal analysis of the solution annealed 2032Nb microstructure with Auger Electron Spectroscopy (AES), and Electron Diffraction Spectroscopy (EDS).

Phase	**Aging**	**Composition (wt%)**							**Number of Points**
		Fe	**Ni**	**Cr**	**Si**	**Nb**	**C**	**N**	
EDS									
Nb(C,N)	Sol. Ann.	bal	11.1 ± 0.4 (10.0 ±)	8.8 ± 0.3 (8.8 ±)	0.5 ± 0.1 (1.0 ±)	49.2 ± 1.8 (25.2 ±)	11.0 ± 1.6 (31.5 ±)	3.3 ± 1.0 (11.1 ±)	25
γ-Fe (boundary)	Sol. Ann.	bal	30.3 ± 0.8 (27.5 ±)	20.7 ± 0.5 (21.2 ±)	1.0 ± 0.1 (1.9 ±)	0.6 ± 0.1 (0.4 ±)	2.9 ± 0.7 (12.4 ±)	-	14
AES									
Nb(C,N)	Sol. Ann.	bal	4.8 ± 2.1 (4.1 ± 2.5)	1.9 ± 1.7 (1.8 ± 1.7)	1.1 ± 1.2 (1.9 ± 2.1)	74.2 ± 5.8 (39.2 ± 3.0)	8.9 ± 0.7 (36.5 ± 2.4)	3.3 ± 0.4 (11.4 ± 1.4)	25
γ-Fe (boundary)	Sol. Ann.	bal	41.8 ± 1.3 (38.7 ± 0.9)	13.1 ± 1.4 (13.6 ± 1.6)	-	-	1.3 ± 0.6 (5.9 ± 1.68)	-	3

Table 5.11: Area Fractions of precipitates after solution annealing the static cast and centrifugally cast components, and button melting.

Phase	**Area Fractions (%)**		
	Centrifugally Cast	**Static Cast**	**Cast**
Nb(C,N) (interdendritic)	3.19 ± 0.69	2.42 ± 0.69	3.30 ± 0.28
Nb(C,N) (intradendritic)	0.19 ± 0.03	0.13 ± 0.03	
Cr-Carbide (intradendritic)	-	-	0.18 ± 0.05

Table 5.12: Precipitate sizes of the solution annealed and as-cast microstructure.

Phase	**Particle Diameter (μm)**					
	Centrifugally Cast	**Counts**	**Static Cast**	**Counts**	**Cast**	**Counts**
Nb(C,N)	0.78 ± 0.23	129	0.85 ± 0.32	133	0.74 ± 0.33	44
Cr-Carbide (intradendritic)	-	-	-	-	0.91 ± 0.25	173

5.5.2 Cast Microstructure

The as-cast microstructure of the ex-service 2032Nb alloys can be simulated with a button melting apparatus, where both the static cast and centrifugally cast components were remelted. Both components showed submicron eutectic Nb(C,N) in the interdendritic regions much like the solution annealed microstructure. The Nb(C,N) precipitates in the remelted microstructure did differ from the solution annealed Nb(C,N), having a more elongated lamellar pattern, appearing less globular, with what is refereed to in Thomas *et al.* as a 'herringbone' structure [6]. The microstructure of the remelted static cast component in Fig. 5.12 shows submicron spherical dark dots in the intradendritic regions. EDS would identify these as being chromium rich, most likely $M_{23}C_6$, or M_7C_3 precipitates. Chen and Lippold *et* *al.* performed a similar button melting operation on the 2032Nb alloy, and identified these chromium rich carbides as $M_{23}C_6$ with EDS [17]. Chen *et al.* also investigated the as-cast microstructure and determined they intradendritic carbides to be $M_{23}C_6$ with Transmission Election Spectroscopy (TEM) [3]. M_7C_3 carbides are common to form in as-cast HP-Nb alloys where the carbon concentration is much higher ($\sim$ 0.44 wt%C) [6, 17, 46, 65], but have not been reported in the 2032Nb system.

Chromium carbides in the static cast component were only found on one side of the button melt, which indicates that the elements in the melt where not homogeneously distributed during the mixing of the button melt process. On the other hand the centrifugally cast component did not contain any chrome carbides after button melting. Since the concentration of carbon is nearly identical in both component chemistries it is assumed that the carbon was concentrated towards one side of the melt which facilitated the precipitation of these intradendritic carbides. The Scheil plots in Fig. 5.2 simulated by ThermoCalc do not show any chrome-carbide precipitation in either the static cast or the centrifugally cast components histories. TiN precipitates are predicted by ThermoCalc for the static cast microstructure, but none where found in the as-cast microstructure.

Both the volume fraction and size of Nb(C,N) precipitates in the cast state are seen to be comparable with that of the centrifugally cast solution annealed component in Table 5.11, and Table 5.12. The intradendritc chromium carbide precipitates were measured to be marginally larger than the Nb(C,N) precipitates, however their morphologies are very different where the Cr-rich carbides are spherical and the Nb(C,N) are more elongated and elliptical. Nb(C,N) also has more variance in its size distribution compared to the intradendritic carbides.

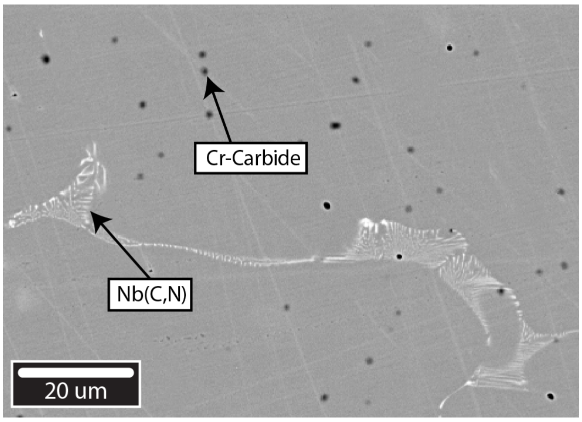

Figure 5.12: Backscattered (BSE) SEM of the static cast 2032Nb component button melted to recreate the as cast condition of the microstructure.

The eventual transformation of the Nb(C,N) precipitates relies heavily on the distribution and concentration of silicon around the primary Nb(C,N) precipitates where silicon raises the chemical potential of carbon and nitrogen, and can eventually destabilize these carbides to form G-phase [30]. Fig. 5.13 shows the distribution of silicon after solution annealing, and button melting where after solution annealing the silicon has diffused somewhat back into the matrix, while in the button melted sample it is fairly segregated. Silicon is a ferrite stabilizer and will prefer diffusing to the interdendritic regions, and out of the austenitic matrix. Although the silicon in the solution annealed sample will eventually segregate to the interdendritic boundaries the precipitation kinetics, and coarsening of G-phase may be delayed during aging compared to the button melted sample.

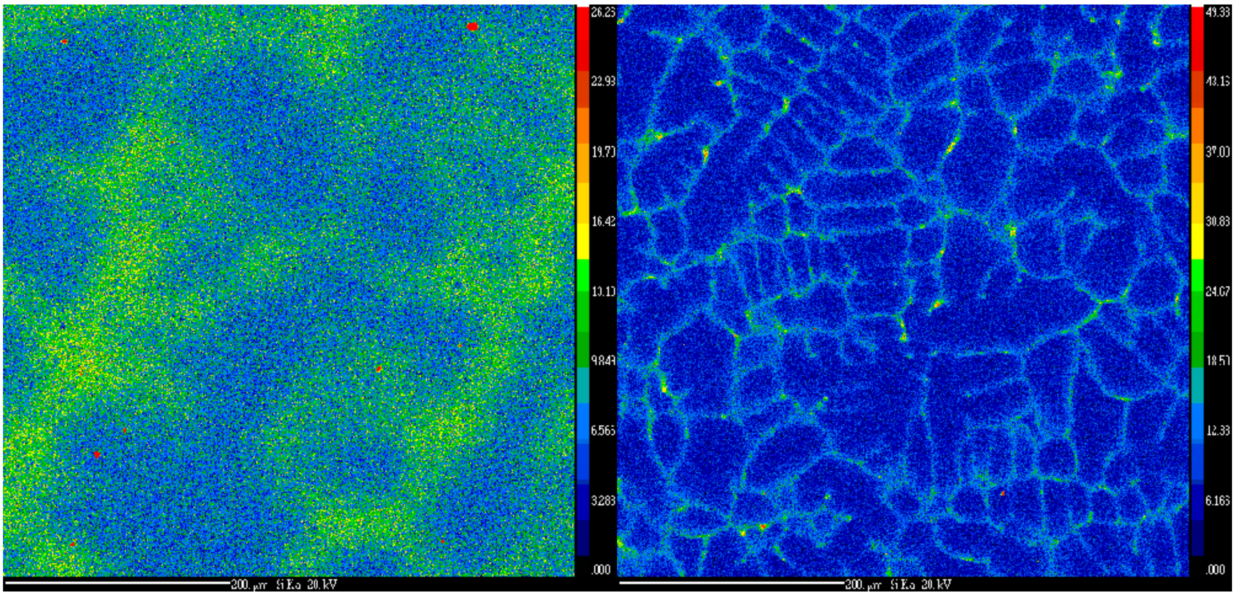
(a)

(b)

Figure 5.13: Silicon segregation in the austenite matrix after a) solution annealing, and b) button melting the static cast 2032Nb component.

5.6 Discussion on the ex-service components

5.6.1 ThermoCalc Comparison

The equilibrium phase fraction plots vs temperature calculated by ThermoCalc in Fig. 5.1, predict the correct stable microconstituents that were observed in the fully aged microstructure of the ex-service components. Due to the discrepancies from the nickel database used for this study it is difficult to compare the ThermoCalc results based on absolute temperature, as the stability of G-phase ($\sim$ 400°C in ThermoCalc) is far lower than the actual operating temperature of $\sim$ 800°C. In the centrifugally cast component G-phase has a $\sim$ 100°C higher stability temperature due to the excess niobium in the system. For the static cast component the excess fraction of niobium is much lower, also limiting the total amount of G-phase able to precipitate. In the ex-service static cast component the G-phase fraction is lower than the centrifugally cast component. However the static cast component is assumed to be in a non-equilibrium state as it has only been aged for four years.

At the onset of Nb(C,N) to G-phase transformation the driving force is very high, where Nb(C,N) is completely transformed after $< 100°\text{C}$. If Nb(C,N) is more stable in the static cast component, it will need to be aged for a longer period to see if the Nb(C,N) phase fraction differs from the one reported in Table 5.8. For the centrifugally cast component it is easier to compare with Fig. 5.1a as it can be assumed that G-phase has nearly completely transformed into Nb(C,N) and should be at its maximum precipitation concentration. On average, the G-phase fraction predicted by ThermoCalc coincides with the interdendritic G-phase fraction, however with the intradendritic G-phase fraction is underestimated by $\sim$ 0.8 vol%. On the other hand $M_{23}C_6$ and Z-phase are both overestimated in the ThermoCalc study by 100 vol%. These fractions may change if performed with an iron database integrated with G-phase, where at a higher temperature their stability and driving force might be affected, changing their fractions. ThermoCalc is still proven to be a useful tool in predicting the microconsituents, and their relative amounts; however, their absolute values need will need to be re-examined with an updated iron database.

5.6.2 Previous 2032Nb Studies

Studies previously done on the 2032Nb system by Chen *et al.* [3], Hoffman [29], and Shi and Lippold [17] are all conducted at different aging times and temperatures making it difficult to directly compare microstructures which are in a non-equilibrium, nearing equilibrium, or in a equilibrium state. This is important for the residual amount of NbC that exists in the microstructure and for predicting if any further transformation into G-phase will occur with further aging. Chen *et al.* [3] examined samples for four years at 760°C, and Hoffman *et al.* [29] aged their samples for 21 months at 824°C, both of which contained a large amount of residual NbC. On the other hand, Shi and Lippold analyzed samples in-service for 12 years at 815°C which contained no observable residual NbC. The equilibrium phase fraction plots calculated by ThermoCalc in Fig. 5.1 shows a large driving force for the dissolution of NbC and the precipitation of $M_{23}C_6$ and G-phase. This means that there is a small window in temperature where residual Nb(C,N) can exist at equilibrium. The percentage of NbC to G-phase transformation is highly dependent on the Nb/C ratio, and silicon concentration, where a low Nb/C ratio, and a low silicon concentration will decrease this transformation rate. The static cast component solution annealed and aged for 3 years contained a significantly larger amount of residual NbC compared to the centrifugally cast component that was aged for 16 years in Table 5.8. Even though the static cast component does have a smaller Nb/(C+N) ratio, and should be expected to contain less G-phase, it is assumed that the static cast component is still in a non-equilibrium state and will transform more residual Nb(C,N).

The intradendritic G-phase displays a clear 90° orientation relationship with the austenitic matrix phase, which has previously been indexed by *Chen et al.* [3] as $[0\,1\,1]_{G-phase} // [0\,1\,1]_{\gamma}$, $[1\,\bar{1}\,1]_{G-phase} // [\bar{1}\,\bar{1}\,1]_{\gamma}$, and $[2\,1\,\bar{1}]_{G-phase} // [1\,\bar{1}\,1]_{\gamma}$. This orientation relationship between G-phase and austenite corresponds to the directionality found in the ex-service alloy investigated in this study. It is proposed that the intradendritic G-phase, and the lamellar interdendritic G-phase nucleate off of dislocation sites in the matrix, which would in part explain their orientation relationship and their elongation along their major axis. However, G-phase is known to form from a transformation process with NbC, where NbC are widely regarded to favor nucleating on dislocation sites [66, 67]. This mutually dependent relationship may cause intradendritic NbC nucleation to precede G-phase precipitation. Since dislocations act as solute collectors [67], silicon could towards these areas and destabilize the Nb(C,N) precipitates to form G-phase.

5.6.3 Static cast vs Centrifugal Cast

Centrifugally casting has the benefits of homogenizing the austenite compositions, increasing segregation time, and thus the precipitation kinetics. However, it also is shown in Table 5.9 to increase the precipitate size, and the degree of coarsening in this component. Coarsening is not beneficial for either the embrittlement of the alloy, or for cracking susceptibility as thick, continuous interdendritic precipitates both increase interdendritic embrittlement, and are more likely to propagate a crack. However, the increase in precipitate size is not that substantial taking into consideration that the static cast component is in a non-equilibrium state, and may still encounter precipitate coarsening. It is assumed that the benefits from homogenizing, and decreasing the precipitation kinetics are still more beneficial than the negative effects from increased coarsening.

A study of precipitate size variation through the thickness of both components was not performed to see if the centrifugal cast precipitates are only coarser in certain sections. In Table 5.7 the dendrite sizes of the centrifugally cast and the static cast component are all within error of each other, becoming finer when traversing from the inner wall to the outer wall. The largest difference in dendrite size is observed in the 3” thick centrifugal casting, having the highest boundary area for precipitation, and thus the least amount of coarsening. In the middle and outer wall sections of the 1” thick castings the centrifugally cast component has slightly more boundary area, however the inner wall section of the static cast component has more boundary area for nucleation. These results are slightly contradictory of the grain size measurements, where the static cast component had much finer grain sizes, than the centrifugally cast component.

The intradendritic G-phase precipitates observed in the centrifugally cast component are viewed to be beneficial to the microstructure, as they are only $\sim 1\mu$m in size. Micron diameter G-phase precipitates are presumed to be small enough to avoid liquation cracking problems, and will restrict the amount of interdendritic G-phase coarsening that can occur. From the 20/25Nb TTP curves drawn by Powell *et al.* [11] Intradendritic G-phase transformation only occurs years into service, where they will exist as intradendritic Nb(C,N) precipitates up until this point. Intradendritic Nb(C,N) will greatly increase the creep rupture strength of the alloy, and produce more homogeneous properties throughout the casting.

5.6.4 Z-Phase

Z-phase which has previously been uncharacterized in 2032Nb stainless steels has strong evidence from XRD, AES, and EDS supporting its existence in the ex-service 2032Nb alloy. In Fig. 5.8, the strong segregation of nitrogen overlapping with chromium at the center of coarsened G-phase lends to a possibility of Z-phase precipitating off of Nb(C,N) during aging, and then consuming the Nb(C,N) during subsequent growth. Z-phase precipitates off of an existing NbC interface, which has been previously documented by Danielsen and Hald [10] as being the preferred nucleation site for Z-phase due to the semi-coherent interface of Nb(C,N), reducing the interfacial energy needed for nucleation. Z-phase will further grow and coarsen by consuming the existing Nb(C,N) precipitate. Z-phase nucleation also seems to be dependent on the diffusional distance of chromium, where most Z-phase precipitates were observed to be adjacent to or within the vicinity of $M_{23}C_6$ particles.

The difficulty in viewing Z-phase in SEM, and EPMA compared to AES lies in the electron emission types used for these microscopy techniques. The interaction volume of Auger electrons (~ 5 nm) is much smaller than backscattered electrons ($\sim 1\ \mu m$). Z-phase consists of one third chromium so there should be a noticeable difference in contrast from G-phase; however, from Fig. 5.5 the contrast difference is barely discernible even when the instrument contrast is overshot. If the morphology of Z-phase is a thin plate it could be possible for the interaction volume of the excited electrons to overlap considerably with G-phase. Interaction volume overlap might cause the contrast in Z-phase to be overshadowed, and to blend in with the surrounding G-phase if the instrument contrast is too low. The interaction volume of characteristic x-rays is larger than backscattered electrons so if the Z-phase regions in Fig. 5.5 are examined under EDS according to the presented hypothesis, the composition gathered by EDS should contain large amounts of G-phase constituents. However the Z-phase composition in Table 5.1 does not show a considerable increases in nickel or silicon when compared to the AES measurements in Table 5.3.

5.7 Precipitation Sequence

This next section will evaluate and compare the microstructural evolution of the solution annealed static cast and centrifugally cast components, as well as the button melted component representing the as-cast microstructure. At logarithmic time increments sectioned samples were removed from the aging furnace and analyzed using SEM, EPMA, and AES characterization methods to determine the area fraction, and precipitate sizes of the alloys microconstituents. The area fractions can be used to determine the driving force of a phase, as well as the precipitation, coarsening, and dissolution rates of precipitates. The precipitate size evolution can contrast the area fraction analysis in providing details into whether the microconstituents are primarily undergoing precipitation or coarsening, and if larger residual Nb(C,N) precipitates are coarsening from the dissolution of the smaller Nb(C,N) or simply transforming directly into other intermetallic phases. Although this study does not consider the mechanical properties, or the hot cracking mechanisms (ie. ductility-dip cracking, or liquation cracking), the works of Nishimoto *et al.* [45], Shi and Lippold [42] and others show that the microstructural evolution is directly related to creep life, and cracking susceptibility.

5.7.1 Solution Annealed Aging

5.7.1.1 Centrifugally Cast

The precipitation sequence and area fraction calculations for the solution annealed centrifugally cast component are presented in Fig. 5.14, where area fraction measurements were fitted with forms of the logistic function or *tanh* function using non-linear regression. The onset of primary Nb(C,N) dissolution around 2 weeks aging time consequently initiates the precipitation of $M_{23}C_6$ as carbon is reintroduced back into solution. Prior studies involving precipitation kinetics of austenitic stainless steels attribute the dissolution of primary Nb(C,N) to the supersaturation of silicon at the dendrite boundary during aging [26, 30]. The high silicon concentration around the Nb(C,N) causes the chemical potential of the carbon and nitrogen constituents to rise significantly promoting the instability of Nb(C,N) in these regions. During the dissolution of Nb(C,N) the composition is shown in Table A.5 to be uniform, where no uptake in nitrogen or decrease in carbon solubility is observed.

Powell *et al.* [11] claims that $M_{23}C_6$ precipitation will only be favorable during the initial stages of the Nb(C,N) to G-phase transformation, where any increases in phase fraction of $M_{23}C_6$ after this point will be exclusively from coarsening. The precipitate size of $M_{23}C_6$ during aging is graphed in Fig. 5.15, and is seen coarsen a great deal after 8 months even though the area fraction of the phase is stunted. If the hypothesis of Powell *et al.* [11] is correct it can be estimated that $M_{23}C_6$ precipitation only occurs within the first few weeks of aging.

Between the two week and one month mark, G-phase will precipitate in the centrifugally cast component. In Fig. 5.14 G-phase undergoes a drastic precipitation rate where around 1 vol% of interdendritic G-phase precipitates within a 2 week period. Most of the precipitation of G-phase occurs within the first year of aging attaining nearly 2.0 vol% of the alloy and a precipitate diameter of almost $4\mu m$, where after 16 years its volume fraction only increases 2.5 vol%, and its effective diameter remains at $4\mu m$. By the 1 year mark most of the G-phase has agglomerated producing a core/rim structure around the residual Nb(C,N). Although, even after 16 years Nb(C,N) remains in the microstructure, its percentage of the total microstructure approaches zero. During aging the interdendritic Nb(C,N) precipitates are seen to increase slightly in size suggesting the absorption of some of the smaller Nb(C,N) precipitates during the Nb(C,N) to G-phase transformation.

In between the two to four month aging times the intradendritic Nb(C,N) precipitates also undergo a transformation into G-phase. After the initial precipitation of $M_{23}C_6$ the volume fraction of intradendritic Nb(C,N) is seen to increase slightly which is reported to recover some of the alloys hot ductility lost from $M_{23}C_6$ and G-phase precipitation [47]. The intradendritic G-phase precipitates eventually grow to the size of the interdendritic Nb(C,N) coarsening between two months and one year.

While Z-phase phase fraction and precipitate size was not calculated, as Z-phase was not visible in SEM, or EPMA; AES identified Z-phase to precipitate between 4-8 months. A delay in Z-phase precipitation could be due to the solubility of chromium in G-phase during its initial precipitation and coarsening stages, seen in Table A.7 at the two week to one month mark. The AES micrographs in Fig. A.14 show a darker contrast for the G-phase precipitates after two weeks, and one month of aging because of this increased chromium solubility. It was not checked with XRD as to whether these dark precipitates were indeed G-phase or perhaps an intermediary phase such as η-phase.

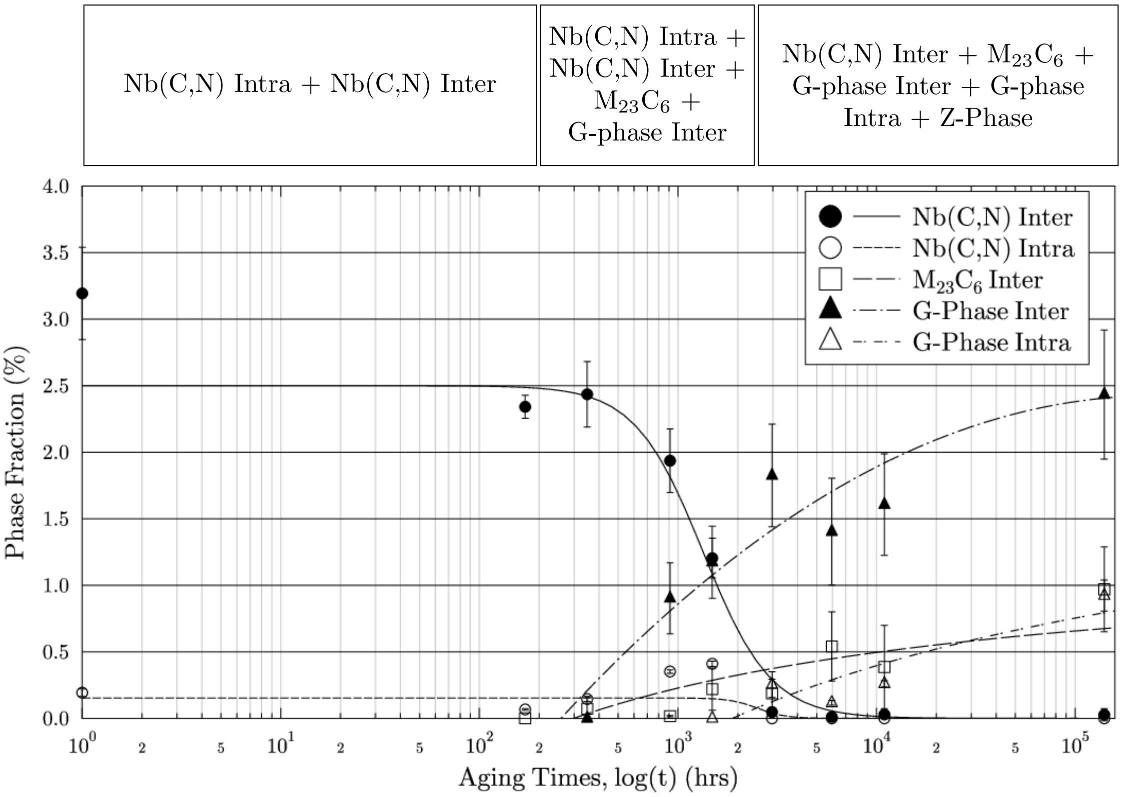

Figure 5.14: Volume fractions calculated from the centrifugally cast component with EPMA element mapping after logarithmic time increments. Non-linear regression fitting was applied to each phase, where intradendritic (intra), and interdendritic (inter) regions are distinguished.

5.7.1.2 Static Cast

The volume fraction of primary Nb(C,N) in the static cast component is calculated to be $\sim 0.25vol\%$ higher than the centrifugally cast component, while maintaining an equal size. The Nb/(C+N) ratio is lower for the static cast component and closer to its stoichiometric value 7.7, where its predicted by Keown and Pickering [13] that Nb(C,N) precipitation is maximized when Nb/(C+N) = 7.7. Once G-phase begins to precipitate and coarsen, the residual interdendritic Nb(C,N) begins to coarsen drastically, peaking at 8 months, $0.25\mu m$ coarser than in the centrifugally cast component. The dissolution rate of

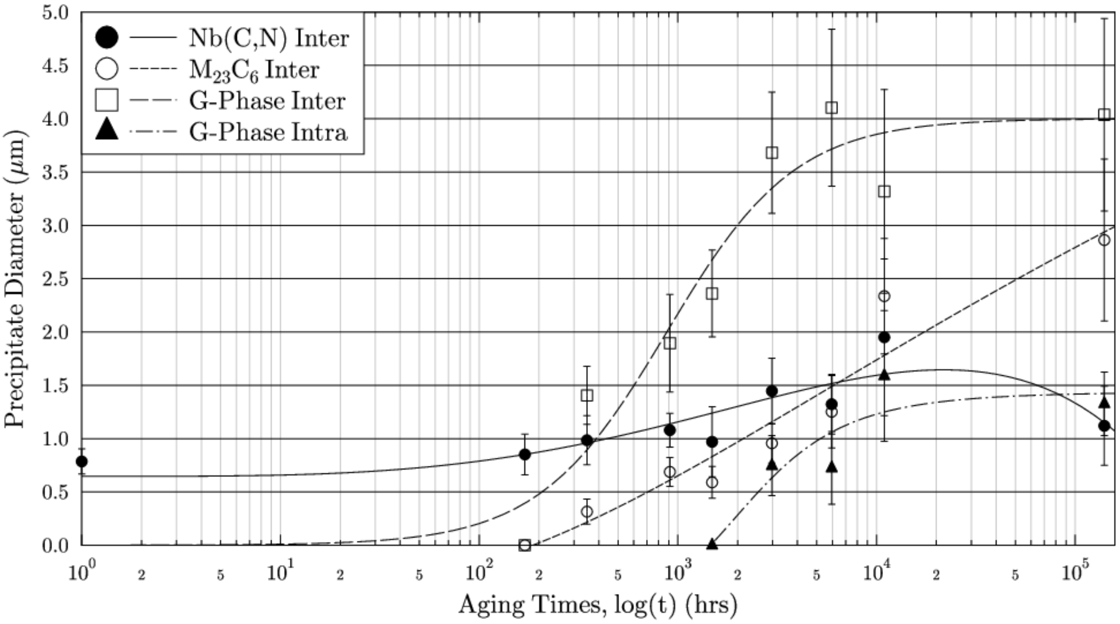

Figure 5.15: Effective diameters of precipitates calculated from the centrifugally cast component after incremental aging times. Non-linear regression fitting was applied to each phase.

Nb(C,N) is also faster in the static cast component evident from the steeper slope of the regression curve. Intradendritic Nb(C,N) evolution is almost equivalent between the two solution annealed components.

$M_{23}C_6$ precipitation occurs earlier in the static cast component visible after one week of aging compared to 1-2 weeks in the centrifugally cast component. Over 50% more $M_{23}C_6$ is calculated to compose the microstructure of the static cast component, however the growth rate of these precipitates will be lower than the centrifugally cast component. In both components, the $M_{23}C_6$ coarsening rate is observed to increase after the precipitation of intradendritic G-phase, which is not emphasized by the regression curves.

Approximately the same amount of interdendritic G-phase will precipitate during the microstructural evolution of the static cast component, even though the precipitation rate of G-phase will be faster than the centrifugally cast component. The large increase in $M_{23}C_6$ and minor decrease in G-phase fractions suggests that decreasing niobium content from 1.17wt% to 1.08wt% has a much more significant effect on promoting $M_{23}C_6$ precipitation than suppressing G-phase precipitation. Intradendritic G-phase evolution was also seen to be comparable to the centrifugally cast component, however the precipitates were measured to be finer overall.

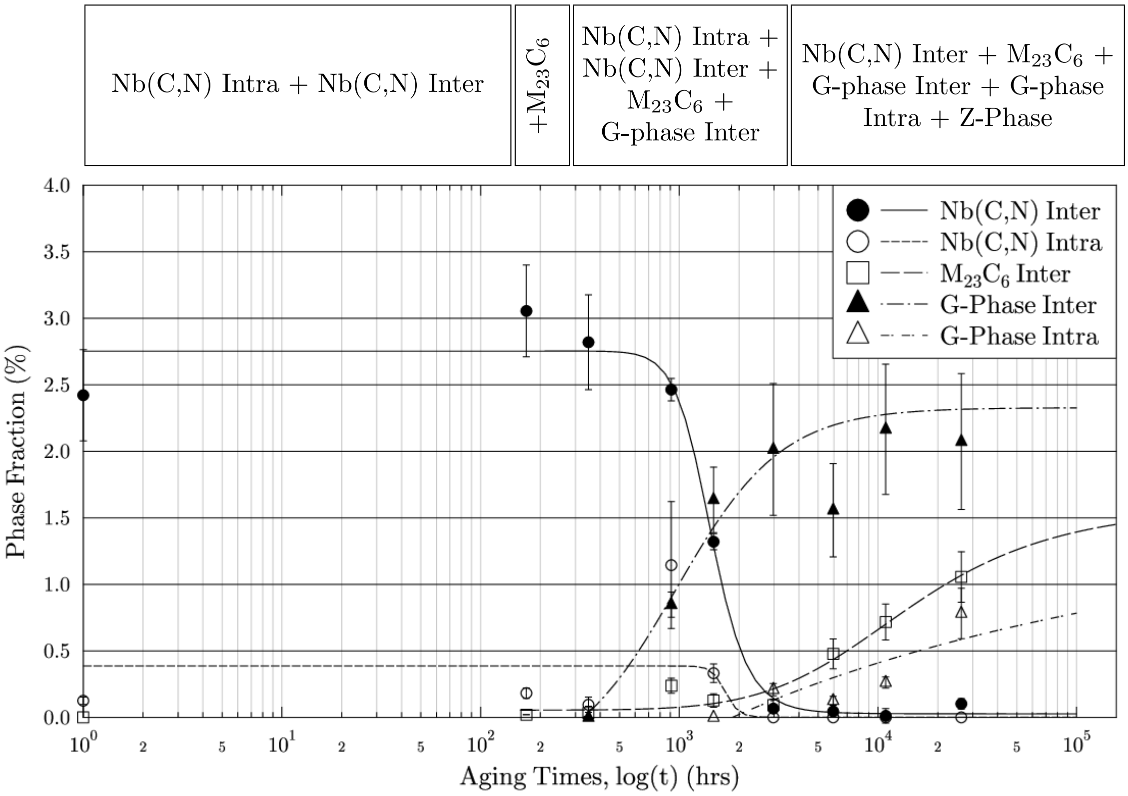

Figure 5.16: Volume fractions calculated from the static cast component with EPMA element mapping after logarithmic time increments. Non-linear regression fitting was applied to each phase, where intradendritic (intra), and interdendritic (inter) regions are distinguished.

5.7.1.3 Discussion

An illustration of the overall precipitation sequence for the solution annealed 2032Nb alloy is presented in Table 5.13. The silicon and chromium distribution after heat treatment is assumed to be the rate determining step in the transformation of Nb(C,N) to G-phase. The nearly equivalent dendrite cell sizes between the two components makes it difficult to determine which has the longer diffusional distances for silicon and chromium to diffuse to the interdendritic boundaries. For the central and outer wall regions of the casting the static cast component should have a slightly longer diffusional distance, however the opposite would true for the inner wall region. Although the static cast precipitation of G-phase is slightly delayed compared to the centrifugally cast component, precipitation of $M_{23}C_6$ is also premature in the static cast alloy. The centrifugally cast component is seen to have a larger fraction of finer $M_{23}C_6$ precipitates during the nucleation of G-phase. $M_{23}C_6$ is reported as being the primary nucleation site for G-phase which could explain the simultaneous precipitation of $M_{23}C_6$ and G-phase in the centrifu-

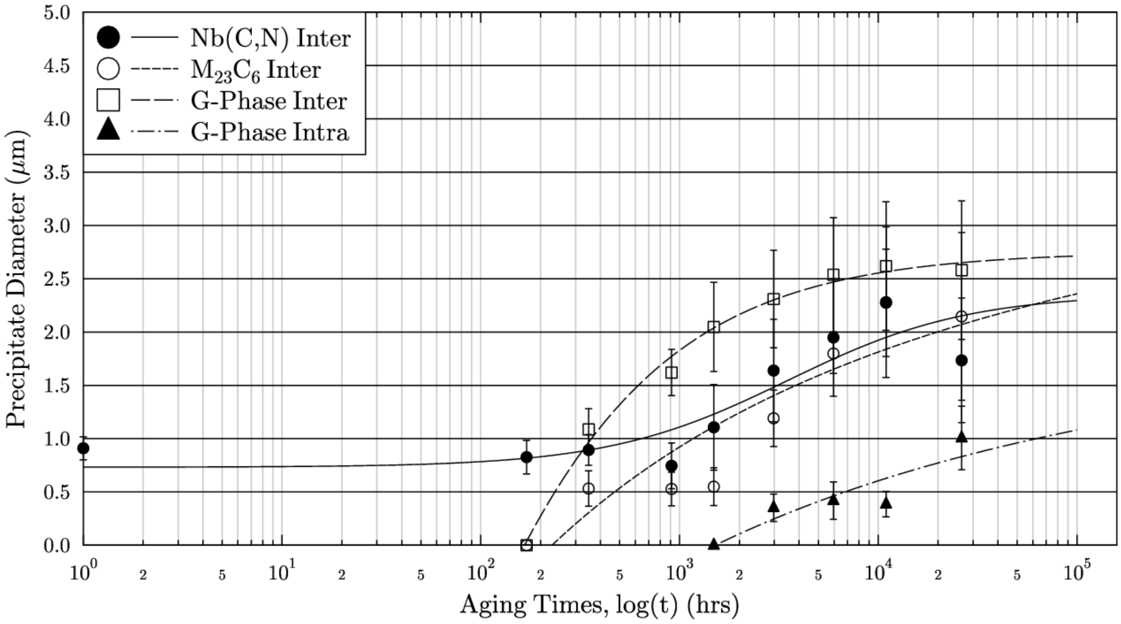

Figure 5.17: Effective diameters of precipitates calculated from the static cast component after incremental aging times. Non-linear regression fitting was applied to each phase.

gally cast component, and delayed G-phase precipitation in the static cast component [11]. It is unclear whether it is possible for G-phase to nucleate off of Nb(C,N), or if a $M_{23}C_6$ interface needs to be present for this to be favorable. For the longer aging times of 1 month and 2 months G-phase precipitates in Fig. A.14 not adjacent to $M_{23}C_6$ may have nucleated off of small $M_{23}C_6$ precipitates which then were dissolved during coarsening.

The nucleation mechanism for Z-phase has been studied extensively in 9%-12% chromium martensitic steels by Danielsen, and Hald [10]. It is widely recognized that MX (Nb(C,N)) precipitates are the predominant nucleation site for Z-phase because of the semi-coherent relationship between these two precipitates, and their similar constituents (i.e. Nb, and N) [10]. Z-phase will continue to grow at the expense of Nb(C,N) similar to the coarsening of G-phase [68]. The transformation mechanism of Nb(C,N) to Z-phase can be characterized by the diffusion of chromium into the MX precipitates, and the subsequent rejection of carbon by Nb(C,N). In most cases Z-phase is seen to compromise creep strength, as it is able to coarsen quite significantly.

The eventual coarsening of the interdendritic microstructure is predicted to embrittle the alloy, and decrease its hot ductility [47]. Replacing G-phase with Z-phase may not decrease the ductility dip cracking in the alloy, but could make the alloy more resistant to liquation cracking. The overall melting point of Z-phase is calculated by ThermoCalc to be 1808°C for Z-phase, versus 1323°C, and 1382°C respectively for G-phase and the austenite matrix. The high melting point of Z-phase leads to the assumption that Z-phase will not experience liquation cracking during repair welding. However, constitutional liquation still might occur in the reaction zone between Z-phase as the austenite matrix. ThermoCalc shows no eutectics between Z-phase and austenite in any of the analyzed isoplethal sections, which dismisses the possibility of constitutional liquation, although this was not determined experimentally. The co-precipitation of Z-phase raises an important issue in regards to the relationship between G-phase and Z-phase. Z-phase appears to be stable in the presence of G-phase even though it is in direct competition with G-phase for niobium.

5.7.2 Cast Alloy

Fig. 5.18, and Fig. 5.19 show the area fractions, and the precipitate sizes for the as-cast microstructure during incremental aging times. The button melted component was only measured up to 4 month aging, where any long term aging effects greater than this period can only be speculated. Primary Nb(C,N) fractions are initially higher, and somewhat finer than both the solution annealed components, where resolidifying the alloy will precipitate more Nb(C,N) than solution annealing. However, the as-cast microstructure does not contain any intradendritic Nb(C,N) which may not be as beneficial during long term aging. After one week of aging the Nb(C,N) fraction is seen to decrease by almost 1vol% where the initial precipitation of $M_{23}C_6$ and G-phase is shown to occur around this time as well. There are also no observed chromium rich intradendritic species, which have all dissolved during this period. After 2 weeks of aging the interdendritic G-phase fraction has increased greatly and calculated to be around 1.5vol%. Interdendritic G-phase was only seen after 1 month of aging in the solution annealed components. The precipitation and coarsening rates of $M_{23}C_6$ are much lower than G-phase, although the $M_{23}C_6$ fraction is still higher in the cast component compared to the solution annealed components. Rapid Nb(C,N) dissolution is shown to occur after 1 month of aging, however the Nb(C,N) fraction at 1 month may be an outlier since a very high fraction of G-phase has already precipitated by this time. Z-phase precipitation is also observed after 1 month of aging, and coincides with the dissolution of the Nb(C,N) phase. At the 2 month mark almost all of the Nb(C,N) has been transformed into interdendritic G-phase, where any intradendritic compounds are still vacant in the microstructure. After 4 months of aging the microstructure remains the same with a limited amount of coarsening of the microconstituents. After 4 months of aging it is presumed that intradendritic Nb(C,N), or intradendritic G-phase will precipitate as observed in the ex-service components.

The lack of intradendritic species is the major difference between the as-cast and the solution annealed components. G-phase and $M_{23}C_6$ are also seen to precipitate much earlier than the solution annealed counterparts, which should be expected due to the silicon segregation maps shown in Fig. 5.13. Z-phase precipitation is also premature in the cast component occurring between 1-2 months of aging compared to the 4-8 months seen in the solution annealed component. Overall, the as cast component contains accelerated precipitation kinetics compared to the solution annealed components, however after one year of aging the cast component may be nearing an equilibrium state where there are only minimal variations in the microstructure.

Table 5.13: Precipitation sequence for a 2032Nb stainless steel alloy at 800°C after solution annealing for 1 hour at 1200°C.

Aging Time	Schematic	Precipitate Characterization	Precipitate Size	Relative Phase Fractions (Vol%)
Solution Annealed	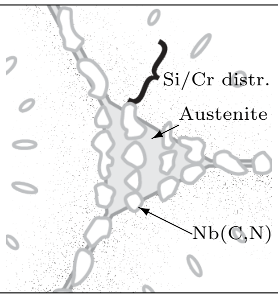	• Nb(C,N) : Globular shaped with a lamellar distribution at the dendrite boundaries. • Intragranular Nb(C,N) outside of the Si concentrated matrix. Orientation relationship with γ-Fe. • Si & Cr concentration is nearly homogeneous throughout.	Nb(C,N) : $0.79 \pm 0.23 \mu m$ $(n = 58)$	$\mathrm{Nb(C,N)}_{\mathrm{inter}}$ $< 3.5\%$ $\mathrm{Nb(C,N)}_{\mathrm{intra}}$ $< 0.2\%$
Onset of G-phase Nucleation	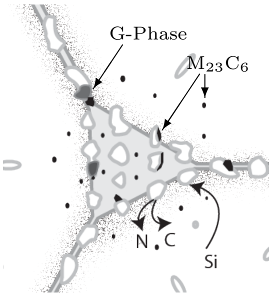	• Nb(C,N) : Dissolution of primary carbides. C & N super-saturate surrounding γ-Fe. No increase in nitrogen concentration of the primary carbides. • $M_{23}C_6$: Blocky, and acicular carbides nucleating along the Nb(C,N)/γ-Fe interface. Small, elliptical carbides throughout matrix. • G-Phase : Small, irregular shaped. Precipitate at $M_{23}C_6$/Nb(C,N) interface. • Si & Cr is concentrated at the dendrite boundaries.	Nb(C,N) : $0.98 \pm 0.46 \mu m$ $(n = 208)$ $M_{23}C_6$: $0.32 \pm 0.24 \mu m$ $(n = 84)$ G-Phase : $1.41 \pm 0.55 \mu m$ $(n = 54)$	$\mathrm{Nb(C,N)}_{\mathrm{inter}}$ $< 2.5\%$ $\mathrm{Nb(C,N)}_{\mathrm{intra}}$ $< 0.3\%$ $M_{23}C_6$ $< 0.05\%$
Onset of Z-phase Nucleation	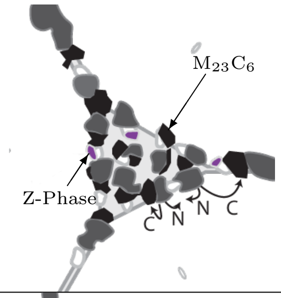	• $M_{23}C_6$: Small secondary precipitates are dissolved and absorbed by larger carbides. Nucleation & coarsening of large heterogeneous secondary carbides. • G-Phase : Globular, and irregular in shape. Increased nucleation & coarsening rates observed. • Z-Phase : Nucleates along surviving Nb(C,N) interfaces, adjacent to or within the vicinity of $M_{23}C_6$ carbides (high local chromium concentration).	Nb(C,N) : $1.32 \pm 0.56 \mu m$ $(n = 13)$ $M_{23}C_6$: $1.25 \pm 0.68 \mu m$ $(n = 280)$ G-Phase : $3.32 \pm 1.91 \mu m$ $(n = 267)$	$\mathrm{Nb(C,N)}_{\mathrm{inter}}$ $< 0.05\%$ $M_{23}C_6$ $< 0.5\%$ $\text{G-Phase}_{\mathrm{inter}}$ $< 2.0\%$ $\text{G-Phase}_{\mathrm{intra}}$ $< 0.2\%$
Fully Aged	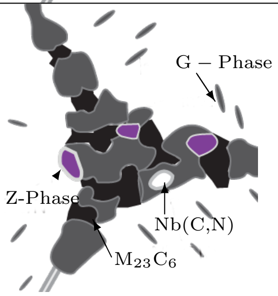	• Z-Phase : Surrounded by G-Phase. Appears to the stable in the presence of G-phase. • $M_{23}C_6$: Large, intergranular precipitates dispersed between G-phase. Some $M_{23}C_6$ have agglomerated. • G-Phase : Almost all Nb(C,N) has transformed to G-phase. G-phase has coarsened, and precipitates have agglomerated. Cubodial, intragranular G-phase decorates the microstructure.	Z-Phase : $1.04 \pm 0.53 \mu m$ $(n = 17)$ $M_{23}C_6$: $1.42 \pm 1.10 \mu m$ $(n = 60)$ G-Phase : $1.63 \pm 0.75 \mu m$ $(n = 69)$	Z-Phase $< 0.1\%$ $M_{23}C_6$ $< 1.5\%$ $\text{G-Phase}_{\mathrm{inter}}$ $< 3.0\%$ $\text{G-Phase}_{\mathrm{intra}}$ $< 1.0\%$

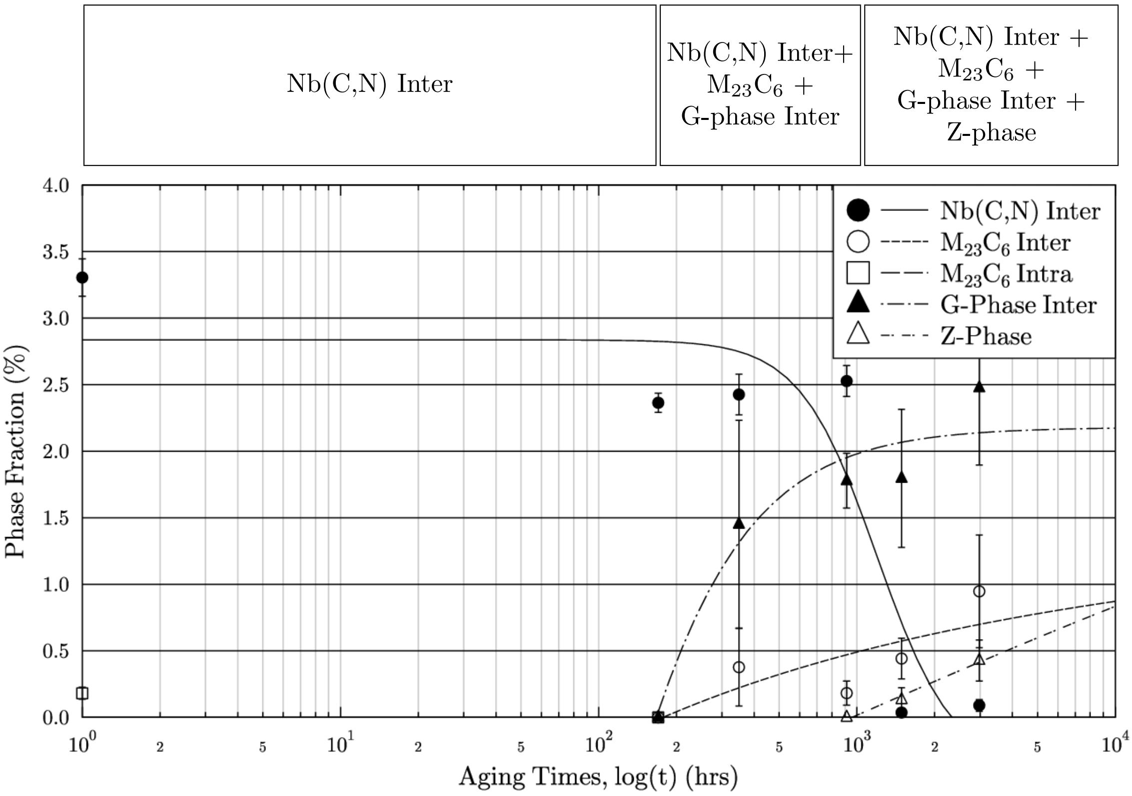

Figure 5.18: Volume fractions calculated from the button melted ex-service component with EPMA element mapping after logarithmic time increments. Non-linear regression fitting was applied to each phase.

5.8 Conclusions

The centrifugally cast 20Cr32Ni-Nb component used in service for 16 years was characterized and showed significant proportions of intradendritic, and interdendritic G-phase as well as $M_{23}C_6$. Some residual Nb(C,N) was also observed, and upon further investigation in AES, a significant amount of Z-phase was discovered. EDS, WDS, and AES chemistry quantification methods were compared, where AES proved to have the most accurate quantification; although, this method is surface sensitive, and does not represent the bulk of the analyzed precipitate. Difficulty in observing Z-phase with SEM, and EPMA, and Nb(C,N) with AES spectroscopy techniques was assumed to be because of the size and morphology of these precipitates, however this is inconclusive. G-phase, $M_{23}C_6$, and Z-phase microconstituents were confirmed with XRD during electrolytic extraction techniques, while the signal for the proposed Nb(C,N) phase was too weak to be validated with any certainty. Phase fractions of the microconstituents were calculated using elemental mapping techniques, and were tested against equilibrium phase fractions

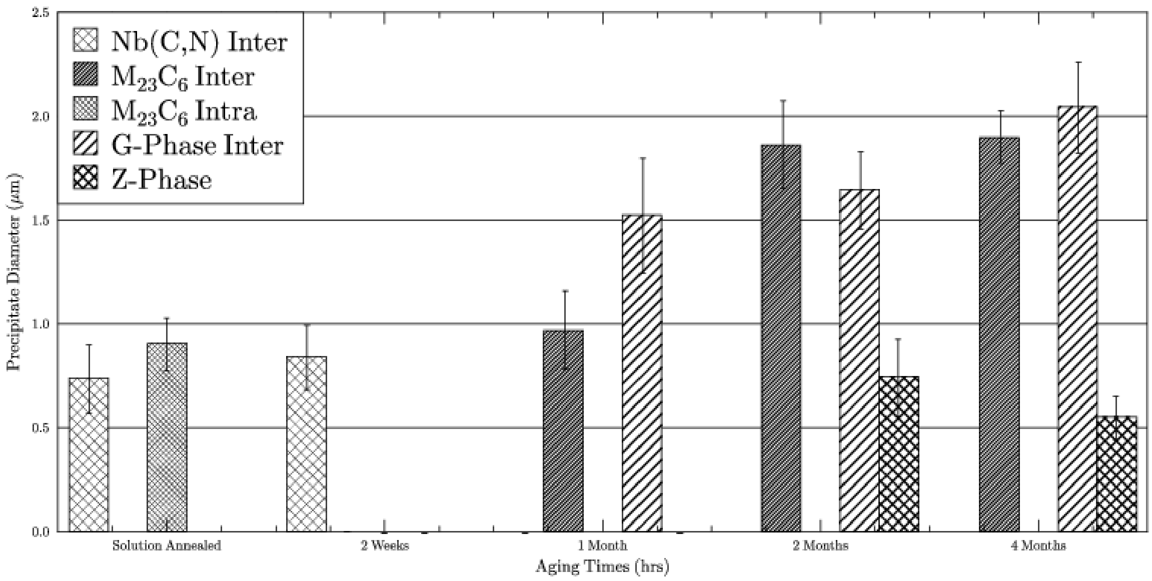

Figure 5.19: Effective diameters of precipitates calculated from button melted ex-service components after incremental aging times.

predicted by ThermoCalc. Although the predicted G-phase fractions from ThermoCalc were within a 1 vol% error from the calculated values, the $M_{23}C_6$, and Z-phase fractions were overestimated due to using a nickel database instead of an iron database as G-phase is only available in the nickel database.

The 3" centrifugal casting is seen to have the coarsest grains in the outer wall and middle cross-sections; however, the inner wall has grains comparable to the middle and outer wall sections of the 1" static cast tee. This is hypothesized to be due to centripetal forces acting on the centrifugal casting during solidification. Dendrite cell sizes did not differ significantly between the 1" and 3" centrifugal casting, and the 1" static casting, where the standard deviations for all measurements coincided with one another. The calculated means of the dendrite cell sizes showed the dendrites in the 3" centrifugal casting were finer than the 1" centrifugal casting, and that the dendrites in the 1" static casting were coarser than the 1" centrifugal casting except for the at the inner wall. Dendrite cell size was observed to decrease from the inner wall to the outer wall for all castings. Embrittlement due to G-phase and interdendritic $M_{23}C_6$ was higher in the centrifugally cast component, and more pronounced in the outer wall regions for both components. The center regions of both components were the softest, where hardness increased nearly linearly in the inner wall region up until the inner wall. This relationship was reiterated in the phase fraction calculations where both G-phase and $M_{23}C_6$ fractions were lower in the center of both castings.

The phase fraction calculations for both the ex-service components showed that a significant portion of residual Nb(C,N) exists in the static cast component, while nearly none exists in the centrifugally cast component. The static cast component was solution annealed and only in service for another four year, so it is presumed that it will undergo more precipitation and coarsening, and more residual Nb(C,N) will be transformed in the G-phase. A lower $M_{23}C_6$ fraction, and a higher G-phase, and Z-phase fraction are observed in the centrifugally cast component. The centrifugal cast component shows a slightly higher degree of precipitate coarsening in the ex-service state which will embrittle the steel, and creates a higher susceptibility to cracking. The homogenized element distributions in the solution annealed centrifugally cast component promotes intradendritic Nb(C,N) precipitation which will later transform into G-phase. Since these precipitates are approximately only one micron in diameter they are assumed to not contribute to the cracking susceptibility of the steel.

The microstructural evolution of the solution annealed centrifugally cast, and static cast alloys were plotted at various time increments up to a year, and regression fitting to non-linear curves. NbC to G-phase transformation occurred slower in the centrifugally cast alloy, however, a higher inter- and intra-G-phase fraction resulted. $M_{23}C_6$ precipitation was retarded slightly in the centrifugally cast component, as was the transformation of intradendritic Nb(C,N) to intradendritic G-phase. Coarsening is much more pronounced for G-phase and $M_{23}C_6$ in the solution annealed centrifugal cast component than the static cast component. Nb(C,N) in the static cast component undergoes much more coarsening than the in the centrifugal cast component, nearly doubling in size. Coarsening rates are also a lot slower in the static cast component especially for intradendritic G-phase.

The button melted alloy contained an initial high amount of primary Nb(C,N), and also had accelerated precipitation kinetics for $M_{23}C_6$, G-phase and Z-phase compared with the solution annealed components. This is primarily due to solidification mechanics (ie. undercooling, segregation), and solute enrichment of the interdendritic zones during solidification. The dissolution rate of Nb(C,N) was the highest in the as-cast component, where the regression curve for G-phase predicts a similar equilibrium phase fraction as compared with the solution annealed static cast component. The coarsening rates are lower in the as-cast state than in the solution annealed state, however after aging the as-cast component for four months the precipitate sizes of G-phase and $M_{23}C_6$ were comparable.

The centrifugally cast component is beneficial for decreasing the precipitation kinetics of secondary embrittling carbides, due to the homogenization of the alloy additions in the austenite. However, These secondary precipitates will coarsen more severely in the centrifugally cast alloy increasing embrittlement, and cracking susceptibility. Homogenization of the component before being put in service is always beneficial irrespective of the casting conditions, as it also decreases the precipitation kinetics, and transformation rate of G-phase.

Chapter 6

Modified 2032Nb Experimental Matrix Results & Discussion

6.1 Introduction

This chapter will investigate the design matrix of modified castings proposed in Table 4.2, looking at a commercial, and modified 2032Nb alloy, 1" and a 3" wall thickness, and homogenized versus non-homogenized alloys. Each samples microstructure will be examined with SEM, and EDS, and the average dendrite cell size, phase fraction, and precipitate size will be reported. Each sample will be aged from its as-received state at $\sim$ 800°C for up to two months. The precipitation sequence for each treatment will be discussed, as well as its microstructural evolution. Finally each effect will be evaluated and ranked in terms of its benefit toward the creep rupture strength of the alloy, and it susceptibility to embrittlement, and cracking.

6.2 Sample Notation

The notation for labeling the samples is adopted from factorial design, where samples including the label *a* have a modified chemistry, and without have the commercial chemistry. Similarly the label *b* is given to samples with a 3" wall thickness, where without a *b* label have a 1" wall thickness. Samples with a *c* label are homogenized, and without are just left in the as-cast state. For example the treatment labeled (1) does not contain any letters so it has a commercial 2032Nb chemistry, a 1" wall thickness, and was not homogenized. On the other hand, the treatment *abc* contains all of the letters so it has a Super 2032Nb chemistry, a 3" wall thickness, and is homogenized. The treatment *bc* has a commercial chemistry with a 3" wall thickness, and was homogenized. In the body of this chapter anytime a specific sample is under discussion, its full parameters (i.e. chemistry, wall thickness, homogenization) will be designated in brackets beside its treatment label.

6.3 ThermoCalc Predictions

Figure 6.1 shows the Scheil solidification predicted by ThermoCalc of the two modified chemistries in Table 4.3. The Super MetalTek 2032Nb alloy contains a small concentration of microalloying elements such as titanium which are observed to precipitate out a fraction of TiC carbides between 1300-1260°C. The thermodynamic modeling of Scheil solidification predicts that 0.06 mol% of NbC, and 0.01mol% of TiC precipitate out of solution during solidification. Whereas for the commercial 2032Nb composition with no microalloyed elements only NbC, and $M_{23}C_6$ form consisting 0.04 mol% and 0.001 mol% of the microstructure respectively. The Nb/C ratios of the Super 2032Nb alloy and the commercial 2032Nb alloy are 7.6 and 5.3 respectively, where the commercial 2032Nb alloy is below the stoichiometric ratio of 7.7, promoting the formation of $M_{23}C_6$ carbides.

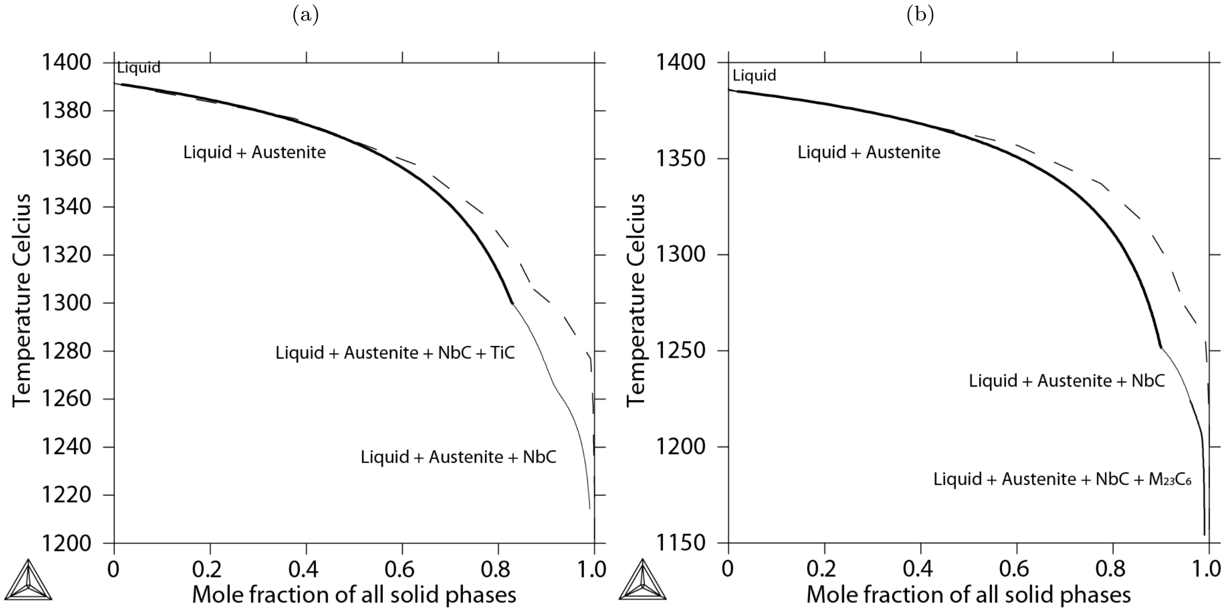

Figure 6.1: Scheil solidification predicted by ThermoCalc using the TCFE6 database for the a) Super 2032Nb alloy, and the b) commercial 2032Nb alloy. The dotted line represents equilibrium solidification.

The equilibrium microstructure for the two alloy chemistries is presented in Fig. 6.2, where the Super 2032Nb chemistry with the stoichiometric Nb/C ratio, and microalloy additions leads to a higher fraction of NbC, and TiC precipitation compared to the commercial 2032Nb chemistry. The stoichiometric Nb/C ratio of the super 2032Nb also impedes $M_{23}C_6$ stability, where the commercial 2032Nb chemistry contains excess carbon which precipitates out of solution into a large portions of $M_{23}C_6$. The titanium additions in the Super 2032Nb alloy allow for more niobium to be in solution to precipitate out of solution as G-phase, increasing its stability by about 100°C. The initial driving force for G-phase is small, exhibiting a plateau region leveling off once all of the excess niobium in solution has precipitated out as G-phase. When the equilibrium temperature is low enough for the transformation of NbC to G-phase to become favorable, the driving force for G-phase precipitation increases drastically.

G-phase stability is also suppressed in the Super 2032Nb alloy by around 50°C compared to the commercial alloy. Although a larger amount of G-phase can eventually precipitate if the temperature is low enough, G-phase may altogether be avoided if the operating temperature of the component is set above the G-phase stability temperature.

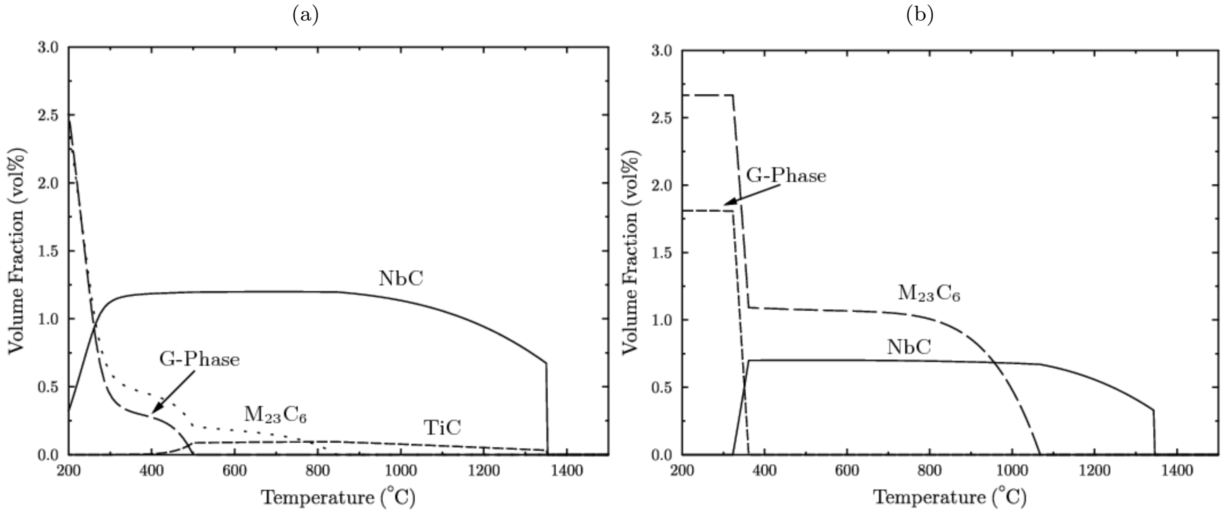

Figure 6.2: Equilibrium volume fractions predicted by Thermocalc using the TTNI8 database of the a) Super 2032Nb chemistry, and the b) commercial 2032Nb chemistry.

Figure 6.3 Shows the equilibrium fractions for the Super 2032Nb alloy without any titanium additions. With a Nb/C ratio of 7.6 no excess niobium exists in solution when titanium is absent from the alloy. This suppresses G-phase stability considerably by ∼ 50°C below that predicted for the commercial 2032Nb alloy. $M_{23}C_6$ precipitation and stability increases with the absence of titanium, however its concentration in the alloy is still lower than the commercial 2032Nb alloy.

6.4 Microstructure

The microstructure of the Super 2032Nb alloy and the commercial 2032Nb alloy differ greatly in terms of microconstituents, and their distribution throughout the microstructure. SEM micrographs in Fig. 6.4 show the microstructure of both alloys after one week of aging. The Super 2032Nb alloy contains coarse, globular interdendritic NbC dispersed throughout the entire interdendritic region. On a small fraction of

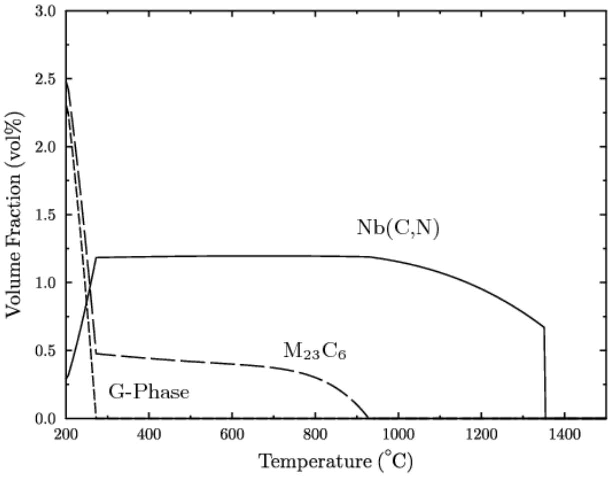

Figure 6.3: Equilibrium volume fractions predicted by ThermoCalc using the TTNI8 database of the MetalTek Super 2032Nb chemistry containing no titanium.

NbC carbides, submicron sized TiC carbides have precipitated at the interface of the interdendritic NbC carbides. The commercial 2032Nb alloy contains fine submicron sized primary NbC formed in clusters, heterogeneously distributed through the interdendritic region of the microstructure. The primary NbC form in a lamellar herringbone structure similar to the cast microstructure of the ex-service 2032Nb components in the previous chapter. Fine spherical intradendritic $M_{23}C_6$ precipitates are found surrounding the dendrite boundaries after one week of aging at 800°C, which were undetected in the unaged samples when examined by SEM. Depending on whether the component had undergone a homogenization heat treatment, the dispersion zone of intradendritic precipitates around the dendrite boundaries is much thicker, and penetrates much deeper into the dendrite.

The silicon distribution in the as-cast versus homogenized treatments is compared in Fig. 6.5 using EPMA element mapping. In the heat treated alloys no elemental segregation is evident, where the major components (ie. silicon, chromium, nickel) are distributed evenly throughout the component. A more homogeneous composition can promote the precipitation of a larger fraction of intradendritic secondary precipitates, which could be beneficial for the strength, creep life, and cracking resistance of the component. The as-cast silicon distribution is clearly segregated around the dendrite boundaries enriching these regions with solute that can promote the precipitation of secondary carbides and other intermetallic phases, particularly G-phase. The diffusional distances of ferrite stabilizers such as silicon and chromium are also significantly decreased in the as-cast alloy where precipitation and coarsening rates will be higher than the homogenized casting. The high silicon regions in the homogenized silicon map in Fig. 6.5b are just silicon inclusions, or artifacts from polishing with SiC.

After 2 months of aging the resulting microstructure of both the Super 2032Nb, and commercial 2032Nb alloys are shown in Fig. 6.6. In the Super 2032Nb components both intradendritic and interdendritic $M_{23}C_6$ have precipitated, while the interdendritic $M_{23}C_6$ have precipitated in regions along the den-

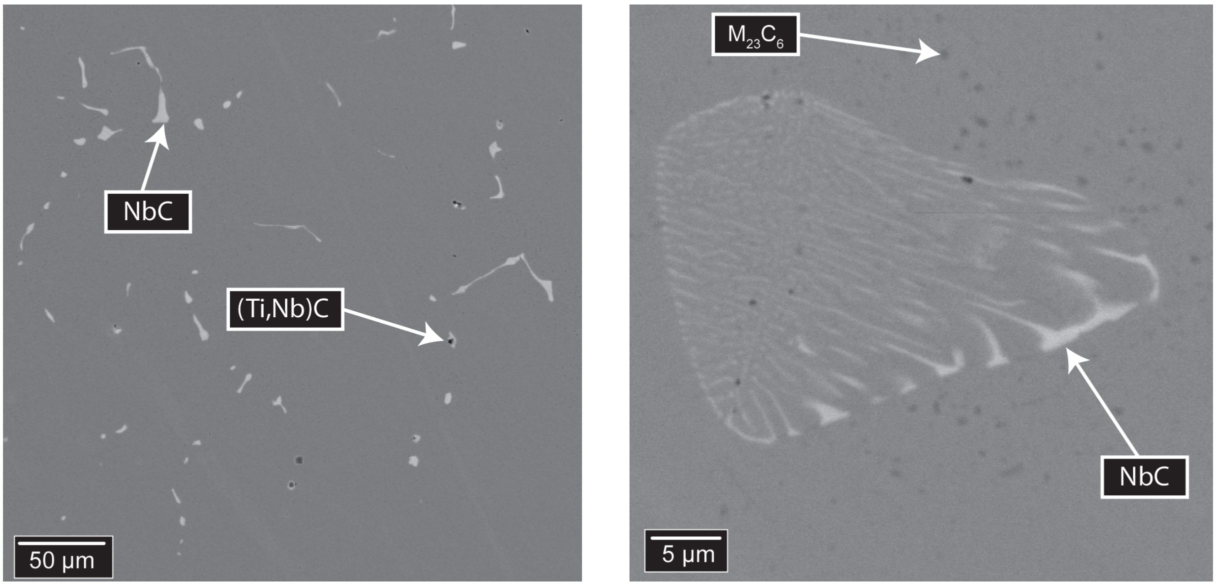

(a) (b)

Figure 6.4: Microstructure of the cast a) MetalTek Super 2032Nb chemistry, and b) Regular MetalTek 2032Nb chemistry after one week of aging.

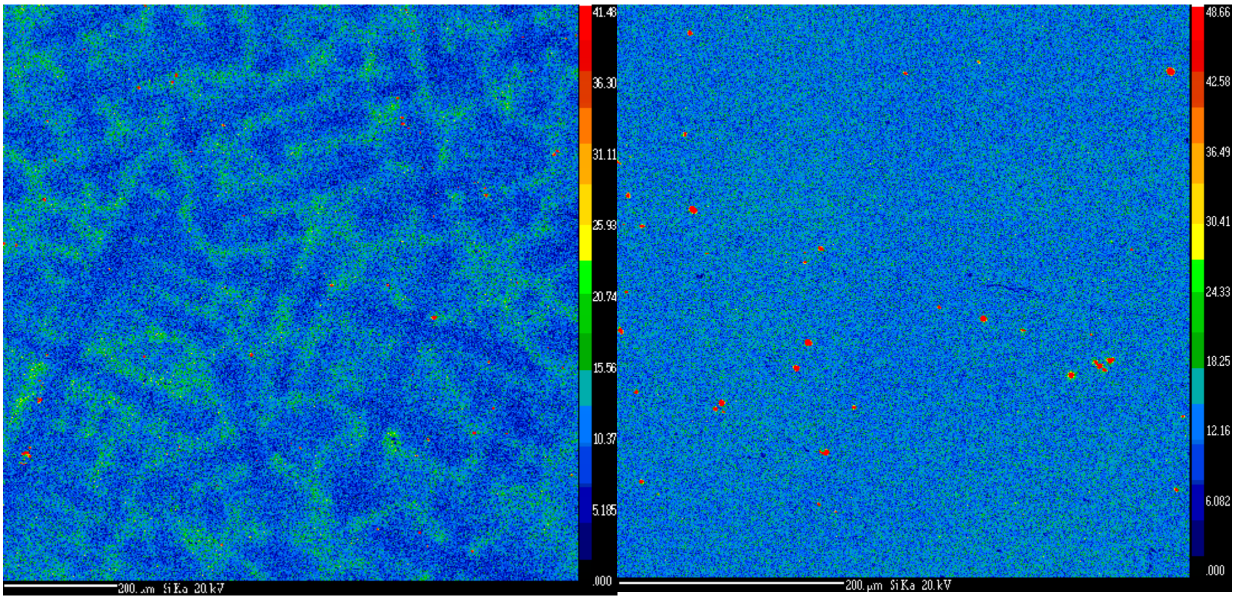

(a) (b)

Figure 6.5: Silicon segregation of an as-cast regular 1” thick Metaltek 2032Nb alloy a) not homogenized, and b) homogenized.

drite boundaries with minimal coarsening. The intradendritic $M_{23}C_6$ both have spherical and ellipical morphologies, occurring in a smaller number fraction than the commercial 2032Nb samples. The interdendritic NbC carbides have coarsened slightly after 2 months of aging and consist of a larger area than the cast components.

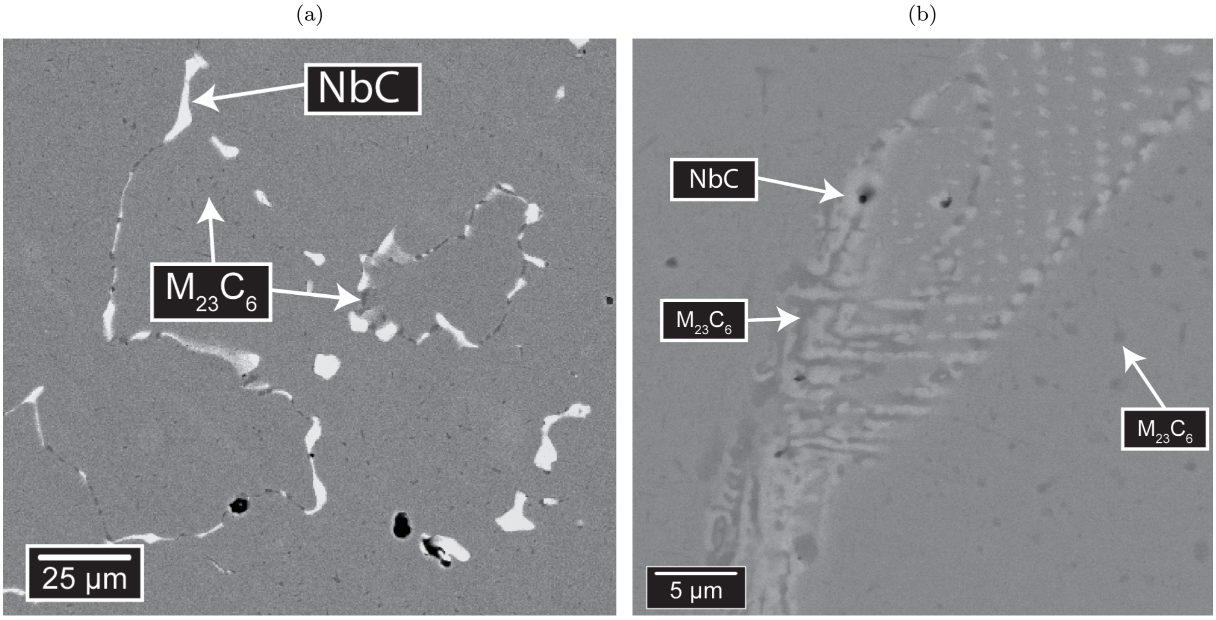

Figure 6.6: Microstructure after 2 months of aging at 800°C of the a) Super 2032Nb chemistry, and b) commercial 2032Nb chemistry.

The (Ti,Nb)C precipitates have also coarsened after 2 months and comprise an aggregated constitution with a dark spherical center encased in a polygonal (lighter contrast) phase as shown in Fig. 6.7. Similar TiC precipitates have been viewed by Piekarski [9] having a primarily titanium TiC core and a mixed (Ti,Nb)C polygonal rim. The (Ti,Nb)C cores in the present study were analyzed with EDS and showed an equal amount of titanium, niobium, and oxygen, tabulated in Table 6.1. However these values may not be accurate as the excitation spot size of the EDS may overlap with the surrounding phases, and the oxygen and carbon concentrations cannot be measured with any certainty due to EDS instrument limitations. Niobium concentration increases when moving further away from the TiC core and into the TiC rim phase. Some of the (Ti,Nb)C cores in the 1” castings such as in sample *a* (as-cast, 1” thick, Super 2032Nb) show a large solubility for zirconium, while some of the (Ti,Nb)C cores in the 3” castings such as treatment *ab* (as-cast, 3” Thick, Super 2032Nb), and *abc* (homogenized, 3” Thick, Super 2032Nb) show a small solubility for aluminum.

After two months of aging the commercial 2032Nb alloy it contains highly coarsened and agglomerated interdendritic $M_{23}C_6$ decorated between NbC carbides along the periphery of NbC clusters. Intradendritic $M_{23}C_6$ have also coarsened and exhibit both spherical morphologies, and needle-like morphologies, and display an orientation relationship similar to that in the ex-service components. It is hypothesized

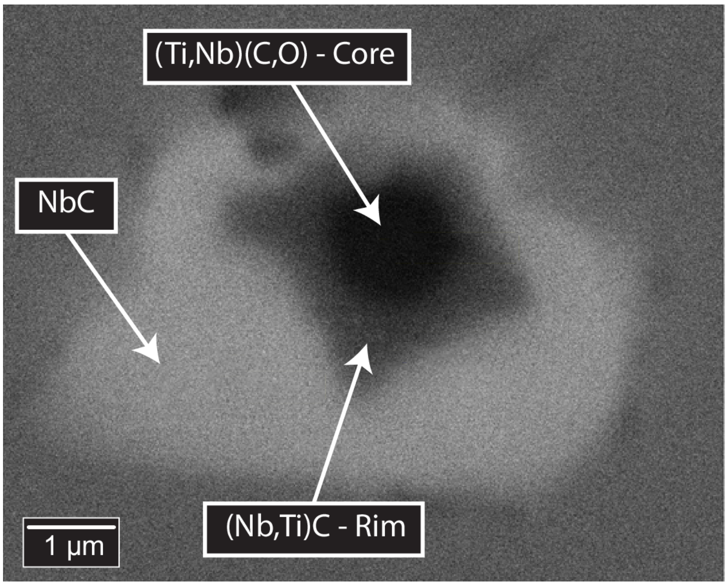

Figure 6.7: SEM micrograph taken at 20 KV of a aggregated carbide with equal concentrations of titanium and niobium at the spherical core, and a 2:1 ratio of niobium to titanium at the polygonal rim surrounded by globular NbC.

Table 6.1: Average EDS composition of the spherical core, and polygonal rim structure of the (Ti,Nb)C carbides.

	Composition (wt%)								
TiC Region	**Fe**	**Ti**	**Nb**	**C**	**O**	**Cr**	**Ni**	**Al**	**Zr**
Core	bal.	23.3 ± 9.2	22.2 ± 9.8	15.5 ± 6.2	21.3 ± 9.1	5.8 ± 2.3	2.5 ± 2.2	0.7 ± 0.8	2.5 ± 5.0
Rim	bal.	28.5 ± 9.4	40.7 ± 7.4	16.9 ± 3.0	-	5.9 ± 3.0	3.9 ± 1.9	-	-

that $M_{23}C_6$ has precipitated and coarsened on dislocations providing a mechanism for a needle-like morphology. The NbC are observed to have not coarsened or precipitated significantly during aging in the the commercial 2032Nb alloy. No G-phase has been observed in either of the alloys after 2 months of aging.

6.4.1 Dendrite cell size

The dendrite cell size for the unaged MetalTek samples was measured from multiple SEM micrographs and tabulated in Table 6.2. The coarsest dendrites were measured in the 3” Super 2032Nb samples, and the finest dendrites were measured in the 1” Super 2032Nb samples. In general the 1” thick castings have finer dendrites than the 3” thick castings. A larger variation in dendrites size is observed in the Super 2032Nb alloy compared to the commercial 2032Nb alloy where the dendrite sizes are within error of each other. Dendrite size between the as-cast and homogenized treatments do not vary by any significant amount, however are coarser in the homogenized samples of the 1” thick casting, and the as-cast samples of the 3” thick casting.

Table 6.2: Dendrite cell size of the cast design matrix in μm.

Composition (A)	**Section thickness (B)** **1” finished wall** **heat treatment (C)** **as-cast**	 **homogenized**	 **3” finished wall** **heat treatment (C)** **as-cast**	 **homogenized**
Commercial 2032Nb	82.5 ± 20.4 (n=123)	88.8 ± 19.5 (n=85)	94.7 ± 20.3 (n=87)	87.8 ± 20.7 (n=125)
Super 2032Nb	74.9 ± 20.6 (n=176)	76.2 ± 19.9 (n=167)	104.8 ± 24.8 (n=158)	93.3 ± 22.2 (n=140)

6.5 Precipitation Sequence

Analysis of the precipitation sequence, precipitation rates, and coarsening rates of the microstructure for each treatment in the factorial design will provide insight into the which factors (i.e. chemistry, heat treatments, casting thickness) are beneficial for long term service, and crack resistance for use in a hydrogen reformer manifold. In the previous section it was determined that after two months of aging none of the treatments displayed any intermetallic phase precipitation (i.e. G-phase) which has been identified as the major factor in the embrittlement, and cracking susceptibility of these alloys. However, analysis of carbide precipitation, coarsening, or dissolution can be used to rank each treatment, and used to propose which one will most likely have the most beneficial effects after long term aging.

Table 6.3 illustrates the precipitation sequence for each treatment from the as-cast condition to two months of aging. All of the Super 2032Nb alloys show the same microstructural evolution of primary NbC and TiC, where after one week secondary $M_{23}C_6$ particles begin precipitating. Interdendritic $M_{23}C_6$ carbides were not observed under SEM in the 3” thick Super2032Nb castings after two months of aging. The longer diffusional distances needed for chromium to segregate to the dendrite boundaries in these treatments may explain the delayed precipitation of interdendritic $M_{23}C_6$.

The commercial 2032Nb alloys precipitate $M_{23}C_6$ carbides after less than one week of aging, however only the as-cast 1” thick samples displayed interdendritic $M_{23}C_6$ precipitation. The homogenized 1” commercial 2032Nb sample showed very tiny submicron sized precipitates with a contrast comparable to the NbC carbides. The carbides were only resolved to be one to two pixels in area in the SEM micrographs, and were undetected in the EPMA element maps, therefore were neglected from area fraction, and size calculations as well as EDS analysis. Intradendritic NbC was also detected in the homogenized 3” inch thick commercial 2032Nb sample after 2 weeks of aging.

Area fractions for each phase resolved in the SEM micrographs were calculated using image analysis techniques discussed in Chapter 4, and are reported in Fig. 6.8 with the error bars representing the computational error associated with each calculation. The average effective diameters of all the precipitates identified as connected components by the image analysis algorithms are calculated in Fig. 6.9, where the error bars represent the confidence interval subject to a 95% level of significance. Nucleation and a

Table 6.3: Precipitation sequence of the 2032Nb alloy design matrix, where particle type and location is noted as "intra" for intradendritic.

	Aging Time (hrs)				
Treatments	**0**	**170**	**349**	**912**	**1488**
a	NbC, (Ti,Nb)C		NbC, (Ti,Nb)C, $M_{23}C_6$, $M_{23}C_6$ (intra)		
ac	NbC, (Ti,Nb)C		NbC, (Ti,Nb)C, $M_{23}C_6$, $M_{23}C_6$ (intra)		
ab	NbC, (Ti,Nb)C		NbC, (Ti,Nb)C, $M_{23}C_6$ (intra)		
abc	NbC, (Ti,Nb)C		NbC, (Ti,Nb)C, $M_{23}C_6$ (intra)		
(1)	NbC	NbC, $M_{23}C_6$, $M_{23}C_6$ (Intra)			
c	NbC, NbC (Intra)	NbC, NbC (Intra), $M_{23}C_6$ (Intra)	NbC, NbC (Intra), $M_{23}C_6$, $M_{23}C_6$ (Intra)		
b	NbC	NbC, $M_{23}C_6$, $M_{23}C_6$ (Intra)			
bc	NbC	NbC, $M_{23}C_6$, $M_{23}C_6$ (Intra)		NbC, NbC (Intra), $M_{23}C_6$, $M_{23}C_6$ (Intra)	

small amount of coarsening of the NbC precipitates is observed during aging for all of the treatments, although it is much more pronounced in the Super 2032Nb alloys. The 1" thick Super 2032Nb castings have a much higher number density of NbC than the NbC in the 3" thick samples, and are noticeably finer. The NbC in the commercial 2032Nb alloy takes up a noticeably lower portion of the microstructure compared to the NbC in the Super 2032Nb, however they are much finer. This might be beneficial for precipitation strengthening of the material. The 1" thick commercial 2032Nb NbC carbides are slightly coarser than the NbC carbides in the 3" thick samples, however this is not very significant in the later stages of aging.

In the initial stages of aging the titanium carbides in the Super 2032Nb samples have a larger number density in the 1" finish wall samples than the 3" finish wall samples, most likely due to the increased dendrite boundary area of the 1" thick casting (Table 6.2). The 3" thick Super 2032Nb samples show coarser TiC carbides than the 1" thick Super 2032Nb.

After two weeks of aging the intradendritic $M_{23}C_6$ precipitates adopt a needle-like morphology, whereas in previous stages of aging only spherical intradendritic $M_{23}C_6$ carbides were observed. Intradendritic $M_{23}C_6$ are coarser and have a larger number fraction in the 1" thick commercial 2032Nb alloy compared to the 3" thick commercial 2032Nb alloy after two weeks of aging. The as-cast components with the commercial 2032Nb chemistry on average have a higher area fraction than the homogenized component

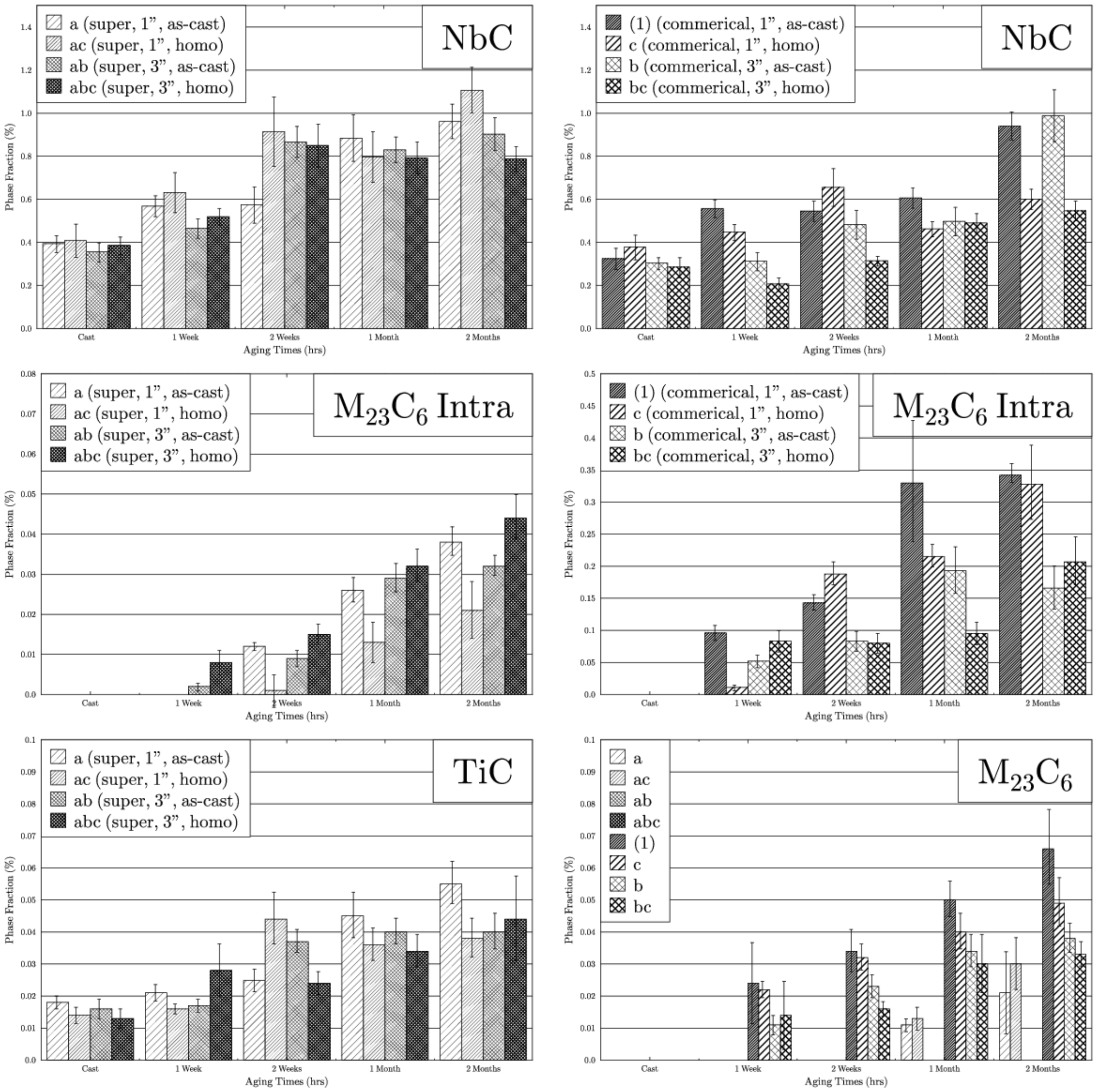

Figure 6.8: Phase fractions in Area% of NbC, TiC, and interdendritic/intradendritic $M_{23}C_6$ carbides for each casting in the MetalTek factorial design matrix

of the same chemistry. However, the intradendritic carbides are more dispersed in the in homogenized alloy which is beneficial for the overall properties of the component. Intradendritic $M_{23}C_6$ area fraction is almost negligible in the super 2032Nb alloys consisting of only ~ 0.03vol % of the total microstructure. In the 1" thick Super 2032Nb sample the intradendritic $M_{23}C_6$ levels are stunted in the homogenized treatment compared to the as-cast treatment. Conversely, in the 3" thick Super 2032Nb samples the intradendritic $M_{23}C_6$ in the homogenized sample are higher in number fraction than the as-cast alloy.

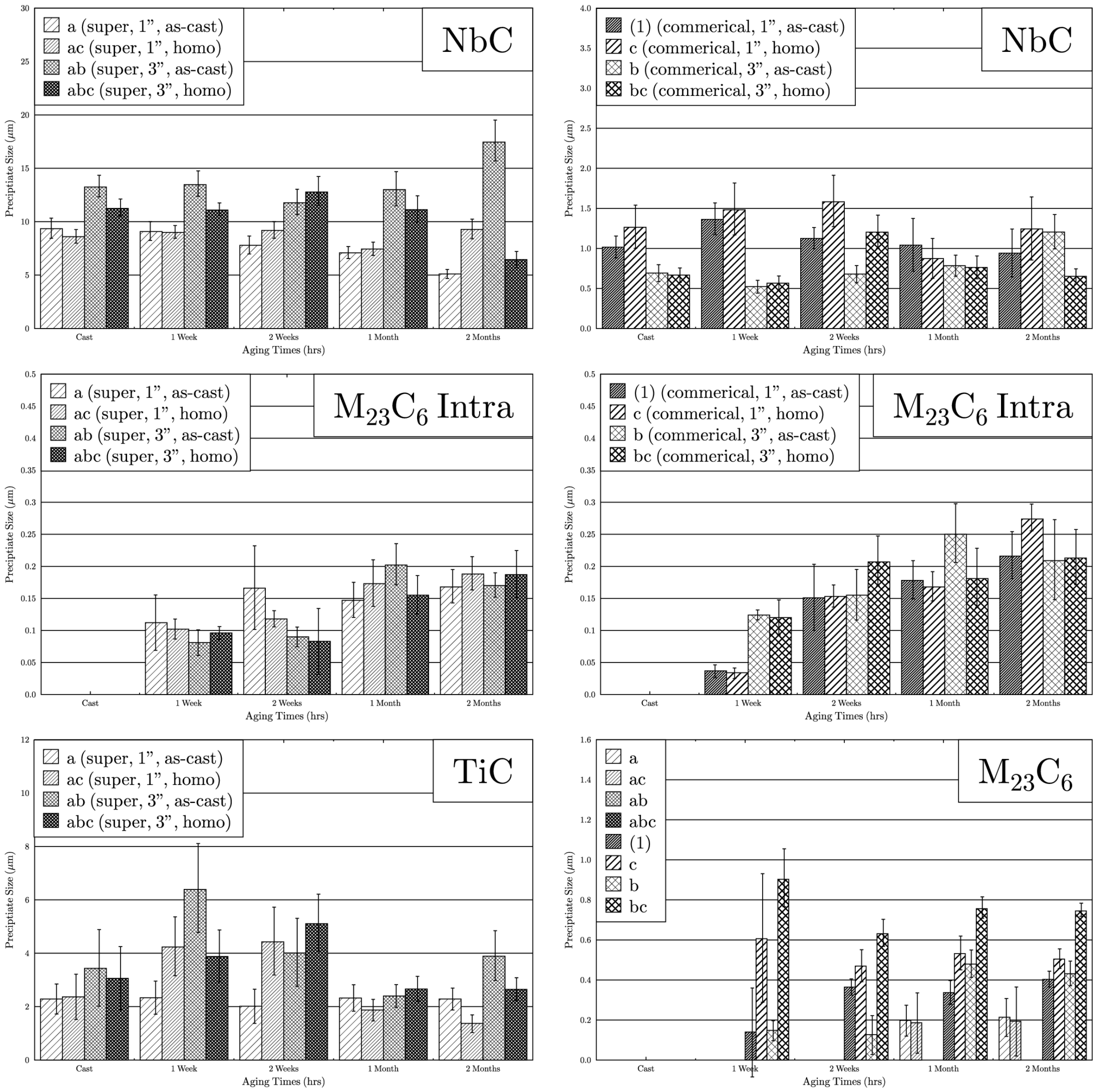

Figure 6.9: Effective precipitate diameter (in μm) of NbC, TiC, and interdendritic/intradendritic $M_{23}C_6$ carbides for each casting in the MetalTek factorial design matrix. The error bars express the confidence interval to a 95% level of significance.

Like the other interdendritic microconstituents, interdendritic $M_{23}C_6$ is finer and has a higher number fraction in the 1” thick commercial 2032Nb components compared to the 3” thick components. The as-cast treatments of the commercial 2032Nb samples also show finer interdendritic $M_{23}C_6$ with a higher number fraction than the homogenized equivalent component. The coarser interdendritic $M_{23}C_6$ in the homogenized sample might be due to the lower density of intradendritic $M_{23}C_6$ around the dendrite boundaries leaving the available chromium, and carbon in solution to be absorbed by the interdendritic species. Interdendritic $M_{23}C_6$ is an undesirable phase compared to intradendritic $M_{23}C_6$ as it can coarsen a considerable amount during long term aging which leads to the embrittlement of the material and ductility dip at the dendrite boundaries which can promote cracking. Interdendritic $M_{23}C_6$ precipitation is delayed in the 1" thick Super 2032Nb samples and non-existant in the 3" thick Super 2032Nb samples. After 2 months of aging the interdendritic $M_{23}C_6$ consists of a lower fraction than the commercial 2032Nb alloys, however the homogenized treatment of the 1" thick Super 2032Nb alloy does show a larger fraction of these precipitates.

6.6 Discussion

6.6.1 ThermoCalc Comparison

The ThermoCalc results in Fig. 6.1 and Fig. 6.2 coincide with what has been observed in the actual microstructures of the Super 2032Nb, and commercial 2032Nb alloys. No $M_{23}C_6$ was seen in any of the cast microstructure for the commercial 2032Nb alloy as predicted by Scheil, however $M_{23}C_6$ could still have been present and unresolvable with a conventional SEM. A lower fraction of $M_{23}C_6$ is measured compared to what is predicted by ThermoCalc even though the microstructure after two months aging time is far below equilibrium. The correct relative proportions of $M_{23}C_6$ between the two alloys is in accordance with the phase fractions measured in Fig. 6.8. The volume fraction of TiC is also measured to be in agreement with the equilibrium predicted by ThermoCalc. From these correlations with ThermoCalc, further aging the components will entail a great amount coarsening of the $M_{23}C_6$ precipitates. Even though G-phase was not observed after two months of aging, the equilibrium microstructure predicted by ThermoCalc shows that G-phase might still precipitate after long term aging. Considering the G-phase database discrepancies in the TTNI8 database it is hard to determine which equilibrium temperature on the ThermoCalc graph corresponds to the actual temperature experienced by the components during aging. G-phase may altogether be avoided in both alloys, however the higher G-phase stability in the Super 2032Nb alloy could cause it to precipitate in that alloy first. The equilibrium microstructure of the Super 2032Nb alloy without titanium in Fig. 6.3 shows an even lower driving force for G-phase precipitation over the commercial 2032Nb alloy, due to the stoichiometric Nb/C ratio and a minimized silicon concentration.

6.6.2 MetalTek Samples vs Ex-service Samples

A significant improvement in NbC intermetallic transformation is seen in both the design alloys compared to the solution annealed and cast ex-service 2032Nb components which developed G-phase after just two weeks of aging. Further aged Commercial 2032Nb, and Super 2032Nb samples will need to be characterized to see if G-phase precipitation was avoided altogether for each chemistry, but seeing no traces of G-phase after two months of aging is a good sign for the delay of embrittlement issues during service. If no G-phase is precipitated after long term aging, interdendritic $M_{23}C_6$ can still cause ductility dip, and embrittlement issues, but these can be fixed with repair welding treatments without removing the components from service.

The main difference between the design alloys compared to the Ex-service alloys is that the Nb/C ratio is ≤ 7.7, and not above 7.7. In the ex-service samples an excess of niobium in part causes the premature development of G-phase. One of the major benefits with the design alloys is that the intradendritic NbC seen in the ex-service alloys are replaced by intradendritic $M_{23}C_6$ due to excess carbon. These intradendritic secondary carbides pose no issue to the properties of the alloy as they will remain relatively fine, and provide precipitation hardening. The commercial 2032Nb samples have a larger fraction of intradendritic $M_{23}C_6$ due to the lower Nb/C ratio and larger carbon concentration.

The titanium carbides are beneficial in the Super 2032Nb alloy, improving the creep strength of the component. However, the Super 2032Nb alloy was engineered to contain a stoichiometric Nb/C ratio, and did not appear to consider the amount of TiC that would form and consume carbon leaving some niobium free in solution. From the ex-service component excess niobium appears to be detrimental to increasing the stability of G-phase. Assuming that first all the titanium will be tied up in TiC, and then the left over carbon will form NbC since TiC has a lower solubility that NbC; from stoichiometry the ratio of niobium to left over carbon will be 8.41. This excess amount of niobium will be free to precipitated out of solution as G-phase once silicon has segregated to the dendrite boundaries.

Nitrogen in the ex-service 2032Nb components was seen to be beneficial for decreasing G-phase stability as more niobium could be tied up into Nb(C,N) without having to increase the carbon concentration, precipitating more interdendritic $M_{23}C_6$. Titanium alloying additions act in the opposite way freeing niobium in solution to precipitate as an intermetallic phase.

6.6.3 Microstructural Correlation With Mechanical Properties

The larger dendrite cell sizes in the 3” thick component compared to the 1” component provide longer diffusional distances for chromium and silicon to segregate and a delayed precipitation of interdendritic $M_{23}C_6$ and G-phase. No interdendritic $M_{23}C_6$ were observed in the 3” thick Super 2032Nb sample after two months of aging which make these samples superior in terms of embrittlement, and cracking susceptibility. In the previous chapter it was speculated that a majority of G-phase nucleation occurs on interdendritic $M_{23}C_6$ interfaces. If interdendritic $M_{23}C_6$ precipitation is significantly delayed G-phase precipitation will also most likely be delayed. It is hypothesized that the 3” thick casting would have a higher fraction of intradendritic $M_{23}C_6$ due to the larger dendrite cell sizes. However, Fig. 6.8 shows the opposite relationship where more intradendritic $M_{23}C_6$ have precipitated in the 1” thick castings.

Although the effects of coarsening are not apparent in Fig. 6.9 since samples only aged up to two months have been investigated; the dendrite size calculations in Table 6.2 show that the 3” thick samples have a smaller boundary area for precipitation. A smaller boundary area is directly related to a lower amount of interdendritic nucleation, and a larger degree of coarsening of these precipitates. Coarse precipitates lead to a larger degree of embrittlement in the alloy, and a higher susceptibility to ductility dip, and liquation cracking. The 3" Super 2032Nb samples show slightly coarser secondary precipitates than the 1" Super 2032Nb samples, however this relationship is not apparent in the commercial 2032Nb samples. The precipitates in the commercial 2032Nb samples are very small, where most of them are $< 1\mu$m. With the image analysis techniques used to calculate precipitate size, these algorithms depend heavily on the resolution of the precipitates. If the precipitates only encompass a few pixels in area the error increases drastically, as noise in the image can be easily mistaken for a precipitate. While this will not effect the area fraction calculations by a great deal, the error in precipitate size will vary considerably.

The fine, submicron interdendritic NbC in the commercial 2032Nb casting provides exceptional mechanical properties compared to the coarse NbC seen in the Super 2032Nb. The larger fraction of these primary carbides in the Super 2032Nb can facilitate coarser, agglomerated G-phase precipitates if the NbC eventually transforms after long term aging. On the other hand, the lower fraction of $M_{23}C_6$ in the Super 2032Nb alloy could impede G-phase nucleation, as the $M_{23}C_6$ interface was previously determined to be the primary site for G-phase nucleation. Since no G-phase was observed in either alloy after two months of aging, it cannot be determined which alloy is superior in term of G-Phase prevention as both alloys might avoid it altogether. The Super 2032Nb chemistry is tailored to maximize NbC precipitation (Nb/C=7.7), and minimize NbC dissolution (minimized silicon), however the microalloyed titanium does negate some of these advantages by freeing up niobium. If no titanium was present in the Super 2032Nb alloy, or if the niobium concentration was lowered to compensate for the titanium, than the Super 2032Nb alloy would be superior in terms of preventing embrittlement, or liquation cracking during welding.

The homogenized samples will also provide exceptional creep and strength properties over the as-cast equivalents due to lower rates of elemental segregation around the dendrite boundaries. The homogeneous composition promotes a more dispersed region of intradendritic precipitates which will improve both the strengthening of the alloy, as well as decrease the amount of interdendritic $M_{23}C_6$ coarsening which embrittles the alloy. The orientation relationship observed in the needle-like morphologies for some of these carbides will promote heterogeneous strengthening in certain directions, which might change the properties of the steel during aging, and coarsening of intradendritic $M_{23}C_6$.

6.7 Conclusions

The design chemistries provided a vast improvement to the microstructural evolution of the 2032Nb alloy, where after two months of aging no transformation of NbC to G-phase was observed. The Super 2032Nb alloy which has a stoichiometric Nb/C ratio, and microalloy additions of titanium, zirconium, and aluminum, precipitated coarse NbC, and fine (Ti,Nb)C precipitates upon solidification. The commercial 2032Nb chemistry containing a 5.3 Nb/C ratio, and no microalloying elements, precipitated fine, lamellar NbC upon casting, where after one week of aging intradendritic and interdendritic $M_{23}C_6$ was observed. ThermoCalc predicted an increased stability for G-phase in the Super 2032Nb alloy due to titanium forming TiC and freeing up niobium in solution which can then precipitate out as G-phase. Finer dendrites were measured in the 1” thick castings, where the Super 2032Nb alloy contained the finest dendrites in the 1” casting, and the coarsest dendrites in the 3” casting. In the commercial 2032Nb alloy, homogenization helped facilitate the precipitation of intradendritic NbC as well as intradendritic $M_{23}C_6$. Homogenization also increases the dispersion of intradendritic $M_{23}C_6$ producing lower fractions of intradendritic, and interdendritic $M_{23}C_6$, and finer precipitates in the microstructure.

The Super 2032Nb alloy has been tailored to be superior to the commercial 2032Nb alloy, containing a stoichiometic Nb/C ratio and a minimized silicon concentration. However, The presence of TiC in the microstructure causes concern with the ability to suppress G-phase formation, as niobium will be free to react with silicon to form G-phase once the silicon has segregated to the dendrite boundaries. The homogenization heat treatment is preferred as it promotes a larger dispersion of intradendritic $M_{23}C_6$,and NbC precipitates. The 3” thick castings produce larger diffusional distances needed for the segregation of chromium and silicon, which will suppress and delay precipitation of interdendritic $M_{23}C_6$ and potential G-phase. However a larger casting thickness will also support a larger degree of interdendritic coarsening which is not beneficial for the service life of the part. No interdendritic $M_{23}C_6$ was observed in the 3” thick Super 2032Nb alloy which could inhibit G-phase precipitation upon further aging.

Chapter 7

ThermoCalc Chemistry Optimization Results

7.1 Introduction

This chapter will investigate how alloying elements of titanium and nitrogen will affect the microstructure of the 2032Nb variant, and which chemistries could potentially minimize or limit embrittling, and liquation cracking from excessive G-phase and interdendritic $M_{23}C_6$ precipitation. Two factorial designs analyzing the compositional ranges for 2032Nb alloys presented in Table 3.3 will be discussed. The first factorial design will consider 3^7 compositions involving three levels of nitrogen additions (0wt%, 0.15wt%, and 0.3wt%), where the main effects from each individual element, and any effects from any element interactions will be assessed for each phase present in the equilibrium microstructure. The second factorial design will consider 3^7 compositions involving three levels of titanium additions (0.05wt%, 0.175wt%, and 0.3wt%). Linear regression will then be used on both factorial experiments to define equations relating phase fraction to alloy composition for each of the stable phases. Methods for using the linear equations to solve for an optimum solution will then be outlined. Finally, a few optimized chemistries with varying amounts of nitrogen are proposed.

7.2 Nitrogen Alloying Additions

The design matrix for the nitrogen factorial design involves seven elements (nickel, chromium, silicon, niobium, carbon, manganese, and nitrogen) at three different concentration levels. Equilibrium was calculated for each composition from room temperature to the melting temperature of the 2032Nb stainless steel. The maximum volume fractions and the stability temperatures were then extracted from each phase fraction plot. Fig. 7.1 shows a matrix plot of the maximum fractions of each phase plotted against the seven elements in the design matrix. Any trends in the maximum phase fraction vs changes in element concentrations are revealed through linear interpolation of the average phase fraction at each composition level. The last column in Fig. 7.1 plots the stabilization ratio against each phase to visualize any 3-way interactions that niobium, carbon, and nitrogen have on phase precipitation. A line at Nb/(C+6/7N) = 7.7 was drawn for clarity to show where the stoichiometric ratio is located in the Nb/(C+6/7N) column. By varying nitrogen content, the stable phases in the system as predicted by ThermoCalc, were Nb(C,N), $M_{23}C_6$, G-phase, Z-phase, and π-phase which forms at higher nitrogen concentration comprising chromium, nickel, and nitrogen. π-phase has a stoichiometry of $Cr_{12.8}(Fe,Ni)_{7.2}N_4$, and is not reported in the literature. However if π-phase is neglected during equilibrium calculations at high nitrogen levels, a third FCC phase similar in composition to π-phase is suggested to form, and the calculated G-phase fraction decreases significantly.

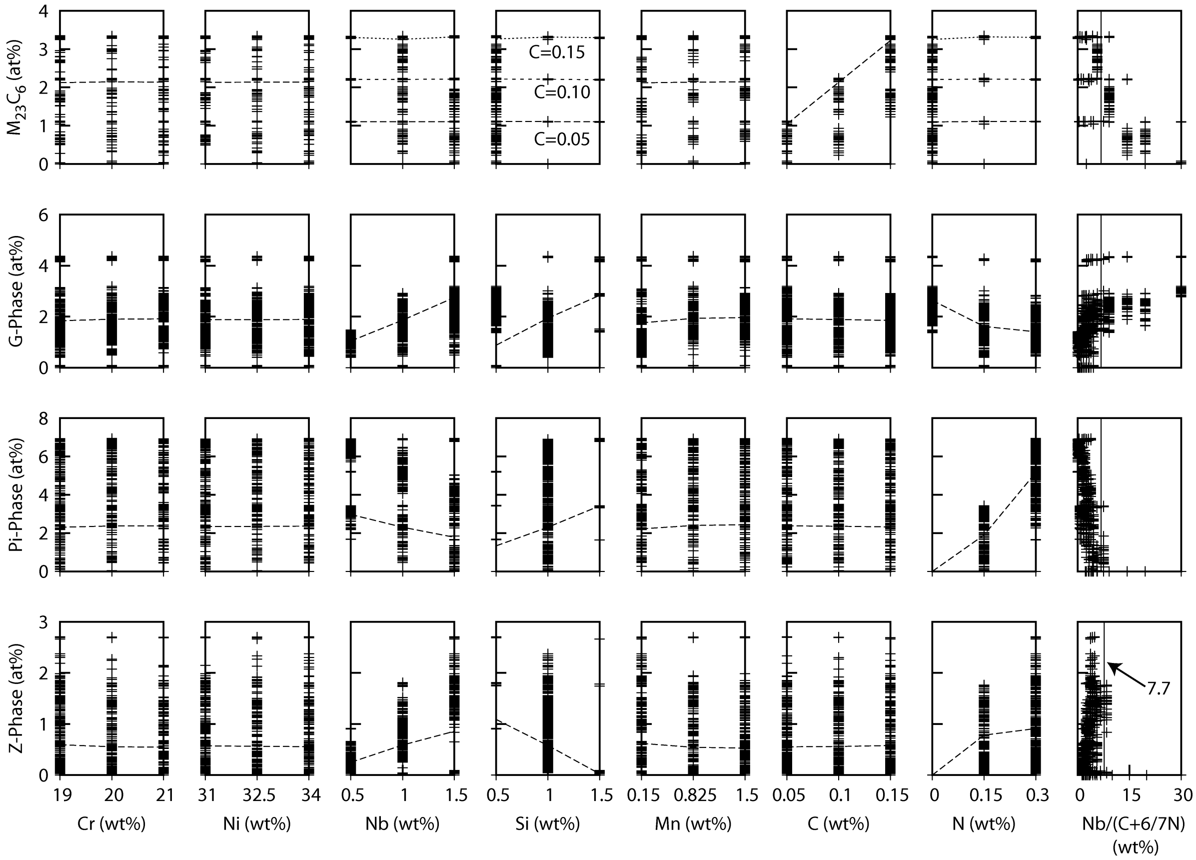

Figure 7.1: Matrix of single element interactions on the phase fractions of stable phases in a 2032Nb alloy with nitrogen additions. The dotted line shows the average relationship of the scatter gathered from ThermoCalc. The last column shows the synergistic interaction from variation in the stabilization ratio.

The maximum G-phase fraction is calculated to decrease when the nitrogen content increases to 0.15wt%. The drop in maximum G-phase fraction is compensated for by increases in π-phase and Z-phase, while

$M_{23}C_6$ is unaffected by increasing nitrogen concentrations. Increasing nitrogen content past 0.3 wt% shows a increased precipitation rate of π-phase while the fractions of G-phase and Z-phase are barely affected. As expected, niobium and silicon both promote G-phase since they are both constituents of this phase. Minimizing silicon is seen to be critical to limiting the amount of G-phase precipitation, and unlike niobium can be adjusted without many consequences to the rest of the microstructure. However, the concentration of silicon required for the alloy will depend on the amount of fluidity needed for casting. Silicon will increase the flowability of the molten steel, where a more complex shape will be able to be cast. A simple pipe might be able to be cast with a minimal amount of silicon, as this shape can be cast with reduced fluidity.

Although niobium has approximately the same influence that silicon does in regards to G-phase precipitation, it is also critical to $M_{23}C_6$ stability, and Z-phase precipitation. As seen in the previous chapter comparing the Super 2032Nb alloy to the commercial 2032Nb alloy, optimizing the Nb/C ratio to 7.7 is critical for maximizing the concentration of NbC, which in turn minimizes $M_{23}C_6$ fraction before G-phase transformation. Minimizing $M_{23}C_6$ is important as it suppresses the temperature in which G-phase becomes stable, and the temperature at which NbC begins to transform into G-phase. If the G-phase stability temperature is suppressed below the operating temperature of the component it will not appear in the microstructure during long term aging. At increased niobium concentrations the driving force for Z-phase will increase as niobium is a constituent of Z-phase. In turn the driving force for π-phase will decrease as all of the niobium will be sequestered into Z-phase. The Nb/(C+6/7N) ratio shows a clear division for all phases around 7.7, where π-phase and Z-phase do not exist when $Nb/(C+6/7N) > 7.7$, and G-phase fraction drops drastically when Nb/(C+6/7N) is below 7.7. Meanwhile $M_{23}C_6$ displays the opposite trend, decreasing when Nb/(C+6/7N) is greater than 7.7.

The significant variables for varying the maximum fractions of each phase calculated to a 95% confidence interval are listed in Table 7.1. Each variable, and variable interactions are listed in decreasing order of importance, and whether they contribute to increasing precipitation of a phase (+), or decrease it (-). For the case of $M_{23}C_6$, carbon was determined to be the only significant variable which is reiterated in the $M_{23}C_6$ plots in Fig. 7.1. As discussed above, the constituents of G-phase, silicon and niobium, have the strongest effect on G-phase precipitation, and contribute to its formation. Nitrogen is the only variable that actively decreases G-phase concentration, while interactions between silicon and nitrogen, and silicon and niobium promote G-phase precipitation. Z-phase precipitation is mostly influenced by silicon, decreasing in fraction as silicon concentration is increased, where G-phase has a higher stability for formation at higher silicon levels. Z-phase is also positively influenced by nitrogen and niobium as they are constituents of this phase. At higher concentrations of nitrogen G-phase is replaced by π-phase which is also controlled by silicon and niobium, and their interactions.

An independent regression analysis was done on each of the maximum phase fraction response variables. The linear regressions calculated by Minitab statistical software are:

Table 7.1: Significant variables in decreasing order for changing the maximum phase fraction of a phase in the nitrogen factorial design.

Element Effects on Maximum Phase Fraction											
	$M_{23}C_6$			**G-Phase**			**Z-Phase**			**Pi-Phase**	
Term	**(+/-)**	**Effect**	**Term**	**(+/-)**	**Effect**	**Term**	**(+/-)**	**Effect**	**Term**	**(+/-)**	**Effect**
C	+	0.022	Si	+	0.019	Si	-	-0.011	N	+	0.052
			Nb	+	0.017	N	+	0.0091	Si	+	0.021
			N	-	-0.012	Si×N	-	-0.0087	Si×N	+	0.017
			Si×N	+	0.010	Nb	+	0.0061	Nb	-	-0.012
			Si×Nb	+	0.0096	Nb×N	+	0.0053	Nb×N	-	-0.011

$$\begin{aligned}
\mathrm{G-Phase} &= -0.020 + 0.02Si + 0.017Nb - 0.0071C - 0.041N \;;\; R^2 = 89.7\% && (7.1)\\
\mathrm{M_{23}C_6} &= -0.0034 + 0.0020Si - 0.0016Nb + 0.22C + 0.0072N \;;\; R^2 = 91.2\% && (7.2)\\
\mathrm{Z-Phase} &= 0.012 - 0.011Si + 0.0061Nb + 0.0022C + 0.030N \;;\; R^2 = 63.0\% && (7.3)\\
\pi-\mathrm{Phase} &= -0.022 + 0.021Si - 0.012Nb - 0.0050C + 0.17N \;;\; R^2 = 85.4\% && (7.4)
\end{aligned}$$

The R^2 value reported is the adjusted value, showing the best fit for the $M_{23}C_6$ data, and the worst fit for the Z-phase data. Improvements to the regression were done by introducing interaction variables producing non-linear equations. The non-linear regression equations for the maximum phase fractions can be found in subsubsection A.14.1.1. The overall objective in optimizing the 2023Nb chemistry is to minimize G-phase, and to limit the precipitation and coarsening of secondary embrittling phases such as $M_{23}C_6$, Z-phase, and π-phase. At this stage it is unknown the extent to which Z-phase and π-phase will embrittle the 2032Nb material. Furthermore, it would also need to be experimentally proven whether Z-phase and possibly π-phase avoid liquating during repair welding. Constraints limiting the amount of Z-phase and π-phase will need to be estimated and adjusted based on prior knowledge of the system and their sensitivity towards the objective function.

Figure 7.2 shows the matrix plots for the stability temperature of each secondary phase present in the microstructure against single interactions from the components of the alloy, along with the stabilization ratio. Reducing the stability of G-phase is perhaps more important than limiting the maximum phase fraction, as if the stability temperature is low enough the phase will be altogether avoided during high temperature aging. For $M_{23}C_6$ and π-phase, the stability temperature shows a clear separation in data, where the corresponding phase can be categorized as forming at either a high temperature or a lower temperature. For $M_{23}C_6$ this separation is dictated by the Nb(C,N) ratio, and as to whether it is above or below 7.7. Below 7.7 $M_{23}C_6$ will start to become stable at a higher temperature ($\sim$ 1000°C), while above 7.7, $M_{23}C_6$ will only start to form at a lower temperature. Z-phase is observed to only form when the stabilization ratio is below 7.7, where excess nitrogen exists in the alloy. The high stability temperatures for Z-phase reveals that Z-phase is very favorable in nitrogen bearing 2032Nb alloys. From factorial analysis the segregation in the π-phase stability plot is from the Nb/N interaction, which is balanced at a value of 6.6 based on stoichiometry. With Nb/N < 6.6, π-phase stability is maximized, forming around $\sim 900°C$, whereas if Nb/N > 6.6 π-phase formation is restricted to lower temperatures. It should be noted that the lower stability limit temperatures ($< 400°C$) shown in Fig. 7.2 are misleading, as precipitation of $M_{23}C_6$, π-phase, and Z-phase are directly related to G-phase, which is known to form at a much higher temperature than predicted by the TTNI8 ThermoCalc database.

The addition of nitrogen concentration appears to play a significant role in suppressing the stability temperature for G-phase, where increasing nitrogen decreases the stability of G-phase, and reduces the overall temperature of formation for this phase. Reducing the stabilization below 7.7 appears to have beneficial effects in reducing G-phase stability. It is possible to have a Nb/(C+6/7N) ratio less than 7.7 without increasing the concentration of $M_{23}C_6$ by only increasing the nitrogen content. Silicon and niobium both have less of an effect on the stability temperature of G-phase compared to the G-phase fraction.

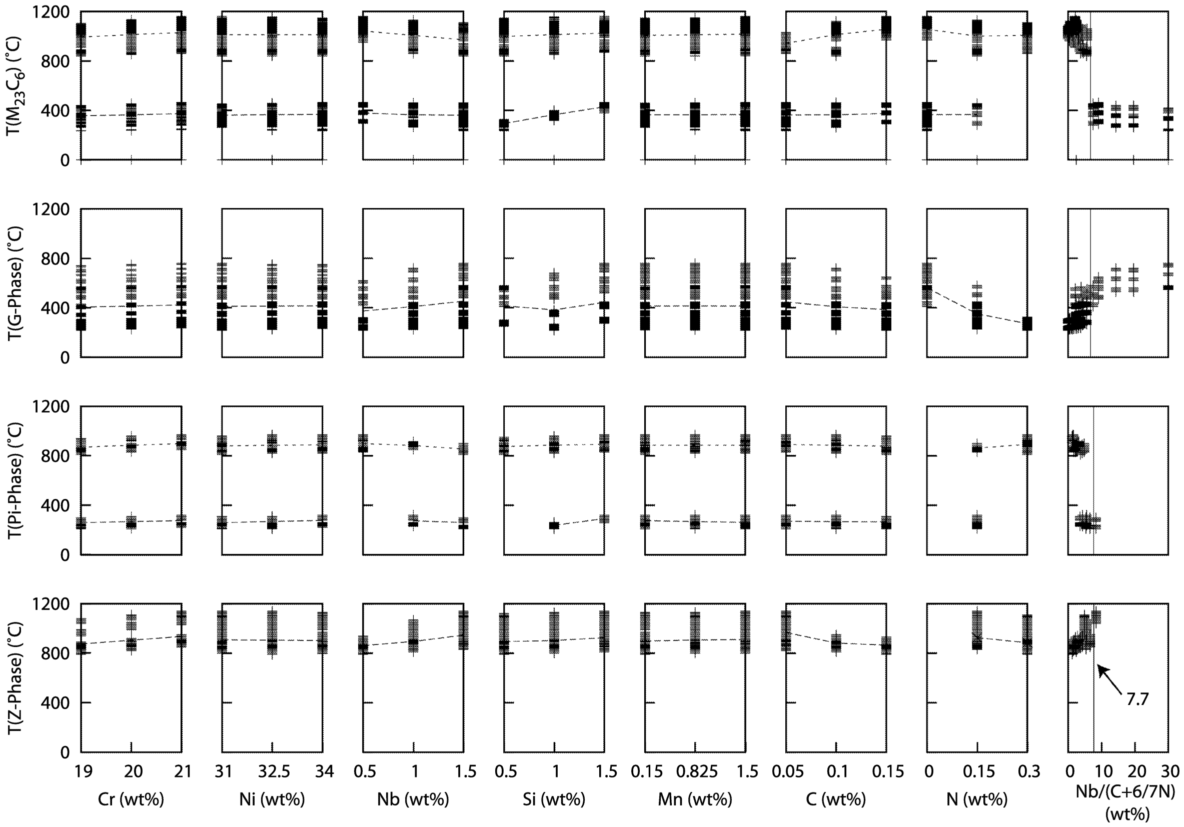

Figure 7.2: Matrix of single element interactions with stability temperatures of stable phases in a 2032Nb alloy with nitrogen additions.

The significant variables determined by factorial analysis are tabulated in Table 7.2. The stability temperature for $M_{23}C_6$ is affected by nitrogen and niobium as well as carbon, where nitrogen has the strongest effect. For $T_{G-phase}$ the major effects were nitrogen, silicon, and niobium. Analysis of $T_{Z-phase}$ showed it is mainly affected by variation in nitrogen composition, and to a lesser degree silicon×niobium, niobium, and silicon. Finally, nitrogen has a very strong effect on $T_{\pi-phase}$, and weaker effects from niobium, silicon, niobium×nitrogen, and chromium.

Table 7.2: Significant variables in decreasing order for the response in stability of a phase in the nitrogen factorial design.

Element Effects on Phase Stability Temperature

$\mathbf{T_{M_{23}C_6}}$			$\mathbf{T_{G-Phase}}$			$\mathbf{T_{Z-Phase}}$			$\mathbf{T_{Pi-Phase}}$		
Term	**(+/-)**	**Effect**	**Term**	**(+/-)**	**Effect**	**Term**	**(+/-)**	**Effect**	**Term**	**(+/-)**	**Effect**
N	+	423	N	-	-382.9	N	+	775.2	N	+	889.8
C	+	303.9	Si	+	214.1	Si×Nb	+	263.1	Nb	-	-271
Nb	-	-278.6	Nb	+	110.3	Nb	+	227.6			
Nb×N	+	238.5				Si	-	-203.1			
C×N	-	-198.6									
Nb×C×N	+	186.2									

Linear regression functions for the stability temperature of each of the stable phases listed below (Eq. 7.5-Eq. 7.8) can be used as constraints for solving the linear programming model described below. It might be more suitable to make the equation for $T_{G-Phase}$ the objective function, as minimizing this is much more important than minimizing G-phase fraction. The low R^2 values for $T_{M_{23}C_6}$, and $T_{Z-Phase}$ represent a large residual error in fitting the data. Along with the P-factor equation (Eq. 2.5), the stabilization ratio, and Eq. 7.1-7.4, the system should be able to be solved using linear programming techniques, or statistical optimization techniques.

$$\begin{aligned}
\mathrm{T}_{\mathrm{G-Phase}} &= 63.8 + 214Si + 110Nb - 532C - 1276N \ ; \ R^2 = 86.0\% && (7.5)\\
\mathrm{T}_{\mathrm{M_{23}C_6}} &= 110 + 63.1Si - 279Nb + 3037C + 1409N \ ; \ R^2 = 65.5\% && (7.6)\\
\mathrm{T}_{\mathrm{Z-Phase}} &= 384 - 204Si + 228Nb - 636C + 2583N \ ; \ R^2 = 57.7\% && (7.7)\\
\mathrm{T}_{\pi\mathrm{-Phase}} &= 31 + 71.8Si - 271Nb - 69.9C + 2966N \ ; \ R^2 = 83.1\% && (7.8)
\end{aligned}$$

The relationship between the fraction of G-phase predicted by ThermoCalc simulations and the empirical P-factor equation, Eq. 2.5, was evaluated for all compositions where nitrogen was equal to 0 wt.pct. Fig. 7.3 shows there is a positive correlation between the parameters, where the adequacy of the regression model, or the R^2 factor, is 0.65. Although this correlation value is not particularly strong, due to the wide range of chemical compositions considered (at the limits of the specified alloy), this correlation agrees with the suggestion by Shibaski *et al.*[18] to reduce the P-factor value during alloy design.

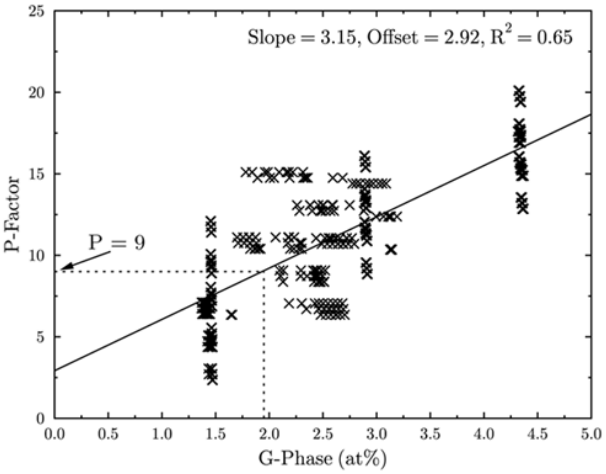

Figure 7.3: Correlation between P-factor, and G-phase fractions predicted by ThermoCalc, when nitrogen equals 0 wt.pct.

7.3 Titanium Alloying Additions

The second factorial design exchanges nitrogen for titanium to look at how the introduction of titanium and the formation of TiC carbides affects the equilibrium microstructure of the alloy. In the previous chapters analysis of the Super 2032Nb alloy, it was concluded that the introduction of titanium increased G-phase stability due to the formation of TiC carbides freeing up niobium which can then precipitate out as G-phase. The matrix plots for maximum phase fractions are presented in Fig. 7.4 including primary NbC, TiC fractions, as well as secondary $M_{23}C_6$, M_6C, and G-phase fractions. The Nb/C stabilization ratio plot shows that a maximum amount of NbC occurs around the stoichiometric value 7.7. TiC precipitation is only predominant when the stabilization ratio is below 7.7 and excess carbon exists in the system.

G-phase fraction appears to have less of a dependency on silicon once it is greater than 1wt%. The positive relationship between G-phase fraction and titanium shows that titanium is indeed detrimental to the alloy, however to a lesser extent than niobium. M_6C which from ThermoCalc is stoichiometrically represented as $Cr_3Ni_2(Nb, Si)C$ is present when the Nb/C ratio is overstabilized above 15. A division in the M_6C fraction occurs at Nb/C=25 where above this value M_6C composes $> 1at\%$ of the composition, and below composes $< 0.5at\%$ of the microstructure. TiC fraction is seen to be dependent on titanium, niobium, and carbon concentrations, increasing with titanium and carbon, and decreasing with niobium. Most TiC precipitation is seen to occur when the alloys Nb/C ratio is understabilized.

The significant variables for determining phase fraction of each phase are shown in Table 7.3. Again, carbon is the only significant variable for $M_{23}C_6$; while for G-phase, silicon which was the most significant variable in the nitrogen design matrix is now much less significant, where niobium and titanium are the most important variables. M_6C is more dependent on the interactions between silicon, niobium, and

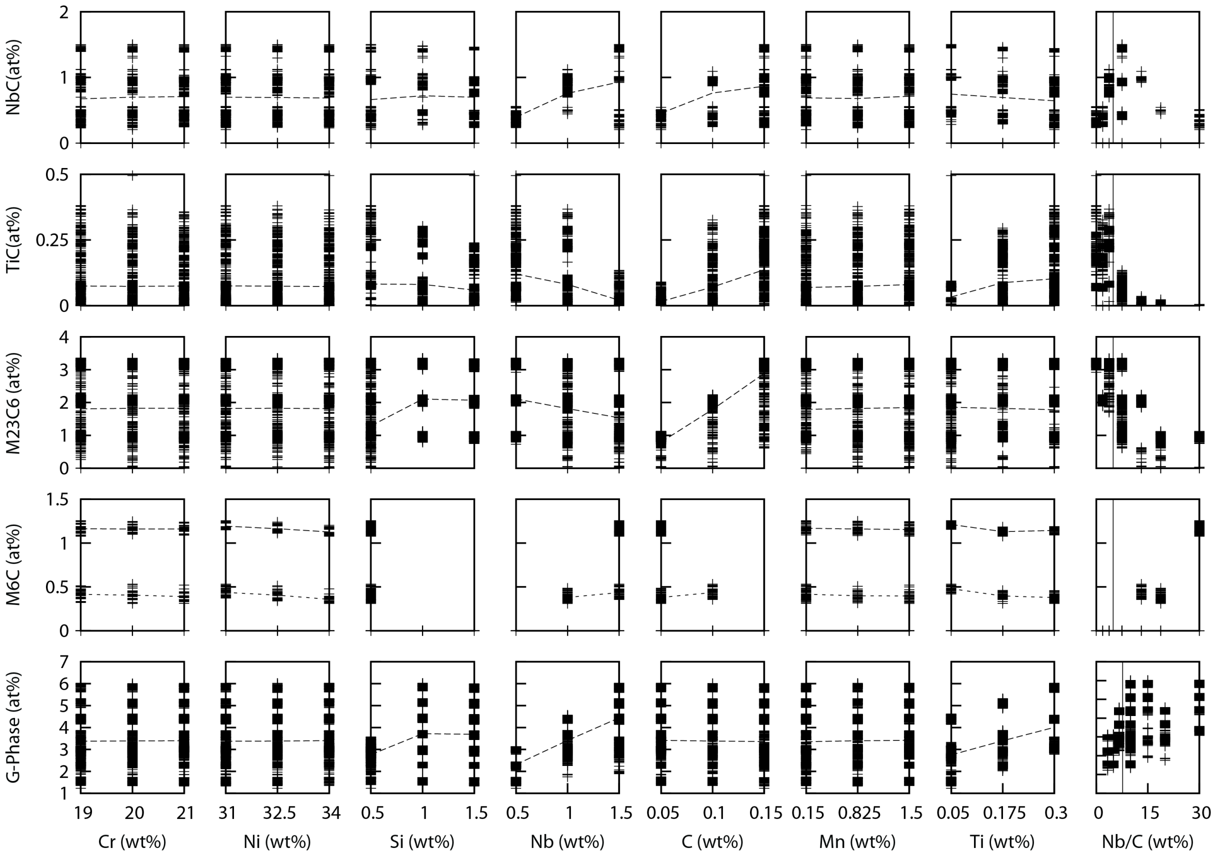

Figure 7.4: Matrix of single element interactions on the phase fractions of stable phases in a 2032Nb alloy with titanium additions.

carbon than any of the individual elements. For NbC and TiC the most important factors are niobium, and carbon respectively. In TiC the effects from other variables and interactions are much smaller than carbon, and are less significant, where titanium does not play as dominant a role compared to carbon.

Table 7.3: Significant variables in decreasing order for changing the maximum phase fraction of a phase in the titanium factorial design.

Element Effects on Maximum Phase Fraction														
NbC			**TiC**			**$M_{23}C_6$**			**G-Phase**			**M_6C**		
Term	**(+/-)**	**Effect**	**Term**	**(+/-)**	**Effect**	**Term**	**(+/-)**	**Effect**	**Term**	**(+/-)**	**Effect**	**Term**	**(+/-)**	**Effect**
Nb	+	0.0053	C	+	0.0012	C	+	0.02	Nb	+	0.021	Si×Nb×C	+	0.29
Nb×C	+	0.0048	Nb	-	-0.001				Ti	+	0.013	Si×Nb	-	-0.23
C	+	0.0041	Ti×C	+	0.00069				Si×Nb	+	0.01	Si×C	+	0.23
Ti	-	-0.001	C×Ti	+	0.00058				Si	+	0.009	Nb×C	-	-0.19
												Si	-	-0.18
												Nb	+	0.16

The matrix plots for the each phases stability temperature are shown in Fig. 7.5. In the nitrogen matrix the stability of phases like $M_{23}C_6$, π-phase, and Z-phase showed a sharp division in temperature depending on the Nb/(C+6/7N) ratio. For the titanium matrix no such division is observed, where the stability of $M_{23}C_6$ is distributed evenly between 300-1100°C. The change in G-phase stability is more limited compared to the nitrogen matrix, where silicon is the only element that looks to have a significant effect. G-phase is more stable in the titanium alloys being on average 300°C higher than in the nitrogen bearing alloys. $M_{23}C_6$ stability is highly dependent on niobium and carbon, where a higher amount of NbC carbides will suppress $M_{23}C_6$ formation. Significant effects determined by factorial analysis on phase stability are reported in Table 7.4, which reiterate the matrix plots in Fig. 7.5.

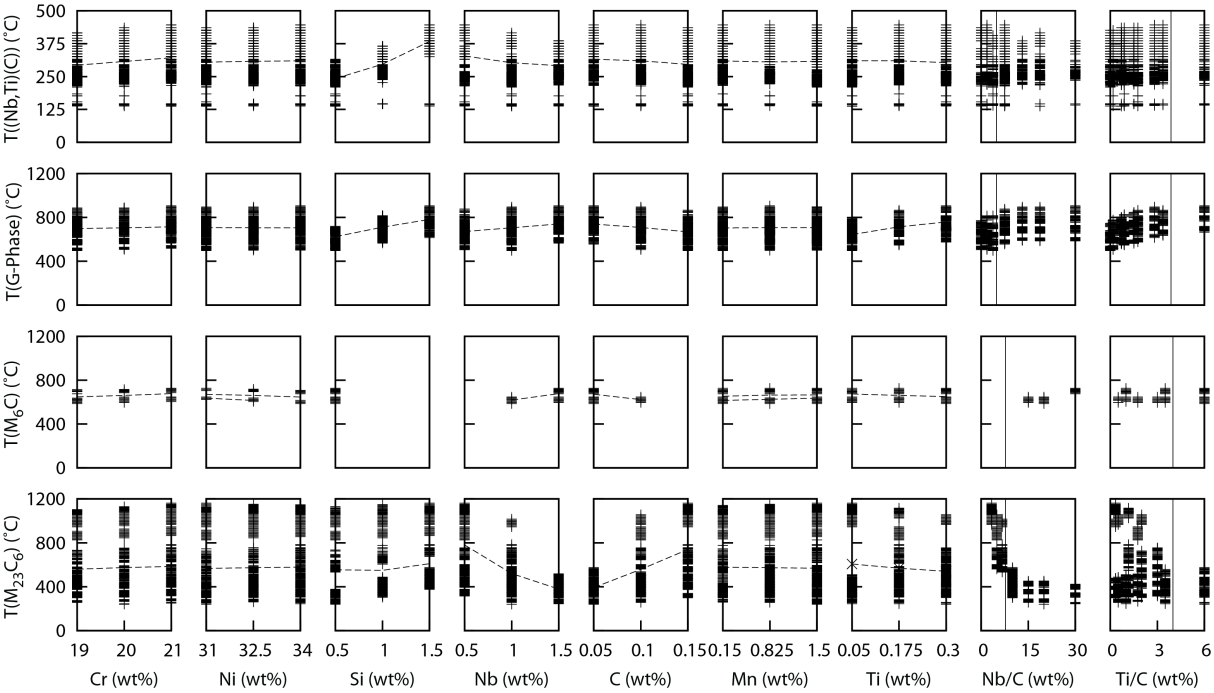

Figure 7.5: Matrix of single element interactions with stability temperatures of stable phases in a 2032Nb alloy with titanium additions.

Table 7.4: Significant variables in decreasing order for the response in stability of a phase in the nitrogen factorial design.

Element Effects on Phase Stability Temperature											
$\mathbf{T_{(Ti,Nb)C}}$			$\mathbf{T_{M_{23}C_6}}$			$\mathbf{T_{G-Phase}}$			$\mathbf{T_{M_6C}}$		
Term	(+/-)	**Effect**	**Term**	(+/-)	**Effect**	**Term**	(+/-)	**Effect**	**Term**	(+/-)	**Effect**
Si	+	140.9	Nb	-	-470.8	Si	+	157.9	Si×C	+	178.7
Nb	-	-36.1	C	+	412.6	Ti	+	115.9	Si×Nb×C	+	176.1
Si×Nb	-	-31.1	Nb×C	-	-237.6	C	-	-70.6	Si×Nb	-	-174.2
Cr	+	27.9	Si	+	188.9	Nb	+	70.3	Si	-	-156.6
C	-	-19.5	Si×Nb	+	100				C	-	-118.7
			Si×C	-	-99				Nb×C	-	-116.6

In general large concentrations of titanium should be avoided. From this analysis it is concluded that titanium concentrations should be limited to $< 0.015wt\%$. If titanium is added in greater concentrations it should be factored into the stabilization ratio, where TiC will form first where then left over carbon will form either NbC or $M_{23}C_6$. If the titanium concentration is too high the TiC will still become unstable at low temperatures causing premature G-phase and $M_{23}C_6$ precipitation before the dissolution of NbC. M_6C precipitation should not be a concern as it is never beneficial to overstabilize the chemistry, therefore this phase will not form in any optimized alloys.

7.4 Discussion

ThermoCalc predictions of π-phase at higher nitrogen concentrations is not supported by any literature on high temperature creep resistant stainless steels; however, π-phase $(\mathrm{Cr}_{12.8}(\mathrm{Fe,Ni})_{7.2}\mathrm{N}_4)$ is closely related to the commonly observed η-phase $(\mathrm{Cr}_3\mathrm{Ni}_2\mathrm{Si}(\mathrm{C,N}))$ in terms of constituents, site fractions, and structure. η-phase is a common phase in variants with higher carbon content ($\sim$ 0.4wt.pct), and is closely associated with Z-phase in alloys such as HP50, and NF709 stainless steels [6, 31, 68]. While π-phase is not experimentally validated it is possible that it could be a stable phase at higher nitrogen concentrations in conjunction with G-phase. Formation of G-phase would sequester the silicon and prevent precipitation of the silicon containing η-phase, leaving nitrogen to precipitate out of solution as π-phase. The reason that π-phase may have never been experimentally observed is that high nitrogen content has not been examined in steels containing G-phase.

The phase fraction matrix plots in Fig. 7.1 shows that nitrogen does have positive effects in minimizing G-phase, and as a result promotes the formation of nitride intermetallics which might avoid liquating during repair welding. The effect that nitrogen has on reducing G-phase also depreciates past 0.15 wt.pct where any increase in nitrogen is considered to be detrimental as it will only promote increased fractions of π-phase and Z-phase. Specific compositions where G-phase did not form appear to be dependent on both minimizing silicon content and understabilizing the Nb/(C+N) ratio below 7.7. For compositions with 0.15 wt.pct nitrogen, zero formation of G-phase occurred when silicon was minimized at 0.5 wt.pct and the Nb(C,N) stabilization ratio was between 1.8 and 2.8. Every chemical composition absent of G-phase contained significant proportions of Z-phase or π-phase, where the sum of these phases equal to at least 1.4 vol%. All compositions with 0 wt.pct nitrogen had G-phase fractions of at least 1.4 vol%.

In Fig. 7.1 and Fig. 7.2, Understabilizing the Nb/(C+6/7N) ratio is seen to be beneficial for reducing the maximum G-phase fraction as well as its stability. In previous studies by Hoffman [29], and Powell [11] a stoichiometric ratio of niobium to carbon is suggested to limit the amount of $M_{23}C_6$ and intermetallic phases that precipitate from excess carbon or niobium respectively. When adding nitrogen into the composition the Nb/(C+6/7N) ratio can be below the suggested 7.7 amount as long as no excess carbon exits in solution to precipitate out as $M_{23}C_6$. Adding nitrogen is a good way of reducing the carbon content, or increasing the niobium content without promoting $M_{23}C_6$ or intermetallic formation. Minimizing the stability temperature of G-phase is more dependent on minimizing silicon, and increasing the concentration of other niobium bearing intermetallics such as Z-phase rather than on a stoichiometric stabilization ratio. For the majority of the data Z-phase and π-phase are not stable when the $\mathrm{Nb}/(\mathrm{C}+6/7\mathrm{N})$ ratio is greater than approximately 8.4-9. Since the experimental alloy used in this study has a Nb/(C+6/7N) ratio of 8.71, this chemical composition might be right at the limit of the stability region of Z-phase.

In Fig. 7.2, the sharp division between high and low stability temperatures was determined to be dependent on the Nb/(C+6/7N) ratio for $M_{23}C_6$ and Z-phase, and the Nb/N ratio for π-phase. It is interesting to note that some elements will only have an effect on the stability temperature for certain phases if these stabilization ratios are above or below their stoichiometric ratios. For example, silicon only effects $T_{M_{23}C_6}$ when Nb/(C+6/7N)> 7.7, where the opposite trend can be seen for carbon. $T_{G-phase}$ does not show this separation in data, and is more or less continuous from 1073K($800°C$) downwards. Nitrogen plays a major effect in minimizing the stability temperature of G-phase, where increasing the nitrogen concentration past 0.15wt.pct might be beneficial for ensuring that the G-phase stability temperature is less than the operating temperature of the component.

The stability temperature of G-phase and other intermetallic, and carbide phases have a direct relationship with the resulting microstructure and the serviceability of the component, as most of these phases are embrittling, or liquating. The outlet manifold system is generally exposed to an isothermal temperature of $\sim$ 800°C. Therefore, if the stability temperature of the embrittling, and liquating G-phase is lower than the operating temperature of the component, then G-phase will not be stable in the microstructure during long term aging, avoiding any possibility of liquation cracking, and improving the serviceability of the manifold. Similarly if the stability temperature of $M_{23}C_6$ is lowered, a smaller fraction of $M_{23}C_6$ will precipitate during aging, reducing the interdendritic embrittlement caused by $M_{23}C_6$.

While the regression fit between the ThermoCalc data and Eq. 2.5 in Fig. 7.3 is fairly weak, prediction of the creep strength in the material may be a result of other factors rather than exclusively G-phase precipitation. However, since degradation in creep performance has been directly correlated to G-phase formation [29], it is not surprising that there is a positive correlation between these two parameters, and that values of $P < 9$ are generally recommended based on empirical testing [18]. Based on these results, it appears that further analysis using ThermoCalc may be useful in refining alloy compositions based on other correlations with the calculated phase fractions.

7.5 Linear Programming Model

Based on the equations derived thus far, an attempt at a linear programming model can be used to optimize the chemistry of the 2032Nb alloy. The goal of this program should be to both minimize the stability of G-phase, and minimize embrittlement in the alloy. The titanium matrix proved to not be beneficial for the alloy so regression analysis from the nitrogen matrix will only be considered. Since G-phase and $M_{23}C_6$ are both responsible for the embrittlement of the 2032Nb alloy, the stability temperatures of these phases should both be minimized. The objective function can either be a double minimization of both $T_{G-phase}$, and $T_{M_{23}C_6}$, or an upper bound can be set for $T_{M_{23}C_6}$ as a constraint where only $T_{G-phase}$ will need to be minimized. Eq. 7.5 will become the objective functions, which will need to be minimized in order to find a solution. The full formulation of the objective function can be written as:

$$\text{minimize } z1 = 63.8 + 8.79\text{Cr} + 0.81\text{Ni} + 214\text{Si} + 110\text{Nb} - 532\text{C} + 3.68\text{Mn} - 1276\text{N} \tag{7.9}$$

The optimized chemistry should also conform to the Nb/(C+N) stabilization ratio of 7.7, and the P-factor equation (Eq. 2.5) which needs to be less than 9 in order for ductility to be retained in the alloy after long term aging [18]. With the addition of nitrogen, understabilization may also be permitted, and may aid in minimizing the stability of G-phase. The effects of drastically understabilizing the alloy with nitrogen are unknown, so a lower limit of 6 is applied. Z-phase and π-phase formation should also be subject to constraint limits, as both of these phases are also known to embrittle other stainless steel variants. By examining Fig. 7.1 Z-phase was determined to be constrained below 1at%, and π-phase was constrained below 2at%. An upper bound for $T_{M_{23}C_6}$ of 900°C will be set to ensure that $M_{23}C_6$ precipitates above 800°C. The constraints can now be written as:

$$\begin{aligned}
Nb - 7.7(C + 6/7N) &\leq 0 && (7.10)\\
Nb - 6(C + 6/7N) &\geq 0 && (7.11)\\
7 * C + 5 * Si - 3 * Mn + 8 * Nb &\leq 9 && (7.12)\\
0.012 - 0.011Si + 0.0061Nb + 0.0022C - 6.84 * 10^{-4}Mn + 0.030N &\leq 0.01 && (7.13)\\
-0.022 + 0.021Si - 0.012Nb - 0.0050C + 0.0015Mn + 0.17N &\leq 0.02 && (7.14)\\
110 + 18.4Cr + 1.67Ni + 63.1Si - 279Nb + 3037C + 8.33Mn + 1409N &\leq 900 && (7.15)
\end{aligned}$$

where the bounds of the variables from Table 3.3 are:
$19 \leq Cr \leq 21$, $31 \leq Ni \leq 34$, $0.5 \leq Nb \leq 1.5$, $0.5 \leq Si \leq 1.5$, $0.15 \leq Mn \leq 1.5$, $0.05 \leq C \leq 0.15$, and $0 \leq N \leq 0.15$

The linear programming model was then run through *Gusek* GNU linear programming toolkit to find a solution. An objective of $T_{G-\text{Phase}} = 322.0$°C, and $T_{M_{23}C_6} = 713.1$°C was found with the *LP Optimization* chemistry shown in Table 7.5. With the optimized chemistry, both the P-factor equation (Eq. 7.12) and the stabilization ratio (Eq. 7.11) were equal to their bounds. Therefore, the optimum solution will be dictated by the values chosen for these constraints. If the stabilization ratio is allowed to be understabilized to 5, the $T_{G-\text{Phase}}$ will decrease by 19.1°C. However, the P-factor constraint will only change the objective function if decreased by a marginal value of two. Z-phase precipitation is seen to be limited by the stabilization ratio constraint, where more will precipitate if the ratio is allowed to decrease. With the optimized chemistry, Z-phase fraction was equal to 0.99 vol%, and π-phase fraction was equal to 0.00 vol%. The Z-phase constraint is not upper bounded, as an increase in the upper bound to 1.5 vol% does not decease the optimum solution. G-phase and $M_{23}C_6$ fractions from the regression equations were 1.38vol%, and 2.26vol% respectively. In terms of the variables, silicon has by far the largest effect where its minimization is key to minimizing the objective function. If the lower bound for silicon is increased by one unit to 1.5wt%, then the objective function ($T_{G-\text{Phase}}$) will increase by 313°C. Even though manganese is seen to decrease the P-factor equation, it was not upper bounded in the solution with lower concentrations contributing to decreasing the objective function.

Table 7.5: Optimized chemistry solved by the linear programming model.

	Composition (wt.pct)							
	Cr	Ni	Mn	Si	C	Nb	N	Nb/(C+6/7N)
LP Optimization	19	31	1.18	0.5	0.119	1.15	0.085	6.0
LP Optimization Stabilized	21	34	1.5	0.5	0.133	1.26	0.035	7.7

The chemistry predicted by the linear programming model is much of what should be expected with both minimizing silicon, and understabilizing to decrease G-phase stability. Fig. 7.6a shows the ThermoCalc output of the optimal solution which is fairly consistent with the maximum phase fractions predicted by the regression model. The stability temperature of $M_{23}C_6$ is vastly underestimated in the regression model by over 200°C, although Eq. 7.6 also has the lowest R^2 fit. The stability temperature of G-phase is only over estimated by 40°C, where its respective regression function has a much better fit. The understabilization of the Nb/(C+N) ratio causes significant phase fractions of $M_{23}C_6$, and Z-phase before the transformation of G-phase. It is hard to say whether these phase fractions will cause substantial embrittlement in the steel, as this depends more on the morphology, size, and distribution of the precipitates. In order to limit Z-phase and $M_{23}C_6$ fractions, Eq. 7.10 in the linear programming model was changed to be a direct equality to reflect a stabilization ratio of 7.7. The optimum solution was found to be 412°C, with the chemistry is listed in Table 7.5. $M_{23}C_6$ and Z-phase fractions are drastically lowered, as is the stability temperature of the two phases. The model predicts that limiting the stabilization ratio to 7.7 will increase the stability temperature of G-phase by 89°C, however this actually turns out to only be a 30°C increase from ThermoCalc. A similar fraction of primary carbides are expected to precipitate, while at lower temperatures a larger fraction of Nb(C,N) are expected to be retained due to the lower secondary phase fraction. The upper bounded chromium and nickel concentrations cause a higher maximum volume fraction of of G-Phase and $M_{23}C_6$, which from the regression is 1.88vol%, and 2.51vol% respectively. From Fig. 7.6b the regression functions predicting G-phase and $M_{23}C_6$ fractions are both underestimated where a very high maximum phase fraction ($\sim 3vol\%$) of $M_{23}C_6$ occurs in the optimized chemistry. A constraint was added to the LP for $M_{23}C_6$ phase fraction; however, if the right hand side is lowered below 1.8 at% no feasible solution is found.

Improving the accuracy of the LP model can be done by improving the error of the regression functions. Doing a piecewise regression fit between the three compositions (low to medium, and medium to high), the low R^2 fits for $T_{M_{23}C_6}$, and Z-phase fraction could be improved. Furthermore, adding weighed coefficients to the objective function and some of the constraints could also improve the accuracy of the model.

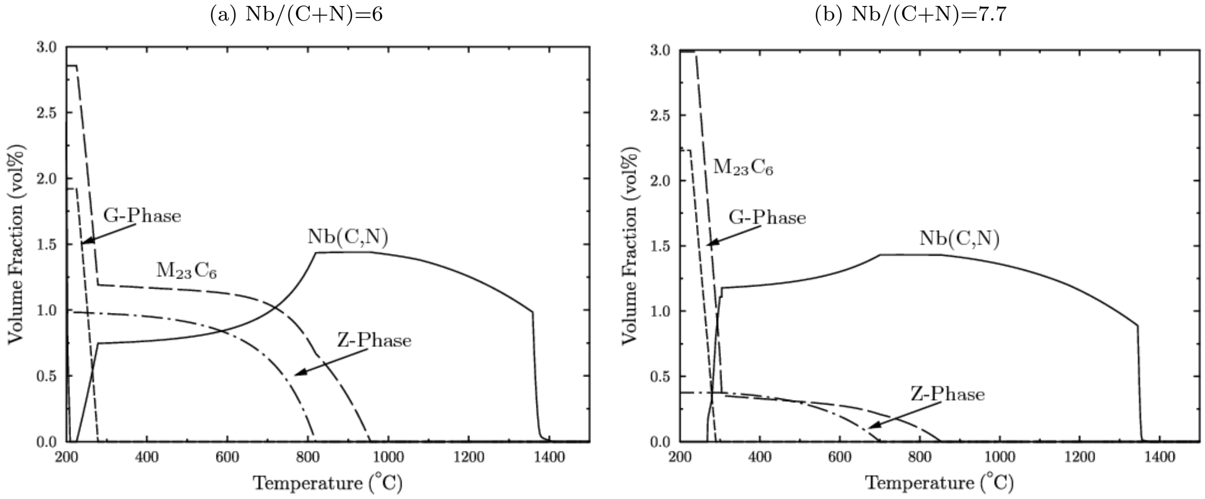

Figure 7.6: Equilibrium phase fraction plot from ThermoCalc of the chemistries derived from the linear programming model.

7.6 Optimized Chemistries

Optimized chemistries with varying amounts of nitrogen are proposed in Table 7.6. From the factorial experiments presented in this chapter it is clear that silicon concentration needs to be minimized to reduce the stability of G-phase. Minimizing G-phase and $M_{23}C_6$ fractions can be achieved by conforming to the Nb/(C+6/7N) = 7.7 ratio. A lower stability for G-phase can be achieved by increasing the nitrogen content up to 0.15wt%, however this promotes the formation of Z-phase and π-phase as a replacement for G-phase. Since these phases have not been observed before in the 2032Nb alloy it is hard to predict how they change the long term properties of the alloy, therefore they should be keep to a minimum concentration.

Fig. 7.7 shows the equilibrium phase fractions for the optimized chemistries containing 0.05wt%, 0.025wt%, and 0wt% nitrogen respectively. All three of these alloys show a considerable improvement over the ex-service ThermoCalc equilibria, and the Super 2032Nb, and commercial 2032Nb ThermoCalc equilibria. While nitrogen does increase Z-phase concentrations it also decreases the stability for $M_{23}C_6$. As seen in the previous chapter, if $M_{23}C_6$ is kept in the intradendritic regions through homogenization treatments, its stability is not considered detrimental. However if interdendritic $M_{23}C_6$ is promoted it is best to minimize the stability and concentration of this phase, as interdendritic $M_{23}C_6$ will embrittle the steel, and cause ductility dip issues. All three of the alloys display the same NbC to G-phase transformation temperature 280°C. Compared to the linear programming optimum solution of 270°C when understabilized to 6, a drastic improvement in limiting secondary phase fraction is seen in these stabilized chemistries. It is difficult to judge whether or not G-phase will be avoided by the in-service component due to the inaccuracies in the nickel ThermoCalc database, where the transformation temperatures have been reported to be above 852°C[29]. The microstructural differences between castings (ie. static cast vs centrifugal cast, and as-cast vs. homogenzied) may also vary in which chemistry would display the best long term creep resistance. For castings left in the as-cast state, the 0.025wt% nitrogen alloy should be used to limit interdendritic $M_{23}C_6$ coarsening. For homogenized castings, the 0wt% nitrogen alloys in Table 7.6 should be used to limit Z-phase precipitation, and increase intradendritic $M_{23}C_6$ precipitation. For a centrifugally cast alloy the 0.025wt% nitrogen chemistry would be best to limit secondary phase fraction, and interdendritic coarsening.

Table 7.6: Composition of the optimized chemistries. Optimized to the stoichiometric ratio Nb/(C+6/7N)=7.7.

	Composition (wt.pct)								
	Cr	Ni	Mn	Si	C	Nb	N	W,V,Mo,Ti,Zr	P,S
High Nitrogen	20	32	1.4	0.5	0.087	1.0	0.05	< 0.05	< 0.02
Low Nitrogen	20	32	1.4	0.5	0.108	1.0	0.025	< 0.05	< 0.02
No Nitrogen	20	32	1.4	0.5	0.129	1.0	0.0	< 0.05	< 0.02

7.7 Conclusions

ThermoCalc equilbiria show that nitrogen has a positive effect in limiting G-phase formation, and suppressing its stability temperature, however increases the stability of other embrittling nitride phase such as Z-phase and π-phase. It is recommended to keep nitrogen below 0.15wt% in order limit the amount of Z-phase and π-phase formation, which in the microstructure could coarsen and agglomerate at the grain boundaries, and promote ductility dip cracking. Z-phase may not experience any liquation issues during repair welding and is deemed favorable over G-phase, although this have yet to be proven experimentally. Z-phase and π-phase are shown to only be stable if the stabilization ratio is below 8.4-9. Conforming to a $Nb/(C+6/7N) = 7.7$ ratio is encouraged in order to balance the amount of $M_{23}C_6$ and G-phase, where understabilization will promote $M_{23}C_6$ formation, and overstabilization will promote G-phase formation. Slight understabilization is better for decreasing the driving force of G-phase, and might be beneficial in homogenized casting as excess $M_{23}C_6$ can precipitate out in the intradendritic region, which does not affect the embrittlement of the steel. Understabilization can be achieved without increasing $M_{23}C_6$ fraction by increasing the nitrogen content. This will permit a higher fraction of Z-phase or π-phase in the alloy, but might be beneficial. Limiting silicon concentration is critical for reducing the driving force of G-phase, however must be balanced depending on the amount of flowability needed to cast the part.

Although titanium increasing the creep strength of the component by precipitating TiC carbides, titanium increases the driving force and stability of G-phase by freeing up niobium in solution to precipitate out with silicon as G-phase. If titanium is to be added, even in microalloy additions, it is recommend to balance the stability ratio by assuming that carbon will form with the titanium first, and the precipitate out with niobium as NbC. It is suggested to limit titanium additions to $< 0.015wt\%$.

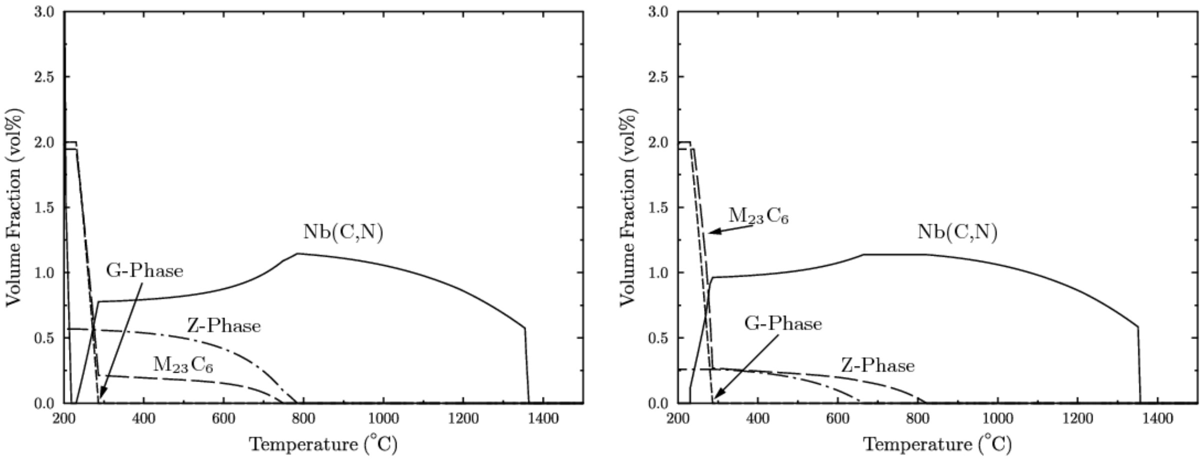

(a) N=0.05wt%

(b) N=0.025wt%

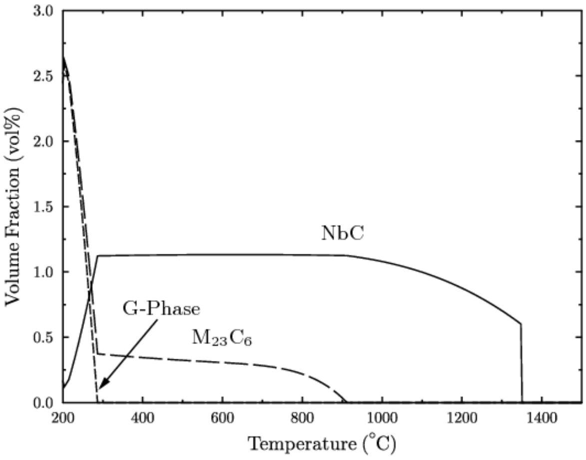

(c) N=0wt%

Figure 7.7: Equilibrium phase fraction plot from ThermoCalc of the optimized chemistries

Chapter 8

Conclusions & Recommendations

8.1 Conclusions

Varying casting parameters such as centrifugally casting, increasing wall thickness, and post homogenization treatment can be beneficial in terms of delaying G-phase precipitation, however these solutions are only beneficial for short term periods. Modifying the chemistry of the alloy is the most valuable way to limit G-phase precipitation, and $M_{23}C_6$ coarsening, reducing the cracking susceptibility of the alloy. A stabilization ratio of Nb/(C+N)= 7.7 is preferred in the chemistry maximizing the fraction of NbC precipitates, and creep rupture strength of the steel. A stabilization ratio of 7.7 will also maximize NbC coarsening during aging, which decreases the NbC to G-phase transformation rate, and increases the amount of residual NbC after long periods in service. Limiting silicon content based on how much flowability is needed in the steel, is very important for minimizing the driving force, and stability of G-phase. Nitrogen is favorable up until 0.15wt% in replacing G-phase with another intermetallic phase Z-phase, which might avoid liquation cracking issues. However, Z-phase is still an embrittling phase, where Z-phase formation and coarsening must be limited. Titanium microalloy addition are commonly used to increase the creep rupture strength of the alloy, however they also increase the stability of G-phase by freeing up niobium in solution. It is recommended to limit titanium concentrations to < 0.015wt%.

Homogenization of the alloy is important in terms of promoting the precipitation of micron sized intradendritic microconstituents which are beneficial to the microstructure, and decrease embrittlement even if they are G-phase precipitates. Understabilizing the Nb/(C+N) ratio is preferred in homogenized steels, as intradendritic $M_{23}C_6$ will precipitate, limiting coarsening of interdendritic $M_{23}C_6$. Homogenization increases the diffusional distances of ferrite stabilizers such as silicon and chromium, which increases the precipitation rates of secondary phases such as $M_{23}C_6$ and G-phase at the grain boundaries. Homogenization procedures are always beneficial, and will increase the creep life of the 2032Nb component.

Centrifugal casting is important to homogenize the grain and dendrite structure of the component, however less boundary area is produced during casting which causes a higher degree of coarsening of the embrittling secondary precipitates which increases cracking susceptibility, and decreases weldability. Centrifugal casting decreases the precipitation rate of G-phase, and increases intradendritic NbC precipitation due to increased diffusional distances for segregation.

Increasing wall thickness simultaneously increases grain and dendrite sizes, which has both positive and negative effects. If the alloy is homogenized, secondary precipitation rates will be decreased even further from the increased diffusional distances of the alloying elements. However, the larger grains produce less boundary area, where the precipitates will be able to coarsen leading to a higher embrittlement of the component. Homogenization of thick casting could influence even more intradendritic precipitation which could be beneficial to the alloy.

The outcomes of the present work shows that through an optimization in chemistry, and casting parameters the microstructure of the 2032Nb alloy after long periods of aging can be significantly improved. Refining the microstructure by limiting interdendritic G-phase and $M_{23}C_6$ precipitation and coarsening, as well as minimizing the stability temperature of G-phase, can mitigate repair weld cracking issues, increasing the serviceability of the component. If the refined chemistry, and casting methods can eliminate, or considerably lower the precipitation of G-phase, liquation cracking issues might be avoided completely.

8.2 Future Work

Further SEM/EDS analysis is needed to be completed on the design matrix samples aged up to one year. This report only analyzes the microstructural evolution up to two months which is fairly early on in the developmental stages to come to any conclusions on what the final microstructure will look like. Longer aging times will need to be analyzed to determine if the commercial 2032Nb, or Super 2032Nb alloy completely avoids G-phase formation, or which alloy better suppresses G-phase stability. Relationships between the coarsening rates of the various precipitates in the eight treatments are also not well defined at such short aging times. Longer aging times are needed to make conclusions on the benefits of wall thickness and homogenization treatments.

Experimental characterization, and aging of the nitrogen optimized chemistries proposed in the Chapter 7 would be beneficial in comparing its microstructural evolution to the design matrix, and ex-service alloys. A deal of work would need to be done on Z-phase in 2032Nb steels to see if liquation is indeed avoided in this phase during repair welding, and if neighboring G-phase could cause constitutional liquation. Mechanical tests to compare the embrittlement, weldability, and creep strength properties of the ex-service, and design matrix alloy would also be beneficial in providing context in which alloy will perform the best in service.

References

[1] C. Jaske, Materials, fabrication, and repair considerations for hydrogen reformer furnace outlet pigtails and manifolds, Technical Report, API, 2011.

[2] J. Hoffman, J. Magnan, Cast 20Cr32Ni1Nb alloy aged mechanical property improvements via chemistry modifications, in: Corrosion 2003, no. 3469, NACE International, 2003.

[3] Q. Z. Chen, C. W. Thomas, D. M. Knowles, Characterisation of 20Cr32Ni1Nb alloys in as-cast and ex-service conditions by SEM, TEM and EDX, Mater. Sci. Eng., A 374 (2004) 398–408.

[4] S. Shi, Repair weldability of heat-resistant stainless steel casings-HP45Nb, HP50Nb and 20-32Nb alloys, Ph.D. thesis, Ohio State University, 2006.

[5] E. Berghof-Hasselbcher, P. Gawenda, M. Schorr, M. Schtze, J. Hoffman, Atlas of Microstructures, Materials Technology Institute, 2008.

[6] C. W. Thomas, K. J. Stevens, M. J. Ryan, Microstructure and properties of alloy HP50-Nb: comparison of as cast and service exposed materials, Mater. Sci. Technol. 12 (1996) 469–475.

[7] T. Shibasaki, T. Mohri, K. Takemura, Experiences with Nb containing cast materials for reformer furnace, Ammonia Plant Safety & Related Facilities 40 (2000) 322–328.

[8] H. Baker, H. Okamoto, Asm handbook, volume 03 - alloy phase diagrams, 1992.

[9] B. Piekarski, Effect of Nb and Ti additions on microstructure, and identification of precipitates in stabilized Ni-Cr cast austenitic steels, Mater. Charact. 47 (2001) 181–186.

[10] H. K. Danielsen, J. Hald, On the nucleation and dissolution process of Z-phase Cr(V,Nb)N in martensitic 12%Cr steels, Mater. Sci. Eng., A 505 (2009) 169–177.

[11] D. J. Powell, R. Pilkington, D. A. Miller, The precipitation characteristics of 20% Cr/25% Ni—Nb stabilised stainless steel, Acta Metall. 36 (1988) 713–724.

[12] C. E. Jaske, Creep strength of welds in hydrogen reformer outlet manifolds, ASME Conference Proceedings 2009 (2009) 1385–1390.

[13] F. B. Pickering, S. Keown, Niobium in stainless steels, in: H. Stuart (Ed.), Niobium, Proceedings of the International Symposium, Met. Soc. AIME, Warrendale, PA, 1981, pp. 1113–1142.

[14] M. Hillert, Phase Equilibria, Phase Diagrams and Phase Transformations: Their Thermodynamic Basis, Cambridge University Press, 2007.

[15] S. G. F. Hans Lukas, B. Sundman, Computational Thermodynamics, Cambridge University Press, 2007.

[16] W. Werner, Interaction of electron beams with matter, 2012.

[17] S. Shi, J. Lippold, Microstructure evolution during service exposure of two cast, heat-resisting stainless steels – HP-Nb modified and 20-32Nb, Mater. Charact. 59 (2008) 1029–1040.

[18] T. Shibasaki, T. Mohri, K. Takemura, Experience with cast material for steam reformer furnaces, Ammonia Plant Saf. Relat. Facil. 34 (1994) 166–176.

[19] R. Singh, Niobium stabilized alloys in steam hydrocarbon reforming, Mater. Performance 49 (2009) 54–58.

[20] T. Sourmail, Literature review precipitation in creep resistant austenitic stainless steels, Mater. Sci. Technol. 17 (2001) 1–14.

[21] D. Dulieu, The role of niobium in austenitic and duplex stainless steels, Technical Report, CBMM, 2002.

[22] J. P. Shingledecker, P. J. Maziasz, N. D. Evans, M. J. Pollard, Creep behavior of a new cast austenitic alloy, Int. J. Press. Vessels Pip. 84 (2007) 21–28.

[23] H. S. Khatak, B. Raj (Eds.), Corrosion of Austenitic Stainless Steel: Mechanism, Mitigation and Monitoring, Woodhead Publishing Limited, 2002.

[24] J. Erneman, M. Schwind, P. Liu, J. O. Nilsson, H. O. Andrén, J. Ågren, Precipitation reactions caused by nitrogen uptake during service at high temperatures of a niobium stabilised austenitic stainless steel, Acta Mater. 52 (2004) 4337–4350.

[25] C. Too, Sensitisation of Austenitic Stainless Steel, Ph.D. thesis, University of Cambridge, 2002.

[26] X.-g. Zhou, Z.-y. Liu, X.-q. Yuan, D. Wu, G.-d. Wang, X.-h. Liu, Modeling of strain-induced precipitation kinetics and evolution of austenite grains in Nb microalloyed steels, J. Iron. Steel Res. Int. 15 (2008) 65–69.

[27] V. T. Ha, W. S. Jung, Effects of heat treatment processes on microstructure and creep properties of a high nitrogen 15Cr15Ni austenitic heat resistant stainless steel, Materials Science and Engineering: A 528 (2011) 7115–7123.

[28] D. Porter, D. Easterling, Phase Transformations in Metals and Alloys, 2nd Edition, Chapman & Hall, 1992.

[29] J. Hoffman, High temperature aging characteristics of 20Cr32Ni1Nb castings, in: Corrosion 2000, no. 512, NACE International, 2000.

[30] R. C. Ecob, R. C. Lobb, V. L. Kohler, The Formation of G-phase in 20/25 Nb Stainless Steel AGR Fuel Cladding Alloy and its Effect on Creep Properties., J. Mater. Sci. 22 (1987) 2867–2880.

[31] T. Sourmail, H. Bhadeshia, Microstructural evolution in two variants of NF709 at 1023 and 1073 k, Metall. Mater. Trans. A 36 (2005) 23–34.

[32] J. K. L. Lai, Precipitate phases in type 321 steel, Mater. Sci. Technol. 1 (1985) 97–100.

[33] P. Landon, R. Caligiuri, P. Duletsky, The influence of the M23(C,N)6 compound on the mechanical properties of type 422 stainless steel, Metall. Mater. Trans. A 14 (1983) 1395–1408.

[34] V. G. Gavrilnjuk, H. Berns, High Nitrogen Steels, Springer, 1999.

[35] M. Atols, Raw material proposal for characterization project, 2010.

[36] I. L. M. L.H. De Almeida, A.F. Ribeiro, Microstructural characterization of modified 25 Cr-35Ni centrifugally caststeel furnaces tubes, Mater. Charact. 49 (2003) 219–229.

[37] H. Danielsen, J. Hald, Influence of Z-phase on long-term creep stability of martensitic 9-12%Cr steels, in: 9th Liege Conference on Materials for Advanced Power Engineering, p. 310.

[38] H. Hughes, Complex nitride in Cr-Nb steels, J.I.S.I. 205 (1967) 775–778.

[39] G. Knowles, The creep strength of a 20%Cr-25%Ni-Nb steel containing controlled particle dispersions, Met. Sci. 11 (1977) 117–122.

[40] A. Golpayegani, H.-O. Andrn, H. Danielsen, J. Hald, A study on Z-phase nucleation in martensitic chromium steels, Materials Science and Engineering: A 489 (2008) 310–318.

[41] H. K. Danielsen, J. Hald, A thermodynamic model of the Z-phase Cr(V,Nb)N, Calphad 31 (2007) 505–514.

[42] S. Shi, J. Lippold, J. Ramirez, Hot ductility behavior and repair weldability of service-aged, heat-resistant stainless steel castings, Weld. J. 89 (2010) 210–217.

[43] D. M. Knowles, C. W. Thomas, D. J. Keen, Q. Z. Chen, In service embrittlement of cast 20Cr32Ni1Nb components used in steam reformer applications, Int. J. Press. Vessels Pip. 81 (2004) 499–506.

[44] R. Colwell, J. Hoffman, Weld cracking in Nb modified heat resistant castings, a microstructural investigation, in: Corrosion 98, no. 423, NACE International, 1998.

[45] K. Nishimoto, K. Saida, M. Inui, M. Takahashi, Evaluation of hot-cracking susceptibility by miniature spot-varestraint testing. repair weld cracking of long term exposed HP-modified heat-resisting cast alloys. (report 1)., Quarterly Journal of the Japan Welding Society 18 (2000) 438–448.

[46] K. Nishimoto, K. Saida, M. Inui, M. Takahashi, Changes in microstructure of HP-modified heat-resisting cast alloys with long term aging. repair weld cracking of long term exposed HP-modified heat-resisting cast alloys. (report 2), Quarterly Journal of the Japan Welding Society 18 (2000) 449–458.

[47] K. Nishimoto, K. Saida, M. Inui, M. Takahashi, Mechanism of hot cracking in HAZ of repair weldments. repair weld cracking of long term exposed HP-modified heat-resisting cast alloys. (report 3), Quarterly Journal of the Japan Welding Society 18 (2000) 590–599.

[48] T. Sourmail, H. K. D. H. Bhadeshia, D. J. C. MacKay, Neural network model of creep strength of austenitic stainless steels, Mater. Sci. Technol. 18 (2002) 655–663.

[49] B. Xiao, J. D. Xing, J. Feng, C. T. Zhou, Y. F. Li, W. Su, X. J. Xie, Y. H. Cheng, A comparative study of Cr 7 C 3 , Fe 3 C and Fe 2 B in cast iron both from ab initio calculations and experiments, Journal of Physics D: Applied Physics 42 (2009) 115415.

[50] T. S. Jo, J. H. Lim, Y. D. Kim, Dissociation of Cr-rich M23C6 carbide in alloy 617 by severe plastic deformation, J. Nucl. Mater. 406 (2010) 360–364.

[51] K. L. Holman, E. Morosan, P. A. Casey, L. Li, N. P. Ong, T. Klimczuk, C. Felser, R. J. Cava, Crystal structure and physical properties of Mg6Cu16Si7-type M6Ni16Si7, for M = Mg, Sc, Ti, Nb, and Ta, Mater. Res. Bull. 43 (2008) 9–15.

[52] Z.-K. Liu, Computational thermodynamics using thermo-calc, 2010. ThemoCalc & Dictra Training Course.

[53] Y. Y. Song, Thermodynamic Study on B and Fe Substituted Cr23C6 Using First-Principles Calculations, Ph.D. thesis, Pohang University of Science and Technology, 2010.

[54] J. Vitek, G-phase formation in aged type 308 stainless steel, Metallurgical and Materials Transactions A 18 (1987) 154–156.

[55] D. Montgomery, G. Runger, Applied Statistics and Probability for Engineers, 4th Edition, John Wiley & Sons, 2006.

[56] H. Spliid, Design and analysis af experiments with k factors having p levels, 2002.

[57] W. Jasiński, Solutionizing of IN 519 superalloy after long-term exposure, Adv. Manuf. Sci. Technol. 32 (2008) 69–80.

[58] T. Balk, J. Nychka, Microscopy Lessons, Technical Report, University of Kentucky, 2006.

[59] K. Shinozaki, H. Kuroki, Y. Nakao, K. Nishimoto, M. Inui, M. Takahashi, Deterioration of weldability of long term aged HP heat-resistant cast steel containing Nb, Mo and W, Quarterly Journal of the Japan Welding Society 16 (1998) 223–232.

[60] T. Zhang, Q. Wang, X. Song, H. Fu, Effect of electromagnetic centrifugal casting on solidification

microstructure of cast high speed steel roll, Materialwissenschaft und Werkstofftechnik 42 (2011) 557–561.

[61] W. Wolczynski, W. Krajewski, R. Ebner, J. Kloch, The use of equilibrium phase diagram for the calculation of non-equilibrium precipitates in dendritic solidification. theory, Calphad 25 (2001) 401–408.

[62] R. C. Gonzalez, R. E. Woods, Digital Image Processing, Addison-Wesley Longman Publishing Co., Inc., 1992.

[63] S. Suzuki, K. be, Topological structural analysis of digitized binary images by border following, Computer Vision, Graphics, and Image Processing 30 (1985) 32–46.

[64] Z. Zhu, C. Cheng, C. Liu, J. Zhao, Microstructure evolution and nitridation in an as-cast 25Cr-35Ni-1Mo radiant tube after long-term service, Metallurgical and Materials Transactions A 43 (2012) 4525–4531.

[65] J. Laigo, F. Tancret, R. L. Gall, J. Furtado, EBSD phase identification and modeling of precipitate formation in HP alloys, Advanced Materials Research 15-17 (2006) 702–707.

[66] B. Dutta, E. J. Palmiere, C. M. Sellars, Modelling the kinetics of strain induced precipitation in Nb microalloyed steels, Acta Materialia 49 (2001) 785–794.

[67] F. Perrard, A. Deschamps, P. Maugis, Modelling the precipitation of NbC on dislocations in [alpha]-fe, Acta Materialia 55 (2007) 1255–1266.

[68] J. Shim, E. Kozeschnik, W. Jung, S. Lee, D. Kim, J. Suh, Y. Lee, Y. Cho, Numerical simulation of long-term precipitate evolution in austenitic heat-resistant steels, Calphad 34 (2010) 105–112.

[69] Minitab, Technical support document rank deficiency, 2010. Http://www.minitab.com/support/documentation/Answers /RankDeficiency.pdf.

Appendices

ThermoCalc Chemistry Optimization Programs & Scripts

A.1 ThermoCalc Scripts

ThermoCalc software contains both a windows version which is a typical user interface, and a classical console version which requires input of subsequent command-line inputs. The console version will be primarily discussed in this document as it will be used later as a subroutine in the executable module to output the equilibrium of the compositional matrix array used for chemistry optimization. The console version is separated into multiple modules for first initializing the system, setting conditions for the equilibrium, running either a *stepping* routine (1-dimenional) for computing property diagrams or *mapping* routines (2-4 dimensional) for computing phase diagrams, and finally a graphing module. A flow chart of each of the modules along with their associated commands is outlined in Fig. A.1.

Typically you will want to create a new file in the computers directory for every equilibrium calculation you are going to run. Inside this folder copy a shortcut to the ThermoCalc classic executable. When you enter the shortcut any files that will be saved will be saved in that directory. Upon entering the console version the first step is to save every command you input in the console into a log file. The command **s-l-f**, or set-log-file will create a .log file in directory that the ThermoCalc shortcut is with the filename specified in the following argument. The next line is the heading information to describe what the following file will do.

```
s-l-f <filename>  @@set log file
```

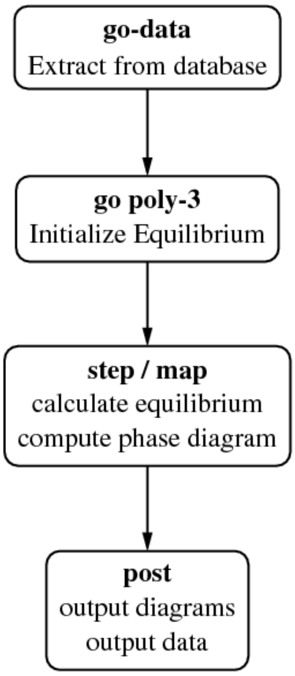

Figure A.1: Flow chart of the set of the modules for calculating phase diagrams with the console version of ThermoCalc. The bolded text in each box are the associated commandeds to enter into each module

```
Calculate isopleth of 2032Nb system @@heading for the .log file
```

The next step is to go into the appropriate initialization module. For equilibrium calculations most of the time you will use the **data** module to first initialize the system. The data module gives the most amount of freedom to set the specific criteria on the system, however there is a simplified module that will ask the user questions to specify the parameters for the system. The simplified module is accessed by first going into the **poly-3** module by typing the command "go p-3", and then typing "def-mat". For the purposes of this script we will need to suspend certain constituents in the G-phase sublattice module so the data module should be used. The last thing to note is that if the user wants to perform Scheil calculations, the module command is simply "go scheil" it is set up the same way as the "def-mat" module where it will ask you a series up questions to set up the parameters.

The default database ThermoCalc will draw from is the **TCFE*** database, TCS Steels/Fe-alloys database. The version used in this document is version 6, and does not contain G-phase; however version 7 has recently been released and does now contain G-phase. The **TTNI8** database, TT Ni-based superalloys database, was appended to the system to include G-phase in the system. It should be noted that the TT databases do not contain volumetic data whereas, the TC databases do. Therefore volumetric parameters will have to be calculated in a post process if the data is imported from a TT database.

The first step is to specify the components in the system and then import the appropriate phases for both the TCFE6 database, and the TTNI8 database. The **rej P *** command on line 5 rejects all the phases in the database, where the * is a wild card term meaning *all*. If the user does not know what phases should be present in the system, the lines 5 and 6 can be omitted an a generic run can be performed. It is necessary to specify the phases in the system, as sometimes phases that are not present in any literature on the alloy will be stable in the equilibrium calculation, which then cannot be verified. In the TCFE6 database every phase specified for the system should be restored in line 6. Be sure to input the **get** command after to pull the relevant information from the database. To reject certain constituents of a phase the command **rej c** < *phase* > < *sublattice* > can be input, where the user will then be prompted for which element they would like to reject. This operation can also be done in the windows version of ThermoCalc.

```
3  go data
4  def-ele Fe Cr Ni Si Nb C Mn N Mo
5  rej P *
6  res P FCC_A1 M7C3 M23C6 M6C MC Liq Z-Phase
7  get
8  app TTNI8
9  def-ele Fe Cr Ni Si Nb C Mn Ti Mo
10 rej P *
11 res P G_Phase
12 rej c g-phase 1
13 fe
14
15 rej c g-phase 3
16 Cr
```

```

rej c g-phase 3
Mn

get
```

After the system has been initialized it is time to set up the conditions for equilibrium. The command **s-c** is short for set-condition, where the intensive properties such as temperature, and pressure, and extensive properties such as the size of the system (e.g. $n = 1mol$), and the composition (x_i) need to be defined. Temperature is in kelvin, and composition is defined as weight fraction **w(element)**, or mole fraction **x(element)**. Weight fractions should be input for all but one of the components, which will be the dependent variables. This will make sure that the sum of the weight fractions is equal to unity. The command **c-e** calculates the equilibrium, while **l-e** lists the equilibrium either on screen or in this case to a file eq.txt. The conditions set will be the initial equilibrium calculated, and does not hold any relevance over the subsequent mapping or stepping functions. Next, is to map the phase diagram over the set axis variable limits. **s-a-v 1 t** sets the y-axis to temperature with a range between 400-1800K, and **s-a-v 2 w(N)** sets the x-axis to the weight fraction of nitrogen. The **map** command will initiate the mapping procedure.

```
go p-3
s-c t=1089 n=1 p=101325
s-c w(Cr)=0.19 w(Ni)=0.31 w(Si)=0.005
 ⋮
```

```
c-e
l-e
eq.txt
VWCS
s-a-v 1 t 410 1800 27.8
s-a-v 2 w(N) 0 0.3 0.001
map
```

Alternatively, to produce property diagrams (dependent vs. independent variables) only the first axis will need to be specified, followed by the **step** command. ThermoCalc will initiate its global minimization procedure, and incrementally step along the axis between the set boundaries. Stepping is a much faster operation than mapping and should be considered depending on what type of information needs to be analyzed. There are numerous options for the stepping function, but in this case the default **NORMAL** command was chosen. More information about these options can be read in the ThermoCalc TCC user manual supplied with the software package.

```
31 s-a-v 1 t 410 1800 27.8
32 step @@ an alternative to the mapping procedure
33 NORMAL
```

After the mapping or stepping functions have completed, the user should proceed to the **post** module for producing phase, and property diagrams. For the mapping command the default diagram contains both of the variable axis set prior to mapping. For stepping the default property diagram sets the y-axis to the molar phase fraction of each stable phase in the system over variable axis set above. The **s-d-a** command stands for 'set-diagram-axis' where in the case of line 35, the x-axis is being changed to display the temperature in Celsius. The **s-s** command stand for 'set-scaling-status', and can be used to set the axis maximum and minimum values. The **plot** will show the resulting diagram in a separate window. It is important to know the composition of each of the phases after stepping or mapping procedures, where the constituents that occupy each sublattice, and their site fractions can be determined. The composition of a phase can be determined by changing the y-axis to represent the mole fraction of a phase, where the wild card represents every component in the phase. Lastly, to export the data of a property diagram, the **l-d-t** command will export the data either to text or to excel. Note that the extension on the excel output is *.xls*, and not *.xlsx*.

```
34 post
35 s-d-a x t-c
36 s-s y n 0 0.1
37 plot
38 s-d-a y x(FCC_A1#1,*)
39 *
```

```
plot
FCC_A1#1.ps
l-d-t
FCC_A1#1.xls
```

After the program is exited, the .log file can be accessed, and will contain all of the commands inpute during the ThermoCalc session. To run the .log file through ThermoCalc, change the extension on the file from *.log* to *.tcm*.

A.2 Batch ThermoCalc Executables

In the present study we are interested in seeing how nitrogen, and titanium affect the resulting microstructure, as well as their interactions with the other components in a 2032Nb alloy. From the ASTM specification for 20Cr-32Nb-Nb the compositional matrix in Table 3.3 can be used see the ranges for each element that will be explored. In ThermoCalc the **stepping** command will be used over the temperature range $T_m - T_{rt}$ for finite compositions of the alloy. Therefore, certain levels in the compositional ranges for each element will need to be decided where then equilibrium will be calculated for all possible combinations of these finite chemistries. If a maximum, median, and minimum values are chosen for each range than ThermoCalc will need to run stepping procedures for $3^7 = 2187$ chemical compositions. Writing these ThermoCalc files out manually would be quite time consuming, so two batch programs were written in Visual C# to automatically write and run numerous ThermoCalc log files.

Table A.1: Range of 20-32Nb Stainless Steel compositions investigated in the ThermoCalc test matrix. Compositional ranges correspond to ASTM A351, grade CT15C.

	Ni	Cr	Nb	Si	Mn	C	N/Ti	W,Mo,Ti,Zr
Compositional Range (wt.pct)	31 - 34	19 - 21	0.5 - 1.5	0.5 - 1.5	0.15 - 1.5	0.05 - 0.15	0 - 0.3	<0.05

The first program titled *BatchTCC_Comp* shown in Fig. A.2 takes the compositional range specified, increments each component by the # of iterations set by the user, and then compiles .tcm files for each chemistry combination and runs the scripts. The y-axis is specified by the user where depending on their choice either a stepping or mapping procedure will take place. For this program the x-axis is suppose to be a component, but other properties like temperature and pressure can be used as well. The program outputs both the postscript, and the excel files for the phase or property diagram, and also graphs the composition for each stable phase in the calculation. For this script the relevant phases must be specified, which can be determined by manually doing a test run of the system through ThermoCalc beforehand. The second program titled *BatchTCC_Temp* is a much simpler version of the first program where only the temperature can be specified as the x-axis for a stepping procedure. If all of the alloy element boxes are used, and the # of iterations is limited to three, the process should be expected to take at least 30 hrs if the '# of simultaneous processes' is set to 3-5. Both the executable installations, and the source code Visual Studio solutions can be downloaded from http://tinyurl.com/9rmjuec.

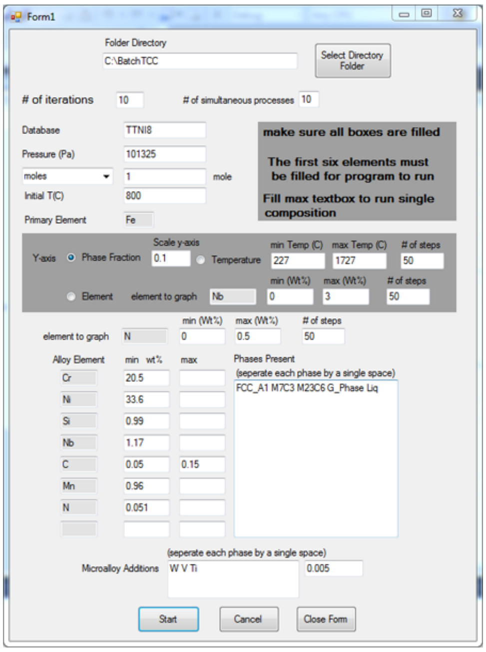

Folder Directory: C:\BatchTCC

# of iterations: 10
# of simultaneous processes: 10

Database: TTNI8
Pressure (Pa): 101325
moles: 1 mole
Initial T(C): 800
Primary Element: Fe

make sure all boxes are filled

The first six elements must be filled for program to run

Fill max textbox to run single composition

Y-axis ● Phase Fraction
Scale y-axis: 0.1
○ Temperature
min Temp (C): 227
max Temp (C): 1727
# of steps: 50
○ Element
element to graph: Nb
min (Wt%): 0
max (Wt%): 3
# of steps: 50

element to graph: N; min (Wt%): 0; max (Wt%): 0.5; # of steps: 50

Alloy Element	min wt%	max
Cr	20.5	
Ni	33.6	
Si	0.99	
Nb	1.17	
C	0.05	0.15
Mn	0.96	
N	0.051	

Phases Present (seperate each phase by a single space): FCC_A1 M7C3 M23C6 G_Phase Liq

Microalloy Additions (seperate each phase by a single space): W V Ti
0.005

Figure A.2: GUI interface for batch running a compositional matrix through ThermoCalc where the x-axis is a component of the system, and the y-axis is either the phase fraction, another component of the system, or temperature.

A.2.1 Preparing for Compilation

After the process has been completed it is important to copy all of the excel file outputs into a separate folder, as some of the subsequent scripts can not handle searching for files through subfolders. Secondly, Thermocalc outputs the excel files in .xls format which conflicts with some of the Matlab code that can

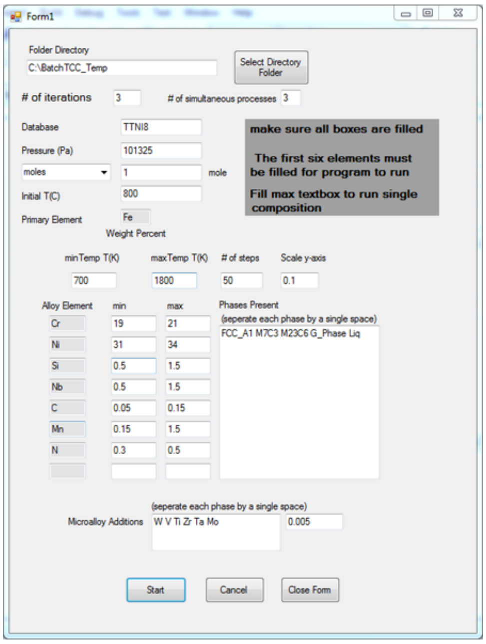

Folder Directory: C:\BatchTCC_Temp

# of iterations: 3

# of simultaneous processes: 3

Database: TTNI8

Pressure (Pa): 101325

moles: 1 mole

Initial T(C): 800

Primary Element: Fe

make sure all boxes are filled

The first six elements must be filled for program to run

Fill max textbox to run single composition

Weight Percent

minTemp T(K)	maxTemp T(K)	# of steps	Scale y-axis
700	1800	50	0.1

Alloy Element	min	max
Cr	19	21
Ni	31	34
Si	0.5	1.5
Nb	0.5	1.5
C	0.05	0.15
Mn	0.15	1.5
N	0.3	0.5

Phases Present (seperate each phase by a single space): FCC_A1 M7C3 M23C6 G_Phase Liq

Microalloy Additions (seperate each phase by a single space): W V Ti Zr Ta Mo 0.005

Figure A.3: GUI interface for batch running a compositional matrix through ThermoCalc where the x-axis is a temperature range.

only open .xlsx formatted excel files. The first step is to go into the top folder of the directory where the batch ThermoCalc process saved the files. The batch process program saves all of the steping, or mapping plots in the format “$< element >< composition >$...”, where for a 20Cr32Ni alloy the file name would be “Cr20Ni32...”. For Windows 7 operating systems, find the search bar in the file explorer, and type “Cr*.xls”. This will find all the excel files that start with the characters ‘Cr’. Copy and save all of these files to another folder. Next, download the files named **xls2xlsx.rar** from http://tinyurl.com/9zsdwf6. Extract, and open the excel file. In the first section type in the path of the copied .xls files in the “Original File Path” cell, and make a new folder for the .xlsx files, and type its path in the “Destination File Path” cell. Click the “Convert to xlsx” button, and all the .xls file should be saved as .xlsx files in the new folder. The same can be done for any compositional data for a specific phase by specifying the cells under the “Compostion xls File” title.

A.3 Matlab Code - Compiling Mass ThermoCalc Data To Excel

Once all of the '.xlx' files have been converted to '.xlsx' format, and are copied to a single file (eg. '_xlsx'), the Matlab distribution files for the batch ThermoCalc application can be employed to extract, and compile all of the relevant information needed to produce matrix arrays, and linear regression fitting. From the volume fraction plots, there are specific points on the curves for each phase that can be useful when trying to quantify the optimization of an alloy based on equilibrium microstructure.

A.3.1 Finding the solubility temperature, and the terminal phase fractions for intermetallics and Chrome Carbides

The first Matlab script will be used for compiling all the relevant information about any intermetallic phases, or chrome carbides that may have precipitated during long term aging. For example, the G-phase curve in Fig. A.4a has three definable points that can be analyzed for all the chemistries when determining the minimization of G-phase. The first definable point is the temperature at which the phase starts to precipitate, referred to as the stability temperature. The chemical formula of G-phase is $Ni_{16}Nb_6Si_7$, where niobium will be needed to facilitate the precipitation of this intermetallic. The precipitation of G-phase is known to occur through a transformation mechanism with NbC [3, 11, 17]; However, if there is excess niobium at the dendrite boundaries the G-phase will be able to precipitate without consuming NbC precipitates. Excess niobium precipitating out as G-phase is indicative of the plateau region shown in Fig. A.4a, where NbC remains unaffected. Once a certain temperature is reached $\mathrm{M_{23}C_6}$ becomes stables, promoting the dissolution of NbC, freeing up the niobium to precipitate even more G-phase. Once all of the NbC has been dissolutioned and all the niobium has been exhausted in solution and precipitated as G-phase; the maximum, and terminal phase fraction for G-phase has been reached, denoted as point 3 on Fig. A.4a. Point 3 must also be defined as the terminal phase fraction, meaning that for any subsequent decreases in temperature there will be only minor fluctuations in the equilibrium phase fraction. This will avoid any situations where the driving force of the examined phase would start to decrease with decreasing temperature, where it could eventually become metastable, and replaced with another phase.

For Matlab to be able to define these points for each chemistry in the design matrix they must be formulated as mathematical expressions. The stability temperature can be defined as $m^\alpha > 0$, where m is the phase fraction (mol%) for phase α. Identifying the Plateau region can be achieved by finding where $\partial m^\alpha / \partial T \approx 0$, and $\partial^2 m^\alpha / \partial T^2 \approx 0$. Finding the maximum terminal phase fraction is done in the same way as the plateau region with the added conditions: $max(m^\alpha)$, and at $max(m^\alpha)$, $m^\alpha / \partial T^2 \approx 0 \; \forall \; T \in \{T_x \ldots T_{rt}\}$, where T_x is the temperature where $max(m^\alpha)$.

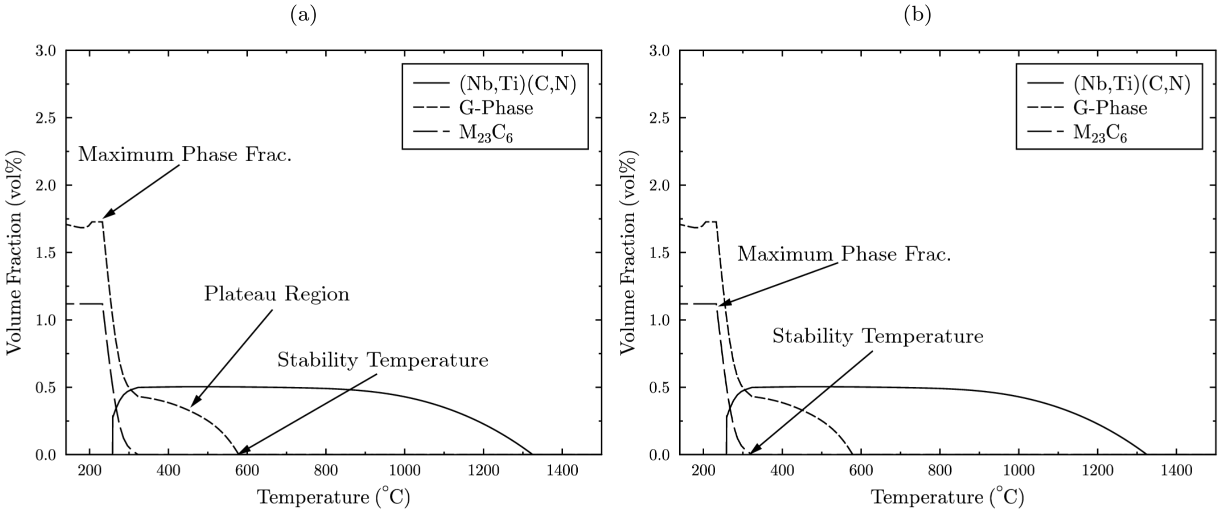

Figure A.4: The volume fraction of each phase over a temperature range contains three notable regions; the stability temperature, the plateau region, and the maximum volume fraction. These three points are outlined for a) G-Phase, b) and $M_{23}C_6$ of an alloy with the composition Cr19-Ni31-Si0.5-Nb0.5-C0.05-Mn0.825-Ti0.05.

The Matlab distribution files for this section can be found at http://tinyurl.com/8fq4mrj, under *'precipitate_script'*. The Matlab files are given separately, but you can download the full distribution by downloading the *'ThermoCalc_Script1.rar'* file. The two main scripts that run the program are *'allxls.m'*, and *'findeq.m'*. *'allxls.m'* is used as a batch processing of all the *.xlsx* files produced by ThermoCalc, where each file in the directory listed on Line 1 of the script will go through the *'findeq.m'* script and then appended to a excel file for further use. *'findeq.m'* is the script that extracts the information described above, shown in Fig. A.4a, and Fig. A.4b.

The first part of the script extracts the relevant data, and filters out all the unnecessary phases. Line 23 & 24 gets the row index for the row closest to T=400°C, and T=100°C. Line 29 extracts the data between this temperature range for the current phase in the for loop. The temperature range 100-400°C was chosen as the intermetallic phases and the the $M_{23}C_6$ phase have been observed to be stable within this temperature range with ThermoCalc. This is mainly due to the underestimation in the driving force of G-phase predicted by ThermoCalc in the TTNI8 database. Once G-phase is added to an iron database (TTFE*), this range is likely to change to above 800°C, as G-phase is seen to be stable in niobium stainless steel alloys at this temperature [11, 18, 42]. The *If* statement in line 31 passes each phase to the next step if the average phase fraction between 100-400K is less than 7%, the maximum phase fraction is less than 10%, and the mean lower threshold is above zero. This is assuming an upper bound on the phases under question, which is a reasonable assumption for the 2032Nb precipitates as literature has never cited a phase fraction for any intermetallics (e.g. G-phase) or chromium carbides above 10 vol%. Setting these bounds also helps filter out strange FCC iterations (eg. FCC_A1#3, FCC_A1#4) that ThermoCalc predicts for very low temperatures, which have a very high driving force. Experimentally no other FCC phases other than MC carbides, and the solution phase were found, so it is appropriate to disregard these other FCC iterations. It should be noted that if this script is to be applied to other systems these conditions may need to be changed. The last conditions filters out the (Nb,Ti)(C,N) phase, or FCC_A1#2 phase, which is addressed in the second, separate script. *finphase* on line 34 collects the phase names of the phases that pass the criteria in Line 32. The next loop goes through each phase in *finphase*.

```
23 [~,Tx]=min(abs(data(:,1)-400));
24 [~,Tend]=min(abs(data(:,1)-100));
25
26 for phase = phases
27   [~,y]=find(ismember(headertext, phase(1,1)));
28  %get submatrix of phase from 400C to rt.
29  subphase=data(Tx:Tend,y);
30
31   if mean(subphase) < 0.07 && mean(subphase) > 6E-4 ...
32           && max(subphase)< 0.10  ...
33           && strcmp(phase(1,1), 'NP(FCC_A1#2)')==0
34                   finphase = [finphase phase(1,1)];
```

```
35   end
36 end
```

For each phase the derivative, and second derivative of the curve are calculated using the forwards difference method ($i \rightarrow i+1$). The slope between points i, and $i+a$ was also calculated where a is an arbitrary value used to determine if the curve has become constant for further decreases in temperature. For the experiments discussed in this thesis the value of a was set at 8.

```
43 % Gets index of current phase for data
44 [~,y]=find(ismember(headertext, phase(1,1)));
45 datPhase = data(:,y);
46 dn = length(datPhase)-1;
47 dphase = zeros(dn,1);
48 dphaseI = zeros(dn,1);
49 ddphase = zeros(dn-1,1);
50 dChange = 8;
51
52 for i=1 : dn-dChange
53   dphaseI(i)=abs((datPhase(i+1)-datPhase(i))/(temp(i)-(temp(i+1)-0.1)));
54 end
55 for i=1 : dn-dChange
56   dphase(i)=abs((datPhase(i+dChange)-datPhase(i))/(temp(i)-temp(i+dChange)))
       ;
57 end
58 for i=1 : dn-dChange
59   ddphase(i)=abs((dphaseI(i+1)-dphaseI(i))/(temp(i)-(temp(i+1)-0.1)));
60 end
61 npm = data(:,y);
62 dtemp = temp(2:length(temp));
```

Line 63 creates an index n, for counting the number of points in *dphase*(i), which calculated the derivative of the original curve between i, and $i+8$. $mxval$ is the maxium phase fraction attained by the original curve, while $mxIdx$ is the index of this value, and $stabTemp$ is the index of first instance of $m^{\alpha} > 0$.

```
63  n = length(dphase)-1;
64  k=1;
65  mxVal = max(npm);
66  mxIdx = find(npm==mxVal, k,'first');
67  stabTemp = find(npm,k,'first');
```

Next, the script needs to go through the phase fraction curve, and its derivative, and find the maximum terminal phase fraction, and if there is a plateau region. This can be achieved by going along each curve, first determining if the driving force for precipitation remains constant, or the phase fraction remains constant, between i and $i+a$, and then if this point is in a plateau region, or if it is the terminal phase fraction.

```
78  if (dphase(k,1) < 2E-5) && (abs(npm(k+1,1)) > 6E-4) ...
79          && mean(npm(k:k+stbRng,1)) <= mxVal ...
80          && mean(npm(k:k+stbRng,1)) > mxVal-0.003 ...
81          && mean(ddphase(k:k+stbRng,1))< 2E-6...
82          && (dtemp(k) < 800)
83          ⋮
```

```
102         break;
103 elseif(dphase(k,1) < 2E-5) && (abs(npm(k+1,1)) > 6E-4) ...
104         && mean(ddphase(k:k+stbRng,1))< 2E-6...
105         && (dtemp(k) < 800) && (dtemp(k) > 250)
106         platArrPh = [platArrPh; {data(k-1,y)}];
107         platArrT = [platArrT; {dtemp(k)}] ;
108         isPlateau = 1;
109 end
```

The If statement in line 78 determines if the driving force remains constant between k (which is just another iterative index similar to i), and $k + stbRng$, where *stbRange* is the a parameter, and if the phase fraction is terminal. This will pass if the first derivative, or the slope of the curve is close to zero ($2E-5$), and if the phase fraction is within a threshold between $mxVal$ (Maximum phase fraction), and an arbitrary lower threshold, $mxVal - 0.003$. The other conditions of this If statement determines if the second derivative, or the curvature between k, and $k + stbRng$ ($i \rightarrow i + a$) is close to zero, and if the temperature is less than a certain temperature (eg. 800). The $T < 800$°C was chosen from examination of ThermoCalc outputs, where G-phase, and $M_{23}C_6$ were never stable at temperatures greater than 800°C. Once G-Phase is included in the TCFE* database this condition may not be true, as the actual transformation temperature for G-phase in creep resistant stainless steels is 852°C[29]. If the phase fraction passes these conditions it will be labeled as $'Stable'$, meaning a terminal phase is found, and it will break out of the For loop.

If these conditions are not met the phase fraction will go through another If statement on Line 103, which is almost the same as the If statement on Line 78 without the conditions that the phase fraction needs to be close to the maximum value $mxVal$. If these conditions pass they will be added to an array $platArrPh$ which will contain the phase fractions for all points on the curve that meet these conditions, and another array $platArrT$ which will contain the temperature. A boolean value called '$isPlateau'$ will be given to this phase. Once the terminal phase fraction is found on Line 78, it will go through a gate labeling the phase as $'Plateau\ Stable'$ to indicate that a plateau was found, and the average of $platArrPh$, and $platArrT$ will be taken and reported as the point where the plateau of the curve is found. If no terminal phase fraction is found, the maximum of the phase will simply be reported, and the phase will be labeled $'Not\ Stable'$ if no plateau is found, and $'Plateau\ Not'$ if a plateau is found.

This script will be executed for each composition in the 'allxls.m' file, and will output the results to a .xlsx file. An example of the resulting table is shown in Table A.2. This table can now be reordered by grouping the data based on each phase for comparative purposes.

Table A.2: Example of the output from the Matlab script ’findeq.m’, which looks at the intermetallic, and chrome carbide phases that might precipitate during long term aging. NPM represents the mole fraction of a phase.

Name	Phase	T (Max Ph.Frac.)	NPM (Max Ph.Frac.)	Stability Temp	Stability Ph.Frac.	Label	T (Plateau)	NPM (Plateau)
Cr19Ni31Si0.5Nb0.5 C0.05Mn0.15Ti0.05	’NP(G_PHASE)’	206.85	0.017219	565.85	0	Plateau Stable	450.85	0.002926
Cr19Ni31Si0.5Nb0.5 C0.05Mn0.15Ti0.05	’NP(M23C6)’	221.85	0.008361	320.7314	0	Stable		
Cr19Ni31Si0.5Nb0.5 C0.05Mn0.15Ti0.175	’NP(G_PHASE)’	212.9412	0.024289	645.85	0	Plateau Not	450.85	0.010134
Cr19Ni31Si0.5Nb0.5 C0.05Mn0.15Ti0.175	’NP(M23C6)’	221.3236	0.010238	335.85	0	Stable		
Cr19Ni31Si0.5Nb0.5 C0.05Mn0.15Ti0.175	’NP(MC)’	287.5816	0	287.5816	0	Not Stable		
Cr19Ni31Si0.5Nb0.5 C0.05Mn0.15Ti0.3	’NP(G_PHASE)’	211.85	0.028125	687.0555	0	Plateau Not	440.85	0.017198
Cr19Ni31Si0.5Nb0.5 C0.05Mn0.15Ti0.3	’NP(M23C6)’	211.85	0.008444	338.5616	0	Not Stable		
Cr19Ni31Si0.5Nb0.5 C0.05Mn0.825Ti0.05	’NP(G_PHASE)’	232.3848	0.01602	565.85	0	Plateau Stable	455.85	0.002844
Cr19Ni31Si0.5Nb0.5 C0.05Mn0.825Ti0.05	’NP(M23C6)’	232.3848	0.01011	315.85	0	Stable		

A.3.2 Finding Maximum (Nb,Ti)(C,N) Phase fraction, composition, and terminal temperature

The second Matlab script will be used to compile useful information on (Nb,Ti)(C,N) for each chemistry in the compositional matrix. Since (Nb,Ti)(C,N) is of a cubic NaCl structure, which is the same structure as the solution phase (austenite), ThermoCalc creates the (Nb,Ti)(C,N) phase as a new composition set of the FCC phase. Therefore, in ThermoCalc the solution phase is denoted as FCC_A1#1, and (Nb,Ti)(C,N) is denoted as FCC_A1#2. For each chemistry iteration, FCC_A1#2 contains the end members $(\mathrm{Nb, Ti})_1(\mathrm{C, N})_1$, but the site fractions, or constituents fractions are uncertain. Furthermore, differentiation between NbC, and TiC is not made, and will be grouped into one phase called FCC_A1#2. This information cannot give us distinct phase fractions of NbC, and TiC, as the solubility of titanium in NbC, and niobium in TiC is unknown. For the purpose of this study it will be assumed that these two constituents (niobium, and titanium) are mutually exclusive to their respective phases, and a volume fraction of each will be presented. To determine the composition of the MC carbides, a plot consisting of the mole fraction of constituents of the FCC_A1#2 phase along the temperature range, $\mathrm{T_{rt}} \rightarrow \mathrm{T_m}$, must be specified. Fig. A.5b illustrates an example of a compositional plot of FCC_A1#2, which shows that the composition of FCC_A1#2 can fluctuate based on the solubility of the elements, and the stable phases in the system. To see how the solubilities of titanium and niobium in (Nb,Ti)(C,N) change with variations in alloy composition, the element fractions in FCC_A1#2 can be extracted at specific temperatures for comparison. As illustrated in Fig. A.5b Matlab should extract the temperatures and the constituent fraction of FCC_A1#2 at the solubility limit of titanium, the maximum phase fraction of FCC_A1#2, and the dissolution temperature of FCC_A1#2. Due to an error in ThermoCalc reporting constituent fractions of a phase, these fractions do not do not drop to zero once the phase becomes unstable as seen in Fig. A.5b.

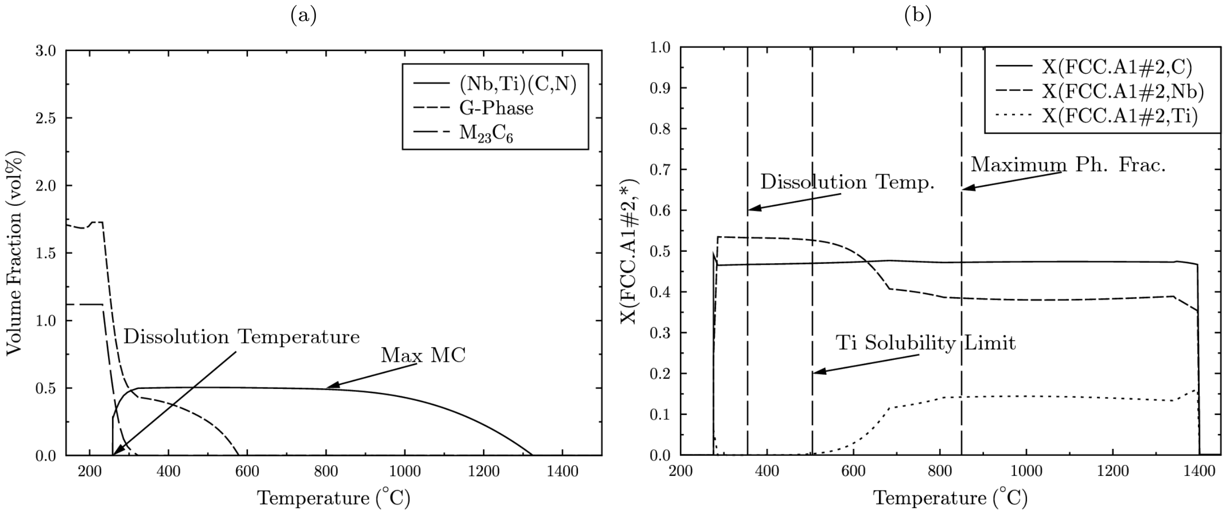
(a)

(b)

Figure A.5: For the (Nb,Ti)(C) phase, or FCC_A1#2, a) the maximum phase fraction, and the dissolution temperature are extracted, along with b) specific composition of FCC_A1#2 at these regions, and the solubility limit of titanium.

The Matlab distribution files for extracting and compiling the NbC precipitates can be found here at http://tinyurl.com/8fq4mrj, under '*NbC_script'*. Odd anomalies from the composition files makes this script much more particular then the previous script, and should be reviewed before trying to modify it to work with other systems. Some tricks are used to avoid any errors in the data that might be unaccounted for, but some instances will still cause the script to error. If this script is providing trouble, and not completing, it is advised to cut certain sections that might not be needed. For example, there are four parts to this script that extract data from the given *.xlsx* files. The first part extracts the dissolution temperature and the maximum FCC_A1#2 fraction from the phase fraction data, the second part determines the solubility limit of titanium, the third part takes the maximum phase fraction and determines the respective amounts of NbC and TiC, and the fourth part finds the maximum amount of titanium in FCC_A1#2 and calculates the fractions of NbC and TiC at this point. The fourth part, finding the maximum titanium concentration, is not used in the presented study, but was included for analysis. This fourth part flags most of the errors, so it can be removed if it does not provide critical information to the study.

```
14 k=1;
15 Tx = find(datPhase,k,'first'); % Finds first non-zero
16 Tend = find(datPhase==0, k,'last'); % Finds last zero for stability range
17 datPhaseSub = datPhase;
18 if(datPhase(Tend-1) > 0.01)
19  datPhaseSub = datPhaseSub(1:Tend-1);
20  Tend = find(datPhaseSub==0, k,'last');
21 end
22 if (Tend < Tx+30)
23  Tend = length(datPhase);
24 end
```

Lines 14-24 determines the suitable range to extract the FCC_A1#2 data. This in an attempt to filter out any noise, or aberrations in the data. T_x finds the first non-zero row, assuming this is the stability temperature for FCC_A1#2, and T_{end} finds the temperature of the last zero row. Sometimes after dissolution of a phase, ThermoCalc predicts this phase to reprecipitate at low temperatures with a drastically different, often nonsensical compositions. It is important to filter out any regions in the FCC_A1#2 that do not have a composition of (Nb,Ti)(C). Setting T_{end} to the last zero row will filter out this data, unless FCC_A1#2 drops back down to zero after it has precipitated the second compositionally different phase. The condition on Line 18 will filter out any secondarily precipitated FCC_A1#2 phases by testing if the dissolutioned phase is above 0.01 mole fraction before dissolution, as these new phases usually have a very high driving force. If the FCC_A1#2 is stable until the end of the data, T_{end} is set to the last temperature in the data as per line 23. Variables *dtemp*, and *npm* are extracted between this temperature range ($T_x \rightarrow T_{end}$), which are the temperature array, and the phase fraction array respectively.

```
31 mxVal = max(npm);
32 mxIdx = find(npm==mxVal, k,'first');
33 mxTemp = dtemp(mxIdx-1);
34 if(Tend == length(datPhase))
35   stabIdx = length(npm);
36 else
37   stabIdx = find(npm==0,k,'first');
38 end
39 stabTemp = dtemp(stabIdx -1);
```

Lines 31-39 will get the maximum FCC_A1#2 phase fraction, its index, and its corresponding temperature, as well as the dissolution temperature of FCC_A1#2 labelled as *stabTemp*. Niobium, and titanium mole fraction arrays are extracted and labeled as *nbTot*, and *TiTot*. The solubility limit of titanium is found on line 52, where the titanium concentration is below a lower threshold. A *While* loop introduced on Line 55 is used to find out if the found value is the actual solubility limit of titanium in FCC_A1#2 or if it was picking up some random fluctuation in the data. If the value picked up is a false positive it will be subtracted from the data, and a new solubility limit will be found until the criteria of the *While* loop is met. The *catch* statement between lines 59-74 will catch any errors that might occur in this while loop (e.g. indicies out of range), save the error to a log file, and break out of the script, and will continue running with the next file iteration. Lines 31-39 will get the maximum FCC_A1#2 phase fraction, its index, and its corresponding temperature, as well as the dissolution temperature of FCC_A1#2 labelled as *stabTemp*. Niobium, and titanium mole fraction arrays are extracted and labeled as *nbTot*, and *TiTot*. The solubility limit of titanium is found on line 52, where the titanium concentration is below a lower threshold. A *While* loop introduced on Line 55 is used to find out if the found value is the actual solubility limit of titanium in FCC_A1#2 or if it was picking up some random fluctuation in the data. If the value picked up is a false positive it will be subtracted from the data, and a new solubility limit will be found until the criteria of the While loop is met. The *catch* statement between lines 59-74 will catch any errors that might occur in this while loop (e.g. indicies out of range), save the error to a log file, and break out of the script, and will continue running with the next file iteration.

```
51 % Finds last non-zero for stability range
52 solIdx = find(tiTot >= 0.5*10^-3, k,'last');
53 tiTotSub = tiTot;
54 try
55  while(tiTotSub(solIdx-1) < 0.5*10^-3)
56   tiTotSub = tiTotSub(1:solIdx-1);
57   solIdx = find(tiTotSub >= 0.5*10^-3, k,'last');
58  end
59 catch err
60  %open file
61  fid = fopen('logFile','a+');
62  % write the error to file
63  % first line: message
64  fprintf(fid,'%s\n',err.message);
65 
66  % following lines: stack
67  for e=1:length(err.stack)
68   fprintf(fid,'%sin␣%s␣at␣%i\n',txt,err.stack(e).name,err.stack(e).line);
69  end
70 
71  % close file
72  fclose(fid)
73  return;
74 end
75 solIdx = find(tiTot == tiTotSub(solIdx), k,'last');
76 tempSol = temp(solIdx);    % temp at the sol limit of Ti
77 phSol = datPhase(solIdx); % phase fraction at the sol limit of Ti.
```

Lines 79-84 splits the maximum phase fraction found before into NbC, and TiC by finding the concentrations of titanium and niobium in FCC_A1#2, and determining their respective phase fractions, assuming there is no solubility for titanium in NbC, and niobium in TiC.

```
79  %Max Phase fraction
80  tiMx = tiTot(mxIdx);
81  nbMx = nbTot(mxIdx);
82  totCon = tiMx + nbMx;
83  tiPh = tiMx/totCon*mxVal; %TiC Phase fraction
84  nbPh = nbMx/totCon*mxVal; % NbC Phase fraction
```

The last part of the script finds the maximum concentration of titanium, checking the validity of the number through a *While* statement, first checking if the found value is just a large fluctuation in the data, and that the value is below an upper threshold, knowing that the maximum concentration of titanium is never above 0.4. Lines 118-125 determine the respective NbC, and TiC concentrations at the found maximum titanium concentration. An example of the resulting output are shown in Table A.3.

```
86  %Max Ti
87  tiTot = tiTot(1:length(tiTot)-1);
88  mxTi = max(tiTot);
89  mxTiIdx = find(tiTot==mxTi, k,'first');
90  tiTotSub = tiTot;
91  try
92   while(abs(mxTi - tiTotSub(mxTiIdx+1)) > 1*10^-3 || mxTi > 0.5)
93          if(mxTiIdx < length(tiTotSub)/2)
94           tiTotSub = tiTotSub(mxTiIdx+1:length(tiTotSub));
95          else
96           tiTotSub = tiTotSub(1:mxTiIdx-1);
97          end
98          mxTi = max(tiTotSub);
99          mxTiIdx = find(tiTotSub==mxTi, k,'first');
100  end
101 catch err
```

Table A.3: Example of the output from the Matlab script 'findeqNbC.m', which looks at the FCC_A1#2 phase or, (Nb,Ti)(C) phase, which extracts the maximum FCC_A1#2 phase fraction, and dissolution temperature, and determines the relative NbC and TiC phase fractions, as well as the solubility limit for titanium.

Name	T (Mx.Ph. Frac.)	NbC (Mx.Ph. Frac.)	TiC (Mx.Ph. Frac.)	T (Dissol)	T (Ti.Sol. Lmt.)	NbC (Ti.Sol. Lmt.)	T (Mx.Ti.)	NbC (Mx.Ti.)	TiC (Mx.Ti.)
'Cr19Ni31Si0.5Nb0.5 C0.05Mn0.15Ti0.05'	486	4.81E-03	2.32E-04	232	436	5.04E-03	1006	3.98E-03	2.80E-04
'Cr19Ni31Si0.5Nb0.5 C0.05Mn0.15Ti0.175'	526	4.41E-03	6.25E-04	288	376	4.99E-03	1136	2.79E-03	6.64E-04
'Cr19Ni31Si0.5Nb0.5 C0.05Mn0.15Ti0.3'	142	1.59E-01	1.29E-04	142	346	4.98E-03	1236	1.73E-03	7.18E-04
'Cr19Ni31Si0.5Nb0.5 C0.05Mn0.825Ti0.05'	486	4.81E-03	2.35E-04	259	436	5.04E-03	1006	3.98E-03	2.84E-04
'Cr19Ni31Si0.5Nb0.5 C0.05Mn0.825Ti0.175'	526	4.40E-03	6.34E-04	259	376	4.99E-03	1136	2.79E-03	6.72E-04
'Cr19Ni31Si0.5Nb0.5 C0.05Mn0.825Ti0.3'	536	4.17E-03	8.57E-04	259	346	4.98E-03	1236	1.73E-03	7.29E-04

A.3.3 Compiling and organizing data in Excel.

Once the Matlab scripts in subsection A.3.1, and subsection A.3.2 have successfully run and output their respective *'.xlsx'* files, download the excel file *'batchTCC.rar'* from this link, http://tinyurl.com/9zsdwf6. Once this file is open, go to the **developer tab**, and click the **Visual Basic** Button. In the *sortMatlab* script, lines 11-12 lines 16-17 refer to the excel files compiled by Matlab. This script will go through the specified files, reorganize, and categorize the data based on the phase and the type of data. The data compiled from subsection A.3.1 is organized in the *findPhase* function, where the string array *strPhase* lists the phases that should be searched for. The *data* array stores the data found for each phase, where this data will be copied to its respective column in the excel table. The phase name, the maximum temperature, and maximum phase fraction, the stability temperature, and any plateau regions, are all stored in the *data* array. The next function *findFCC* does the same thing as the *findPhase* function, but applies it to the second excel file discussed in subsection A.3.2. The *organize*, and *organizeFCC* functions take the *data* arrays returned from *findPhase* and *findFCC*, and sort them into their appropriate columns. To run the *sortMatlab* script press the the **sort** button on the excel table. Once that has completed the next step is to insert columns after the **Name** column for each element in the compositional matrix. In the Visual Basic Window click on **Model 2** in the Modules folder located on the left-hand side project tree, and run the *SplitName* script. This takes each string in the **Name** column and splits the string as to fill the element columns just created. An example of the resulting excel file can be downloaded here, http://tinyurl.com/ccuqjpt. Finally select the header row click on the **Data** tab in the excel ribbon, and select the **Filter** option. Each column can now be arranged in ascending or descending order, or with various conditional statements. A supplemental graphing program is included in the *.xlsm* file, and can be executed by running the *openGraphMaker* function in Module 2. The X-,Y-,and Z- variables should be selected by clicking the header cells for the columns to be graphed. Up to three constant variables can be selected, by again clicking the header cell of the wanted column, and setting their values to the values you want to keep constant. A text file with the appropriate columns is output for further analysis with other plotting programs (e.g. GLE, or GNUPlot). Fig. A.6 shows how this plotting tool can be used with the resulting output.

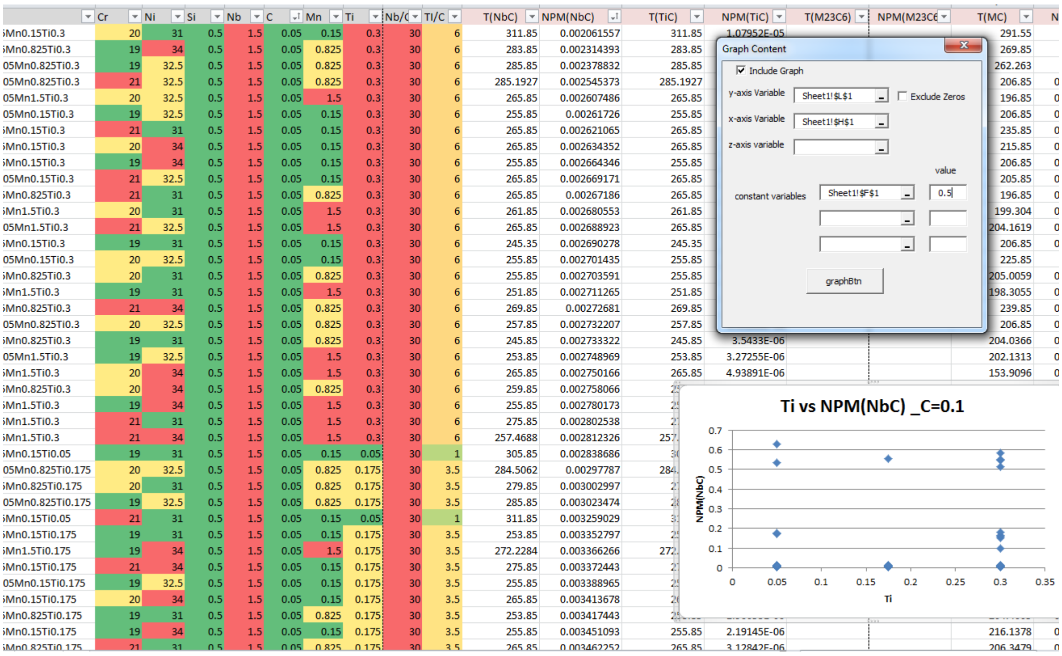

	Cr	Ni	Si	Nb	C	Mn	Ti	Nb/C	Ti/C	T(NbC)	NPM(NbC)
Mn0.15Ti0.3	20	31	0.5	1.5	0.05	0.15	0.3	30	6	311.85	0.002061557
Mn0.825Ti0.3	19	34	0.5	1.5	0.05	0.825	0.3	30	6	283.85	0.002314393
05Mn0.825Ti0.3	19	32.5	0.5	1.5	0.05	0.825	0.3	30	6	285.85	0.002378832
05Mn0.825Ti0.3	21	32.5	0.5	1.5	0.05	0.825	0.3	30	6	285.1927	0.002545373
05Mn1.5Ti0.3	20	32.5	0.5	1.5	0.05	1.5	0.3	30	6	265.85	0.002607486
05Mn0.15Ti0.3	19	32.5	0.5	1.5	0.05	0.15	0.3	30	6	255.85	0.00261726
Mn0.15Ti0.3	21	31	0.5	1.5	0.05	0.15	0.3	30	6	265.85	0.002621065
Mn0.15Ti0.3	20	34	0.5	1.5	0.05	0.15	0.3	30	6	265.85	0.002634352
Mn0.15Ti0.3	19	34	0.5	1.5	0.05	0.15	0.3	30	6	255.85	0.002664346
05Mn0.15Ti0.3	21	32.5	0.5	1.5	0.05	0.15	0.3	30	6	265.85	0.002669171
Mn0.825Ti0.3	21	31	0.5	1.5	0.05	0.825	0.3	30	6	265.85	0.00267186
Mn1.5Ti0.3	20	31	0.5	1.5	0.05	1.5	0.3	30	6	261.85	0.002680553
05Mn1.5Ti0.3	21	32.5	0.5	1.5	0.05	1.5	0.3	30	6	265.85	0.002688923
Mn0.15Ti0.3	19	31	0.5	1.5	0.05	0.15	0.3	30	6	245.35	0.002690278
05Mn0.15Ti0.3	20	32.5	0.5	1.5	0.05	0.15	0.3	30	6	255.85	0.002701435
Mn0.825Ti0.3	20	31	0.5	1.5	0.05	0.825	0.3	30	6	255.85	0.002703591
Mn1.5Ti0.3	19	31	0.5	1.5	0.05	1.5	0.3	30	6	251.85	0.002711265
Mn0.825Ti0.3	21	34	0.5	1.5	0.05	0.825	0.3	30	6	269.85	0.00272681
05Mn0.825Ti0.3	20	32.5	0.5	1.5	0.05	0.825	0.3	30	6	257.85	0.002732207
Mn0.825Ti0.3	19	31	0.5	1.5	0.05	0.825	0.3	30	6	245.85	0.002733322
05Mn1.5Ti0.3	19	32.5	0.5	1.5	0.05	1.5	0.3	30	6	253.85	0.002748969
Mn1.5Ti0.3	20	34	0.5	1.5	0.05	1.5	0.3	30	6	265.85	0.002750166
Mn0.825Ti0.3	20	34	0.5	1.5	0.05	0.825	0.3	30	6	259.85	0.002758066
Mn1.5Ti0.3	19	34	0.5	1.5	0.05	1.5	0.3	30	6	255.85	0.002780173
Mn1.5Ti0.3	21	31	0.5	1.5	0.05	1.5	0.3	30	6	275.85	0.002802538
Mn1.5Ti0.3	21	34	0.5	1.5	0.05	1.5	0.3	30	6	257.4688	0.002812326
Mn0.15Ti0.05	19	31	0.5	1.5	0.05	0.15	0.05	30	1	305.85	0.002838686
05Mn0.825Ti0.175	20	32.5	0.5	1.5	0.05	0.825	0.175	30	3.5	284.5062	0.00297787
Mn0.825Ti0.175	20	31	0.5	1.5	0.05	0.825	0.175	30	3.5	279.85	0.003002997
05Mn0.825Ti0.175	19	32.5	0.5	1.5	0.05	0.825	0.175	30	3.5	285.85	0.003023474
Mn0.15Ti0.05	21	31	0.5	1.5	0.05	0.15	0.05	30	1	311.85	0.003259029
Mn0.15Ti0.175	19	31	0.5	1.5	0.05	0.15	0.175	30	3.5	253.85	0.003352797
Mn1.5Ti0.175	19	34	0.5	1.5	0.05	1.5	0.175	30	3.5	272.2284	0.003366266
Mn0.15Ti0.175	21	34	0.5	1.5	0.05	0.15	0.175	30	3.5	275.85	0.003372443
05Mn0.15Ti0.175	19	32.5	0.5	1.5	0.05	0.15	0.175	30	3.5	255.85	0.003388965
Mn0.15Ti0.175	20	34	0.5	1.5	0.05	0.15	0.175	30	3.5	265.85	0.003413678
Mn0.825Ti0.175	19	31	0.5	1.5	0.05	0.825	0.175	30	3.5	253.85	0.003417443
Mn0.15Ti0.175	19	34	0.5	1.5	0.05	0.15	0.175	30	3.5	255.85	0.003451093
Mn0.825Ti0.175	21	31	0.5	1.5	0.05	0.825	0.175	30	3.5	265.85	0.003462252

☑ Include Graph
y-axis Variable: Sheet1!$L$1
☐ Exclude Zeros
x-axis Variable: Sheet1!$H$1
z-axis variable:
constant variables: Sheet1!$F$1 value 0.5

Figure A.6: Excel output after running scripts in the *'batchTCC.rar'* distribution. Supplemental plotting tool is also displayed where data can be plotted quickly and easily for fast analysis.

A.4 Matrix Plots with GNUPlot

After the data is compile, and organized successfully (Columns represent the different phases, row represent the different chemistries), the data can now be used to output phase matrix plots, to visually represent the relationships between changes in composition and their equilibrium microstructure. Fig. A.7 is an example of a final matrix plot where influences from individual elements can be observed, made with GNUPlot. GNUPlot is an open source plotting program useful in converting large amounts of data, and displaying the information in various ways. GNUPlot for windows is distributed as an app package, meaning that for installation all that is needed is to extract the folder to somewhere in your computers directory. Then to open up GNUplot go to the *Binary* folder and double click the *wgnuplot.exe* executable. You can download all of the GNUplot matrix plot files discussed in this document by following the instructions in this link, http://tinyurl.com/8k5zfqt.

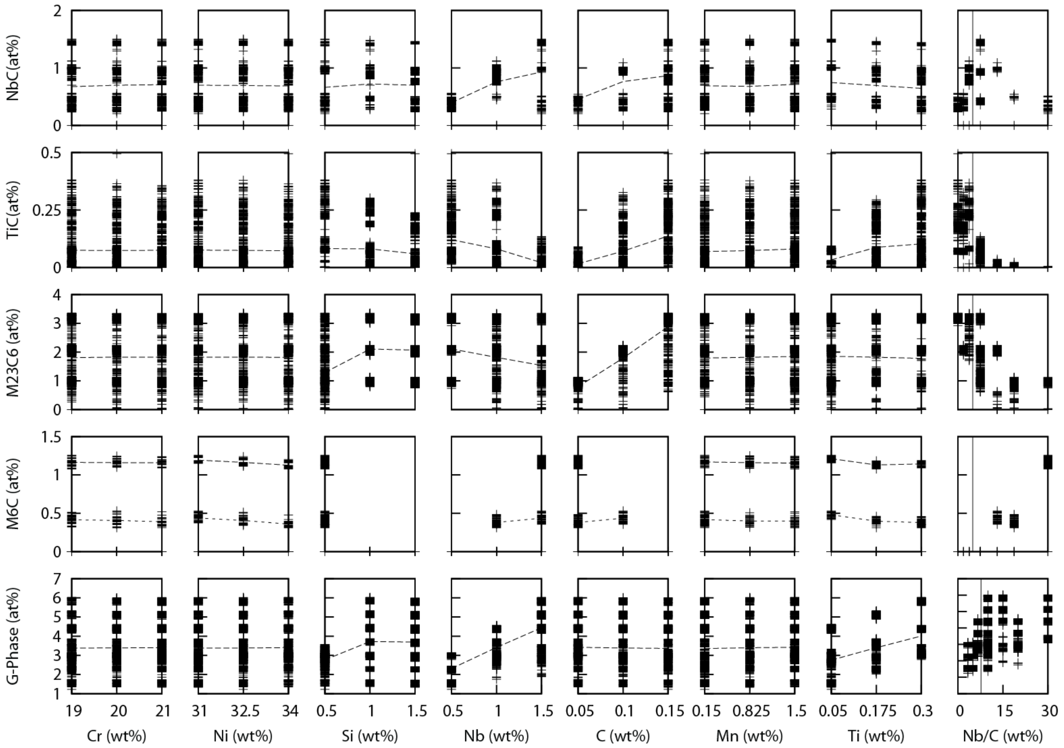

Figure A.7: A matrix plot looking at the maximum phase fraction of a 2032Nb microstructure with titanium additions, vs. compositional changes of individual elements. Relative effects from each component in the composition can be visually compared for analysis and discussion.

To run the GNUPlot (.gp) script, in the *wgnuplot.exe* environment type "cd *path*", where *path* is the full directory where the .gp files are found (eg. C:\user\downloads). Then type "call *filename*", where *filename* is the name of the .gp script you want to run (eg. multiple_Phase.gp). The scripts should run and output a postscript file (.ps) of the resulting matrix plot. To view the code of the .gp file open it up in a text editor, or a coding environment such as Visual Studios, or Dreamweaver.

The first five lines of the GNUplot script set the output to a postscript file, and the height and width of the document. The name of the postscript file is “*matrixPhase.ps*″. To produce multiple plots in the same document the *multiplot* command is issued on line 7, creating a multiplot with 5 rows, and 8 columns. *tmargin*, *bmargin*, *leftmargin*, *rmargin* set the top, bottom, left, and right margins respectively for each plot. For GNUPlot to read the compiled excel data, the data should be saved as a .txt file (tab delimited) or a .csv file. Any columns that will not be used in the matrix plot should be deleted. It is also necessary to fill all empty empty cells with zeros, as empty cells cause indexing errors in GNUPlot. The zero cells can be filtered out in the script with conditional statements, as shown below.

```
1   reset
2   set terminal postscript size 1650,750
3   set output ”matrixPhase.ps”
4   set term postscript enhanced font ”Times–Roman” 12
5   unset key
6
7   set multiplot layout 5,8
8    set tmargin 0.8
9    set bmargin 0.8
10   set lmargin 1.8
11   set rmargin 1.8
```

The next code block will plot the first row of Fig. A.6. “*MT_Phase.txt*″ is the excel data containing the maximum phase fractions, *u* is shorthand for ‘using’, where 1 : (100∗$$10) refers to the *column*1 : *column*2 indices of the .txt file. Post operations can be performed on the rows and columns where the data in row 10 is multiplied by 100 to get a percentage. Whenever doing a row or column operation the row and column must be referred to with $$. The command *smoothuniquewithlines* will plot a dotted line averaging each X-axis values which will be used to observe any trends in the data. Line 25 plots the Nb/C fraction as shown in Fig. A.6, where a line at Nb/C = 7.7 is drawn by referencing a separate text file containing x, and y line coordinates. In this instance it is referring to line 1 $\{7.7, 7.7\}$, and line 3 $\{0, 2\}$.

```
13   set format y ”%g”
```

```
14 set ytics 1 nomirror
15 set ylabel ”NbC(at%)”
16 plot ”MT_Phase.txt” u 1:(100*$$10), ”” u 1:(100*$$10) smooth unique with
       lines
17 set format y ””
18 unset ylabel
19 plot ”MT_Phase.txt” u 2:(100*$$10), ”” u 2:(100*$$10) smooth unique with
       lines
20 plot ”MT_Phase.txt” u 3:(100*$$10), ”” u 3:(100*$$10) smooth unique with
       lines
21 plot ”MT_Phase.txt” u 4:(100*$$10), ”” u 4:(100*$$10) smooth unique with
       lines
22 plot ”MT_Phase.txt” u 5:(100*$$10), ”” u 5:(100*$$10) smooth unique with
       lines
23 plot ”MT_Phase.txt” u 6:(100*$$10), ”” u 6:(100*$$10) smooth unique with
       lines
24 plot ”MT_Phase.txt” u 7:(100*$$10), ”” u 7:(100*$$10) smooth unique with
       lines
25 plot ”MT_Phase.txt” u 8:(100*$$10), ”Nb_C.txt” u 1:3 with l lt 1 lw 1
```

Line 13-25 are repeated until the final row where the x-axis needs to be generated. If there is a clear division in the data like that shown for the M_6C row in Fig. A.7, the division can be analyzed by filtering the data in excel (explained above), and coloring the rows by selecting the row, and clicking the **Conditional Formatting** button in the **Home** tab, and choosing a **Color Scales** option. In this case there is a clear division when Nb/C ≈ 25. To filter the data and draw lines for when Nb/C > 25, and Nb/C < 25 a conditional statement given on Line 57 is given, which says that if column 8 (Nb/C row) is greater than 25 and column 14 (M_6C row) is greater than zero then print the value in column 14, else print 1/0, where 1/0 is an undefined value and will not be included in the interpolation line. In coding vernacular, ?, is another way of writing an If statement, and the proceeding : is an Else statement.

```
57 plot ”MT_Phase.txt” u 1:($$14), ”” u 1:((($$8 > 25) && ($$14 > 0))? $$14 :
```

```
    1/0) smooth unique with lines, ”” u 1:((($$8 < 25) && ($$14 > 0))? $$14
    : 1/0) smooth unique with lines
```

For the last row of the plot the x-axis tics need to be set, along with the x-axis label, and the x-axis range.To end the script unset the x-axis, y-axis, and multiplot, and reset the default conditions. If the script should error midway in order to run the script again you may need to manually input the commands on lines 100-102 in order to get out of the multiplot environment. For students/members of the CCWJ more information about GNUPlot can be found here,http://tinyurl.com/8oskjrr, double clicking *textbooks* and then *Gnuplot*.

```
69  set format y ”%g”
70  set ylabel ”G–Phase␣(at%)”
71  set ytics 1 nomirror
72  set xtics 1 nomirror
73  set xlabel ”Cr␣(wt%)”
74  plot ”MT_Phase.txt” u 1:(100*($$15)), ”” u 1:(100*($$15)) smooth unique
        with lines
75  set format y ””
76  unset ylabel
77  set xlabel ”Ni␣(wt%)”
78  set xtics 31,1.5,34
79  plot ”MT_Phase.txt” u 2:(100*($$15)), ”” u 2:(100*($$15)) smooth unique
        with lines
```

```
98              unset xlabel
99              unset ylabel
100 unset multiplot
101 set key
102 reset
```

A.4.1 Minitab Output

3^K ANOVA, and regression is performed on the compiled data, using Minitab software. This will provide statistical data, and confidence as to what elements, or interactions of elements play a significant role in the precipitation of a phase. Regression modeling will be used to provide a mathematical basis for explaining the optimization of an alloy based on equilibrium microstructure for a matrix of alloy compositions. The visual representation of the data described in Section A.4 provides a quick, and easily comprehensible analysis of how single elements affect the stability of a phase. From these graphs it is hard to distinguish, with a certain degree of confidence, how significant each of these factors is, or if they are even significant at all. ANOVA and regression can provide this kind of insight, and certainty that analyzing graphs cannot give. After regression has been performed on each individual phase, linear programming or other optimization techniques (response surfaces, and method of steepest accent [55]) can be employed to characterize the best alloy that meets certain microstructure conditions (i.e. min G-phase, maximum solubility of NbC). The following sections will describe the procedure in how to use Minitab to output the ANOVA, and regression data.

A.4.1.1 Factorial Design Output

If a 3^K ANOVA is computed with the imported data it is most likely to error, as some of the experiments during the ThermoCalc simulation error, and do not complete. To test this we can check the rows in the compiled excel sheet and compare them to the total number of expected combinations, in this case $3^7 = 2187$, whereas only 2159 row of data were compiled. Moreover, Rank deficiency during ANOVA can occur with empty data, meaning matrix calculations cannot be performed [69]. Lastly, since not all phases are present in each chemistry, running an ANOVA on the 3^K experiment can also throw an error. An alternative would be to perform three 2^K ANOVAs (low/high levels, low/medium levels, medium/high levels), determine the significant effects, and then perform regression with the significant effects. Setting a 95% confidence interval, if $P - Value < \alpha$ the null hypothesis can be rejected, and the current factor, or interaction of factors can be said to play a significant role in the precipitation of the phase, i.

1. Once Minitab is open, import text data by clicking **File** → **Open Worksheet**, then selecting either the *text*, *csv*, or *excel* options in the **file of type** section box, and then selecting one of the files

with the compiled data used to make the matrix plots.

2. select **Stat** → **DOE** → **Factorial** → **Analyze Factorial Design**
3. In the **Define Custom Factorial Design** window select all the elements as factors. Leave the selection as a 2-level factorial.
4. Click the **Low/High** button to change the low and high values that will be used in the 2^K ANOVA. These will need to be changed depending on which set of values you are dealing with (i.e. low/high, low/medium, medium/high). Once finished Select OK, and OK again.
5. For the responses Choose the Y-axis columns of the data.
6. Click the **graph** button select the **Histogram**, and **Residuals Versus Fits** options. In the **storage** options choose **Fits**, **Residuals**, **effects**, **coefficients**, and **factorial**. Select OK
7. Once the ANOVA has finished, select the **Show Sessions Folder** button shown in Fig. A.8.

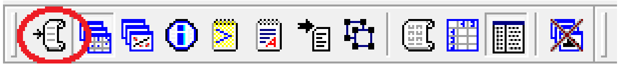

Figure A.8: The “Show Sessions Folder” button in Minitab

8. For each section that needs to be saved right click the section in the project manager and choose **Append To Report**
9. Select the **Show ReportPad** button shown in Fig. A.10.
10. In the projects panel right-click the ReportPad file and click **Save Report As...** button. This file can now be opened in an editing program like word, or excel for further processing and analysis.
11. For the Low/Medium, and Medium/High ANOVA sets perform steps 1-10 again, this time changing the Low/High values to represent the current interval of values.
12. Once all the reports have been exported open them up, or copy the data into an excel document. Select the first column for each data block and select the **Test to Columns** button in the Data tab. Highlighting all the data in the block click **Filter** button, and then order the P column from smallest to largest. Any terms with a P-value greater than 0.05 are not significant and can be discarded. Also look at the significance of the Interactions (2-Way Interactions, 3-Way interactions), where if they are $\gtrsim 0.05$, Any of these effects are most likely not significant.

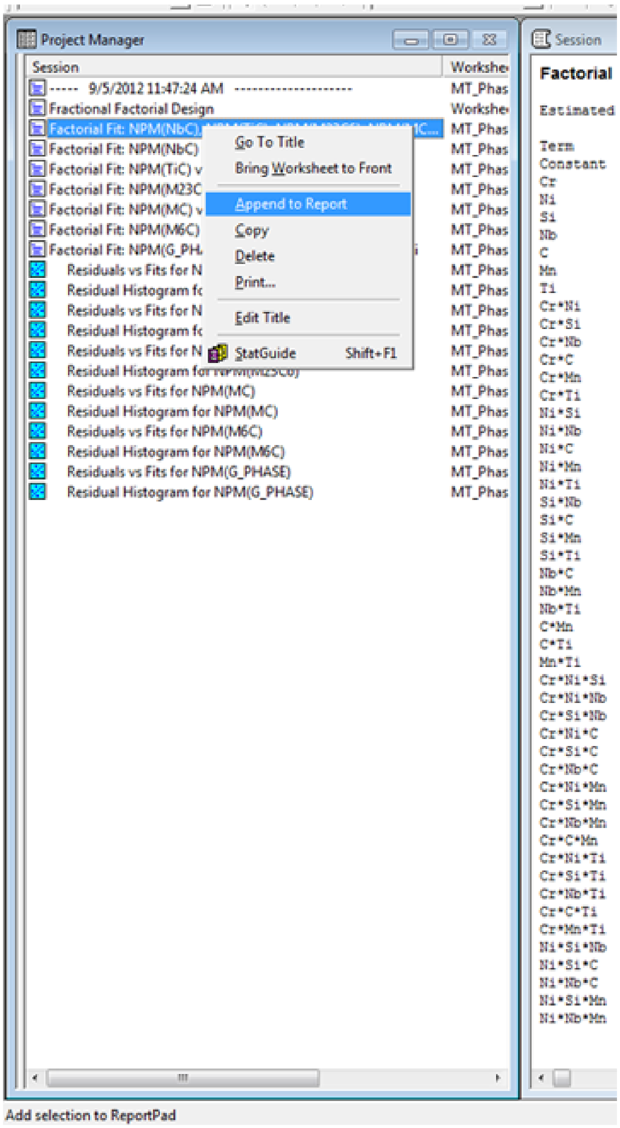

```
Factorial

Estimated

Term
Constant
Cr
Ni
Si
Nb
C
Mn
Ti
Cr*Ni
Cr*Si
Cr*Nb
Cr*C
Cr*Mn
Cr*Ti
Ni*Si
Ni*Nb
Ni*C
Ni*Mn
Ni*Ti
Si*Nb
Si*C
Si*Mn
Si*Ti
Nb*C
Nb*Mn
Nb*Ti
C*Mn
C*Ti
Mn*Ti
Cr*Ni*Si
Cr*Ni*Nb
Cr*Si*Nb
Cr*Ni*C
Cr*Si*C
Cr*Nb*C
Cr*Ni*Mn
Cr*Si*Mn
Cr*Nb*Mn
Cr*C*Mn
Cr*Ni*Ti
Cr*Si*Ti
Cr*Nb*Ti
Cr*C*Ti
Cr*Mn*Ti
Ni*Si*Nb
Ni*Si*C
Ni*Nb*C
Ni*Si*Mn
Ni*Nb*Mn
```

Figure A.9: append the session data to report in Minitab

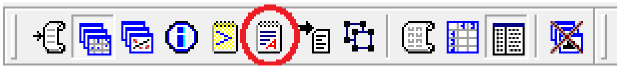

Figure A.10: The “Show ReportPad” button in Minitab

13. For each report (Low/High, Low/Medium, and Medium/High) compare the top 10 common significant factors for each phase (or factors where P-Value = 0), and make note of them (i.e. Highlight the cells). For the regression these common factors will be included for each phase.

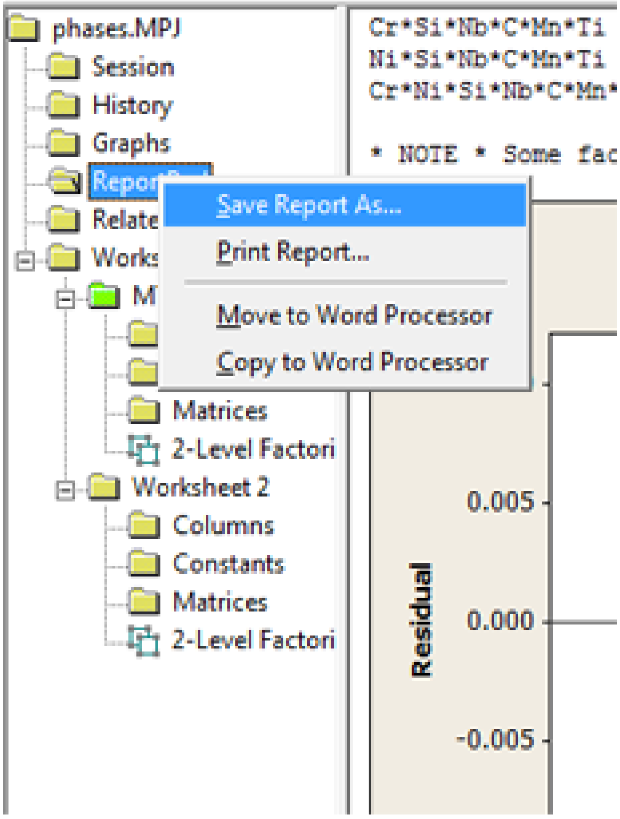

```
Cr*Si*Nb*C*Mn*Ti
Ni*Si*Nb*C*Mn*Ti
Cr*Ni*Si*Nb*C*Mn*

* NOTE * Some fac
```

Figure A.11: Save the report in Minitab as an .RTF, or .html file.

A.4.1.2 Regression Output

1. Significant interactions of elements determined by ANOVA will need to be added as columns in the data. To multiply columns together first right click where you want the column, and choose **Insert Columns**, and name the column appropriately. Next, choose **Calc** → **Calculator** Choose the newly created column as the column to store the data. Input the value of that column, for example for a Nb × C interaction type $Nb * C$. Repeat this for the remaining significant interactions.

2. For the regression output select **Stat** → **Regression** → **Regression** from the main menu.

3. Choose your response variable, note you can only choose one variable at a time, so this procedure will need to be repeated for all of the response variables.

4. In the **Graphs** section again choose the Histogram, and the Normal plot options. In the **storage** option select $Coefficients$, $Fits$, and MSE. The press OK to run the regression. This will perform

linear regression fitting on the given data. If the R^2 value is insufficient, look through the factorial analysis to determine the next most significant effect(s) and input them as described in step 1.

5. Repeat steps 1-4 for all the remaining response variables.

Image Processing Scripts & Programs

A.5 Thresholding scripts

A.5.1 Setting up the Photoshop connections to Matlab

In every distribution for Photoshop there is a plugin for connecting it to Matlab. This is useful if a file has multiple layers that need to be sequentially called to Matlab. Instruction for how to set up this connections can be found in the *Adobe/Photoshop/MATLAB* directory typically found in Program Files.

A.5.2 Image analysis toolbox for Matlab

Image processing with Matlab, and the following scripts require the *Image Processing Toolbox* that can be purchased from Matlab from their website, http://tinyurl.com/8os5tvo.

A.5.3 Thresholding Scripts

A.5.3.1 Photoshop Script

The following section will go through the photoshop script used to threshold EPMA EPMA element maps. The script **EPMAColorThreshold** can be downloaded at http://tinyurl.com/8cu6gve in the *Photoshop Scripts* folder. This script is specifically developed for the 2032Nb alloy, and uses the nickel, niobium, silicon, and chromium maps. The script is written where the first function *SelectAll Phases* is the main function, and all subsequent functions are called from it.

Lines 32-55 will initiate a cropping function to crop out the false color map, and get rid of the color scale and the measurement scale. It does this with the nickel map, as nickel is found at a relatively high concentration throughout the entire microstructure. The function *CropArea* selects the black area outside of the map in the nickel layer, and then inverts the selection, so that the map area is highlighted. This function returns the width and height of this bounding box. The *If* statement on line 35 is needed if the map is a merged map that has multiple images stacked on the y-axis.

```
32 var refLay = docRef.layers[”Ni”];
33 crop = cropArea (refLay);
34 if (crop.y > 512){
```

Lines 57-70 selects the niobium map and chooses and red colors that show up on the map. If there are no red pixels on the map then any yellow pixels are selected. A NbC layer is made, and all of the selected pixels are copied over to this layer and changed to white.

```
57 var actLay = docRef.layers[”Nb”];
58 var layerRef = docRef.layers[1];
59 isLayer0(actLay);
60
61 docRef.activeLayer = actLay;
62 showLayer();
63
64 multiColorChooser (10, c.colorRed.lab.l , c.colorRed.lab.a , c.colorRed.lab
       .b)
65 //IF NbC does not have red Choose a yellow color to define layer
66 var isRed = true;
67 if(!hasSelection()){
68         multiColorChooser (10, c.colorYellow.lab.l , c.colorYellow.lab.a ,
              c.colorYellow.lab.b);
```

```
        isRed = false;
}
docRef.artLayers.add();

var nbcLayer = docRef.layers[0];
nbcLayer.name = ”NbC”;

docRef.activeLayer = nbcLayer;
docRef.selection.fill(c.colorWhite);

 docRef.selection.deselect();
```

Any other color pixels that have been identified to be associated with the NbC phase are then selected and copied over to the NbC layer, after this is complete all the other pixels in the layer are filled black, and the layer is deselected.

```
colSpecPick (c.colorDarkRed, c.colorDarkOrg, nbcLayer);
colSpecPick (c.colorOrg, undefined, nbcLayer);
}
//Add Background layer to NbC layer
docRef.artLayers.add();
var backLayer = docRef.layers[0];
backLayer.name = ”Background”;
backLayer.move (nbcLayer, ElementPlacement.PLACEAFTER);
docRef.activeLayer = backLayer;
docRef.selection.fill(c.colorBlack);
docRef.activeLayer = actLay;
hideLayers();

docRef.activeLayer = nbcLayer;
docRef.mergeVisibleLayers();
```

For all of the other phases the lines 99-130 are used to copy relative pixel color intensities over the new phase layers. Lines 99-130 need to formatted for each phase by changing the layer selected in line 104, defining the new layer to store the binary selection (lines 108-109), and the colors selected (lines 113-117). The function *colSpecPick* finds the colors specified and copies them to the layer specified in the last argument. All of the colors in the EPMA spectra are defined in the *spectraColors* function and can be found there for naming declarations used for the first two arguments of *colSpecPick*. The rest of the script makes new layers for a silicon rich phase, and a chromium rich phase.

```
99   //Deselect NbC contents hide NbC layer
100 docRef.selection.deselect()
101 selectAllLayers();
102 hideLayers();
103 //make active layer the Nb layer
104 docRef.activeLayer = actLay;
105 showLayer();
106 // Make GNbRich Layer
107 docRef.artLayers.add()
108 var GNbLayer = docRef.layers[0]
109 GNbLayer.name = ”NbRich”
110
111  //———————Nb for G—phase ——————————————
112 {
113 colSpecPick (c.colorMidYellow, c.colorYellow, GNbLayer);
114 colSpecPick (c.colorBritGreen, c.colorMidGreen,GNbLayer);
115 colSpecPick (c.colorDarkGreen, c.colorTeal, GNbLayer);
116 colSpecPick (c.colorSkyBlue, c.colorPurple, GNbLayer);
117 colSpecPick (c.colorMidPurple, undefined, GNbLayer);
118 }
119 //Add Background layer to carbide layer
120 docRef.artLayers.add();
121 var backLayer = docRef.layers[0];
```

```
backLayer.name = "Background";
backLayer.move (GNbLayer, ElementPlacement.PLACEAFTER);
docRef.activeLayer = backLayer;
docRef.selection.fill(c.colorBlack);
docRef.activeLayer = actLay;
hideLayers();

docRef.activeLayer = GNbLayer;
docRef.mergeVisibleLayers();
```

A.5.3.2 Matlab Script

Color thresholding operations can also be performed in Matlab, where this might be more efficient than calling Photoshop to run its thresholding script, and then sending the data (aka. layers) into Matlab for further processing. The function discussed in this section is called **EPMAsegmentation**, and can be found at http://tinyurl.com/8cu6gve under the *Matlab/Threshold Scripts* directory. Color choices are more limited compared to the Photoshop script where each color designation covers a few color intensities in the EPMA maps.

Calling the thresholding function requires defining 5 arguments; the first argument is the image, the second argument is the color designation (eg. 'r' for red, 'b' for blue), and the third argument is a boolean for displaying the image after the function. The forth argument is a boolean for a black background otherwise a grayscale background of the other pixels, and the fifth argument is for changing the selected pixels to white, or otherwise not changing their color. For thresholding multiple colors the following format must used:

```
nb = EPMAsegmentation(p1, 'w',0,1,1)+...
EPMAsegmentation(p1, 'r',0,1,1)+...
EPMAsegmentation(p1, 'o',0,1,1)+...
EPMAsegmentation(p1, 'y',0,1,1)+...
EPMAsegmentation(p1, 'g',0,1,1)+...
```

```
EPMAsegmentation(p1, 't',0,1,1)+...
EPMAsegmentation(p1, 'b',0,1,1);
```

A.5.4 Matlab phase fraction script for element mapping

Batch Matlab scripts were developed to calculate area fractions for phases characterized in the microstructure of sequentially aged 2032Nb alloys. The element maps processed by EPMA were compiled into .psd files, and cropped using scripts in the *Maps2PSD*, and *Photoshop Scripts* folders at http://tinyurl.com/8cu6gve. The Matlab script discussed in this section is only applicable to the fully aged component of the in-service 2032Nb alloy discussed in his document, but can be modified to work for other systems, and aging times following the same steps.

The Matlab script can be downloaded in the *Matlab/EPMA Script* directory at http://tinyurl.com/8cu6gve. The Matlab script contains one function for batch processing .psd element maps provided two arguments: the top directory level of the .psd files, and how many subfolders deep the .psd files are located. Lines 5-20 initiate a looping process to go through each .psd file in the directory. Valid .psd files are found by breaking down the path string until the characters ‘cc’ or ‘sc’ are found designating a folder with .psd files from the same samples. The folder title will be used to label the data and should be descriptive in providing what sample it is and how long it was aged for.

```
1  function [data] = EPMAInter_GPhase(toplevel, depth)
2  %UNTITLED3 Summary of this function goes here
3  %   Detailed explanation goes here
4  
5  [files,total] = file_list(toplevel,'*.psd', depth);
6  for i=1:total
7   %Load .psd in photoshop
8   psopendoc(files{i});
9   [pathstr, name, ext] = fileparts(files{i});
10  remain = pathstr;
11  while true
```

```
12          [str, remain] = strtok(remain, '\\');
13          if isempty(str), break; end
14          if (strncmpi(str, 'cc', 2)== 1)
15                  break;
16          end
17          if (strncmpi(str, 'sc', 2)== 1)
18                  break;
19          end
20         end
```

Line 25 and 26 run the color thresholding script written for Photoshop designated by the path where the script is found on the hard drive. Line 29 sets the active layer in Photoshop to the layer with the name ‘NbC’, and Line 30 sends this layer to Matlab and converts the image into a binary format. Lines 31-32 import the SiRich binary image.

```
25  pstext = ['var␣run_EPMA␣=␣File␣(␣"D:\\University\\EPMA\\Data\\2011-11Nov
        -30\\EPMAColorThreshold.jsx");'...
26                                              '\$.evalFile(run_EPMA);'];
27  psresult = psjavascriptu(pstext);
28
29  pssetactivelayer('NbC');
30  nb=im2bw(psgetpixels());
31  pssetactivelayer('SiRich');
32  si=im2bw(psgetpixels());
```

Line 35 calculates the binary area of the ‘NbC’ map. Lines 36-40 separate the interdendritic niobium rich phases from the intradendritic phases, where line 36 defines a 2 × 2 structuring element and dilates the ‘NbC’ map with it in line 37. Line 38 closes the dilated images by the same element to fill any holes in the connected components. An area threshold in Line 39 is then set to make a mask of the interdendritic area of the microstructure, which is then multiplied with the original ‘NbC’ map in line 40 resulting in only the interdendritic precipitates remaining. Lines 41-45 convert the image back to a proper format which is then passed back to Photoshop as a new layer with a name specified in line 44.

```
34 Anb = bwarea(nb);
35 se = strel(ones(2,2));
36 I2 = imdilate(nb,se);
37 I2 = imclose(I2,se);
38 inter = bwareaopen(I2,25);
39 inter = immultiply(nb,inter);
40 p = bw2rgb(inter);
41 p = im2uint8(p);
42 psnewlayermatrix(p);
43 pstext = 'app.activeDocument.layers[0].name="NbC_Gphase_Inter";';
44 psjavascriptu(pstext);
```

Lines 47-52 multiply the interdendritic area with the silicon map which is then sent back to Photoshop. The area fraction for G-phase is then calculated from the silicon map, and the NbC fraction is found by subtracting the interdendritic silicon map from the interdendritic niobium map. The $M_{23}C_6$ area fraction is simply calculated from the chromium binary map produced from the Photoshop script.

```
47 B=immultiply(inter,si);
48 p = bw2rgb(B);
49 p = im2uint8(p);
50 psnewlayermatrix(p);
51 pstext = 'app.activeDocument.layers[0].name="G–Phase";';
52 psjavascriptu(pstext);
```

The area fractions are then sent to populate and array which is then sent to a database configured in Matlab. The Photoshop file is saved and closed, where a new .psd file in opened in the loop.

```
73         %populate two area arrays, name array, and file array
74         data(i,1) = {str};
75         data(i,2) = {name};
76         data(i,3) = {interNbC};
```

```
        data(i,4) = {M23C6Tot};
        data(i,5) = {GPhaseInter};

        pstextsave = ['app.activeDocument.save();'];
        psresult = psjavascriptu(pstextsave);
        psclosedoc;
end
%export to database
conn = database('EPMADB', '', '');
colnames = {'Sample_Name', 'Sample_Number', 'NbC_Inter', 'M23C6_Tot', 'GPhase_Inter'};
get(conn, 'AutoCommit');
fastinsert(conn, 'EPMA_Area_Table', colnames, data);
close(conn);
```

A.5.5 Python phase fraction script for backscattered images

For the MetalTek samples area fraction and precipitate size calculations were done using the OpenCV computer vision library with Python. Instructions on how to install OpenCV and connect its library to Python are provided at http://tinyurl.com/9sa6prc. The current section will go through the script *process_36D* located in the *Python/MetalTek Scripts* directory found at http://tinyurl.com/8cu6gve. Many functions defined in this script will not be explained past a general understanding of what they do, however, more insight into function from the OpenCV library can be found at http://tinyurl.com/cmf5fed. The script is organized with the main function at he bottom of the document with all of its internal functions ordered above it. The script is specifically set to handle BSE micrographs from the Tescan Vega-3 SEM, and would need to be modified to work on other SEM micrographs.

After the image is loaded on line 306, a function was written to extract the scale bar that is located in the same position on every micrograph. This functions used Hough Lines to find the length of the scale bar, and OCR to extract the text to find out the real length of the scale bar. A ratio is then defined to convert all pixel measurements into their actual size. The excess parts of the image are then cropped out leaving the micrograph, where its overall area is calculated to be used for area fraction calculations later.

```
im = Image.open(”overall2.tif”)
scale = scaleExtract(im)
scaleRatio = scale[0]
scaleAmt = scale[2]
img = cropImg(im)
pil = cv2pil(img)
imdem = pil.size
area = imdem[0]*imdem[1]*(scaleRatio**2)
```

Lines 319-326 will threshold the greyscale image between the values specified in line 319, and then find the contours of each connected component, where the area fraction and the size of the NbC precipitates can then be determined. The contrast threshold is predetermined by the user and must be done for each phase and each micrograph, as there is no way in fully automating this process. An area threshold is done on lines 321 and 326 for any components with an area greater than 2px. This is done to eliminate any noise that has been picked up after thresholding. ’contourWrapFill’ differs from ’contourWrap’ in that the contour boundaries are filled disregarding any holes in the components. Two dilation masks are produced in lines 323 and 324 which will be used by the subsequent phases to determine the interdendritic regions of the microstructure.

```
319 nbC = binArray(pil, 255, 124) # ****** Change Binary Threshold
320 nbC= np2cv(nbC)
321 [nbC, dump] = contourWrapFill(nbC, 2, high, color= False)
322 mask = dilateImg(nbC, 3, 3, 2)
323 cv.SaveImage(’mask.jpg’, mask)
324 mask2 = dilateImg(nbC, 4, 4, 4)
325 cv.SaveImage(’mask2.jpg’, mask2)
326 [nbPhase, dump] = contourWrap(nbC, 2, high, color= False) # ’−1’ means no
        area threshold ***** Inter Array
```

The mask in line 323 is used for the TiC phase to separate it out from the chromium carbide phases. TiC are generally seen to be situated inside of NbC precipitates as multiphase aggregated carbides with a TiC composition at their center where niobium is progressively exchanged with titanium as you reach the rim of the precipitates. The smaller mask defined in line 323 will separate the TiC from the chrome carbides that are typically seen adjacent to the NbC precipitates. Line 333 subtracts the masked TiC image from the NbC image to get rid of any overlapping regions. An area threshold is then conducted between 0-200 pixels.

```
330 TiCBefore = cv.CreateImage(cv.GetSize(img), 8, 1)
331 cv.Mul(carbides, mask, TiCBefore) # get inter M23C6 from G-phase inter mask
332 TiC = cv.CreateImage(cv.GetSize(img), 8, 1)
333 cv.Sub(TiCBefore, nbC, TiC) # subtract any G-phase overlap with M23C6
334 [TiCphase, dump] = contourWrapFill(TiC, 0, 200, color= False) # area <= 10
        removed
335 #Subtract TiC From NbC
```

The resulting TiC image is then subtracted from the original carbide image leaving behind the chromium carbides in line 348. The intradendritic carbides are then separated from the interdendritic carbides, and labeled as M7C3 and M23C6 respectively. Both carbides undergo a size threshold from 0-200 pixels. The size and area fraction data is then output as both a csv file, and a histogram plot like that shown in Fig. A.12. An example .zip file of the resulting output after image analysis can be downloaded at http://tinyurl.com/8qvmfql.

```
346  #M7C3
347 M7 = cv.CreateImage(cv.GetSize(img), 8, 1)
348 cv.Sub(carbides, TiCphase, M7)
349 [M7C3, M7C3Arr] = contourWrapFill(M7, 0, 200, color= True)
350 areaArr.append(scaleArray(M7C3Arr,scaleRatio**2))
351 namArr.append('M7C3')
352 cv.SaveImage('M7C3.jpg', M7C3)
353  #M23C6
354 M23 = cv.CreateImage(cv.GetSize(img), 8, 1)
```

```
cv.Mul(M7, mask2, M23)
[M23C6, M23C6Arr] = contourWrapFill(M23, 0,  200, color= True)
areaArr.append(scaleArray(M23C6Arr,scaleRatio**2))
namArr.append('M23C6')
cv.SaveImage('M23C6.jpg', M23C6)
```

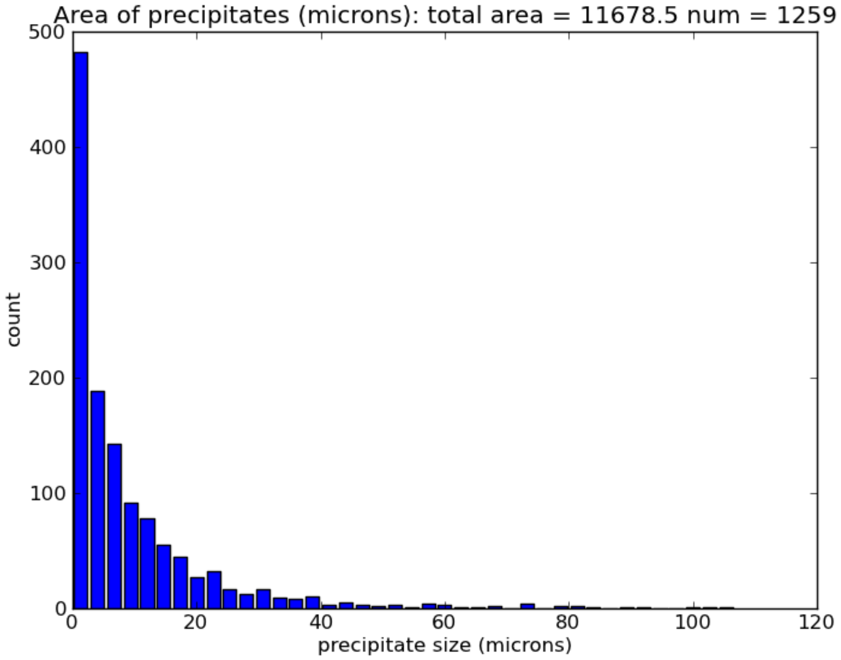

Figure A.12: Python histogram output of NbC precipitate size in design treatment *c* (commerical 2032Nb alloy, 1” wall thickness, and homogenized) aged after 2 months.

In-service 2032Nb Experiment Data

A.6 Grain Size & Dendrite Cell Size Data

Table A.4: Dendrite cell size for both ex-service components after solution annealing at 1200°Cfor 1 hour, and button melting.

Casting Type	**Dendrite Cell Size** (μm)	**Counts**
Button melt		
CC Component	33.4 ± 10.1	97
SC Component	44.3 ± 16.2	54
Sol anneal		
Centrifugally cast	79.3 ± 18.5	58
Static Cast	107.5 ± 31.8	56

A.7 AES Aging Compositions

Table A.5: AES composition of Nb(C,N) precipitates during the initial aging of the SC,CC, and cast components.

		Nb(C,N)							
Age Time (hrs)	**Comp.**	**Composition (wt%)**							**Number of Points**
		Fe	**Ni**	**Cr**	**Si**	**Nb**	**C**	**N**	
0	CC	bal	4.8 ± 2.1 (4.1 ± 2.5)	1.9 ± 1.7 (1.8 ± 1.7)	1.1 ± 1.2 (1.9 ± 2.1)	74.2 ± 5.8 (39.2 ± 3.0)	8.9 ± 0.7 (36.5 ± 2.4)	3.3 ± 0.4 (11.4 ± 1.4)	25
0	Cast	bal	4.1 ± 2.3 (4.4 ± 2.4)	1.8 ± 0.9 (2.1 ± 1.0)	0.9 ± 0.4 (2.0 ± 0.9)	81.7 ± 5.0 (55.1 ± 3.9)	3.6 ± 0.5 (18.6 ± 2.5)	2.7 ± 0.4 (11.9 ± 1.8)	7
170	SC	bal	4.8 ± 7.4 (4.0 ± 6.0)	0.9 ± 2.2 (0.9 ± 2.0)	0.8 ± 1.3 (1.5 ± 2.3)	78.4 ± 12.4 (42.8 ± 7.6)	8.9 ± 0.8 (37.6 ± 3.3)	2.9 ± 0.9 (10.4 ± 3.1)	12
170	CC	bal	7.1 ± 9.3 (6.2 ± 8.2)	2.1 ± 3.2 (2.1 ± 3.3)	1.6 ± 0.8 (2.9 ± 1.4)	73.6 ± 15.26 (39.8 ± 7.92)	8.5 ± 1.5 (35.4 ± 5.7)	2.6 ± 0.9 (9.3 ± 3.1)	8
349	SC	bal	2.6 ± 3.5 (2.4 ± 3.3)	4.1 ± 6.8 (4.0 ± 6.4)	0.1 ± 0.3 (0.3 ± 0.5)	79.8 ± 12.7 (47.2 ± 8.7)	6.8 ± 0.8 (30.7 ± 2.9)	3.1 ± 0.9 (12.1 ± 3.5)	13
349	CC	bal	1.5 ± 1.3 (1.3 ± 1.1)	2.1 ± 1.4 (2.0 ± 1.3)	-	83.4 ± 4.6 (45.8 ± 3.2)	8.9 ± 0.4 (37.9 ± 1.5)	3.3 ± 0.2 (12.2 ± 0.5)	3
349	Cast	bal	6.0 ± 0.5 (5.5 ± 0.4)	5.1 ± 1.0 (5.3 ± 1.0)	-	71.1 ± 2.4 (41.0 ± 2.0)	5.6 ± 0.1 (24.8 ± 1.0)	4.1 ± 0.5 (15.7 ± 1.6)	4
912	SC	bal	4.3 ± 1.6 (3.7 ± 1.4)	2.1 ± 0.7 (2.0 ± 0.7)	-	79.8 ± 3.1 (43.4 ± 1.1)	9.0 ± 0.7 (37.7 ± 2.4)	3.2 ±0.6 (11.6 ± 1.8)	5
1488	CC	bal	5.9 ± 3.0 (4.8 ± 2.5)	0.7 ± 1.1 (0.7 ± 0.9)	0.4 ± 0.7 (0.7 ± 0.7)	76.8 ± 4.6 (39.7 ± 2.9)	10.5 ± 0.5 (41.7 ± 1.7)	3.0 ± 0.5 (10.2 ± 1.3)	3
2975	Cast	bal	10.2 ± 7.2 (10.0 ± 7.0)	2.5 ± 1.2 (2.8 ± 1.3)	1.2 ± 1.1 (2.5 ± 2.2)	77.9 ± 4.8 (48.0 ± 2.9)	5.1 ± 0.3 (24.5 ± 1.3)	3.0 ± 0.2 (12.4 ± 0.7)	3

Table A.6: AES composition of the austenitic matrix near the interdendritic boundary during the initial aging of the SC,CC, and cast components.

		Austenite							
Age Time (hrs)	**Comp.**	**Composition (wt%)**							**Number of Points**
		Fe	**Ni**	**Cr**	**Si**	**Nb**	**C**	**N**	
0	CC	bal	41.8 ± 1.3 (38.7 ± 0.9)	13.1 ± 1.4 (13.6 ± 1.6)	-	-	1.3 ± 0.6 (5.9 ± 1.68)	-	3
0	Cast	bal	36.4 ± (34.1 ±)	14.4 ± (15.2 ±)	-	-	0.6 ± (2.8 ±)	-	1
170	SC	bal	37.7 ± 1.9 (30.7 ± 1.3)	14.1 ± 2.9 (12.9 ± 2.7)	-	-	4.6 ± 0.8 (18.4 ± 2.7)	0.2 ± 0.4 (0.7 ± 1.3)	6
170	CC	bal	39.8 ± (35.9 ±)	14.5 ± (14.8 ±)	-	-	1.7 ± (7.6 ±)	-	8
349	SC	bal	38.5 ± 0.9 (34.6 ± 1.7)	15.1 ± 1.5 (15.4 ± 2.0)	-	-	2.1 ± 0.6 (9.0 ± 2.4)	0.0 ± 0.1 (0.2 ± 0.3)	6
349	CC	bal	30.7 ± 4.7 (27.4 ± 4.8)	19.0 ± 3.4 (19.0 ± 3.1)	-	-	2.3 ± 1.2 (9.8 ± 5.0)	0.0 ± 0.1 (0.2 ± 0.3)	6
349	Cast	bal	34.9 ± 2.1 (30.8 ± 1.7)	16.9 ± 2.0 (16.9 ± 1.8)	0.2 ± 0.4 (0.3 ± 0.7)	4.0 ± 5.0 (2.2 ± 2.8)	2.5 ± 0.6 (10.8 ± 2.4)	0.2 ±0.2 (0.6 ± 0.7)	6
912	SC	bal	36.1 ± 1.0 (33.3 ± 1.2)	16.4 ± 2.0 (17.1 ± 2.1)	-	-	1.0 ± 0.4 (4.5 ± 1.7)	-	5
912	Cast	bal	31.8 ± (29.4 ±)	16.2 ± (16.9 ±)	-	-	0.9 ± (3.9 ±)	-	1
1488	CC	bal	37.9 ± 1.1 (33.7 ± 0.9)	13.6 ± 1.3 (13.7 ± 1.5)	-	0.6 ± 1.2 (0.3 ± 0.7)	2.1 ± 0.7 (9.1 ± 2.8)	0.08 ± 0.2 (0.3 ± 0.6)	4
1488	Cast	bal	36.9 ± 1.1 (34.4 ± 0.5)	11.8 ± 0.8 (12.5 ± 1.1)	-	-	0.8 ± 0.5 (3.8 ± 2.1)	-	4
2975	Cast	bal	33.0 ± 2.9 (29.1 ± 4.0)	14.5 ± 3.0 (14.4 ± 3.4)	-	2.1 ± 3.6 (1.1 ± 1.8)	2.7 ± 2.2 (11.1 ± 8.5)	-	3
140160	CC	bal	36.7 ± 1.6 (32.3 ± 2.0)	17.50 ± 3.8 (17.3 ± 3.2)	-	-	2.43 ± 1.4 (10.2 ± 5.6)	-	4

Table A.7: AES composition of G-Phase precipitates during the initial aging of the SC,CC, and cast components.

		G-Phase							
Age Time (hrs)	**Comp.**	**Composition (wt%)**							**Number of Points**
		Fe	**Ni**	**Cr**	**Si**	**Nb**	**C**	**N**	
349	SC	bal	30.8 ± 2.5 (25.6 ± 2.5)	22.2 ± 2.1 (20.9 ± 2.3)	7.5 ± 0.7 (13.1 ± 0.9)	30.0 ± 2.2 (15.7 ± 0.8)	2.9 ± 0.4 (11.8 ± 1.3)	2.8 ± 0.3 (9.8 ± 0.9)	2
349	CC	bal	32.1 ± 0.8 (26.9 ± 1.5)	23.1 ± 3.3 (21.7 ± 2.5)	4.3 ± 3.2 (7.4 ± 5.4)	20.8 ± 7.4 (10.9 ± 3.5)	2.6 ± 0.3 (10.8 ± 1.7)	2.7 ± 1.4 (9.3 ± 4.7)	4
912	SC	bal	36.6 ± 5.0 (30.7 ± 3.6)	9.8 ± 12.4 (9.0 ± 11.3)	7.6 ± 3.1 (13.4 ± 5.4)	33.8 ± 15.1 (18.1 ± 8.5)	3.9 ± 1.1 (16.0 ± 4.9)	2.1 ± 0.9 (7.4 ± 3.0)	5
912	Cast	bal	49.7 ± 4.3 (45.4 ± 2.4)	0.7 ± 0.8 (0.7 ± 0.8)	10.9 ± 1.3 (20.9 ± 2.6)	30.9 ± 2.6 (17.9 ± 1.8)	1.3 ± 0.3 (5.8 ± 1.4)	1.1 ± 0.2 (4.1 ± 0.7)	5
1488	CC	bal	50.8 ± 2.3 (45.0 ± 3.0)	0.9 ± 1.4 (0.9 ± 1.4)	11.5 ± 1.0 (21.3 ± 1.6)	31.9 ± 1.4 (17.9 ± 0.7)	2.3 ± 0.4 (10.0 ± 1.4)	0.9 ± 0.4 (3.5 ± 1.4)	6
1488	Cast	bal	53.5 ± 3.8 (49.4 ± 3.3)	-	12.5 ± 1.5 (24.2 ± 2.8)	31.7 ± 4.8 (18.5 ± 3.0)	1.1 ± 0.4 (4.9 ± 1.8)	0.7 ± 0.6 (2.6 ± 2.5)	7
2975	Cast	bal	52.6 ± 1.5 (47.7 ± 2.2)	1.8 ± 1.8 (1.8 ± 1.8)	11.9 ± 0.8 (22.5 ± 1.5)	28.7 ± 4.1 (16.5 ± 2.7)	1.3 ± 0.3 (5.6 ± 1.2)	0.9 ± 0.6 (3.2 ± 2.1)	9
140160	CC	bal	52.0 ± 3.4 (48.6 ± 2.9)	0.3 ± 0.6 (0.3 ± 0.6)	11.6 ± 1.5 (22.5 ± 2.5)	33.6 ± 4.3 (20.0 ± 3.0)	1.1 ± 0.2 (5.2 ± 0.9)	0.7 ± 0.6 (2.8 ± 2.4)	14

Table A.8: AES composition of $M_{23}C_6$ precipitates during the initial aging of the SC,CC, and cast components.

		$M_{23}C_6$							
Age Time (hrs)	**Comp.**	**Composition (wt%)**							**Number of Points**
		Fe	**Ni**	**Cr**	**Si**	**Nb**	**C**	**N**	
349	SC	bal	8.2 ± 2.8 (5.9 ± 1.6)	57.0 ± 11.1 (46.7 ± 5.0)	-	12.1 ± 17.1 (6.0 ± 8.4)	8.6 ± 1.1 (30.5 ± 1.5)	0.1 ± 0.1 (0.3 ± 0.4)	2
349	CC	bal	8.2 ± 3.6 (5.9 ± 2.6)	66.7 ± 7.3 (53.2 ± 4.9)	-	0.9 ± 0.1 (0.4 ± 0.4)	8.6 ± 0.9 (29.7 ± 3.0)	0.1 ± 0.2 (0.3 ± 0.5)	8
912	SC	bal	10.8 ± 5.4 (8.0 ± 4.1)	66.6 ± 9.8 (54.9 ± 7.1)	-	3.0 ± 3.1 (1.7 ± 1.3)	7.2 ± 0.6 (25.8 ± 1.6)	0.0 ± 0.1 (0.3 ± 0.4)	9
912	Cast	bal	14.8 ± 16.5 (11.3 ± 12.7)	69.0 ± 19.4 (59.0 ± 16.2)	2.3 ± 4.0 (3.7 ± 6.4)	-	4.4 ± 2.1 (16.1 ± 7.7)	0.9 ± 1.6 (3.0 ± 5.3)	3
1488	CC	bal	12.1 ± 8.0 (9.0 ± 6.7)	64.0 ± 14.1 (51.5 ± 9.8)	-	1.8 ± 2.5 (0.8 ± 1.1)	8.0 ± 1.5 (27.7 ± 4.2)	0.1 ± 0.1 (0.1 ± 0.3)	9
1488	Cast	bal	5.6 ± 1.1 (4.3 ± 0.8)	78.5 ± 1.7 (67.3 ± 1.6)	0.2 ± 0.3 (0.4 ± 0.7)	-	5.4 ± 0.4 (19.9 ± 1.2)	-	5
2975	Cast	bal	7.7 ± 1.7 (5.9 ± 1.4)	75.7 ± 4.2 (64.9 ± 2.4)	-	-	5.5 ± 0.5 (20.3 ± 1.6)	-	5
140160	CC	bal	3.3 ± 0.6 (2.5 ± 0.5)	82.7 ± 0.7 (70.9 ± 1.7)	-	-	5.3 ± 0.6 (19.6 ± 2.0)	-	12

Table A.9: AES composition of Z-Phase precipitates during the initial aging of the SC,CC, and cast components.

		Z-Phase							
Age Time (hrs)	**Comp.**	**Composition (wt%)**							**Number of Points**
		Fe	**Ni**	**Cr**	**Si**	**Nb**	**C**	**N**	
912	Cast	bal	31.9 ± (27 ±)	26.7 ± (25.5 ±)	7.5 ± (13.2 ±)	27.3 ± (14.6 ±)	0.8 ± (3.5 ±)	4.1 ± (14.7 ±)	1
1488	Cast	bal	39.2 ± 2.2 (31.5 ± 1.2)	32.5 ± 4.7 (29.4 ± 3.4)	7.8 ± 1.7 (13.1 ± 2.5)	14.1 ± 6.8 (7.3 ± 3.8)	1.0 ± 0.2 (3.9 ± 0.7)	4.1 ± 0.6 (13.7 ± 1.8)	9
2975	Cast	bal	36.3 ± 1.7 (30.0 ± 1.3)	19.5 ± 11.6 (18.2 ± 10.6)	7.7 ± 1.8 (13.3 ± 3.0)	26.1 ± 9.7 (13.6 ± 5.0)	1.6 ± 0.8 (6.6 ± 3.0)	4.2 ± 1.3 (14.3 ± 3.8)	6
140160	Cast	bal	1.4 ± 1.6 (1.2 ± 1.4)	31.1 ± 1.2 (29.2 ± 0.7)	0.2 ± 0.6 (0.4 ± 1.0)	55.4 ± 2.0 (29.1 ± 1.7)	1.4 ± 0.3 (5.6 ± 1.0)	9.7 ± 0.8 (33.9 ± 2.0)	14

A.8 EPMA Elemental Maps

(a) BSE (b) Chromium

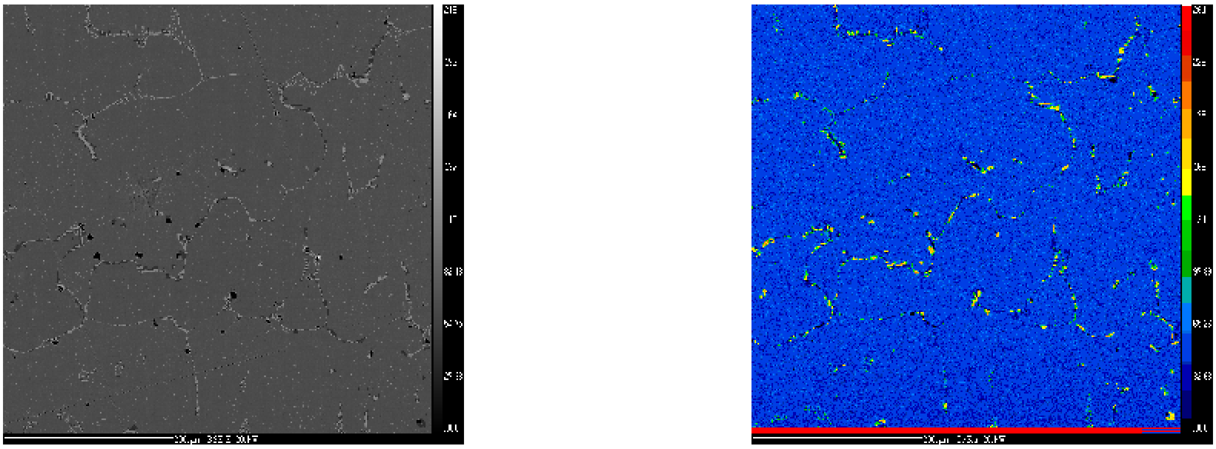

(c) Nickel (d) Niobium

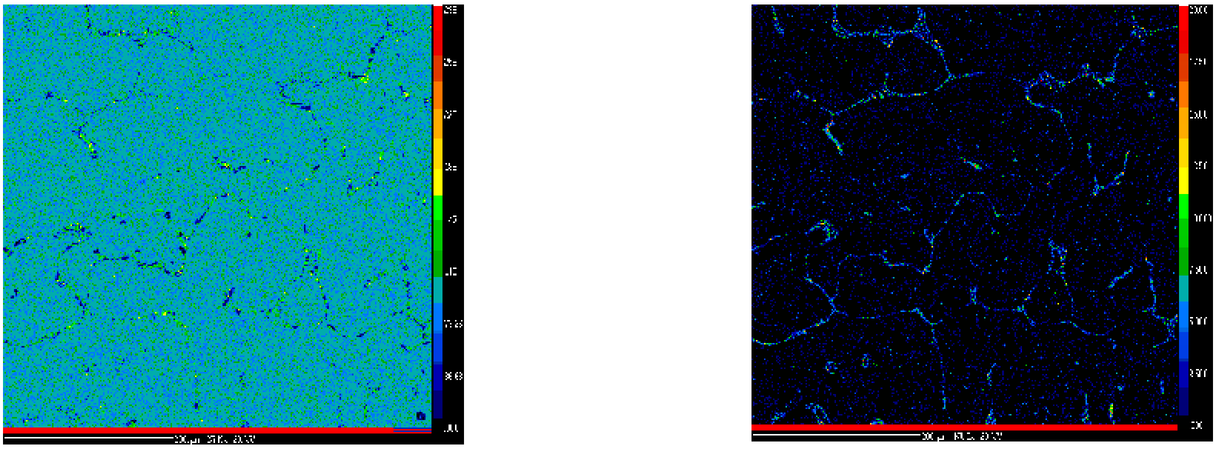

(e) Silicon (f) Carbon

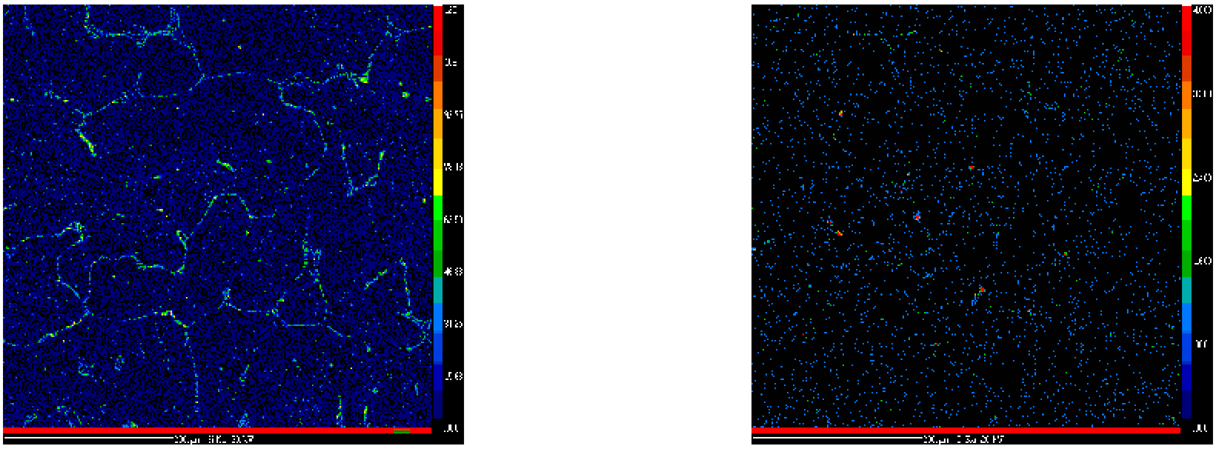

Figure A.13: EPMA maps of a static cast ex-service component that has been aged for 3 years after solution annealing.

A.9 Solution annealed Aging Micrographs

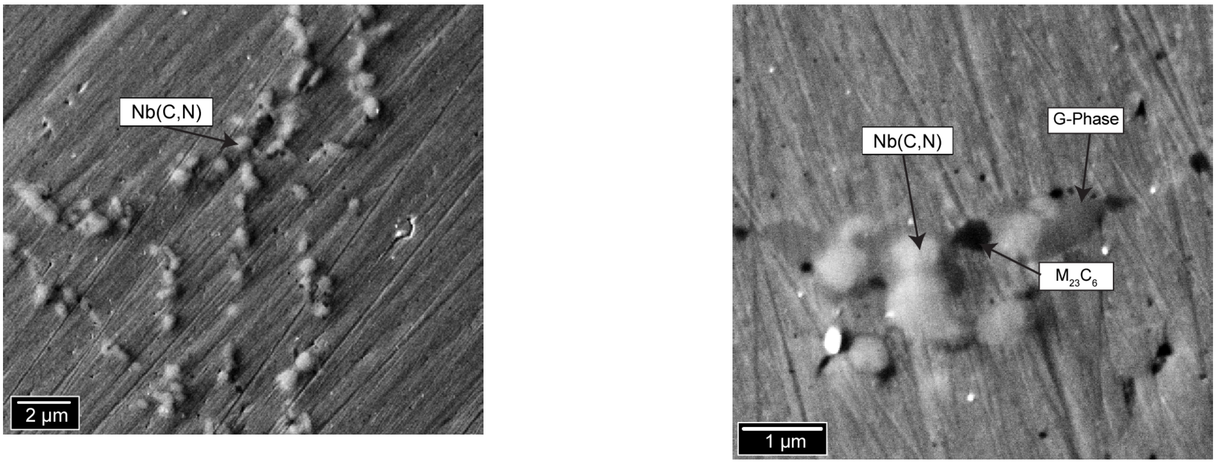
(a) 1 Week

(b) 2 Weeks

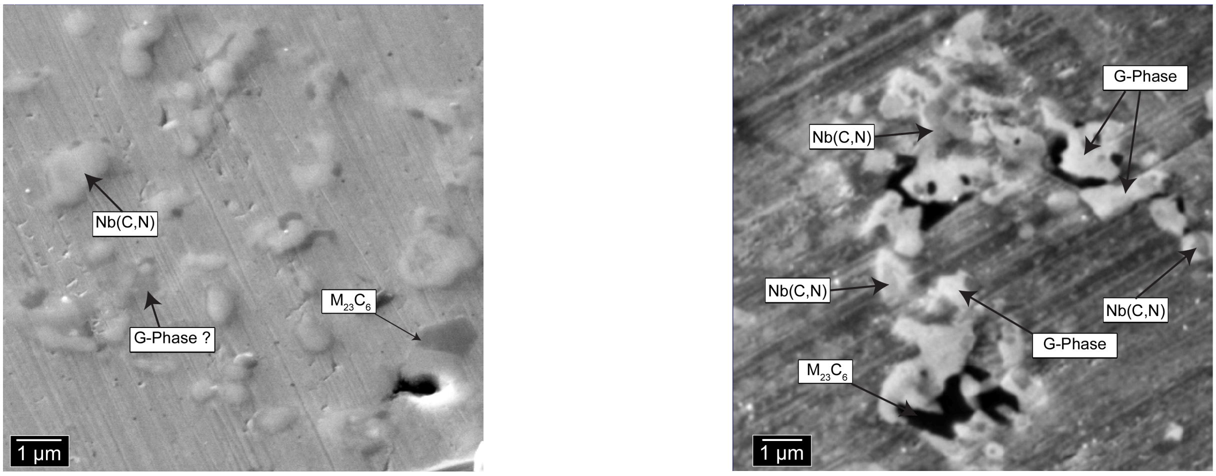
(c) 1 Month

(d) 2 Months

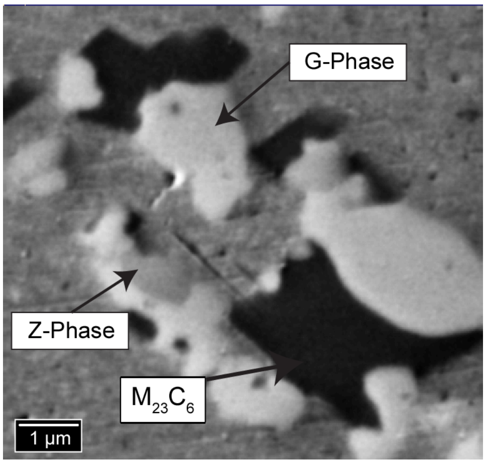
(e) 1 Year

Figure A.14: AES micrographs of the solution annealed microstructure at various aging times.

A.10 Cast Aging Micrographs

(a) Cast (b) 2 Weeks

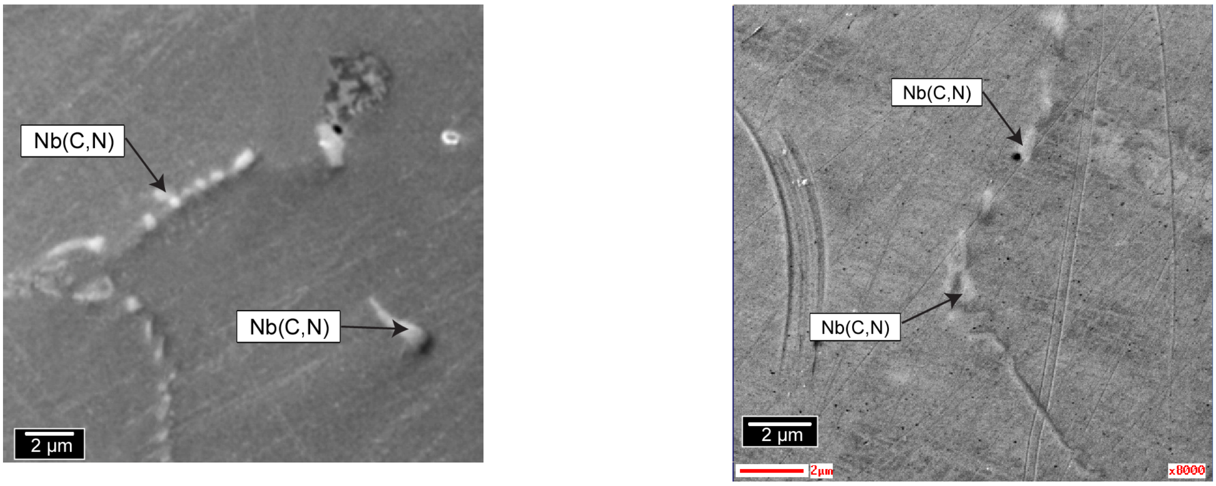

(c) 1 Month (d) 2 Months

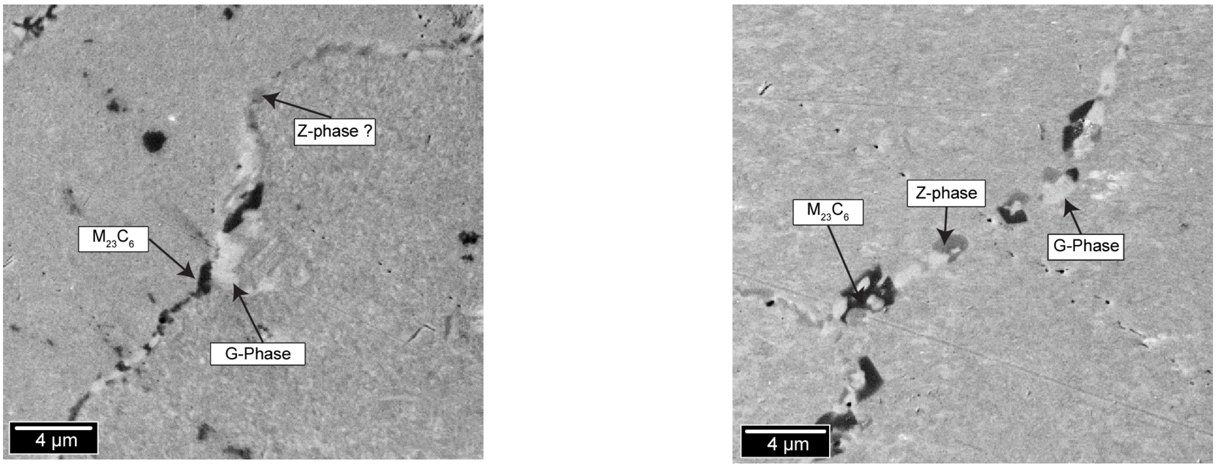

(e) 4 Months

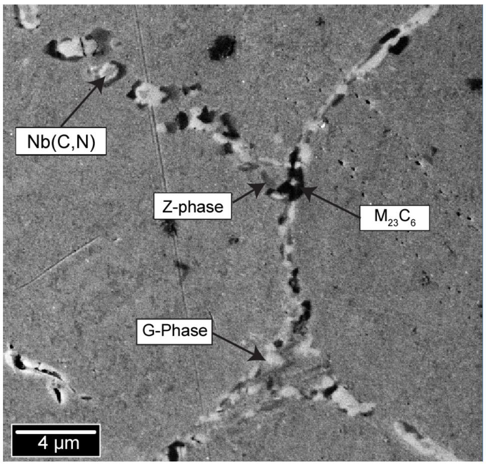

Figure A.15: AES micrographs of the cast microstructure at various aging times.

A.11 Volume Fraction Data

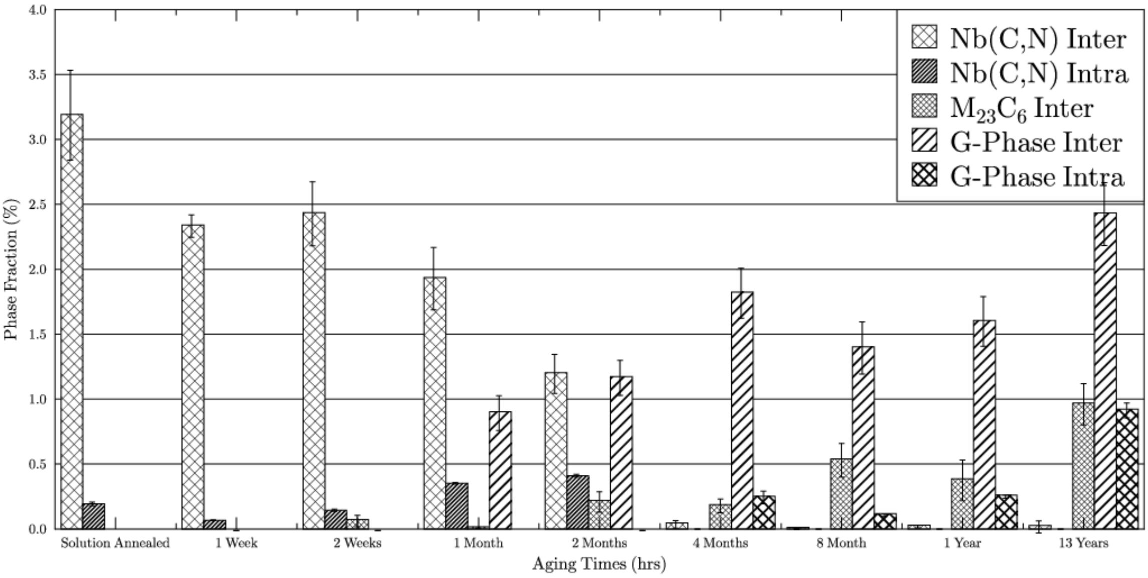

Figure A.16: Bar chart of volume fractions of precipitates in the centifugally cast ex-service component after various aging times.

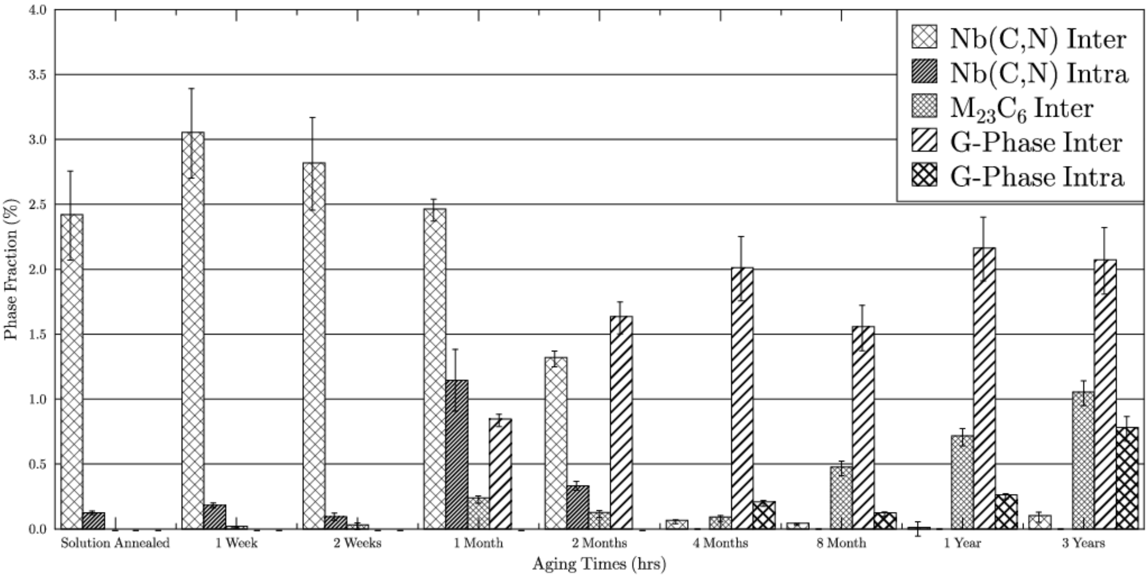

Figure A.17: Bar chart of volume fractions of precipitates in the static cast ex-service component after various aging times.

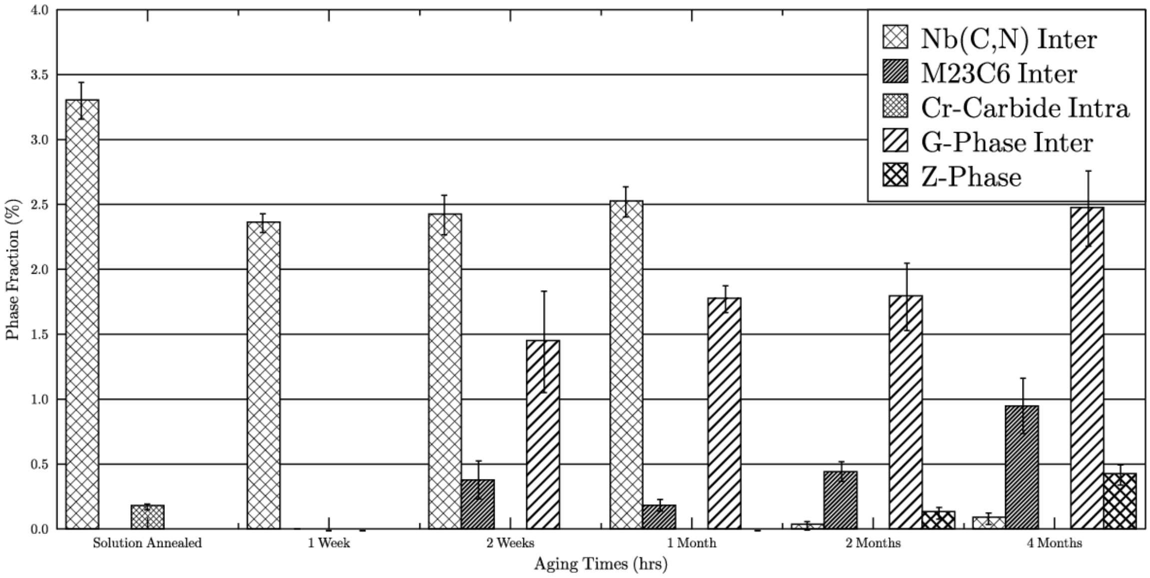

Figure A.18: Bar chart of volume fractions of precipitates in the button melted ex-service 2032Nb sample

A.12 Precipitation Size Data

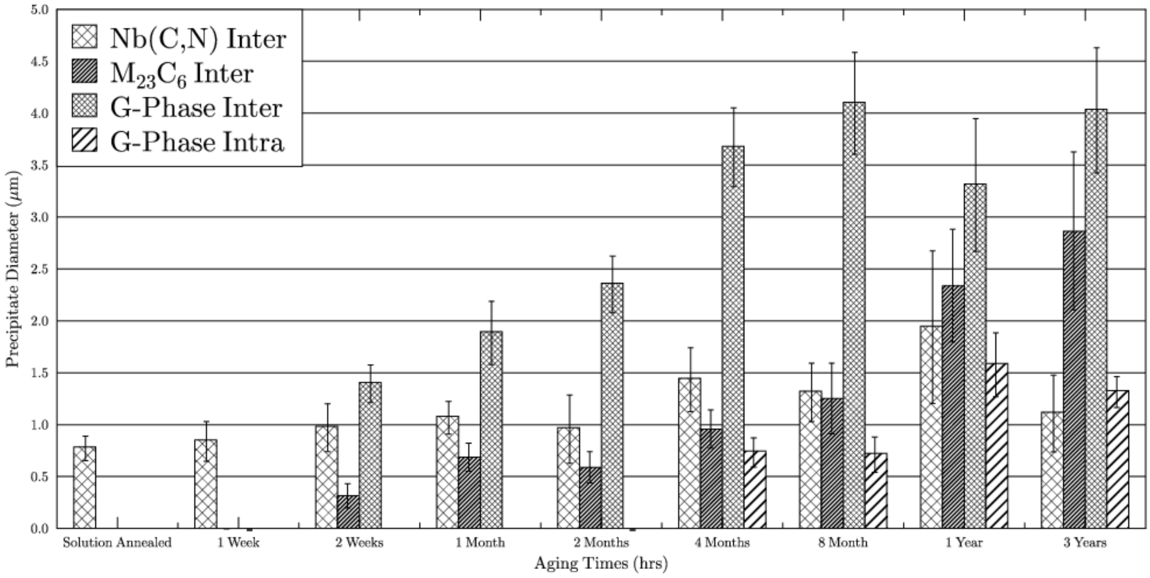

Figure A.19: Bar chart of effective diameters of precipitates during aging of the centrifugally cast ex-service component.

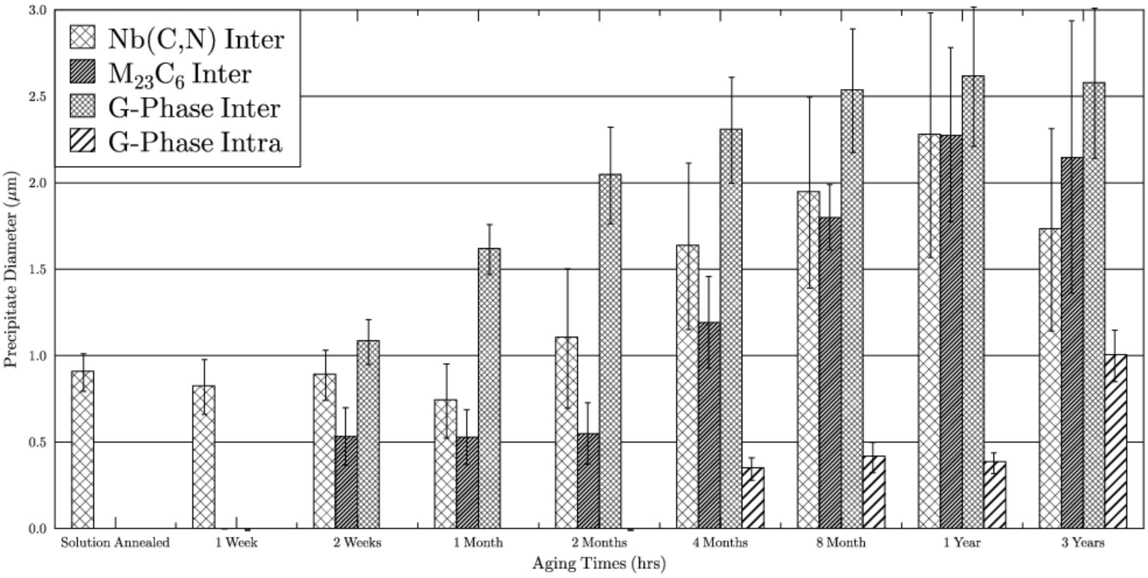

Figure A.20: Bar chart of effective diameters of precipitates during aging of the static cast ex-service component.

MetalTek Factorial Experiment Data

A.13 Mechanical Properties

Table A.10: Mechanical properties for each of the MetalTek experimental design treatments, including the yield strength (0.2 YS), the ultimate tensile stress (UTS), and the ductility (RA,E4D) at room temperature.

Treat.	**Chem.**	**HT**	**Thickness (inches)**	**0.2 YS (MPa)**	**UTS (MPa)**	**RA (%)**	**E4D (%)**
(1)	2032Nb	A	1	185.5	479.9	36.3	39
b	2032Nb	A	3	205.5	485.4	39.8	43
a	Super32	A	1	185.5	449.5	44.4	31
ab	Super32	A	3	194.4	464	25.3	29
abc	Super32	D	3	222.7 (ID)	422.0 (ID)	18.1 (ID)	18.9 (ID)
				226.2 (OD)	435.1 (OD)	18.4 (OD)	17.9 (OD)
c	2032Nb	D	1	213.0	495.0	28.9	33.6
ac	Super32	D	1	215.8	486.8	24.3	27.9
bc	2032Nb	D	3	213 (ID)	487.5 (ID)	31.4 (ID)	37.6 (ID)
				215.1 (OD)	487.5 (OD)	31.4 (OD)	37.6 (OD)

Chemistry Optimization

A.14 Nitrogen Factorial Design

A.14.1 Non-linear Regressions

A.14.1.1 Maximum Phase Fraction

$$\begin{aligned}
\mathrm{G-Phase} &= -0.0031 - 0.0032Si + 0.0093Nb - 0.0066C + 0.0023Mn - 0.032N \qquad \text{(A.1)} \\
&+ 0.028Si \times N + 0.014Si \times Nb - 0.0762Nb \times N - 0.0014Si \times Mn + 0.036Si \times Nb \times N \\
&+ 0.0042Si \times Mn \times N \;;\; R^2 = 89.7\% \\
\mathrm{Z-Phase} &= 0.00164 + 0.00216C + 0.00659Mn - 0.00397N + 0.0929Nb \times N \qquad \text{(A.2)} \\
&- 0.0570Si \times Nb \times N \;;\; R^2 = 87.6\% \\
\pi-\mathrm{Phase} &= 0.0011 + 0.00138Si - 0.00502C - 0.0165Mn + 0.247N - 0.00299Si \times N \qquad \text{(A.3)} \\
&- 0.194Nb \times N + 0.116Si \times Nb \times N + 0.00193Si \times Mn \times N - 0.00256N \times Mn \\
&+ 0.00836Nb \times Mn \times N \;;\; R^2 = 94.8\%
\end{aligned}$$

A.14.1.2 Phase Stability Temperature

$$\begin{aligned}
\mathrm{T}_{\mathrm{M_{23}C_6}} &= -243 + 115Si - 306Nb + 9893C + 3937N - 311Si \times N \\
&+ \ 136Si \times Nb - 3479Nb \times C - 446Nb \times N - 1388Si \times C - 445Si \times Nb \times N \\
&+ \ 4297Si \times C \times N - 42358C \times N + 24820Nb \times C \times N \ ; \ R^2 = 81.1\%
\end{aligned} \tag{A.4}$$

$$\begin{aligned}
\mathrm{T}_{\mathrm{G-Phase}} &= 114 + 76.8Si + 252Nb - 1660N + 545Si \times N - 699Nb \times C - 362Nb \times N \\
&- \ 186Si \times C - 110Si \times Nb \times N - 92Si \times Nb \times C + 835Si \times C \times N + 990C \times N \\
&+ \ 1278Nb \times C \times N \ ; \ R^2 = 89.7\%
\end{aligned} \tag{A.5}$$

$$\begin{aligned}
\mathrm{T}_{\mathrm{Z-Phase}} &= -1461 + 1032Si + 816Nb + 870C - 806Mn + 4976N - 3243Si \times N \\
&- \ 1396Nb \times N - 520Si \times Nb + 1361Si \times Mn + 2556Si \times Nb \times N - 2165C \times N \\
&- \ 1178Nb \times C - 404Si \times Mn \times N + 292Mn \times N \ ; \ R^2 = 66.7\%
\end{aligned} \tag{A.6}$$

$$\begin{aligned}
\mathrm{T}_{\pi-\mathrm{Phase}} &= 228 - 330Nb - 69.8C + 2304N + 64Si \times N - 287Nb \times N + 87.8Si \times Nb \\
&+ \ 44.0Cr \times N + 22.6Nb \times Mn \ ; \ R^2 = 83.3\%
\end{aligned} \tag{A.7}$$

A.15 Titanium Factorial Design

A.15.1 Non-linear Regressions

A.15.1.1 Maximum Phase Fraction

$$\begin{aligned} \mathrm{NbC} &= -0.006 + 0.00082Cr + 0.012Si - 0.0070Nb - 0.056C \\ &- 0.0093Ti + 0.097Nb \times C - 0.0007Cr \times Si \\ &+ 0.0018Nb \times Si + 0.0053Nb \times Ti \ ; \ R^2 = 77.9\% \end{aligned} \tag{A.8}$$

$$\begin{aligned} \mathrm{TiC} &= 0.00038 + 0.0091C - 0.0023Nb \times C + 0.076C \times Ti \\ &- 0.0030Si \times C - 0.0014Si \times Ti - 0.030Nb \times C \times Ti \ ; \ R^2 = 71.0\% \end{aligned} \tag{A.9}$$

$$\begin{aligned} \mathrm{G-Phase} &= 0.0036 - 0.0096Si + 0.0079Nb - 0.0065C \\ &+ 0.00040Mn + 0.070Ti - 0.0093Si \times Ti + 0.015Si \times Nb \\ &- 0.041Nb \times Ti + 0.030Si \times Nb \times Ti \ ; \ R^2 = 91.1\% \end{aligned} \tag{A.10}$$

$$\begin{aligned} \mathrm{M_6C} &= -1 + 0.99Si + 2.18Nb + 9.34C - 1.63Si \times Nb \\ &- 15.5Nb \times C - 7.03Si \times C + 11.7Si \times Nb \times C \ ; \ R^2 = 67.0\% \end{aligned} \tag{A.11}$$

$$\begin{aligned} \mathrm{M_{23}C_6} &= 0.00301 - 0.0043Si - 0.00881Nb + 0.311C \\ &- 0.0171Ti + 0.0064Si \times Nb - 0.135Nb \times C - 0.069Si \times C \\ &+ 0.102Si \times Nb \times C + 0.014Si \times Ti \ ; \ R^2 = 90.8\% \end{aligned} \tag{A.12}$$

A.15.1.2 Phase Stability Temperature

$$\begin{aligned}
\mathrm{T}_{\mathrm{(Ti,Nb)C}} &= -133 + 203Si + 26Nb - 243C - 21.4Ti \\
&- 66Si \times Nb - 335Si \times Nb \times C \;;\; R^2 = 79.0\%
\end{aligned} \tag{A.13}$$

$$\begin{aligned}
\mathrm{T}_{\mathrm{M_{23}C_6}} &= -578 + 13009C - 1978Si \times C - 5952Nb \times C \\
&- 12308C \times Ti + 6868Nb \times C \times Ti \;;\; R^2 = 91.3\%
\end{aligned} \tag{A.14}$$

$$\begin{aligned}
\mathrm{T}_{\mathrm{M_6C}} &= 214 - 233Si + 1403Nb + 4623C + 298Ti - 839Si \times Nb \\
&- 3481Si \times C - 224Si \times Ti - 9383Nb \times C \\
&+ 7052Si \times Nb \times C \;;\; R^2 = 62.2\%
\end{aligned} \tag{A.15}$$

$$\begin{aligned}
\mathrm{T}_{\mathrm{G-Phase}} &= 370 + 149Si - 1040C + 362Ti - 210Si \times C + 74.5Si \times Ti \\
&+ 497Nb \times C + 271Nb \times C \times Ti \;;\; R^2 = 96.2\%
\end{aligned} \tag{A.16}$$

$$\tag{A.17}$$

A.16 Linear Programming Output

A.16.1 GLPK Output

A.16.1.1 Nb/(C+N)=6

```
Problem:    chemOpt
Rows:       14
Columns:    7
Non-zeros:  45
Status:     OPTIMAL
Objective:  z1 = 322.1090447 (MINimum)

No.   Row name   St   Activity     Lower bound   Upper bound    Marginal
```

```
------ ------------- -- ------------- ------------- -------------
   -------------
1 z1            B        258.309
2 niHigh        B             31                        34
3 crHigh        B             19                        21
4 siHigh        B            0.5                       1.5
5 nbHigh        B        1.15242                       1.5
6 cHigh         B       0.119174                      0.15
7 nHigh         B      0.0850592                      0.15
8 mnHigh        B        1.18453                       1.5
9 stabRatioHigh
                                                      B      -0.330015

                                                          -0
10 stabRatioLow NL              0            -0                  88.2078
11 Pfactor      NU              9                         9     -3.30861
12 zPhase       NU        -0.0023                   -0.0023     -1169.05
13 piPhase      NU         0.0223                    0.0223     -4574.98
14 m23Temp      B         603.043                       790

No. Column name  St   Activity    Lower bound   Upper bound    Marginal
------ ------------- -- ------------- ------------- -------------
   -------------
1 Nb            B        1.15242          0.5
2 Si            NL           0.5          0.5                   313.311
3 C             B       0.119174         0.05
4 N             B      0.0850592            0
5 Mn            B        1.18453         0.15
6 Cr            NL            19           19                   10.4883
7 Ni            NL            31           31                   1.01573
```

```

Karush-Kuhn-Tucker optimality conditions:

KKT.PE: max.abs.err = 1.14e-013 on row 14
        max.rel.err = 6.80e-017 on row 11
        High quality

KKT.PB: max.abs.err = 0.00e+000 on row 0
        max.rel.err = 0.00e+000 on row 0
        High quality

KKT.DE: max.abs.err = 1.14e-013 on column 3
        max.rel.err = 1.58e-016 on column 5
        High quality

KKT.DB: max.abs.err = 0.00e+000 on row 0
        max.rel.err = 0.00e+000 on row 0
        High quality

End of output
```

A.16.1.2 Nb/(C+N)=7.7

```
Problem:      chemOptStoic
Rows:         14
Columns:      7
Non-zeros:    49
Status:       OPTIMAL
Objective:    z1 = 411.2449283 (MINimum)

```

```
No.    Row name    St    Activity      Lower bound   Upper bound     Marginal
------ ------------ -- ------------- ------------- ------------- 
   -------------
1 z1            B        347.445
2 niHigh        NU            34                            34     -0.355037
3 crHigh        NU            21                            21      -4.04634
4 siHigh        B            0.5                           1.5
5 nbHigh        B        1.25848                           1.5
6 cHigh         B       0.133167                          0.15
7 nHigh         B       0.035104                          0.15
8 mnHigh        NU           1.5                           1.5      -15.4686
9 stabRatioHigh
                                                           NS             0
                                                                         -0
                                                                          =
                                                                    340.204
10 Pfactor       NU            9                             9      -4.44579
11 zPhase        B   -0.00398156                       -0.0023
12 piPhase       B     0.0138761                        0.0223
13 m23Temp       B           590                           790
14 m23TempHigh   NL          590           590                     0.697627

No. Column name  St    Activity      Lower bound   Upper bound     Marginal
------ ------------ -- ------------- ------------- ------------- 
   -------------
1 Nb            B        1.25848           0.5
2 Si            NL           0.5           0.5                      192.209
3 C             B       0.133167          0.05
4 N             B       0.035104             0
5 Mn            B            1.5          0.15
```

```
6 Cr             B                21                19
7 Ni             B                34                31

Karush-Kuhn-Tucker optimality conditions:

KKT.PE: max.abs.err = 5.68e-014 on row 1
        max.rel.err = 6.34e-017 on row 10
        High quality

KKT.PB: max.abs.err = 0.00e+000 on row 0
        max.rel.err = 0.00e+000 on row 0
        High quality

KKT.DE: max.abs.err = 4.55e-013 on column 3
        max.rel.err = 1.01e-016 on column 4
        High quality

KKT.DB: max.abs.err = 0.00e+000 on row 0
        max.rel.err = 0.00e+000 on row 0
        High quality

End of output
```